OPEN ACCESS

University of BRISTOL

This electronic thesis or dissertation has been downloaded from Explore Bristol Research, http://research-information.bristol.ac.uk

Author:
Hayes, Nick R

Title:
Critically Evaluating The Role of The Deep Subsurface In The Chemical Weathering Thermostat

General rights
Access to the thesis is subject to the Creative Commons Attribution - NonCommercial-No Derivatives 4.0 International Public License. A copy of this may be found at https://creativecommons.org/licenses/by-nc-nd/4.0/legalcode This license sets out your rights and the restrictions that apply to your access to the thesis so it is important you read this before proceeding.

Take down policy
Some pages of this thesis may have been removed for copyright restrictions prior to having it been deposited in Explore Bristol Research. However, if you have discovered material within the thesis that you consider to be unlawful e.g. breaches of copyright (either yours or that of a third party) or any other law, including but not limited to those relating to patent, trademark, confidentiality, data protection, obscenity, defamation, libel, then please contact collections-metadata@bristol.ac.uk and include the following information in your message:

• Your contact details
• Bibliographic details for the item, including a URL
• An outline nature of the complaint

Your claim will be investigated and, where appropriate, the item in question will be removed from public view as soon as possible.

Critically Evaluating the Role of the Deep Subsurface in the Chemical Weathering Thermostat

Nicholas Hayes

Supervisors: Heather L. Buss, Dan J. Lunt

A dissertation submitted to the University of Bristol in accordance with the requirements for award of the degree of Doctor of Philosophy in the Faculty of Science

School of Earth Sciences

July 30, 2019

Word Count: 37474

ABSTRACT

The drawdown of atmospheric CO_2 by the chemical weathering of silicate rocks represents one of the primary controls on the long-term climate of the Earth (Walker et al., 1981; Berner et al., 1983). Chemical weathering rates are themselves modulated by climate conditions and atmospheric CO_2 concentrations, with this feedback cycle termed the ”Chemical Weathering Thermostat”. However, the depth at which weathering occurs, and to what extent different parameters affect weathering, is poorly constrained and hinders our ability to investigate the impact of weathering on climate in palaeo settings.

This thesis investigated weathering-climate interactions at a range of spatial and temporal scales. Initially, the impact of climate on weathering profile morphology and chemical weathering rates were examined at the profile-scale using geochemical data from granitic field sites in the literature, as well as new analyses from a temperate granitic critical zone. Secondly, Reactive Transport Modelling was used to simulate the response of simple granitic weathering profiles to differing climate regimes and subsurface architecture conditions. Finally, insights from field site investigations and Reactive Transport Modelling were applied to the global scale using a coupled geochemical and climate model, GEOCLIM, to investigate the impact of changing palaeogeography on potential weathering fluxes through the Cretaceous-Eocene period.

This thesis identifies a strong hydrological control on chemical weathering rates, supporting the findings of previous studies (Maher, 2010; Goddéris et al., 2014; Ibarra et al., 2016) and further challenging the concept of global temperatures as a strong control on chemical weathering rates. Furthermore, climate conditions determine the morphology of a weathering profile. Under humid conditions, weathering fronts become sharper and the impact of temperature is amplified. Finally, palaeogeographical configurations have a substantial impact on long-term CO_2 concentrations by affecting the distribution of precipitation/runoff and thus chemical weathering rates.

Author's Declaration

I declare that the work in this dissertation was carried out in accordance with the requirements of the University's Regulations and Code of Practice for Research Degree Programmes and that it has not been submitted for any other academic award. Except where indicated by specific reference in the text, the work is the candidate's own work. Work done in collaboration with, or with the assistance of, others, is indicated as such. Any views expressed in the dissertation are those of the author.

.....

Nicholas Hayes

July 30, 2019

Acknowledgments

A huge number of people have in some way, great or small, helped the production of this thesis and as such it is nigh impossible to thank them all (although I will give it a good go). Below are the people, groups, items, and concepts that have made a big difference over the last three and a half years.

First and foremost I want to thank my supervisory duo of Heather and Dan, who have managed the mammoth task of dealing with my general blundering, intermittent ineptitude, and heavy to industrial scale pessimism and helped craft this thesis. Undoubtedly, it would have been impossible without them, so a big thank you for all your help over the past three and a half years! It's been a great pleasure working with you both, and thank you for putting up with all of my moaning when models didn't work!

In addition to my supervisors, there have been a host of people with whom I have collaborated and all have helped make this thesis possible. In no particular order, I want to send a big thank you to Ollie Moore, Maria Chapela Lara, Pavel Krám, Jenny Druhan, Yves Goddéris, Stuart Kearns, Ben Buse, Rich Pancost, Rachel Flecker, and Laura Robinson. I also want to thank T-GRES and the ERC for funding my PhD project meaning that I did not have to live on spaghetti hoops and toast for three and a half years and also enabling my reading addiction, which undoubtedly has been as culturally enriching as it may have been financially draining.

The denizens of G44 have also helped by coming to my rescue when I have played fast and loose with the rules of mathematics or broken chemistry, so thank you to my fellow dungeon dwellers. They, along with the regular lunch crowd have also kept lunchtimes entertaining with bizarre conversations which have (probably) helped me maintain my sanity over the past three and a half years.

I also want to thank Ludwig Roselius and co who in 1903 stumbled upon the process of decaffeination. Without this serendipitous discovery, my love of coffee would likely have led to me never sleeping again.

Finally, I want to thank The Witch. With the completion of this thesis, I guess she has been found at last.

Contents

List of Figures

List of Tables

Chapter 1

Introduction to Silicate Chemical Weathering and the Chemical Weathering Thermostat

Chemical weathering is the process by which minerals are broken down by chemical interactions with their environment (Ebelman, 1845). The majority of silicate minerals are unstable under surface conditions and as a result these minerals will be broken down by a range of reactive processes, such as dissolution by interaction with acidic aqueous solutions or oxidative reactions (e.g., Fletcher et al., 2006; Brantley et al., 2014). Although chemical weathering is a relatively slow process, requiring 10^3 to 10^6 years to weather metres of rock (e.g, Berner et al., 1983; Brown et al., 1995; Chabaux et al., 2013; Goddéris et al., 2014; Vázquez et al., 2016), its impacts have significant implications at the level of human lifetimes. In the geological short term ($<10^3$ years), chemical weathering is responsible developing soils and releasing nutrients (especially Ca, K, Mg, and Na) into the environment. This process can determine soil fertility and shape ecosystems (e.g., Brantley et al., 2007; Brantley and Lebedeva, 2011; Krám et al., 2012). As a result, understanding chemical weathering processes provide key insights for industries such as agriculture, and for policymakers managing food supplies (Oliver and Gregory, 2015). On geologically long timescales ($>10^6$ years), chemical weathering plays a role in shaping landscapes and, perhaps most crucially, moderating global climate and as a result ensuring the long-term habitability of the planet (Berner et al., 1983; Taylor et al., 2015).

Studying chemical weathering is complicated by its many interactions with the environment. At the most fundamental level, chemical weathering is believed to be determined by climate conditions (e.g., Walker et al., 1981; Berner et al., 1983; White and Blum, 1995; Dessert et al., 2003; Oliva et al., 2003; West et al., 2005; West, 2012). However, chemical weathering of silicate minerals in turn affects climate conditions by drawing down CO_2 (Walker et al., 1981; Berner et al., 1983). Chemical weathering also affects the chemistry of the environment around it, altering reaction rates

and processes (e.g., Maher, 2010, 2011).

As a result of both the short and long-term implications, understanding chemical weathering, its effects on the environment, and the processes involved holds great value for scientists from a range of different fields. For example, chemical weathering releases nutrients to the environment and produces soils, and thus understanding the processes involved in weathering has implications for geomorphologists, biologists, ecologists, and geochemists (e.g., Banwart et al., 2012; Giardino and Houser, 2015; Oliver and Gregory, 2015). In the context of this thesis however, chemical weathering is primarily of interest due both to its ability to affect the long-term climate of the Earth and the impact of climate on chemical weathering processes.

1.1. Weathering, Climate, and Environmental Feedbacks

1.1.1. Climate Interactions

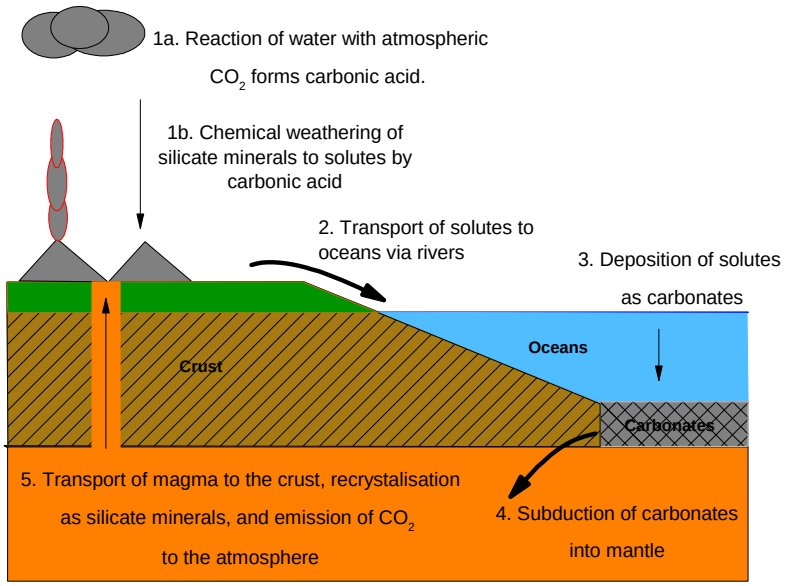

Figure 1.1: Simplified overview of the Chemical Weathering Thermostat. (1a-b) Atmospheric CO_2 produced by volcanic degassing reacts with water in the atmosphere to produce carbonic acid, which reacts with silicate minerals producing bicarbonate and base cations. These weathering products are transported (2) to the oceans, where they are deposited (3) as carbonate rocks. These carbonates are eventually subducted (4) and incorporated into magma bodies, where they are eventually re-incorporated (5) into the crust as intrusive rocks or erupted by volcanoes.

Over geological timescales, chemical weathering is believed to be one of the primary factors moderating global climate (Walker et al., 1981; Berner et al., 1983; Foster et al., 2017). In the atmosphere, CO_2 (from volcanic degassing) reacts with water to produce carbonic acid (Equation 1.1.), resulting in precipitation that is slightly acidic. The acidic precipitation reacts with silicate minerals (such as Ca bearing anorthite; Equation 1.2.) producing bicarbonate and base cations, which are transported to the oceans via rivers and runoff. Within the oceans, bicarbonate and the base cations are deposited as carbonate rocks, effectively sequestering atmospheric CO_2 until these carbonates are subducted and incorporated into magma bodies (Berner et al., 1983, Figure 1.1).

$$CO_2\,(g) + H_2O\,(aq) = H_2CO_3\,(aq) \tag{1.1}$$

$$CaAl_2Si_2O_8\,(s) + H_2CO_3\,(aq) + H_2O\,(aq) + H^+ = Ca^{2+}\,(aq) + 2\,HCO_3{}^-\,(aq) + Al_2Si_2O_5(OH)_4\,(s) \tag{1.2}$$

The breakdown of silicate minerals removes CO_2 from the atmosphere, in turn reducing the acidity of precipitation and reducing weathering rates. Within the atmosphere, CO_2 acts as a greenhouse gas, reducing the outgoing flux of shortwave radiation from the Earth to space. As such, higher quantities of atmospheric CO_2 result in warmer global temperatures. In turn, warmer global temperatures increase evaporation rates, resulting in increased precipitation rates. Similarly, lower atmospheric CO_2 concentrations result in a cooler and drier global climate. As such, any significant change in CO_2 levels ($>$ 100 ppm) will also result in changes to the climate, which in turn is known to be a control on chemical weathering rates, with warmer and more humid conditions typically resulting in faster weathering rates (e.g., Dessert et al., 2003; Oliva et al., 2003; West et al., 2005; Goddéris et al., 2014). This climate-weathering feedback system is known as the chemical weathering thermostat, and although it represents one of the key controls of long-term climate, the factors that influencing climate-weathering feedbacks are not well constrained.

Multiple studies have found relationships between chemical weathering rates and climate variables (e.g., temperature, precipitation, runoff), although such studies often disagree on which variable exerts the strongest influence (Berner et al., 1983; Oliva et al., 2003; Riebe et al., 2004; West et al., 2005). Early research into weathering-climate feedbacks modelled the weathering response as an Arrhenius relationship, assuming temperature to be the controlling factor on chemical weathering rates (Berner et al., 1983). Some studies have found a temperature control on weathering rates; monitoring of stream solute fluxes from basaltic catchments in Iceland found an increase in weathering rates as temperatures increased over a four-decade period (Gislason et al., 2006). However, precipitation is also enhanced under warmer conditions due to warmer air being able to hold more moisture. Precipitation is also believed to exert an influence on

weathering rates, as water is the primary solvent involved in the dissolution of silicate minerals, while the amount of water has implications for geochemical saturation states with respect to weatherable minerals (Maher, 2010; Maher and Druhan, 2014). Thus, the abundance of water present is believed to impact silicate weathering rates. Indeed, Gislason et al. (2006) also identified a roughly proportional increase in chemical weathering rates as runoff increased. The inherent interconnectivity between temperature and precipitation complicates efforts to separate the individual effects of the two climate variables, especially as the regions in the world where precipitation is greatest (e.g., tropical mountain ranges) often also exhibit high mean annual temperatures.

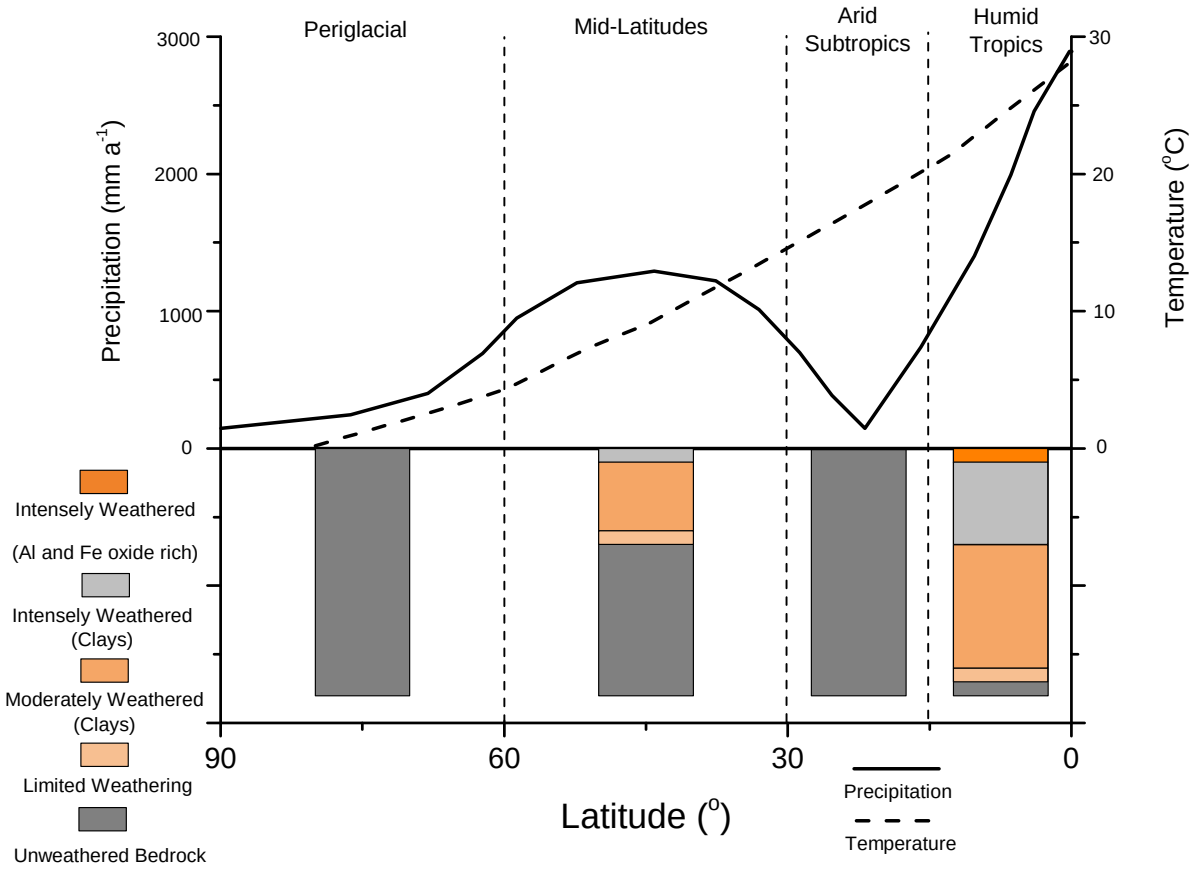

Figure 1.2: Simplified schematic of general trends in weathering intensity and morphology with latitude, showing approximate mean annual precipitation and temperature values and typical weathering profiles. Typically, weathering is limited in arid regions, such as periglacial or arid subtropical environments, while more intense and deeper ($>$ 10 m) weathering occurs in the humid mid latitudes, with the most intense weathering occurring within the humid tropics. Based on Strakhov (1967).

Regardless of the individual impact of different variables, climate is well established as a control on chemical weathering rates and is sufficiently well understood that broad latitudinal trends in weathering morphologies can be drawn (Strakhov, 1967, Figure 1.2). Tropical environments often

exhibit layers of weathered material (regolith) that are thick (> 10 m) and intensely weathered, although only low intensity weathering occurs in the subtropical desert regions (Strakhov, 1967). More intensely weathered environments typically have high weathering rates and weathering fluxes (e.g., White and Buss, 2014), although there are some intensely weathered environments with low weathering rates (e.g., Braun et al., 2005; Hewawasam et al., 2013). Regolith thickness and intensity increases again at the temperate mid-latitudes, but weathering intensity is typically lower than in the tropics, and weathering is limited in the cool and arid polar regions.

1.1.2. Environmental Interactions

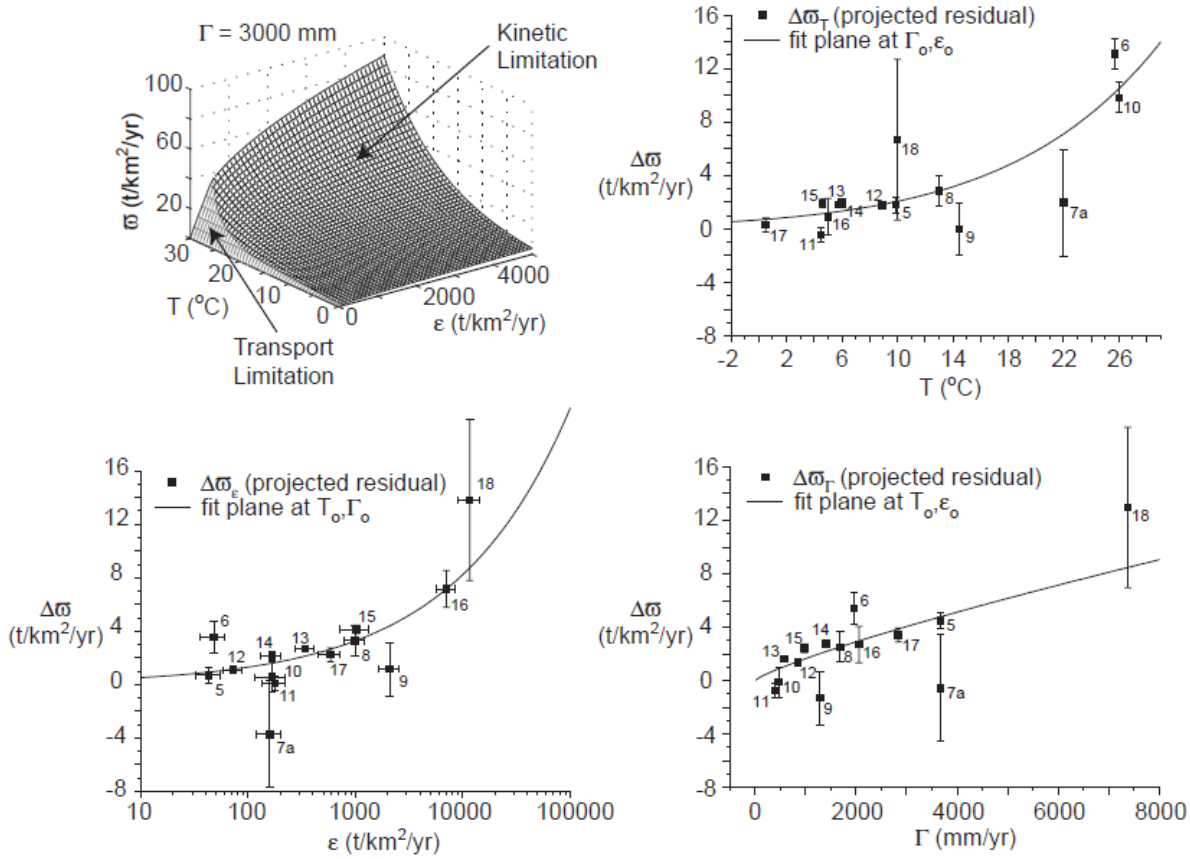

Figure 1.3: Four panels showing chemical weathering rates,ω (compiled from literature data by West et al. (2005)) in response to varying temperature $T\,^{\circ}C$ (top-right), runoff Γ (bottom-right), erosion ε (bottom-left) and all three factors as a combined plot (top-left). The top-left panel shows that chemical weathering rates are limited under low erosion rates, but high weathering rates occur under high erosion rates in warm-humid climates. From West et al. (2005).

Although the chemical weathering thermostat is primarily a feedback between chemical weathering and climate, the effects of physical weathering, primarily erosion, are also believed to exert an impact on chemical weathering rates (e.g, Riebe et al., 2004; West et al., 2005; West, 2012; Ferrier and West, 2017). Erosion removes weathered material from the surface, exposing fresh material to weathering (e.g., Viers et al., 2014). The thickness of the regolith may also

affect weathering rates, with thick regolith layers reducing the exposure of unweathered bedrock to reactive fluids, while thinner regolith layers promote weathering by increasing the exposure of weatherable minerals to reactive fluids (Gabet and Mudd, 2009). Since chemical weathering produces regolith, and physical erosion removes regolith, the balance of these two processes is important (Dosseto et al., 2011). In many locations, regolith thickness is considered to be in steady-state over geological timescales, where chemical weathering and physical erosion are in balance such that regolith thickness remains effectively constant (e.g., White, 2002; Phillips, 2010). A steady-state regolith thickness is often assumed for the purposes of weathering rate calculations, an assumption considered to be something of 'a convenient fiction' (Phillips, 2010).

The interactions between chemical and physical weathering become quite significant at the global scale, and on geological timescales raises questions about the role of tectonics in moderating the Earth's climate (e.g., Raymo and Ruddiman, 1992; Ruddiman, 1997; Hilley and Porder, 2008). Erosion is typically high in active mountain belts, such as the Southern Alps of New Zealand (Larsen et al., 2014) and on volcanic islands (Gaillardet et al., 2012). If erosion promotes weathering rates by exposing fresh material at the surface, periods of mountain building may be associated with enhanced drawdown of atmospheric CO_2 due to increased chemical weathering (e.g., Dupont-Nivet et al., 2008). Indeed, it has been proposed that the transition of the Earth from a greenhouse to an icehouse state during the mid-Cenozoic was due to the weathering of the developing Himalayan range (Raymo and Ruddiman, 1992). This hypothesis has been disputed, with some arguing that the Himalayan range contains too few silicates relative to carbonates to have caused a sufficient magnitude of CO_2 drawdown seen at the end of the Eocene (e.g., Goudie and Viles, 2012), while others have proposed alternative hypotheses that do not invoke tectonically enhanced CO_2 drawdown, such as the potential role of land plants in attenuating varaibiltiy in long-term CO_2 concentrations (Pagani et al., 2009).

Vegetation's effect on chemical weathering rates is also unclear. Some studies conclude that weathering is massively enhanced on the order of 10-60 times by vegetation (Berner et al., 1983; Lenton et al., 2012; Porada et al., 2014, 2016). Vegetation is believed to enhance chemical weathering through both chemical and physical means. The root zones of plants release CO_2 into the soil, leading to greater acidity in the subsurface, while roots also cause fractures in rock, exposing a greater surface area to weathering (e.g., Morris et al., 2015; Quirk et al., 2015). This enhancement by vegetation has led some to conclude that the large and sustained falls in atmospheric CO2 during the Ordovician and the Devonian periods were associated with the evolution of early plant life and their subsequent enhancement of chemical weathering (Lenton et al., 2012).

In contrast, other studies have concluded that vegetation only has modest impacts on weathering rates (˜1.5 times greater), or in some cases actually reduce weathering rates (e.g., Drever and Zobrist, 1992; Drever, 1994; Lawrence et al., 2014). Drever and Zobrist (1992) found that the

increases in acidity from vegetation had relatively limited impacts on weathering rates, while Lawrence et al. (2014) found that although vegetation caused an initial increase in weathering rates, organic compounds released from vegetation increased the content of Al in solution, which had the effect of suppressing feldspar weathering rates. Debate continues as to the effects of vegetation on chemical weathering rates, and further research will likely be needed to better understand these impacts, and to distinguish between purely vegetation induced effects and those from the climate conditions prevalent in the wider environment.

1.2. The Critical Zone

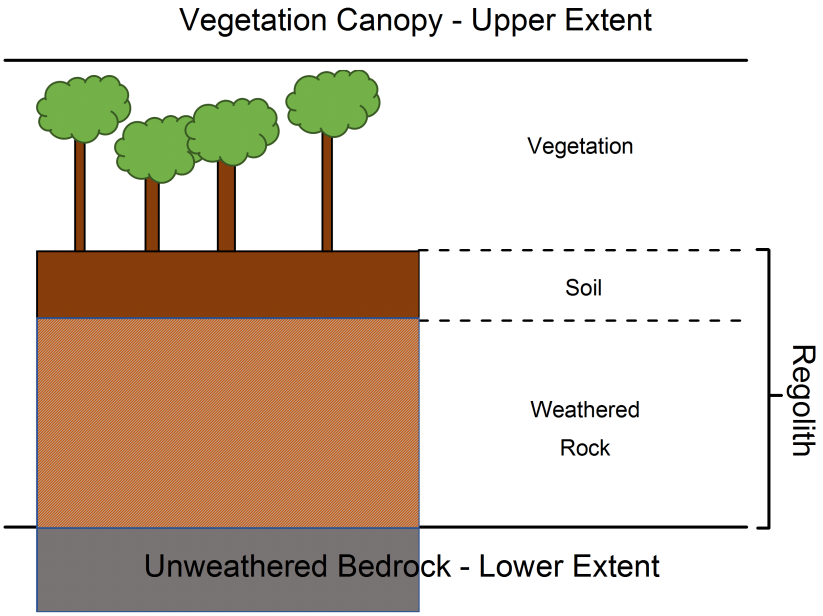

Figure 1.4: Simplified schematic of the extent of the Critical Zone, which is considered to extend from the top of the vegetation canopy to boundary between weathered and unweathered bedrock. Weathered material exhibits different physical and chemical characteristics with varying degrees of weathering, with different terms used to describe such characteristics. Typically, all disaggregated material overlying is broadly referred to as regolith.

Because of its inherent complexity, study of the area in which chemical weathering occurs, known as the Critical Zone, has been defined as its own field of science (e.g., Giardino and Houser, 2015). Although the definition has evolved over time, the Critical Zone is commonly and broadly defined as the zone extending from the top of the tree canopy to the depth of unweathered bedrock (Brantley and Lebedeva, 2011; Giardino and Houser, 2015). The Critical Zone can also be thought of as the

area where multiple Earth systems interact, including the lithosphere, atmosphere, biosphere, and sometimes the cryosphere (Brantley et al., 2007; Gamache et al., 2015). These definitions exclude weathering in marine environments or as a result of hydrothermal activity, focusing rather on the interactions with meteoric and "freely circulating" groundwater (Giardino and Houser, 2015).

Specific sites, known as Critical Zone Observatories (CZOs), have been established to study interactions between particular processes and the Critical Zone (e.g., White et al., 2015). The interactions of forest management (White et al., 2015) or pollution recovery (Krám et al., 2012) with the Critical Zone are but two examples of many monitoring schemes built upon the interdisciplinary science enabled by CZOs (Banwart et al., 2012). Critical Zone science is by its very nature multidisciplinary, requiring expertise from fields such as geology, biology, chemistry, and climatology to fully investigate the nature of chemical weathering (Li et al., 2017). Critical Zone observatories have contributed significant quantities of data on chemical weathering, providing invaluable insights into the relationships between chemical weathering and the wider environment (e.g., Braun et al., 2005; Dethier and Lazarus, 2006; Buss et al., 2008; Ma et al., 2011; Krám et al., 2012)

1.3. Weathering Processes and Controls

Although there are a range of reactions that occur as a result of chemical weathering, the primary silicate weathering reaction is the aqueous dissolution of silicate minerals by carbonic acid, typically in the form of precipitation (Equations 1.1 and 1.2). Typically, silicate weathering is accelerated under more acidic conditions and higher temperatures (e.g., Viers et al., 2014; Brantley et al., 2014). The chemical and physical composition of the rock (termed lithology) also affects weathering rates. Early weathering studies noted that minerals that crystallised out of magmas at higher temperatures were those that weathered most quickly, and minerals that crystallised at lower temperatures were less susceptible to weathering (Goldich, 1938). This relationship is known as the Goldich Stability Series, occurring due to increased linkage between silica tetrahedra within minerals that crystallise at lower temperatures, while minerals that crystallise at high temperatures have fewer links between silica tetrahedra and are more susceptible to weathering (Goldich, 1938). As such, mafic rocks like basalt and gabbro typically weather more rapidly than their felsic counterparts, such as rhyolite and granite (e.g., Dessert et al., 2003).

While the Goldich Stability Series is accurate in principal, in reality many other factors act to determine weathering rates beyond mineral composition (e.g., White and Buss, 2014). As a result, lithological composition is not always a good predictor of weathering rates, especially where differences in lithological composition are comparatively minor, such as those distinguishing different granite sub-types (e.g., plagioclase composition and abundance) (e.g., Melfi et al., 1983; Oliva et al., 2003). Similarly, studies investigating the effect of mineral surface area on weathering rates indicate that greater surface area promotes weathering rates (e.g., Brantley and Mellott, 2000;

Sak et al., 2010).

1.4. Weathering Profiles and Weathering Fronts

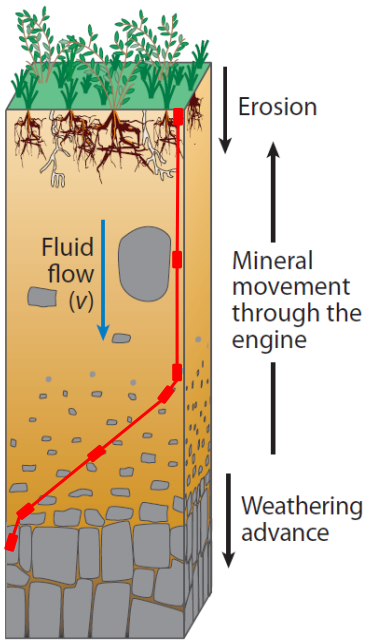

Figure 1.5: 1D schematic of a weathering profile and key processes, described as the "weathering engine". Red line and squares represent the weathering front, showing the location and degree of weathering from the bedrock boundary, which increases towards the surface as weatherable minerals are dissolved by contact with reactive fluids (fluid flow). The weathering boundary moves downward through the bedrock and weathered material is removed at the surface by erosion. Modified from Brantley and Lebedeva (2011).

The physical and chemical changes that occur as a result of weathering produce distinct morphologies in terms of rock structure, chemical composition, and physical appearance (e.g., Strakhov, 1967, Figure 1.5). Silicate minerals within the bedrock are dissolved by reactive fluids and release base cations and other elements into the environment, with minerals such as plagioclase eventually weathering to form secondary clay minerals such as kaolinite (Melfi et al., 1983). There are terms to describe particular states of weathered material, such as saprolite, where the physical structure of the rock has been altered but has weathered isovolumetrically (e.g., Brantley and Lebedeva, 2011). However, many weathering studies do not make such distinctions, referring to any weathered material as regolith regardless of the degree of weathering or structural changes (e.g., Dosseto et al., 2012). Regolith covers the zone from the surface to unweathered bedrock;

referred to as a weathering profile within Critical Zone science (e.g., Brantley et al., 2008). These profiles can either be observed as outcrops in the field (e.g., Vázquez et al., 2016) or reconstructed from drill-core data (e.g., Buss et al., 2008).

Weathering profiles exhibit a wide range of physical appearances, physical structures, chemical compositions, and thicknesses, reflecting the processes occurring within the local weathering environment. Some show only limited weathering (Vázquez et al., 2016), other show relatively shallow but intensely weathered regolith (Hewawasam et al., 2013; Buss et al., 2017), while others display extensive weathering resulting in 10s of metres of regolith (Braun et al., 2005; Yusoff et al., 2013). Weathering profiles can be determined from visual analysis, observing the transition from fresh bedrock to weathered material, or from tracing mass and mineral losses using geochemical and mineralogical data (Brimhall and Dietrich, 1987; Anderson et al., 2002; White, 2002).

The area or areas over which significant weathering occurs within a weathering profile is referred to as a weathering front (Brantley et al., 2008). These fronts show significant variation in intensity and extent. Fronts causing gradual weathering over 10s of metres have been observed in some profiles (e.g., White et al., 2001; Vázquez et al., 2016), while other profiles exhibit small, intense fronts that transition rapidly from fresh to near-totally weathered material over sub-metre scales (e.g., Buss et al., 2008; Yusoff et al., 2013). In some profiles, multiple active weathering fronts have also been observed (Turner et al., 2003). The sharpness of the weathering front (i.e., the distance between unweathered bedrock and near-totally depleted material or the surface) is known as the weathering gradient. The processes controlling the morphology and intensity of weathering fronts and gradients are still not well understood but are likely controlled by a combination of intrinsic characteristics within the rocks (e.g., chemical composition, porosity, mineral grain sizes), and extrinsic characteristics determined by the local environment (e.g., temperature, water supply, and water chemistry) (Maher, 2010; Bazilevskaya et al., 2013; Brantley et al., 2014)

Granitic lithologies show a particularly wide array of weathering morphologies accompanied by significant variation in weathering depth and intensity (e.g., Bazilevskaya et al., 2013). For example, weathering profiles in the Río Icacos catchment all show intense weathering but vary significantly in thickness, ranging from 5-30 m (Orlando et al., 2016). These profiles contrast with the thick but only lightly weathered Curacavi weathering profile, for example (Vázquez et al., 2016). It is unclear why such a degree of variability should exist within this lithological group. Granites exhibit some lithological variability, primarily expressed as differences in the abundance and composition of feldspar phases (e.g., albite and anorthite) (e.g., White et al., 2001). While large scale lithological variation (i.e., mafic vs felsic) has been shown to have an impact on weathering rates (Dessert et al., 2003; Viers et al., 2014), the differences between granites may be too small to have a significant effect (e.g., White et al., 2017). Structural differences, such as mineral surface area and connected porosity may be a potential cause for the variability in weathering morphologies; granites tend to have a much greater degree of connected porosity relative to more

rapidly weathering lithologies, such as a basalt (e.g., Bazilevskaya et al., 2013). A higher degree connected porosity would allow for greater penetration of water into the bedrock and potentially permit deeper weathering (White et al., 2001). Variations in initial porosity may represent a control on the depth of granitic profiles, although as with mineral surface area, it is exceptionally difficult to determine the possible impact of initial porosity on weathering profiles from field data.

1.5. Quantifying Weathering

Although significant quantities of weathering data have been gathered from field sites, laboratory studies have also been used to explore weathering under experimental conditions (e.g., White and Brantley, 2003; White et al., 2017). Laboratory studies have the advantage of being able to observe and measure weathering under controlled conditions, however laboratory studies are conducted on far shorter timescales (i.e., 1-10 years) relative to the timescales of weathering profile development (e.g., White et al., 2017). Additionally, laboratory studies often produce weathering rates that are orders of magnitude faster than those measured from field data (e.g., White and Brantley, 2003). In contrast, field data capture weathering processes that are occurring on 10^3 – 10^6 year timescales, but it can be difficult to detangle the individual impacts of factors affecting weathering (e.g., climate, erosion).

Weathering fluxes and rates can be measured in a number of ways, either from analysis of weathering profiles (i.e., solid-state) or from solutes in streamwater (e.g., White and Buss, 2014), with time constraints provided by inflitration or discharge rates. Weathering fluxes and rates calculated from streamwater solute concentrations are typically normalised to the watershed scale (e.g., White et al., 1999). Within weathering profiles, weathering rates and fluxes can be calculated from elemental concentrations (obtained using geochemical analysis techniques such as inductively coupled plasma mass spectrometry (ICP-MS)) and from changes in mineral abundance with (e.g., White et al., 2001; Buss et al., 2008; Vázquez et al., 2016). Time constraints on weathering profiles can be obtained using isotopic age estimates from ^{10}Be (e.g., Brown et al., 1995) or U/Th disequilibria (e.g., Chabaux et al., 2013).

A number of techniques have been developed to provide quantitative estimates of weathering degrees and rates. This section will summarise some of the more commonly used methods.

1.5.1. Chemical Index of Alteration

The Chemical Index of Alteration (CIA) (Nesbitt and Young, 1982) estimates the degree of weathering using the ratio of Al_2O_3 to the oxides of Ca, K, and Na within a sample, and assumes that Al is immobile during weathering. Chemical Index of Alteration values are useful for determining the degree of weathering present in a sample, if conclusively unweathered samples are unavailable, or if microscopic analyses are not possible.

$$CIA = \frac{Al_2O_3}{Al_2O_3 + CaO + K_2O + Na_2O} * 100 \tag{1.3}$$

The Chemical Index of Alteration returns a dimensionless value between 0 and 100, with 100 indicating total loss of the base metal oxides. Values for fresh silicates typically range between 30 and 55, with fresh basalt being between 30 and 40 and fresh granites between 40 and 55 (Bahlburg and Dobrzinski, 2011). Values below 30 are typically only reached in samples where minerals such as calcite are in high abundance (Bahlburg and Dobrzinski, 2011).

1.5.2. Mass Transfer

Many weathering studies frame weathering as a mass transfer process, which is quantified using an approach developed in the late 1980s by Brimhall and Dietrich (1987) and later simplified by Anderson et al. (2002). Their approach estimates the relative mass changes between two samples as a dimensionless mass transfer coefficient, commonly referred to as tau τ:

$$\tau = (\frac{C_{j,w}}{C_{j,p}} \frac{C_{i,p}}{C_{i,w}}) - 1 \tag{1.4}$$

Where $C_{j,w}$ and $C_{j,p}$ are the concentrations of an element or mineral considered "mobile" during weathering in the weathered sample and the unweathered parent sample (typically in ppm or wt %), respectively, to the concentration of a component considered "immobile" during weathering in the parent sample $C_{i,p}$ and the weathered sample $C_{i,w}$, respectively. The resulting value is subtracted by 1, such that mass loss relative to the parent sample is represented by values <0 and mass gain is >0. A value of -1 indicates total depletion of the mobile component. Elements used as the mobile component are typically base cations lost from silicate minerals during weathering (Ca, K, Mg, Na), while the immobile components are elements which are retained during weathering (e.g. Ti, Zr, Nb). While these elements are often considered to be totally immobile, they may become mobilised under certain conditions, and thus a mobility analysis should be performed when considering which element to use as the immobile component (Hodson, 2002). Under isovolumetric weathering conditions, the immobility can be approximated by calculating volumetric strain (volume changes due to physical deformation from the chemical weathering of rock into soils) (Equation 1.5); an immobile element should have a near-zero volumetric strain value.

$$\varepsilon_{i,w} = \frac{\rho_p C_{i,p}}{\rho_w C_{i,w}} - 1 \tag{1.5}$$

Equation 1.5 provides a dimensionless value for volumetric strain within a weathered sample ($\varepsilon_{i,w}$) where ρ_p (g cm^{-3}) is the bulk density of the parent material and $C_{i,p}$ is the concentration of the immobile element (mol kg^{-1}) in the parent samples, respectively. Similarly, ρ_w is the density of the weathered material and $C_{i,w}$ is the concentration of the immobile element in the weathered sample. No volumetric strain is indicated by a value of 0. Immobile elements have a relatively constant mass within a weathering profile due to having little to no loss during weathering and no external input sources of the element to the profile. Strain increases when rock density decreases relative to the parent sample, for example during the development of secondary porosity during weathering (Anderson et al., 2002).

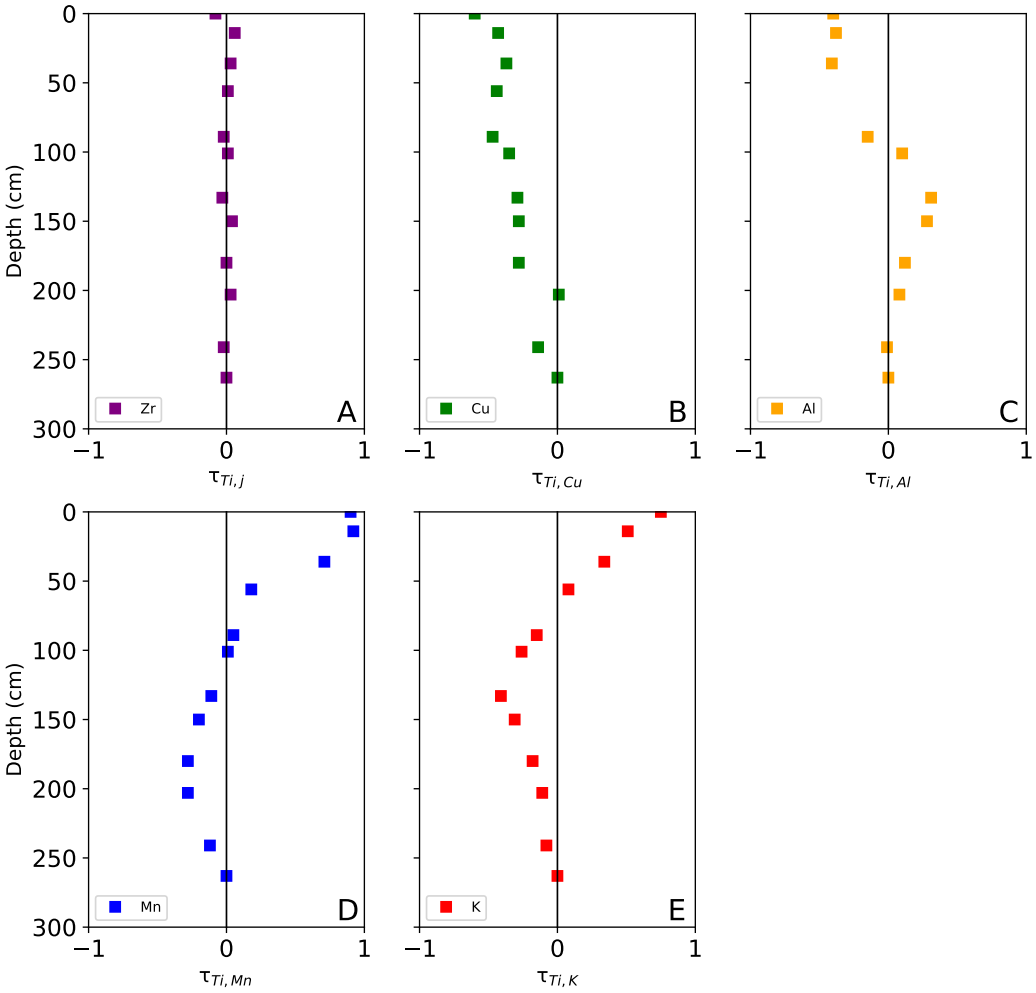

Figure 1.6: Examples of different types of mass transfer profiles produced by different processes. (A) Shows immobile element profiles, where little to no change in abundance of Zr occurs relative to the parent sample. (B) Shows a depletion profile, where Cu is lost relative to the parent sample. (C) Is an example of an addition-depletion profile, where Al is lost at the surface due to organic complexation, but gained at depth as Al is reprecipitated. (D) Shows examples of addition profiles, where Mn is added to the soil by dust deposition. (E) Shows an example of a biogenic profile, where K is removed by roots at depth but added at the surface by biological activity. Based on Brantley et al. (2007)

Mass transfer coefficients, unlike CIA, can provide useful information about changes in abundance of individual elements, shedding light on weathering processes within a profile (Brantley et al., 2007). For example, mass loss of only one mobile element may indicate that a mineral within a profile is being preferentially weathered. Mass transfer coefficients can also indicate whether

elements are being added to a profile from an external source such as from biological activity or from pollution (Brantley et al., 2007). Figure 1.6 shows some examples of different types mass transfer profiles that may be produced by different processes.

Mass transfer coefficients are also useful for calculating weathering gradients, (i.e., mass loss with depth in a profile). Such gradients are useful for calculating both mineral specific and whole-rock weathering rates (White, 2002).

1.5.3. Weathering Rates

Weathering rates can be calculated as mineral specific (i.e., the mass loss rate of an individual mineral) or whole-rock (i.e., the mass loss rate of the entire weathering profile). Such rates can be normalised to a land surface area (typically watershed area) when calculating weathering rates from stream solute data, or can be normalised to mineral surface areas if weathering rates are calculated using data from solid-state weathering profiles (e.g., White and Buss, 2014).

Weathering rates are typically expressed as moles per m^2 per second (mol m^{-2} s^{-1}) (White, 2002), or as a weathering advance rate in metres per second or metres per million years (e.g., Brown et al., 1995; White et al., 1998). Mineral specific rates are usually expressed in molar form (e.g., White, 2002; Buss et al., 2008), while whole-rock weathering rates are expressed as a distance or mass per time (e.g., m Myr^{-1} or t km^{-2} yr^{-1}) (e.g., White, 2002; West et al., 2005; Dannhaus et al., 2018). Weathering can be calculated at the catchment scale level over time from stream or river solutes (if discharge rates and solute contributions from other sources such as precipitation and biological activity are known), often represented by silica or base cation fluxes (e.g., White et al., 1999). Alternatively, weathering rates can also be calculated from weathering gradients and mineral abundances in solid-state profiles (White, 2002). Stream solute data is typically used for examining weathering rates and their responses over relatively short timescales (10^0-10^2 years) (e.g., Krám et al., 2012), while solid-state profiles provide long-term weathering rates and processes (10^3-10^6) (e.g., Buss et al., 2008; Hewawasam et al., 2013).

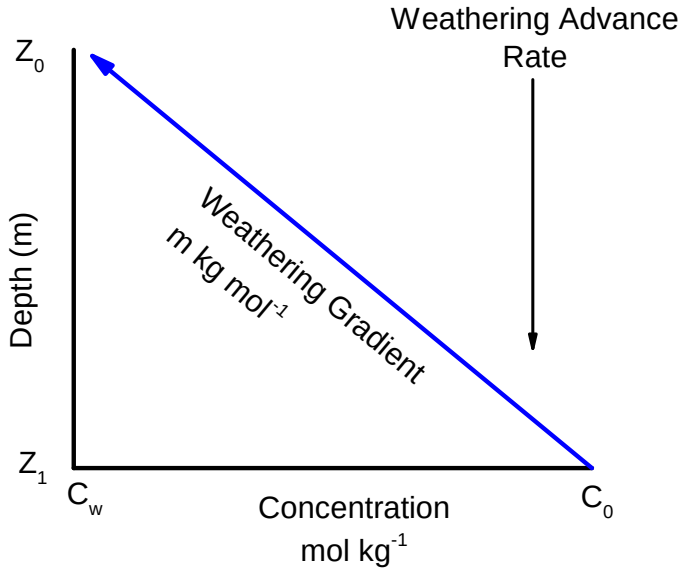

Figure 1.7: Conceptual figure showing weathering gradient as a function of changing concentration with depth. Z_0 and Z_1 represent the ground surface and the depth at which unweathered bedrock is reached, respectively. C_0 and C_w represent the concentration of a mineral or minerals within a weathering profile within the parent material and within a weathered sample, respectively. Thus, the weathering gradient is the rate at which mass is lost over distance. The weathering advance rate represents the rate at which the weathering boundary moves downward through the bedrock. Modified from White (2002).

Weathering rates can be calculated from weathering gradients of elements or minerals, expressed as m kg^{-1} mol^{-1}, if the age of the profile is known (White, 2002). Given the timescales involved in producing a weathering profile, age estimates are often derived from isotopic sources, such as ^{10}Be or U/Th disequilibria (e.g., Pavich, 1985; Chabaux et al., 2013). If the age of the profile and weathering gradients are known, a weathering rate can be calculated. There are a range of approaches, depending on whether one calculates an element or mineral specific rate, but most involve similar methods. A common approach involves the use of volumetric mineral surface areas (White, 2002),

$$R = 10^{-3} \frac{1}{\Phi \beta s} \frac{\omega}{b_s} \tag{1.6}$$

where R is the mineral specific weathering rate in mol m^{-2} s^{-1} , Φ is the mineral mass fraction within the regolith (g g^{-1}), β is the stochiometric coefficient of the element in the mineral (mol mol^{-1}), s is the volumetric surface area of the mineral in m^2 g^{-1}, the weathering advance rate ω in m s^{-1}, and the weathering gradient b_s in m kg mol^{-1}. In this method, if the element used

for β is present in multiple minerals, the weathering gradient must be weighted appropriately to reflect the contributions of multiple mineral phases (Buss et al., 2008). For example, K is present in both K-feldspar and biotite, which often occur concurrently within lithologies. Variations on this method exist where an element specific rate can be calculated, or where the elemental gradient is substituted for a mineral gradient which requires the mineralogical abundances within samples to be well constrained(Moore et al., 2019).

1.6. Modelling Chemical Weathering in the Critical Zone

Chemical weathering is an exceptionally complex process when one considers the large number of potential factors that affect weathering rates (e.g., climate variables, lithology, rock structure). Decoupling the individual impact from different factors is difficult in natural settings, and laboratory experiments are typically less practical due to the long timescales involved in weathering, although laboratory based dissolution experiments have been used to investigate weathering rate responses to changes in temperature, for example (e.g., Sverdrup and Warfvinge, 1995; White et al., 1999). As such, modelling weathering environments using computer simulations has become an attractive alternative within Critical Zone science (Li et al., 2017). Early modelling work focused on modelling reaction pathways within closed systems, although the applications of these models were limited due to the crucial role of transport within natural fluid-rock systems (Steefel and Maher, 2009). Reactive Transport Models (RTMs) were born out of the natural combination of the reaction component (reaction pathways, thermodynamics), and the need to consider transport processes (fluid flow, diffusive or advective). RTMs began to emerge in the 1980s, but development of the RTMs familiar to many geochemists began in the mid-1990s as the codes now widely used in reactive transport modelling (e.g., PHREEQC, PHT3D, HPx) were produced and large geochemical databases were developed (Steefel et al., 2014). Since then, RTMs have been applied in geochemical studies at a wide range of spatial and temporal scales with the prospect of being applied much further than at present (Li et al., 2017).

Within RTMs, the reaction and transport processes involved in weathering are defined mathematically and are updated and solved as the model progresses. This section will provide a brief overview of the key processes involved in chemical weathering and how they are handled by RTMs.

1.6.1. Transport Processes

Within most developed weathering profiles, water movement through the regolith is primarily advective in nature, although some diffusive activity likely occurs at the bedrock-weathering interface where porosity and permeability are low (Maher, 2010). Advective fluxes of dissolved species can be defined as:

$$J_{adv} = \phi v C_i \tag{1.7}$$

Where J_{adv} represents the flux of dissolved species, Φ is the porosity of the media (%), v is the average linear velocity (typically m s^{-1}) and C_i is the concentration of a species. In most cases, fluid flow through porous media is described using Darcy's law:

$$q = \phi v = -K\Delta h \tag{1.8}$$

where q is the volumetric water flux (m^3 m^{-2} s^{-1}), K is the hydraulic conductivity in m s^{-1}, and h is the hydraulic head gradient. Φ and v are the porosity and linear velocity respectively (Darcy, 1856). Hydraulic conductivity is a function of the permeability of the medium and the physical characteristics of the fluid (viscosity and density). Darcy's law can also be defined in terms of pressure, defining the hydraulic head thusly:

$$h = z + \frac{P}{\rho g} \tag{1.9}$$

where z is depth (typically m), P is fluid pressure (typically Pa) and ρ and g are fluid density (typically kg m^{-3}) and acceleration due to gravity (m s^{-2}), respectively.

1.6.2. Reaction Processes

Mineral rate laws are somewhat context specific, depending on the factors involved in the reaction and the complexity of both the environment in which the reaction occurs and the model parameters. Reactive Transport Models commonly use Transition State Theory (TST), which relates the mineral reaction rate to additional factors such as mineral volume, surface area, kinetic constants and chemical conditions in the reaction environment (Aagaard and Helgeson, 1982). Transition State Theory describes the overall reaction rate of a mineral in mol m^{-2} s^{-1}, R thusly,

$$R = k \prod_j a_j^{n_j} [1 - e \frac{(-\Delta G_r)}{\sigma RT}] \tag{1.10}$$

K is the intrinsic rate constant of the mineral in mol m^{-2} s^{-1}, $\frac{-\Delta G_r}{RT}$ represents the Gibbs free energy of the system (J), R is the gas constant (J mol^{-1} K), and T is temeprature (K). $\frac{-\Delta G_r}{RT}$ is also known as reaction affinity (i.e., the capability of chemical species to form chemical compounds). σ

is the dimensionless Tempkin's coefficient, and a_j is the activity of any species that may inhibit or catalyse the reaction dependent on n_j, the number of species. An estimate of the bulk rate can be obtained by multiplying the reaction rate by the surface area of the reacting phase per unit volume ($m^2\ L^{-1}$).

1.6.3. Geochemical Saturation

The geochemical saturation state (also termed thermodynamic saturation) of an environment governs the ability for a solute to dissolve a substance. A geochemically saturated state ($\Omega = > 0$) means that the solute cannot dissolve more of a substance. In contrast, a geochemically undersaturated state ($\Omega = < 0$) means that the solute will be able to dissolve more of the substance until the solute reaches geochemical saturation. Geochemical saturation states of a reactive fluid are referred to with respect to a mineral or minerals (e.g., plagioclase), and are expressed in logarithmic terms (e.g., Steefel and Maher, 2009).

In terms of weathering studies, the geochemical saturation state is an important consideration, as geochemically undersaturated conditions with respect to weatherable minerals are necessary for chemical weathering to occur. Reactive transport modelling studies have indicated that the most rapid weathering rates occur in environments that are strongly geochemically undersaturated with respect to weatherable minerals (Maher, 2010, 2011; Maher and Druhan, 2014). It is difficult to test such theories using field data however, as saturation states are spatially and temporally heterogeneous (e.g., Steefel and Maher, 2009), making representative sampling difficult.

1.7. Global Weathering Models

Reactive Transport Models provide solutions for modelling weathering at the pore to profile scales but have not found widespread use at scales greater than that of the profile to watershed level due to the requirement of larger datasets and increasing computational demands or reduced model complexity with increasing scale (e.g., Goddéris et al., 2006; Maher, 2011; Li et al., 2017). Given the need to consider climate and weathering fluxes at the global scale when dealing with climatological changes over geological timescales, alternative solutions are needed to model global weathering fluxes. As with RTMs, global weathering models began their development in the early 1980s, with the pioneering work of Berner et al. (1983) and Walker et al. (1981) marking a major step forwards in modelling the long-term effects of the chemical weathering thermostat in the form of the BLAG and WHAK models respectively. The BLAG model used a carbon mass balance model combined with estimations of seafloor spreading rates and the total continental area of the Earth over the last 100 Myr to derive estimates of palaeo-atmospheric CO_2 levels and mean surface temperatures (Berner et al., 1983). The WHAK model used correlations between silicate weathering rates and environmental variables such as temperature and atmospheric CO_2 to demonstrate that the Earth's climate was stabilised by silicate weathering rates, even though solar

luminosity increased during the planet's early history (Walker et al., 1981). These early efforts used relatively simplistic zero-dimensional models however, which do not account for spatial variability in climate or lithology across the Earth's surface. Advancements in the late 1980s and the 1990s resulted in models that included spatial constraints on climate and continental configuration, but at low spatial resolution (Barron et al., 1989; Otto-Bliesner, 1995).

The proliferation of GCMs (General Circulation Models) has greatly expanded the climatological data available for deep time scenarios. Since the early 2000s, it has become commonplace for global weathering models to use modelled climate data produced from GCMs such as FOAM as initial inputs (e.g., Berner and Kothavala, 2001; Donnadieu et al., 2004; Goddéris et al., 2014). Early uses of GCM model outputs provided refined estimates of mean global temperatures (Berner and Kothavala, 2001), but later works have made use of regional temperature and precipitation values (Donnadieu et al., 2004). Since the year 2000, global weathering models have expanded their applications from simply reconstructing past CO_2 levels to addressing specific questions regarding weathering and climate interactions. For example, the GEOCLIM model (Donnadieu et al., 2004; Goddéris and Joachimski, 2004) was used to examine potential triggers for a Snowball Earth event in the Neoproterozoic, concluding that weathering of an erupting flood basalt in the tropics likely would have resulted in sufficient drawdown of atmospheric CO_2 to trigger a global glaciation event (Donnadieu et al., 2004). Recent studies using GEOCLIM have highlighted the role of palaeogeography in determining runoff regimes, and the resulting impacts on silicate weathering fluxes (Goddéris et al., 2014), as well as evaluating the potential impact of regolith thickness on global CO_2 drawdown (Goddéris et al., 2017). These simulations however were carried out using relatively low spatial resolution climate inputs from the venerable Fast Ocean Atmosphere Model (FOAM), and global weathering studies have yet to use climate input data from more advanced GCMs.

1.8. Summary and Thesis Aims

1.8.1. Summary

Although chemical weathering is a slow process, it nonetheless has a profound impact on the wider Earth system, affecting geological, geochemical, biological, and climatological spheres of influence. Chemical weathering feedbacks are believed to have kept the Earth's climate relatively stable for long periods of time by moderating atmospheric CO_2 levels, allowing the planet to remain habitable (Walker et al., 1981; Berner et al., 1983). While the controls on silicate weathering rates, such as climate and lithology, have been broadly defined (e.g., Goldich, 1938; Strakhov, 1967; Dessert et al., 2003; Oliva et al., 2003; Riebe et al., 2004), how these factors interact within natural environments to determine silicate weathering rates is still an area of ongoing work within weathering studies (Li et al., 2017; Riebe et al., 2017). The difficulty in distinguishing the individual impacts of these factors on weathering rates hinders our ability to

apply weathering knowledge backwards into geological time, and forwards into the future under a rapidly changing climate. These uncertainties also affect our ability to explain the weathering morphologies we see in the present.

The questions surrounding the potential impacts of chemical weathering rates, and the extreme complexity and interconnectedness of the factors that affect these rates has led to the development of Critical Zone science, a field in which the study of weathering and its environmental interactions forms a major component (Giardino and Houser, 2015). This multi-disciplinary field has provided invaluable insights into weathering over the past few decades and has provided a framework and focus for techniques from disparate fields to be applied in the study of weathering, combining knowledge from fields such as chemistry, biology, geology, and climatology. The development of specialised Critical Zone Observatories has produced large datasets which have allowed for the comparison of weathering processes under a range of conditions around the world (White et al., 2015).

The advancement of Critical Zone science has benefited from the establishment of a range of standard techniques to describe and quantify weathering, enabling for easier comparison of weathering processes across different sites. Critical Zone science has also benefited from the development and proliferation of computer models. The complexity of the natural environment complicate efforts to test specific hypotheses in field settings, and the temporal and spatial scales involved in weathering make laboratory experiments impractical. Computer models allow for the simplification and acceleration of weathering experiments and make it easier to test specific hypotheses at a host of scales. The last two decades have also reaped the benefits of GCMs, making it possible to model aspects of weathering at the global scale and at geological timescales.

1.8.2. Thesis Aims

The issues and techniques outlined within this section form the framework for this thesis. In broad terms, this thesis deals with examining the key controls on granitic weathering rates and profile morphology development and investigating the effect of these controls at a range of spatial and temporal scales. These broad aims can be subdivided into more specific goals addressed by individual chapters.

Chapter 2) What are the controls on weathering profile morphology and gradient sharpness within granitic profiles? Using new geochemical analysis of a temperate granitic weathering profile and additional granitic profiles from the literature from diverse climates, this chapter identifies controls on weathering front morphology (i.e., location and sharpness of the weathering gradient) and the location and sharpness of weathering gradients. From these sites, this chapter examines whether large-scale processes (i.e., climate) or small-scale processes (i.e., erosion rates, permeability variations) are stronger controls on profile morphology, weathering rates, and gradient sharpness.

Chapter 3) What are the impacts of individual factors (i.e., climate variables, erosion, rock structure) on weathering profile morphology when other factors are held constant? This chapter identifies dominant controls on weathering profile morphology and gradient sharpness, and determines the mechanisms by which such controls occur, using reactive transport models to overcome the limited number of well-sampled field sites.

Chapter 4) What are the controls on potential weathering rates at the global scale in geological time? Studies of global weathering have favoured different controls on global weathering rates (e.g., temperature *vs* precipitation), and studies have struggled to apply global controls to individual weathering profiles. This chapter investigates the sensitivity of the Earth system to changing potential weathering rates during the Cretaceous-Eocene period, identifying dominant controls on long-term CO_2 levels under constant degassing rates using the global biogeochemical model GEOCLIM. Furthermore, this chapter determines whether controls on weathering at the global scale agree with those identified in previous chapters and whether such controls remain constant through geological time.

Chapter 5)This chapter summarises the conclusions of the previous chapters, providing an overall conclusion for the thesis as a body of work. This chapter also identifies potential avenues for future work based around the findings of this thesis.

Chapter 2

Controls on Granitic Weathering Fronts in Contrasting Climates

Author contributions and declaration: This chapter has been submitted to Chemical Geology. Rock cutting and crushing of rock samples were performed by Nicholas Hayes. Geochemical analysis was performed by SGS Mineral Laboratories, Ontario, Canada. Thin sections were prepared by Spectrum Petrographics. SEM and EDS analysis of Lysina thin sections were carried out by Nicholas Hayes with guidance from Oliver Moore, Stuart Kearns, and Ben Buse. Drilling and sampling of the LY-V1 core was conducted by the Czech Geological Survey and samples were provided by Pavel Krám. Richard Pancost provided helpful comments emphasising the wider-scale impact of this work. Some minor changes here, such inclusion of statistical power, and changes from American to English spelling conventions have been made.

Abstract Granitic weathering profiles display highly diverse morphologies, reflecting the complex relationships between climate and weathering rates. Some profiles exhibit abrupt transitions from fresh bedrock to highly weathered material over short (<1 m) distances, while others exhibit only limited weathering extending 10s of metres into the bedrock. Although granitic weathering processes have been well studied, the controls on profile morphology and weathering rates within granitic, and many other lithologies remain poorly understood; these are likely influenced by a range of both intrinsic and extrinsic factors, which in turn will have crucial implications for understanding, for example, climate-weathering feedbacks. In this study we present multi-scale elemental and mineralogical analyses of a >30 m granitic weathering profile from the cool, temperate, Lysina catchment in the NW Czech Republic, from which we calculated mass transfer, weathering indices, and mineral specific weathering rates. The Lysina profile exhibits limited weathering extending >30 m into fractured bedrock, dominated by albite weathering at a rate of 9.3 x 10^{-17} mol m^2 s^{-1}.

To identify environmental and geological controls on weathering front morphology and chemical weathering rates, Lysina was compared to previously published granitic weathering profiles from around the world. Weathering front morphology and weathering rates were calculated for the additional sites from published data and were correlated to mean annual precipitation (MAP), mean annual temperature (MAT), and erosion rates, with MAP having the strongest relationship. Higher MAP likely promotes lower saturation indices in pore waters, allowing weathering reactions to occur further from equilibrium. Comparison of erosion rates amongst the granitic catchments revealed an inconsistent effect on chemical weathering rates, but high erosion rates may promote weathering by reducing the thickness of the regolith and exposing the bedrock to reactive fluids. Mean annual temperatures appear to only have significant impacts on weathering fronts in environments with high precipitation and high erosion rates. Fractured bedrock profiles (Lysina and Río Icacos) have higher weathering intensities, than the other sites studied here. High connected porosity in fractured rocks enhances water movement allowing more efficient removal of weathering products, thus reducing thermodynamic saturation, increasing weathering rates, and producing sharper weathering gradients. These findings indicate that CO_2 drawdown on geological timescales is also likely to be governed by precipitation rates, as well as temperature, and that much of the climate-significant weathering may occur within very narrow zones of the Earth's surface.

2.1. Introduction

The chemical weathering of silicate minerals is generally accepted to be one of the primary controls on atmospheric CO_2 over geologic timescales and thus the long-term climate ($>10^6$ years) of the Earth (Berner et al., 1983). Although numerous factors operate on a range of scales to determine long-term silicate weathering rates, it is believed that the primary controls on these rates are climate and lithology (e.g., White and Blum, 1995; Riebe et al., 2004; Maher, 2010). The relative influence of these two factors remains disputed, but typically, mafic lithologies weather more rapidly than felsic ones, and warmer, wetter climates promote more rapid weathering, with broad latitudinal trends identified in weathering profile morphology (Strakhov, 1967). Granitic lithologies, in particular, display large variations in weathering intensity compared to their mafic counterparts (Bazilevskaya et al., 2013). Although granitic weathering rates and mechanisms have been well studied (e.g., Melfi et al., 1983; White and Blum, 1995; Oliva et al., 2003; Riebe et al., 2004; Buss et al., 2005; Fletcher et al., 2006; Pierson-Wickmann et al., 2009; Frey et al., 2010), the controls that produce the variations in weathering front morphology, depth, and rates are not well understood. Greater constraint on these controls would enhance our ability to predict weathering responses through geologic time, as well as responses to future land use and climate change.

Most chemical weathering occurs in the Critical Zone, commonly defined as the region of Earth spanning the upper extent of vegetation to the lower extent of bedrock weathering. Significant differences exist in the intensity and depth of granitic weathering and the thickness of the weathering fronts in the critical zone. Some critical zone profiles exhibit only a few metres of weathering, whereas others show weathering to tens of metres deep (Bazilevskaya et al., 2013). The intensity of granitic weathering also varies significantly; some profiles weather from fresh bedrock to completely depleted regolith over weathering fronts less than 1 m thick, whereas other profiles show gradual alteration over tens of metres (e.g., Schaffhauser et al., 2014; Buss et al., 2017). It is unclear to what extent these variations are a product of the weathering environment or subtle differences in the mineralogy or intrinsic rock structure such as porosity and permeability. Regardless, these variations in weathering are likely to have implications for water flow rates and residence times within granitic profiles, which in turn could affect the coupling (or decoupling) of surface processes to those at depth and the flux of weathering products from the watersheds.

The depth of the bedrock-weathering boundary may also impact the initial weathering reactions. Weathering and biological reactions above weathering fronts can alter saturation indices and consume or produce reactants, such as CO_2 or O_2 in reactive fluids (Buss et al., 2005; Brantley et al., 2014). The manner and rate at which secondary porosity develops also affects weathering mechanisms and fluid transport and can lead to distinct weathering morphologies (Navarre-Sitchler et al., 2011; Goodfellow et al., 2016).

Initiation of weathering in granitic rocks generally begins with either dissolution of highly reactive

accessory minerals such as calcite (White et al., 2005) or oxidation of Fe(II) (Buss et al., 2008; Goodfellow et al., 2016). However, the majority of porosity formed during granitic weathering stems from the dissolution of aluminosilicate minerals, dominantly plagioclase (e.g., Buss et al., 2008). Typically, Ca and Na rich feldspars dissolve more rapidly than K rich feldspars (e.g., Bandstra et al., 2008). Relatively small variations in the composition and abundance of feldspars amongst granitic rocks may affect weathering rates within granitic lithologies (e.g., White et al., 2001). Furthermore, as the most abundant Ca-containing silicate mineral within most granitic rocks, the weathering of plagioclase is the dominant granitic weathering reaction contributing to CO_2 drawdown (e.g., Brantley et al., 2014).

As such, the chemical weathering of plagioclase minerals within the critical zone represents a major control on long-term climate. The initiation of weathering can begin 10s of metres below the rock-regolith interface (e.g., Riebe et al., 2017), the practical difficulties in accessing and sampling weathering bedrock at depth means there are few available datasets that extend below the augerable, or outcropping, regolith (here defined as all disaggregated material overlying intact bedrock). The relatively limited number of such investigations means that our understanding of the fundamental processes that govern weathering profile development remain poorly understood (e.g., Bazilevskaya et al., 2013). In this study, we present new elemental and mineralogical data from a core drilled 30.3 m into a temperate granitic weathering profile, representing one of the first deep critical zone granitic weathering studies from such settings (e,g., White et al., 2001; Schaffhauser et al., 2014). Bulk rock and mineral-specific chemical weathering rates were calculated, and the intensity, depth, and morphology of the weathering fronts were analysed. We compare these findings to granitic weathering profiles from the literature, spanning a range of precipitation and temperature regimes. These comparisons were used to assess the relative impact of weathering factors such as climate, lithology, and subsurface architecture (i.e., variations in primary and secondary porosity and permeability with depth) on the resulting weathering front morphologies and chemical weathering rates.

2.2. Methods

2.2.1. Primary field site

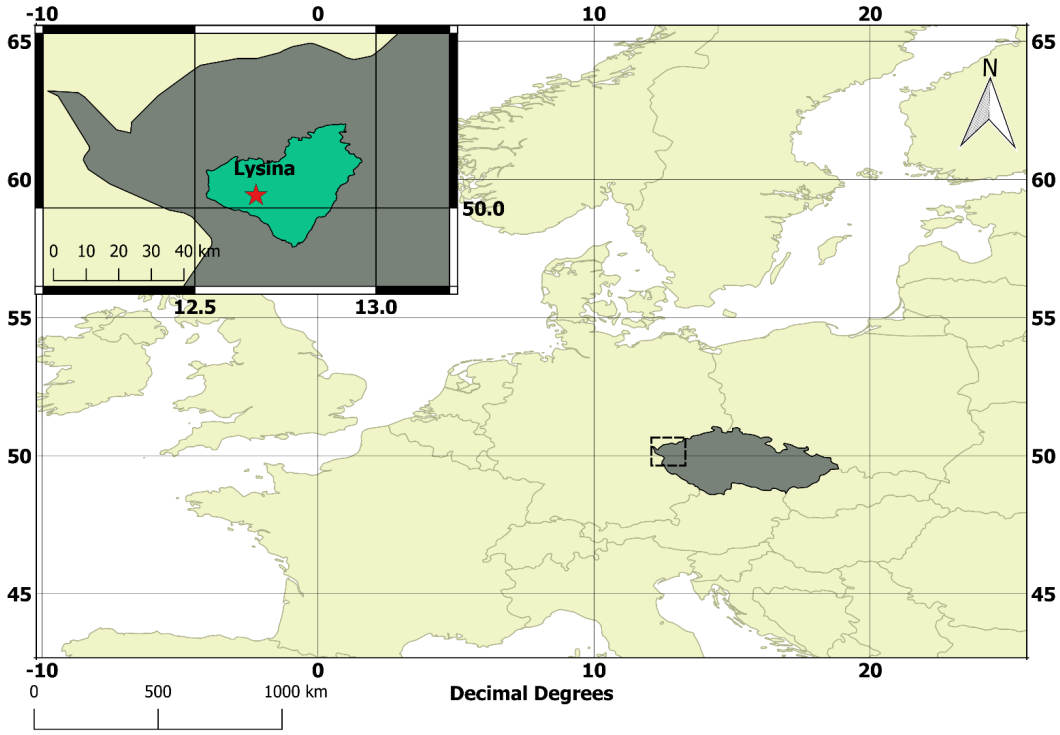

Figure 2.1: The field study was located in the west (dashed box) of the Czech Republic (dark grey). The inset shows the location of the Lysina catchment (red star) within the Slavkov Forest region (green).

The small granitic catchment (0.273 km^2) of Lysina is part of the Slavkov Forest Critical Zone Observatory in the NW Czech Republic (Krám et al., 2012, 2017, Fig 1). The region is located within the so-called 'Black Triangle', an area of Central Europe heavily affected by pollution from coal-fired power plants (Krám et al., 1999; Kopacek et al., 2016). The region has been formally monitored by the Czech Geological Survey since 1989, with a focus on the recovery from anthropogenic acidification since the collapse of the Communist government of Czechoslovakia and the subsequent decommissioning or retrofitting of the power plants (Hruska et al., 2002; Krám et al., 2014).

The Lysina bedrock is classified as a leucogranite: high in silica, deficient in base metals (particularly Mg) (Krám et al., 1997), and containing a relatively high proportion of Li, present within micas such as zinnwaldite (Navrátil, 2000; Krám et al., 2012; Štědrá et al., 2016) . Although a separate formation, the Lysina granite is associated with the Younger Intrusive Complex (YIC), a series of granitic intrusions dating from the late Carboniferous to early Permian (˜300 Ma) (Blecha

and Štemprok, 2012). The broad region remains hydrothermally active, and the Lysina catchment is located about 25 km from the spa town of Karlovy Vary which is renowned for its therapeutic, mineral-rich hot springs (Vylita et al., 2007).

Table 2.1: Site locations and environmental data

Site	Location	MAT (° C)	MAP (mm yr^{-1})	CWR (m Myr^{-1})	Erosion (m Myr^{-1})	Regolith Depth (m)	Lithology
Curacavi[a]	Chile	16	380	4.5	40.5 ± 22.5	> 33	Granodiorite
Davis Run[b,c]	Virginia, USA	10	1040	4	8.75 ± 4.25	11	Granodiorite
Hakgala[d]	Sri Lanka	16	2013	11	11	6	Granitic Gneiss
Lysina[e,f]	Czech Republic	5	950	7.1	63	2.6	Leucogranite
Nsimi[g,h]	Cameroon	26	1700	2.8	1.9	38	Granite
Panola[b,c]	Georgia, USA	17	1240	7	8.75 ± 4.25	4.3	Granodiorite
Río Icacos [i,j,k]	Puerto Rico	22	4200	43	43	5	Tonalite

[a]Vázquez et al. (2016),[b]White et al. (2001),[c]Brantley et al. (2017),[d]Hewawasam et al. (2013),[3]Krám et al. (2012),[f]Dannhaus et al. (2018),[g]Braun et al. (2005),[h]Braun et al. (2012),[i]White and Blum (1995),[j]Chabaux et al. (2013),[k]Buss et al. (2017), MAT - Mean Annual Temperature, MAP - Mean Annual Precipitation, CWR - Chemical Weathering Rate (whole rock).

Lysina is situated at a relatively high altitude (˜900 m), experiences a cool humid climate, and supports a managed coniferous forest consisting almost exclusively of Norway spruce (*Picea abies*). Mean annual precipitation is approximately 950 mm yr^{-1} and the MAT is 5 °C (Table 2.1; Krám et al., 1997). The region is not believed to have been affected by glaciation, despite its cool climate and high altitude (Hruska et al., 2002; Krám et al., 2012) . The base-poor nature of the underlying bedrock makes the catchment highly susceptible to acidification, and as a result, the Lysina brook has a discharge-weighted annual mean pH of 4.2. This vulnerability to acidification was exacerbated, in particular, by sulfur pollution during the 1980s. While the catchment has recovered significantly, the Lysina brook remains acidified relative to pre-1980s levels (Krám et al., 1999; Hruska et al., 2002; Kopacek et al., 2016).

The total denudation rates within the Lysina catchment, calculated from $^{10}Be/^{9}Be$ ratios, is 185 ± 23 t km^{-2} yr^{-1} (70 m yr^{-1}), although only 10% of the total denudation is believed to be from chemical weathering (Dannhaus et al., 2018). Assuming that total denudation in Lysina is comprised of a 90/10 split of erosion (phyiscal) to chemical weathering, erosion rates are therefore ˜63 m Myr^{-1} and chemical weathering rates are ˜7 m Myr^{-1}. Erosion rates within the Lysina

catchment are considerably higher than those of the nearby Pluhův Bor (serpentinite bedrock 25 m Myr^{-1}) and Na Zelenem (amphibolite bedrock, 19 m Myr^{-1}) catchments, although chemical weathering rates are lower (Dannhaus et al., 2018).

2.2.2. Additional Sites

To investigate the impact of climate on weathering front morphologies, geochemical data from previous studies of other granitic profiles were compiled for comparison to the Lysina profile. These sites experience a range of climates from cool temperate to humid tropical and have been extensively studied over the last two to three decades (Table 2.1). Bulk chemistry data were used to calculate mass transfer coefficients (normalized to Ti, due to its low mobility) and weathering indices for each site (e.g., Pavich, 1989; White et al., 2001; Buss et al., 2017). The deepest sample was used as the parent material in each case.

Davis Run, Virginia, USA

Davis Run is located within the Virginia Piedmont of the Eastern USA, and the catchment overlies the Cambrian-Ordovician age Occoquan granite (Pavich, 1989; White et al., 2001). The Occoquan granite is classified as an adamellite, consisting primarily of K-feldspar and sodic to calcic plagioclase phases (White et al., 2001). The catchment experiences a temperate climate but is warmer and slightly more humid than Lysina (Table 2.1).

Panola, Georgia, USA

The Panola catchment overlies the same Piedmont formation as Davis Run, although the Panola granite contains more Ca plagioclase and is substantially younger (˜320 Ma) (White et al., 2001, 2002). The Panola site experiences a subtropical climate, significantly warmer and more humid than Davis Run.

Río Icacos, Puerto Rico, USA

The Río Icacos catchment is located within the Luquillo Critical Zone Observatory (LCZO) in northeastern Puerto Rico. The local bedrock is the Río Blanco Quartz Diorite formation, formed during the Eocene (Seiders, 1971). Despite its name, the bedrock is now classified as a tonalite, and is notably lacking in K-feldspar relative to the other granitic profiles (Buss et al., 2017). The primary plagioclase minerals have similar quantities of Na and Ca, although are slightly more Na rich, and are of similar composition to andesine or labradorite (Buss et al., 2008). The Río Icacos catchment has one of the highest granitic chemical weathering rates in the world (43-58 m Myr^{-1}) (White et al., 1998; Chabaux et al., 2013). The region experiences a humid tropical climate, with strong altitudinal variations in annual precipitation, and year-round warm temperatures (McDowell and Asbury, 1994, Table 2.1). Puerto Rico is regularly affected by tropical cyclones, and major hurricanes hit the region every few decades. Recent examples include Hurricane Hugo in 1989 and

Hurricane Maria in 2017 (Shuckburgh et al., 2017). Río Icacos is the warmest of the four sites, and the site is substantially more humid than the next most humid site, Panola.

2.2.3. Sample Collection and Analysis

In 2012, continuous cores were drilled in three Slavkov Forest catchments as part of the Soil Transformations in European Catchments (SoilTrEC) Critical Zone Observatory project (Banwart et al., 2017). The drilling program, led by the Czech Geological Survey, recovered a 30.3 m core from Lysina (LY-V1, Štědrá et al., 2015, 2016). The Lysina core has been used to quantify bedrock solute contributions to streamwater chemistry and was the focus of a mineralogical study of the Lysina granite (Štědrá et al., 2016; Krám et al., 2017). Štědrá et al. (2016) documented three facies in the Lysina bedrock core: quartz monzonite in the upper ˜20 m, leucogranite below about 28 m, and alkali-feldspar granite in between. Sericitization and hematitization was observed throughout the upper 28 m, but evidence of hydrothermal alteration was most intense in the alkali-feldspar granite zone, where hematite caused a distinct pinkish discoloration of the core and clumps of secondary fluorite and carbonate were observed in association with feldspar and topaz.

For the present study, nine additional samples were taken from the Lysina core. One sample is a rock from the regolith at 1.85 m depth; the other eight samples were taken from zones of fractured rock below the rock-regolith interface, in contrast to previous samples (e.g., Štědrá et al., 2016) which were taken from zones of un-fractured, visibly pristine rock. Each sample was split in two, with one half prepared as a thin section and the other half pulverized and sieved (<63 μm) for geochemical analysis using a jaw crusher and ball mill. All equipment was cleaned with ethanol between samples. The milled powder was analysed by SGS Mineral Services, Ontario by ICP-OES after Li metaborate fusion digestion (major and some minor elements), inductively coupled plasma mass spectrometry (ICP-MS) after multi-acid digestion (for minor and trace elements), and titration for FeO. To assess the accuracy of the ICP analysis, an additional sample containing a granite standard (GSP-2) was included with the Lysina samples. Values from the SGS analysis of GSP-2 were within acceptable limits (appendix A). Uncertainties based upon the analytical detection limits, were propagated through all calculations. These data were combined with geochemical data from Nwaogu (2014) and Štědrá et al. (2016)(Table 2) to produce mass transfer profiles and a 30.15 m profile of weathering intensity.

Thin sections were prepared by Spectrum Petrographics, (Vancouver, WA, USA). Thin sections were carbon coated and analysed by SEM (Hitachi S-3500N) in backscattered electron (BSE) mode with energy dispersive spectrometry (EDS, Thermo Scientific 10 mm^2 Silicon Drift Detector). Mineral identification and abundance were determined from EDS data of nine 0.86 x 0.86 mm squares on each thin section. Minerals were identified by EDS phase analysis using NSS 3.0 software, which was also used to measure mineral grain sizes for volumetric mineral surface area calculations. Mineral volumes from EDS analysis were converted to weight % values to allow for

estimations of bulk-density using mineral density values from the literature (Deer et al., 2013). Images were obtained at a resolution of 1024 x 1024 pixels with an acquisition time of 4500 seconds per frame and a dwell time of 1 µs per pixel. Porosity values were also determined by EDS phase analysis.

2.2.4. Weathering Calculations

Weathering intensity was assessed using the mass transfer coefficient (τ) (Brimhall and Dietrich, 1987) and the chemical index of alteration (CIA) (Nesbitt and Young, 1982). The mass transfer coefficient represents changes in the relative concentration of elements or minerals considered mobile during weathering, such as Ca or anorthite, normalized to a relatively immobile element or mineral, such as Ti or quartz (Brimhall and Dietrich, 1987; Anderson et al., 2002). These mass changes are normalized to concentrations in the parent material:

$$\tau = (\frac{C_{j,w}}{C_{j,p}} \frac{C_{i,p}}{C_{i,w}}) - 1 \tag{2.1}$$

Where C is concentration of the mobile, j, or immobile, i, component of interest in the weathered, w, or parent, p, material. The equation is such that τ = 0 if no change in concentration relative to the parent material has occurred (i.e., the component is immobile), τ = -1 indicates total depletion of the mobile component, and a τ value > 0 indicates enrichment of the mobile component relative to the parent material.

Immobile elements can become mobilized under certain conditions such as high acidity (Hodson, 2002). Volumetric strain (Eq. 2.2) was used to provide an indicator of element immobility (a near-zero value is considered ideal for an immobile element in an isovolumetric weathering profile (Chadwick et al., 1990).

$$\varepsilon_{i,w} = \frac{\rho_p C_{i,p}}{\rho_w C_{i,w}} - 1 \tag{2.2}$$

Here, $\varepsilon_{i,w}$ is the volumetric strain in the weathered samples, ρ_p and ρ_w are the densities (g cm^{-3}) of the parent and weathered samples, respectively, while $C_{i,p}$ and $C_{i,w}$ are the concentrations of the immobile element in the parent and weathered samples. Sample densities were estimated from the phase analysis-derived mineral area percentages and mineral density values from the literature (Deer et al., 2013). Titanium was found to be slightly less mobile than Zr in the Lysina profile.

The "freshness" of individual samples were assessed by calculating the CIA, which measures the degree of aluminosilicate weathering, independent of the parent material (Nesbitt and Young, 1982):

$$CIA = \frac{Al_2O_3}{Al_2O_3 + CaO + K_2O + Na_2O} * 100 \tag{2.3}$$

Equation 2.3 assumes that Al_2O_3 is immobile during weathering, such that a greater proportion of Al_2O_3 relative to the mobile oxides is considered to be indicative of weathering. A CIA value of 100 indicates total loss of the mobile oxides (Bahlburg and Dobrzinski, 2011). Values of CIA for unweathered aluminosilicate rocks vary depending on their composition; granites are typically in the 40-55 range.

The dimensionless mass transfer coefficient (Eq. 2.1) can be re-cast as a mass fraction (mol kg^{-1}) of element (or mineral) loss during weathering, C_w:

$$C_w = C_{j,p}(\tau_{i,j} + 1) \tag{2.4}$$

A weathering gradient is described by C_w with depth through a weathering profile, which was then used to calculate mineral-specific weathering rates (White, 2002):

$$R = 10^{-3} \frac{1}{\Phi \beta s} \frac{\omega}{b_s} \tag{2.5}$$

where R is the mineral-specific weathering rate in mol m^{-2} s^{-1}; Φ is the mineral mass fraction in the weathering material (g g^{-1}); β is the mineral stoichiometry (mol element mol^{-1} mineral), s is the specific surface area of the mineral (m^2 g^{-1}); ω is the weathering advance rate of the profile (m s^{-1}); and b_s is the elemental weathering gradient (m kg mol^{-1}). In many cases, the total denudation rate (surface lowering rate) is used as ω, where the profile is assumed to be in steady state such that surface lowering rate = the weathering front advance rate (White, 2002; Phillips, 2010). Using total denudation as ω, where chemical weathering comprises a relatively small amount of the total surface lowering, may not be appropriate, as is believed to be the case for Lysina (Dannhaus et al., 2018). As such, using a whole-rock chemical weathering rate as ω may provide a more realistic estimate of weathering front advance rates where soil erosion and chemical weathering are not in steady state. Weathering rates were calculated for albite and K-feldspar using mineral-specific gradients (Eq. 2.5). Whole-rock chemical weathering rates (ω) from Dannhaus et al. (2018) were used. Gradients were calculated between 14.64 m and the shallowest sample, across zones where mass transfer profiles revealed trends in mass loss and to avoid lithological differences in samples below 14.64 m (Štědrá et al., 2016). Mineral abundance data in Štědrá et al. (2016) excluded porosity and secondary clays, and primary minerals were normalized to 100 %. As such, they are not compatible with the mineral abundance dataset in this study.

Geometric surface areas of minerals were calculated (White and Peterson, 1990):

$$s = \frac{6\lambda}{\rho_m D} \tag{2.6}$$

where s is the specific surface area of a mineral ($m^2\ g^{-1}$), 6 is the geometric grain size parameter (6 indicates cubic geometry); the roughness factor, λ (100 for Li-mica and 7 for all other silicate minerals) (White and Brantley, 2003); the mineral density ρ m (g cm^{-3}), and D, the mineral diameter (μm) (White and Peterson, 1990). The accuracy of the measuring tool in NSS 3.0 was assessed using 100 measurements of the 500 μm scale bar, indicating a tendency to under-measure the scale bar with an average error of 0.2% (mean measurement value = 499 μm, range = 481-507 μm) (Moore et al., 2019). Mineral diameters for specific minerals were calculated as the average between the square root of the long and short axes where mineral grains had an elongated shape. The number of mineral grains measured varied depending on mineral abundance and grain size within the samples. 15-45 grains of each mineral were measured in samples with large grain sizes, and 50-200 grains in samples with smaller grain sizes. Clay minerals were too small to accurately resolve individual grains. Uncertainty values for average mineral diameters within samples were estimated using standard error.

2.3. Results

2.3.1. Lysina Mineralogy

Table 2.2: Lysina Bulk Elemental Geochemistry[a]

Depth (m)	SiO_2 (wt %)	Al_2O_3 (wt %)	CaO (wt %)	Fe_2O_3 (wt %)	FeO[d] (wt %)	K_2O (wt %)	Li_2O (wt %)	MgO (wt %)	Na_2O (wt %)	TiO_2 (wt %)	CIA
Detection Limit	**0.01**	**0.01**	**0.01**	**0.01**	**0.1**	**0.01**	**0.0001**	**0.01**	**0.01**	**0.01**	**-**
0.15	nd[e]	9	0.11	0.82	nd[e]	2.01	0.1	0.1	1.61	0.23	
0.30	nd	11.7	0.09	0.93	nd	2.68	0.17	0.11	2.08	0.28	nd
0.45	nd	12.4	0.1	1.62	nd	2.64	0.16	0.17	1.94	0.26	nd
0.60	nd	13.7	0.15	2.24	nd	2.70	0.17	0.29	1.95	0.27	nd
0.75	nd	12.9	0.1	2.06	nd	2.72	0.13	0.21	1.99	0.32	nd
0.90	nd	12.3	0.18	1.65	nd	2.69	0.17	0.23	1.93	0.18	nd
1.05	nd	14.4	0.24	1.73	nd	3.03	0.17	0.27	2.22	0.19	nd
1.20	nd	13.5	0.26	1.6	nd	2.73	0.19	0.29	1.96	0.24	nd
1.35	nd	16.6	0.19	1.28	nd	3.32	0.23	0.22	2.27	0.19	nd
1.50	nd	15.2	0.18	1.22	nd	3.18	0.21	0.19	2.15	0.2	nd
1.65	nd	11	0.12	1.21	nd	2.38	0.13	0.15	1.73	0.17	nd
1.80	nd	12.5	0.1	1.17	nd	2.65	0.17	0.16	1.92	0.18	nd
1.85[b]	72.1	13.7	0.67	1.77	1.6	4.2	0.17	0.55	1.19	0.08	64.4
2.10	nd	14.1	0.1	1.22	nd	2.97	0.18	0.19	2.19	0.22	nd
2.40	nd	13.5	0.1	1.21	nd	2.86	0.19	0.18	2.07	0.21	nd
2.65	nd	15.9	0.3	1.35	nd	3.27	0.22	0.22	2.41	0.1	nd
2.77[b]	75.1	13.4	0.35	1.53	1.4	4.64	0.15	0.15	2.49	0.07	58.0
3.10	nd	14.3	0.21	1.36	nd	3.01	0.2	0.55	1.43	0.08	nd
3.40	nd	13.9	0.24	1.3	nd	2.74	0.21	0.68	1.14	0.08	nd
3.68	nd	13.3	0.23	1.3	nd	3.02	0.22	0.21	2.05	0.09	nd
4.20	nd	13.8	0.34	1.2	nd	3.25	0.21	0.13	2.34	0.08	nd
4.30[b]	73.5	13.9	0.52	1.52	1.4	4.54	0.16	0.18	2.52	0.07	57.8
4.65[c]	72.8	14.3	0.5	1.17	1	4.66	0.12	0.19	3.29	0.08	55.7
4.70	nd	13.3	0.3	1.25	nd	3.02	0.2	0.16	2.19	0.09	nd
5.20	nd	13.4	0.3	1.18	nd	3.14	0.2	0.15	2.28	0.06	nd
5.90	nd	13.8	0.34	1.13	nd	3.27	0.2	0.14	2.30	0.07	nd

6.17[b]	72.5	13.4	0.42	1.24	1.2	4.69	0.16	0.15	2.67	0.05	57.1
6.40	nd	13.1	0.29	1.23	nd	3.16	0.23	0.16	2.08	0.08	nd
6.80	nd	13.6	0.26	1.10	nd	3.48	0.21	0.15	2.22	0.07	nd
7.10[c]	74.7	13.1	0.42	1.17	1.10	4.54	0.13	0.14	2.99	0.07	55.3
7.45	nd	13.4	0.39	1.15	nd	3.24	0.23	0.18	2.39	0.07	nd
7.95	nd	13.7	0.35	1.2	nd	2.97	0.23	0.17	2.42	0.07	nd
8.45	nd	9.70	0.23	0.87	nd	2.38	0.18	0.09	1.77	0.04	nd
8.90	nd	13.4	0.38	1.14	nd	3.00	0.23	0.12	2.54	0.06	nd
9.40	nd	13.6	0.35	1.35	nd	3.30	0.27	0.12	2.43	0.07	nd
10.00	nd	13.2	0.31	0.99	nd	3.02	0.22	0.1	2.51	0.06	nd
10.40	nd	13.1	0.38	1.03	nd	3.02	0.22	0.14	2.45	0.06	nd
11.00	nd	12.8	0.39	0.92	nd	2.8	0.21	0.15	2.43	0.06	nd
11.45	nd	13.1	0.46	0.92	nd	2.88	0.21	0.15	2.41	0.06	nd
11.90	nd	12.9	0.36	1.00	nd	2.89	0.22	0.11	2.51	0.06	nd
12.45	nd	12.8	0.38	1.07	nd	2.98	0.24	0.13	2.39	0.06	nd
12.65[c]	74.3	13.3	0.63	1.04	1	3.97	0.12	0.16	3.08	0.07	55.9
13.00	nd	13.1	0.49	1.07	nd	3.04	0.21	0.15	2.39	0.06	nd
13.45	nd	13.4	0.38	1.03	nd	2.98	0.23	0.12	2.57	0.06	nd
14.00	nd	14.4	0.48	0.95	nd	3.18	0.23	0.14	2.7	0.05	nd
14.40	nd	13.3	0.37	1.24	nd	3.06	0.28	0.18	2.41	0.08	nd
14.64[b]	71.9	14.3	0.46	1.05	1.1	4.35	0.14	0.12	3.44	0.05	56.5
15.04	nd	13.1	0.41	0.88	nd	3.05	0.2	0.15	2.39	0.05	nd
15.35	nd	14	0.42	0.94	nd	3.07	0.22	0.18	2.62	0.06	nd
15.90	nd	13.2	0.78	1.00	nd	2.94	0.24	0.19	2.26	0.05	nd
16.35	nd	13.4	0.36	0.98	nd	3.17	0.22	0.12	2.47	0.06	nd
16.95	nd	13.9	0.4	1.03	nd	3.19	0.25	0.13	2.49	0.06	nd
17.45	nd	13.2	0.38	1.17	nd	3.16	0.27	0.15	2.24	0.07	nd
17.90	nd	15.1	0.45	0.94	nd	3.38	0.27	0.21	2.36	0.05	nd
18.25[c]	71.4	14.9	1.25	0.87	0.7	3.55	0.17	0.28	2.54	0.03	59.2
18.40	nd	14.1	0.46	1.01	nd	3.19	0.27	0.22	2.26	0.06	nd
18.95	nd	14.9	0.43	1.07	nd	3.50	0.3	0.19	2.38	0.06	nd

19.45	nd	14.5	0.6	1.28	nd	3.94	0.34	0.26	1.8	0.05	nd
20.05	nd	15.4	0.95	1.46	0.8	2.93	0.4	0.22	2.43	0.06	nd
20.22[b]	75.6	13.4	2.03	1.01	nd	3.32	0.27	0.22	0.92	0.03	61.0
20.45	nd	11.2	0.55	1.06	nd	1.94	0.26	0.21	1.47	0.05	nd
20.90	nd	12.4	0.47	1.68	nd	2.23	0.4	0.16	0.75	0.07	nd
21.40	nd	12.1	1.65	0.85	nd	2.27	0.24	0.16	1.82	0.03	nd
22.05	nd	13.6	0.51	0.87	nd	2.82	0.27	0.27	1.64	0.04	nd
22.35[c]	65.4	18.6	0.63	1.09	0.8	6.97	0.16	0.31	1.53	0.07	62.4
22.45	nd	13.1	0.45	0.67	nd	2.68	0.2	0.25	1.77	0.03	nd
22.95	nd	18.40	0.71	0.98	nd	5.47	0.28	0.09	0.26	0.04	nd
23.45	nd	13.7	0.55	0.87	nd	3.05	0.2	0.16	2.38	0.05	nd
23.68[b]	69.5	15.9	0.8	1.31	1.1	5.77	0.22	0.13	3.1	0.05	56.3
23.95	nd	12.2	0.75	0.88	nd	2.77	0.15	0.13	1.99	0.03	nd
24.45	nd	14.4	1.02	1.57	nd	3.31	0.35	0.19	2.30	0.08	nd
24.95	nd	13.6	0.58	1.10	nd	3.06	0.26	0.13	2.43	0.05	nd
25.63[b]	73.9	13.9	0.45	1.63	1.5	3.95	0.19	0.22	3.03	0.07	59.2
26.00[c]	69.5	15.4	0.54	1.09	1.1	6.86	0.16	0.23	2.54	0.09	55.0
27.75[c]	71.4	22.9	0.51	1.82	1.5	5.7	0.3	0.23	2.4	0.15	54.8
28.75[b]	59.6	22.9	0.57	1.79	1.5	8.67	0.25	0.45	3.07	0.08	59.7
30.15[c]	72.9	13.6	0.47	1.09	1	5.94	0.16	0.2	2.37	0.09	54.9

[a]Lysina bulk chemistry measured using ICP-OES after Li metaborate fusion using data from Nwaogu (2014), [b]samples analysed in this study, and [c] Štědrá et al. (2016). [d]FeO concentrations were measured by titration methods and Li and other trace elements measured by ICP-MS after multi-acid digest. Detection limits are shown in the second row. [e] SiO_2 and FeO concentrations were not determined by Nwaogu (2014).

Table 2.3: Lysina Mineralogy[a]

Depth (m)	Quartz (wt%)	Albite (wt%)	K-Feldspar (wt%)	Kaolinite (wt%)	Illite (wt%)	Li-Mica (wt%)	Density[c] (g cm^{-3})	Notes
1.85	33.4	4.30	15.9	24.9	nd[b]	10.9	2.53	1.9 % Jarosite
2.77	38.1	24.4	20.5	5.12	4.5	6.92	2.65	
4.30	29.7	27	27.3	6.05	5.05	4.28	2.47	
6.17	27.5	29.5	29.8	3.02	5.65	2.65	2.49	
14.64	35.5	30.3	16.8	5.18	5.27	5.72	2.59	
20.22	40.8	7.33	22.2	18.3	2.84	6.32	2.59	0.61 % Fe-oxides, fractured
23.68	24.9	25.8	25	8.76	1.11	3.33	2.72	3 % fluorite
25.63	30.7	27.8	25.5	2.71	1.95	5.97	2.54	
28.75	10.9	19.9	35.5	12.7	8.04	12.1	2.52	Heavily fractured

[a]Mineralogical abundances of Lysina samples derived from EDS phase analysis of thin sections and converted to wt % using mineral density values from the literature (Deer et al., 2013). [b] = not detected. [c]Density values were calculated using sample porosity values and literature values of mineral densities. Some minor minerals present (e.g., monazite) are not shown in this table due to low abundance and absence from some samples.

Phase analysis of the Lysina core samples indicate the primary minerals are quartz, K-feldspar, and albite, with some variation in their relative abundances through the core (Table 2.3). Albite abundance decreases significantly from 2.77 to 1.85 m depth, across the rock-regolith interface (Table 2.3). No Ca-rich plagioclase phases such as anorthite were identified, in contrast to previous studies on fresher samples (Štědrá et al., 2016). Much of the Ca concentration within our rock samples appears to be associated with apatite, which comprises $<$ 1 vol % of the Lysina bedrock. A Mg-poor, but Li-rich, mica is also relatively abundant within the core (5-10 vol %). Within deeper sections of the core ($>$ 20 m), mineral grain sizes are relatively large, with some exceeding 1 mm in size. Previous studies of the core suggest Li-rich micas are relatively abundant (Navrátil, 2000; Štědrá et al., 2016), however the EDS detector used in this study is not capable of identifying elements lighter than Be. Overall, the Lysina granite is Mg-poor ($<$ 0.6 wt %), although Li (measured using ICP-MS) is relatively abundant (0.1-0.2 wt %, Table 2.2). The stoichiometric ratios (excluding Li) of the mica were most similar to a Li-rich mica called zinnwaldite (Deer et al., 2013), the type locality (Zinnwald, Cínovec) of which is located in the neighboring mountain range (Ore Mountains), on the German/Czech border, 110 km NE from Lysina. Zinnwaldite and other Li-micas have been previously identified in the Lysina granite, and no other Li-bearing minerals were identified (Navrátil, 2000; Štědrá et al., 2016). Other studies identified multiple mica phases, including biotite and muscovite, based on optical and luminescence petrography (Nwaogu, 2014; Štědrá et al., 2016); however the stoichiometric ratios indicated by EDS phase analyses of micas in this study did not match those of biotite or muscovite due to low Mg and high Fe content, respectively.

SEM analyses of thin sections show secondary clays within all samples (Table 2.3). These clays appear at the edges of fractures, particularly in samples deeper than 20 m. In the thin section from the deepest sample (28.75 m), secondary clays have an abundance of 12.5 vol % comprised mainly of kaolinite, with some illite. Below 20 m in the core, secondary clay volumes reach their highest

value of 20.9 % at 20.22 m depth. Within the core as a whole, the highest secondary clay content (24.2 vol %) is observed in the shallowest sample (1.85 m). Although CIA values in the centre of the core (7.1 m – 14.64 m) are near or within the upper range of "fresh" granites, the central part of the core still shows ˜10 vol % of secondary clays.

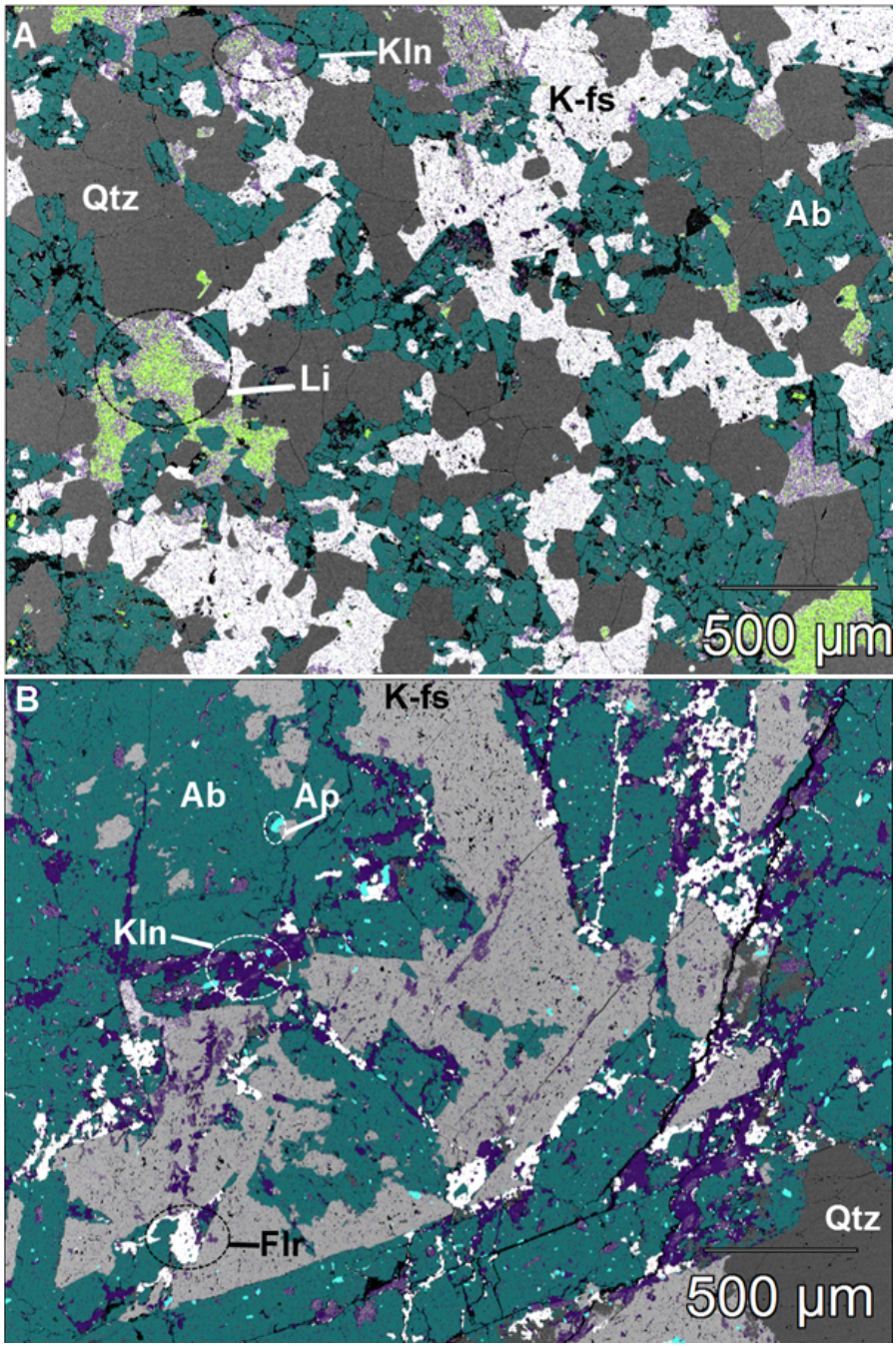

Figure 2.2: (A) False colour BSE image of weathering Li-micas from a sample at 6.17 m depth from the Lysina core. Li-micas (Li) are highlighted in green, kaolinite (Kln) is highlighted in purple, and (Ab) albite in blue. The Li-micas maintain distinct mineral grains despite undergoing extensive alteration, as evidenced by the high abundance of clays within the mineral grains. Albite also shows extensive alteration and grains are beginning to lose their structure. Also shown are (Qtz) quartz in dark grey and (K-fs) K-feldspar grains in lighter grey. (B) False colour BSE image of fluorite grains (flr, white) occupying pore spaces within albite grains (Ab, blue) with kaolinite (Kln, purple) in the Lysina core from 23.68 m depth. Also shown are apatite (Ap, cyan), K-feldspar (K-fs, light grey) and quartz (Qtz, dark grey). Fluorite grains are restricted to the more heavily weathered albite crystals and are absent from the less weathered K-feldspar and quartz grains, suggesting that fluorite formation occurred post albite weathering.

Nearly all minerals within the core show some degree of alteration to secondary clays or porosity development in SEM images. Weathering appears to be most pronounced in the albites, with significant porosity development and alteration to secondary clays. The highest secondary clay volumes are associated with significantly reduced albite volumes, relative to the rest of the core. EDS phase analysis indicates clays within the mica pore spaces (Fig. 2.2A). Weathering of K-feldspar is also evident, but to a lesser degree than albite. Fluorite occupies apparent pore spaces within weathered albites at 20.22 and 23.68 m (Fig. 2.2B). Small quantities of Fe-oxides (<5 vol%) exist within these samples, which also occupy apparent pore spaces within weathered minerals.

Table 2.4: Lysina Mineral Diameters[a]

	Sample Depth (m)	n	Mean Diameter[b,c] (μm)	Max Diameter (μm)	Min Diameter (μm)	Range (μm)
Albite	**1.85**	51	46 ± 4	168	14	154
	2.77	193	102 ± 4	323	18	305
	4.30	147	233 ± 14	1140	47	1093
	6.17	120	232 ± 20	1980	41	1939
	14.64	37	599 ± 89	1840	53	1787
K-feldspar	**1.85**	52	88 ± 7	224	24	200
	2.77	173	100 ± 6	549	21	528
	4.30	109	264 ± 23	1470	40	1430
	6.17	75	252 ± 44	2620	43	2577
	14.64	40	414 ± 62	1740	41	1699
Quartz	**1.85**	53	133 ± 24	1210	33	1177
	2.77	160	144 ± 19	2510	18	2492
	4.30	171	172 ± 10	712	31	681
	6.17	131	192 ± 11	675	49	626
	14.64	21	680 ± 146	2220	32	2188
Li-Mica	**1.85**	29	99 ± 31	928	17	911
	2.77	56	111 ± 12	440	16	424
	4.30	96	142 ± 8	432	30	402
	6.17	65	154 ± 11	438	51	387
	14.64	11	462 ± 155	1870	84	1786

[a]Diameters of the four primary minerals within the Lysina core. [b]Mineral diameters were measured using NSS 3.0. As many of the minerals had an elongated shape, the diameter was estimated as the square root of the sum of the long and short axes of a mineral grain. Secondary clays such as kaolinite had mineral grain sizes too small to accurately measure. [c]Uncertainty for mean diameter values was estimated from standard error calculations.

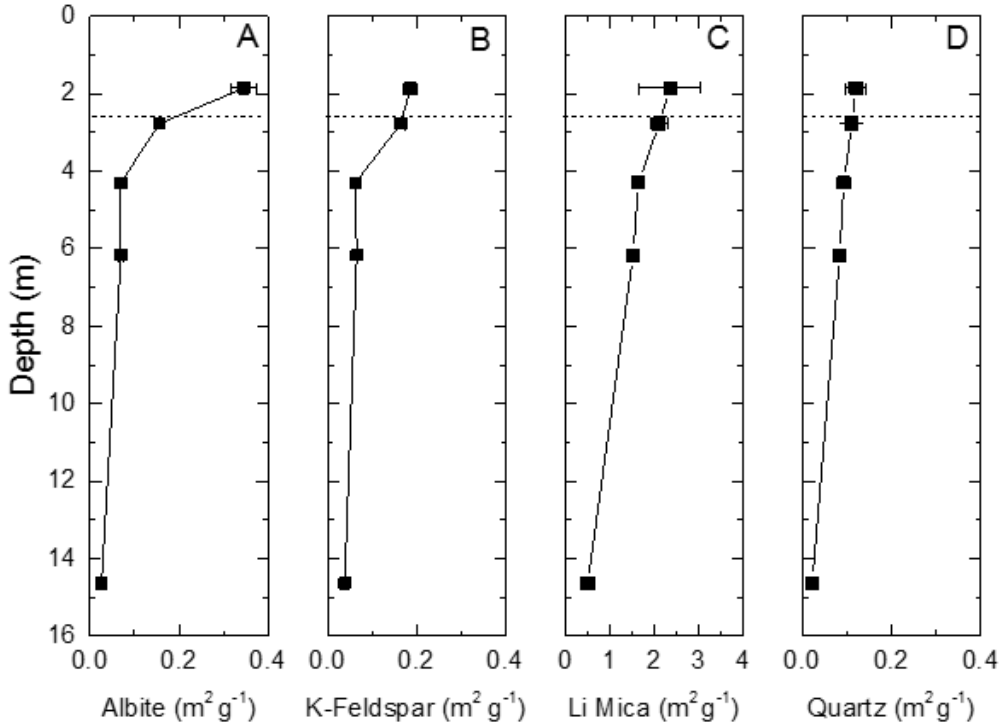

Figure 2.3: Geometric surface areas (Eq. 2.6) for the four key minerals within the Lysina profile. Dotted lines indicate the regolith-bedrock boundary. Note differing x-axis scale on panel c due to larger Li-mica surface area values. Uncertainty values were derived from standard error calculations on mineral diameters in each sample. Mineral surface areas increase relative to the parent sample in the upper 6.17 m of the core, particularly for (A) albite and (B) K-feldspar. (D) Quartz shows minimal significant changes in mineral surface areas through the profile. Uncertainty values for mineral surface areas are propagated from uncertainties in mineral diameters using standard error calculations.

Albite surface areas averaged 0.027 m^2 g^{-1} in the parent sample, while K-feldspar and the Li-mica had larger average surface areas at 0.040 m^2 g^{-1} and 0.53 m^2 g^{-1}, respectively. Clay mineral surface areas were not determined as individual grains were too small to accurately measure. Our surface area values are consistent with those from the literature with similar mean grain sizes (Bandstra et al., 2008). Mineral surface areas increase from 14.64 m towards the surface, especially from 4.3 m upwards, where albite, and to a lesser degree, K-feldspar, surface areas increase substantially (Fig. 2.3).

2.3.2. Lysina Weathering Parameters

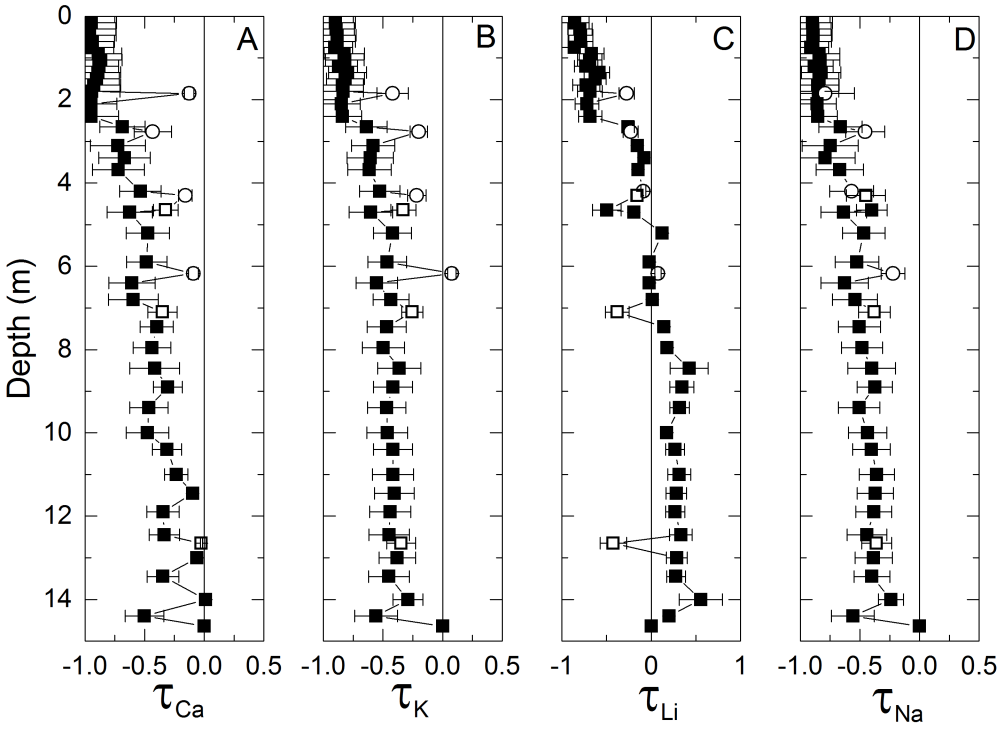

Figure 2.4: Mass transfer coefficient (τ, Eq. 2.1) of select mobile elements within the Lysina profile, normalised to Ti. Black squares indicate data from Nwaogu (2014), open squares indicate data from Štědrá et al. (2016), while open circles indicate data produced in this study. Note differing x-axis scale on panel c due to enrichment of Li relative to the parent sample. All elements show a general depletion trend above 14.64 m except Li which shows depletion above 5 m. Uncertanties are based on analytical technique detection limits and propagated using standard error calculations.

The strongest depletion in the Lysina profile is exhibited by Ca (τ = -0.94 at the shallowest sample) and displays a clear depletion trend with two primary zones of depletion (14.64-12.6 m and 2.77-1.85 m, respectively; Fig. 2.4A). There is a notable steepening of the weathering gradient between 2.77 m and 1.85 m depth, which covers the zone where bedrock transitions to disaggregated regolith. Sodium and K also show a depletion trend through the profile (Fig. 2.4B and D). Lithium shows a general depletion trend above 5 m, but is slightly enriched between 14.64 m and 7 m, (Fig. 2.4C).

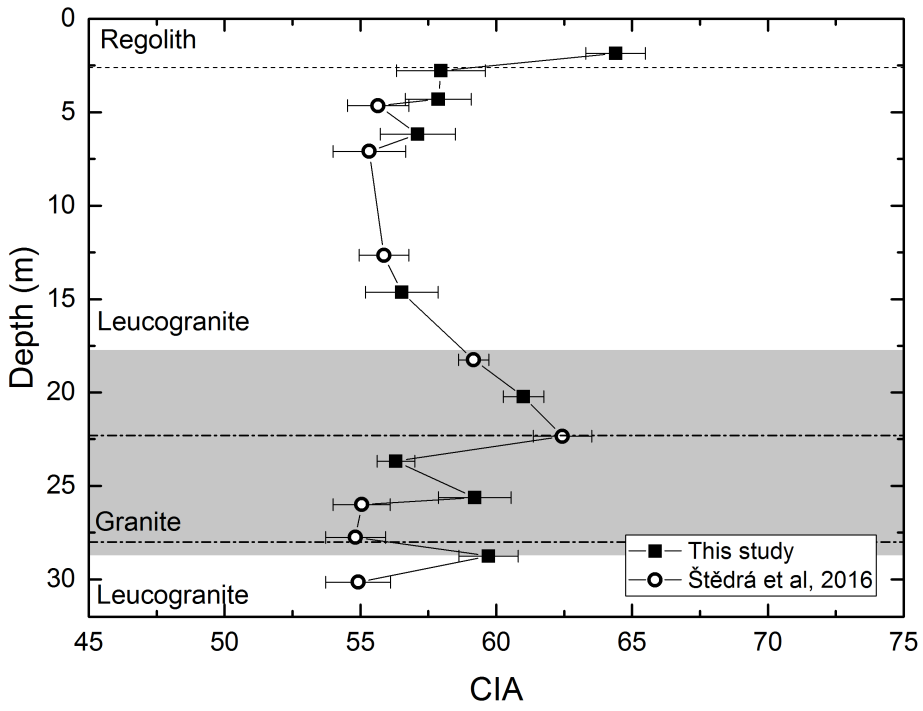

Figure 2.5: The chemical index of alteration (CIA, Eq. 2.3) with depth in the Lysina core. The Lysina profile shows only limited weathering (CIA = 54-64); unweathered granites typically have CIA values of 40-55 (Bahlburg and Dobrzinski, 2011). Open circles indicate CIA values calculated using bulk geochemistry data from Štědrá et al. (2016). Error bars represent potential range of CIA values based on uncertainties in oxide abundance. Shaded area indicates hydrothermally altered zone while dotted-dashed lines indicate boundaries of a zone of lithological variation identified by Štědrá et al. (2016) between 22.3 and 28 m depth.

The CIA profile (Fig. 2.5) shows a bimodal weathering pattern, with the highest values occurring at 1.85 m (CIA = 64.4) and 22.35 m (CIA = 62.4); lowest values are observed at the base of the core (CIA = 54.9) and between 7 and 15 m (CIA = ˜56). Such values are generally higher than those expected for fresh granites (CIA = 40-55; Bahlburg and Dobrzinski, 2011). From 7 m towards the surface CIA values increase, whereas below about 24 m CIA is variable (Fig. 2.4).

Bulk density values show no obvious trend within the core (Table 2.3). Similar rock densities are observed in the deepest and shallowest samples (2.52 g cm^{-3} and 2.53 g cm^{-3}, respectively). The highest density (2.72 g cm^{-3}) occurs at 23.68 m depth, and the lowest density occurs at 4.3 m (2.47 g cm^{-3}).

Table 2.5: Mineral Specific Weathering Rates

	Lysina[a]	**Davis Run**[b]	**Panola**[b]	**Río Icacos**[d]
Plagioclase (log mol m^{-2} s^{-1})	-16.1	-16.4	-15.7	-13.0
K-Feldspar (log mol m^{-2} s^{-1})	-16.3	-16.8	nd	nd
Mica (log mol m^{-2} s^{-1})	nd	nd	-16.4[c]	-15.0

[a]This Study. [b]White et al. (2001). [c]White et al. (2002). [d]Buss et al. (2008)

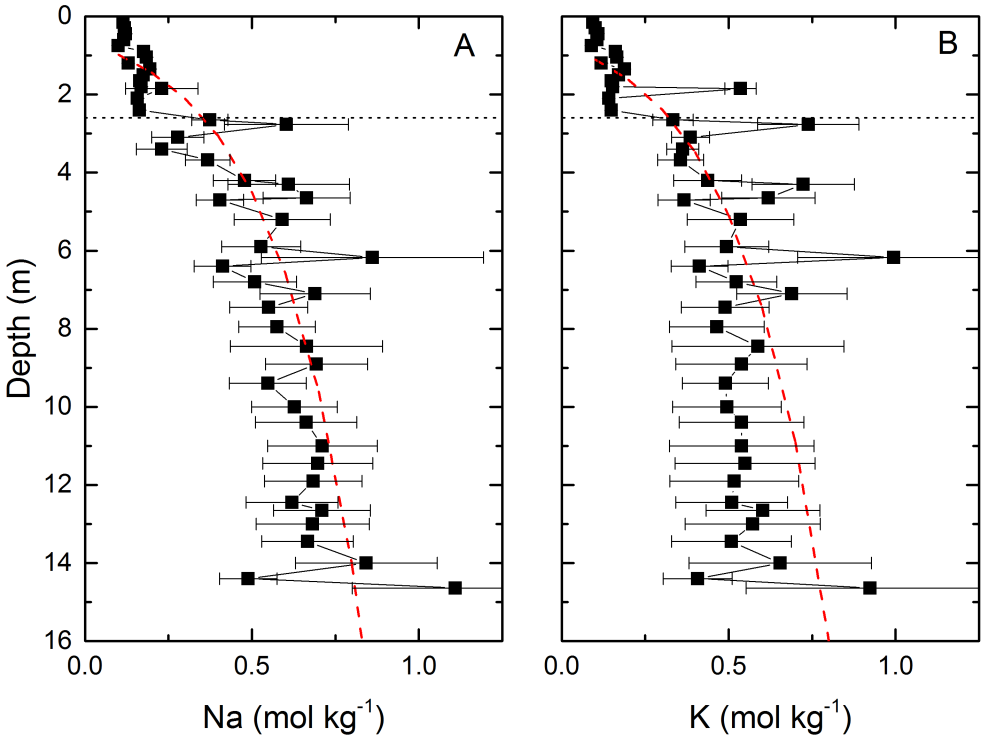

Figure 2.6: Lysina elemental concentrations (C_w) normalised to Ti (Eq. 2.4) in the upper 14.64 m of the Lysina core. Dashed red lines show gradients used in weathering rate calculations (Eq. 2.5) and dotted lines indicate the bedrock-regolith boundary. (A) Na shows gradual loss from 14.64 m to 4.3 m and more significant losses above 4.3 m. (B) K shows initial loss between 14.64 m and 14.4 m but remains relatively stable until 4.3 m, above which loss occurs towards the surface. Uncertanties are based on analytical technique detection limits and propagated using standard error calculations.

Elemental mass losses (C_w) at Lysina are minimal in most of the bedrock, although there is an increase in elemental mass loss (Eq. 2.4) in the shallower samples ($<$ 4.3 m; Fig. 2.4 and 6). Weathering rates calculated using Equation 2.5, are fastest for albite (9.3 x 10^{-17} mol m^{-2} s^{-1}), while K-feldspar weathers somewhat slower (5.7 x 10^{-17} mol m^{-2} s^{-1})(Table 2.5).

2.3.3. Weathering Mass Transfer at Additional Sites

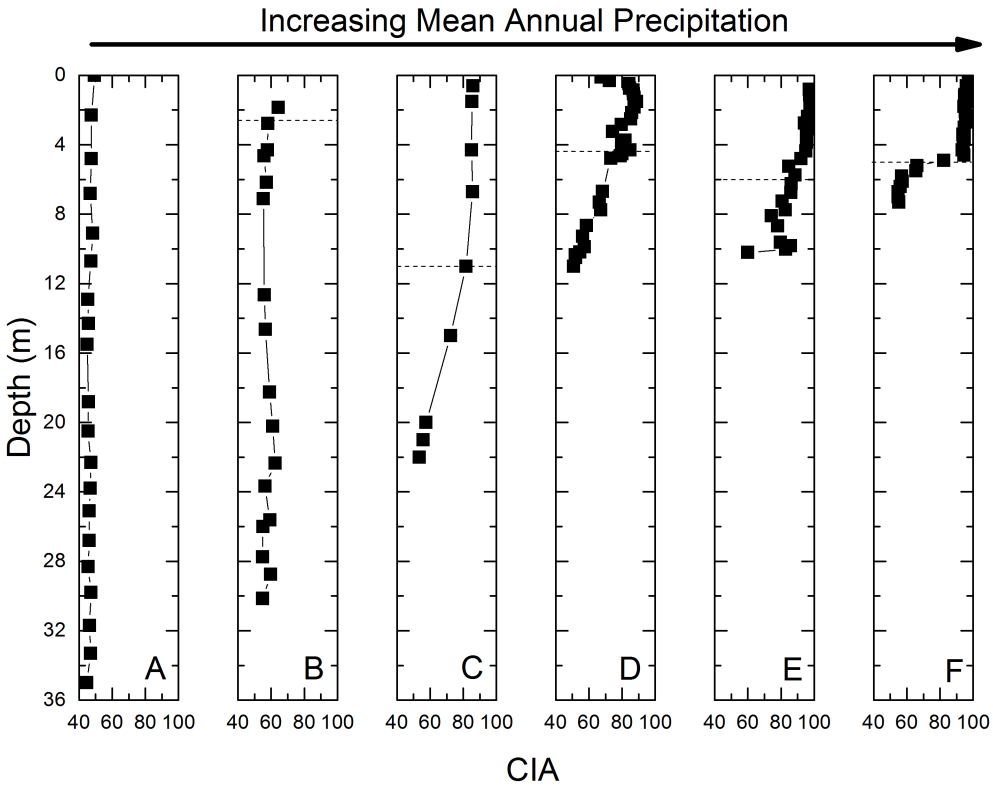

Figure 2.7: Chemical Index of Alteration (CIA, Eq. 2.3) with depth for (A) Curacavi, (B) Lysina, (C) Davis Run, (D) Panola, (E) Hakgala, and (F) Río Icacos in order of increasing MAP. Dotted lines indicate the bedrock-regolith boundaries. The Curacavi profile is entirely saprolite and fresh bedrock was not reached. Curacavi and Lysina show deep profiles with only limited changes in CIA values, while Davis Run, Panola, and Hakgala show clear transitions from fresh to more highly weathered material over 5-10 m distances. Río Icacos displays a sharp transition from fresh to nearly totally depleted material over only 1 m distance. Nsimi is excluded due to non-continuous sampling methods used on that profile.

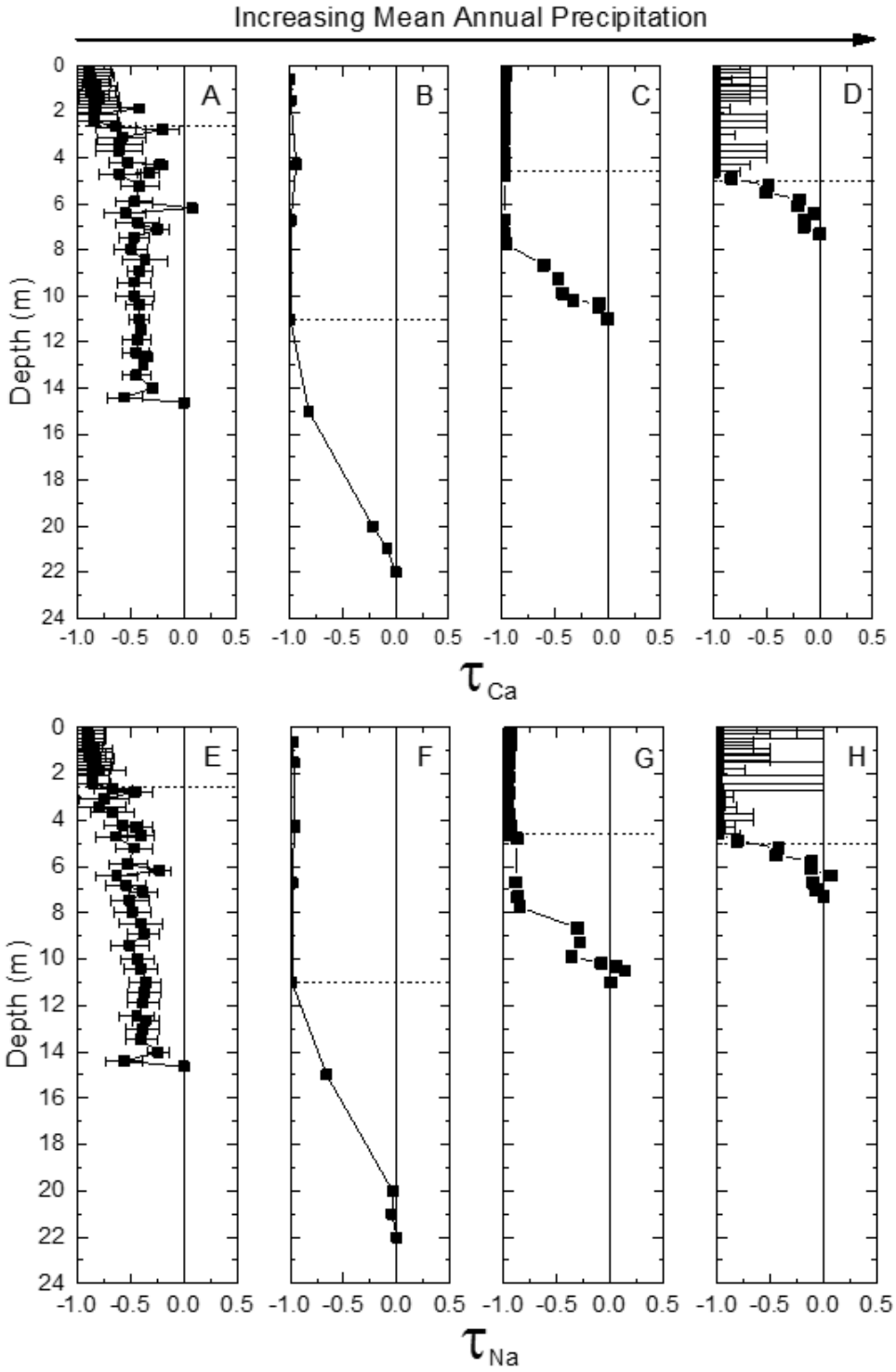

Figure 2.8: Ca mass transfers, τ_{Ca} (Eq. 2.1), normalised to Ti for (A) Lysina, (B) Davis Run, (C) Panola, (D) Río Icacos, and Na mass transfer coefficients normalised to Ti for (E) Lysina, (F) Davis Run, (G) Panola, and (H) Río Icacos. The dotted line indicates the regolith- bedrock boundary. Uncertanties are based on analytical technique detection limits and propagated using standard error calculations. Uncertainty estimates are unavailable for Davis Run and Panola.

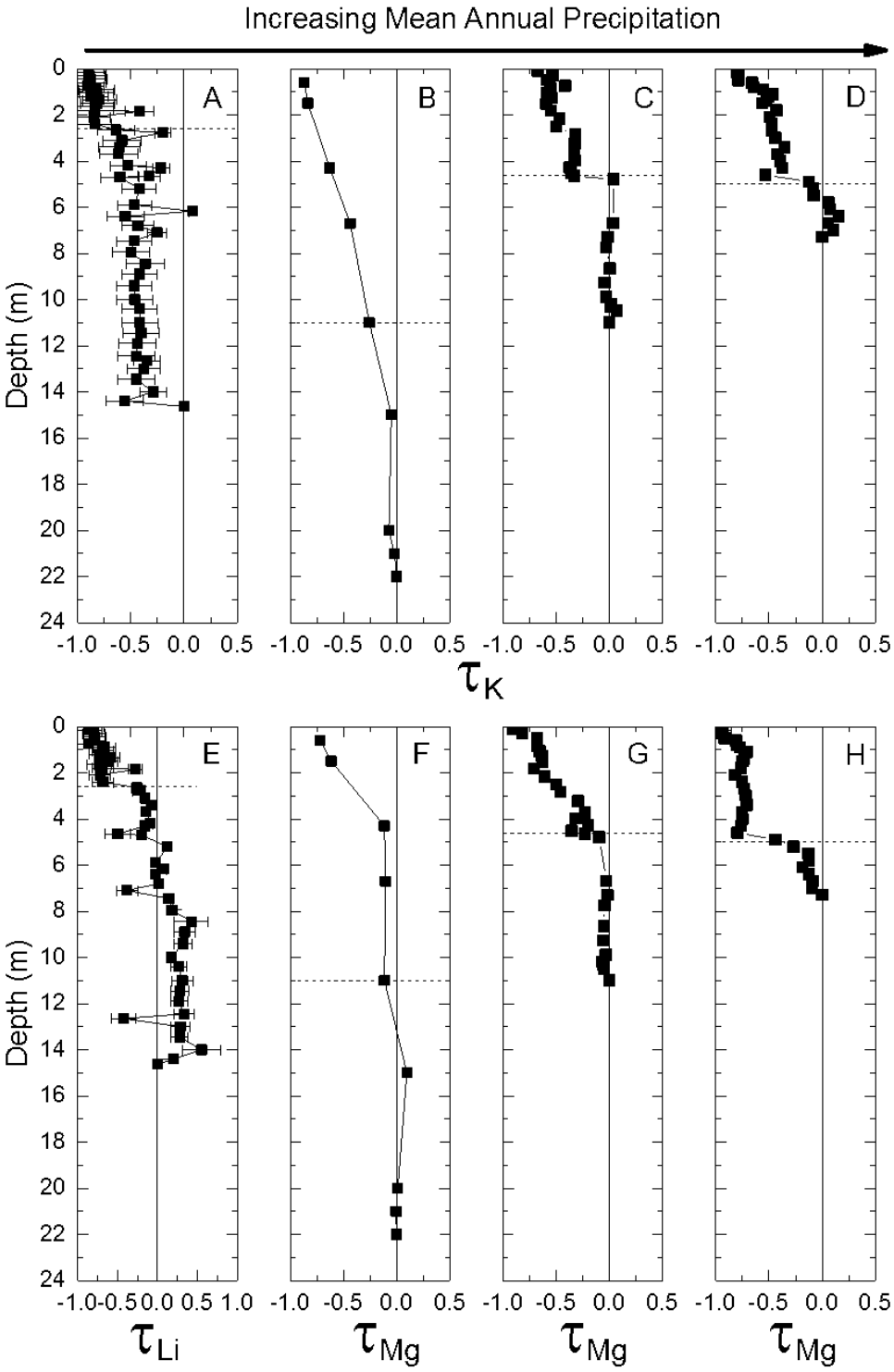

Figure 2.9: K mass transfer coefficients, τ_K (Eq. 2.1), normalised to Ti for (A) Lysina, (B) Davis Run, (C) Panola, (D) Río Icacos, and Li or Mg mass transfer coefficients normalised to Ti (τ_{Li} for Lysina and τ_{Mg} for the other sites) for (E) Lysina, (F) Davis Run, (G) Panola, and (H) Río Icacos, representing mica weathering fronts at each site. Note differing x-axis scale on panel e to show enrichment of Li in the Lysina profile. Dotted line indicates the regolith-weathering boundary. Uncertanties are based on analytical technique detection limits and propagated using standard error calculations. Uncertainty estimates are unavailable for Davis Run and Panola. Uncertainty values are sufficiently small at Río Icacos to be contained within the symbols.

Davis Run

Weathering in the Davis Run profile extends down to approximately 22 m, with much of this weathering occurring at depth (Pavich, 1989). CIA values show the greatest change from 22 to 11 m depth (CIA = 53.6 and 81.6, respectively) coincident with a zone of Na and Ca loss (Fig. 2.7C, 8B and F). The profile becomes mostly depleted in Ca (Fig. 2.8B) and Na (Fig. 2.8F) by 11 m depth, while K (Fig. 2.9B) and Mg (Fig. 2.9F) show more gradual mass loss. Potassium and magnesium depletion profiles become sharper from 11 m towards the surface, with an increase in Mg loss above 5 m.

Panola

The Panola profile is weathered to 11 m, with Ca and Na approaching total depletion around 8 and 4.5 m, respectively (White et al., 2001, Fig.2.7D,2.8C and G, 2.9C and G). Potassium and Mg show little evidence of mass loss below 4.8 m, and the Mg gradient is steeper relative to K between 4.8 m and the surface (Fig. 2.9C and G). CIA values show steady depletion from fresh values of 50 at 11 m to values of 84 near the surface (Fig. 2.7D). An apparent decrease in CIA values near the surface may be caused by loss of Al, as Tau profiles show no evidence of base metal enrichment near the surface (Fig. 2.8C and G, 2.9C and G).

Rio Icacos

Weathering depths within the Rio Icacos catchment varies from site to site, but transitions from fresh to near totally depleted material generally occur over a distance of 1 m or less (Buss et al., 2008; Orlando et al., 2016). The profile assessed here reaches fresh bedrock at approximately 7 m, although other cores show much deeper (>25 m) profiles with mostly fresh, spheroidally weathering corestones embedded in highly weathered regolith (Buss et al., 2008; Orlando et al., 2016). Calcium and sodium show near total depletion between 5.2 and 4.6 m depth (Fig. 2.8D and H). Significant loss of Mg also occurs over this zone but does not reach total depletion (τ = -0.8; Fig. 2.9D). Potassium remains slightly enriched relative to the bedrock through much of the profile, likely due to mineral heterogeneity in the parent sample (Fig. 2.9H). The Rio Icacos bedrock contains little to no K-Feldspar and thus K is a relatively minor component of the bedrock chemistry, compared to the other sites in this study. Nonetheless, K tau values decrease between 5.2 and 4.6 m. Chemical Index of Alteration values reflect the rapid loss of Ca and Na, with a rapid transition from fresh values to near totally weathered values (˜95) (Fig. 2.7F).

2.4. Discussion

The depth and thickness of weathering fronts affect numerous critical zone characteristics such as water flow paths (e.g., Schaffhauser et al., 2014; Orlando et al., 2016), subsurface microbial communities (e.g., Buss et al., 2005), stream solute sources (e.g., Calmels et al., 2011) and isotope

fractionation mechanisms (e.g., Schaffhauser et al., 2014; Lara et al., 2017). Granitic weathering front depth and thickness, as well as weathering intensity and rates, vary significantly around the globe, but the controls that produce these variations are not well understood. Below we interpret the weathering front characteristics from the new Lysina weathering profile and then compare them to deep granitic weathering profiles from a range of precipitation and temperature regimes to assess the effects of these climate variables on weathering profiles. We further assess the roles of lithology (plagioclase composition), erosion, and subsurface architecture (i.e., variations in primary and secondary porosity and permeability with depth) on the resulting weathering front morphologies and chemical weathering rates.

2.4.1. Weathering and Alteration Processes Within the Lysina Profile

The dominant weathering reactions, as well as the initial weathering reactions, govern the development of a weathering profile (e.g., Buss et al., 2008; Goodfellow et al., 2016), and such reactions vary from site to site. The dominant weathering reaction in the Lysina profile is the dissolution of albite. In contrast, K-feldspar shows relatively limited alteration to secondary clays and remains relatively stable in abundance below 6.17 m depth, while Li-Micas increase in abundance towards the surface, despite a gradual depletion trend in Li above 6 m depth (Table 2.3; Fig. 2.4C). SEM analysis of quartz grains shows little evidence of weathering, and quartz shows no appreciable decrease in abundance towards the surface (Table 2.3).

Albite dissolution appears to precede the weathering of other minerals in the Lysina profile. Albite crystals show evidence of alteration to secondary clays in the deepest samples of the profile (below 25 m), whereas other minerals (e.g., K-feldspar and Li-micas) show comparatively little evidence of alteration. As such, the dissolution of albite is likely the first weathering reaction to occur and is the primary mechanism of secondary porosity development in the Lysina profile. In contrast, dissolution or oxidation of minor minerals (e.g., calcite and biotite) are the initial weathering reactions in Panola and Río Icacos (e.g., White et al., 2001; Buss et al., 2008).

An episode of hydrothermal alteration within the Lysina profile likely occurred after the onset of albite weathering. In general, weathering profiles result from the interaction of weatherable minerals with meteoric water in the critical zone and hydrothermal alteration is not typically considered to be part of this process (e.g., Giardino and Houser, 2015). The Lysina core is altered to at least 30 m and possibly beyond the depth of the core, as evidenced by secondary clay abundances throughout the core and similar observations of a previous petrographic study (Table 2.3; Štědrá et al., 2016). However, weathering and hydrothermal alteration cannot be easily assessed independently in a quantitative way (e.g., Eq. 2.1-4) below about 20 m depth. The concentrations of fluorite and Fe-oxides within pore spaces between 25 and 20 m depth are interpreted as evidence of hydrothermal alteration that occurred after initial weathering, consistent with the observations of Štědrá et al. (2016). Fluorite was not observed in other sections of the

core. Furthermore, fluorite grains are restricted to pore spaces within or associated with albite and do not occur in association with less weathered minerals like quartz and K-feldspar, consistent with formation after the onset of weathering. The hydrothermally altered zone also coincides with a band of higher CIA values, while CIA and tau values between 6.17 m and 14.64 m are relatively consistent (Fig. 2.4 and 2.5). The regolith layer (above 2.6 m depth) is more intensely weathered than the bedrock as evidenced by higher CIA values and secondary clay volumes in addition to lower primary mineral volumes. Weathering in the regolith layer is likely enhanced by the acidic porewaters (pH = 3.5-4.6; Krám et al., 2012). Much of the mineral mass loss occurs within the upper 3-4 m of the profile, although only a thin layer of soil and regolith exists (2-3 m). Despite the presence of hydrothermal overprinting below 20 m, the profile above 15 m is sufficient to assess weathering processes within the Lysina profile, including calculation of mineral weathering rates and correlating weathering front characteristics with climate parameters.

2.4.2. Weathering Fronts in Different Climate Regimes

Sites from around the world exhibit significantly different weathering profiles, both in depth and the intensity of weathering (CIA) (Fig. 2.7). Lysina shows limited weathering over 10s of metres of bedrock under a thin (2.6 m) regolith, while the Río Icacos profile has a dramatic transition from fresh to near totally weathered regolith over only 1 m below a 5 m thick regolith. Although higher elevation weathering profiles in the Río Icacos catchment can have thicker regolith ($>$ 25 m), the embedded bedrock corestones have similarly sharp transitions from un-weathered rock to highly depleted regolith (Orlando et al., 2016), reflecting rapid weathering (e.g., White et al., 1998; Buss et al., 2008). Davis Run and Panola represent intermediate profiles, with more gradual but deeper weathering at Davis Run and a shallower but sharper transition from fresh to weathered material at Panola. Thus, the weathering gradients become thinner (sharper) with increasing MAP and MAT (Fig. 2.7).

Globally, weathering intensity correlates well with climatic factors, with intense weathering commonly found in warm, humid environments (Strakhov, 1967; Goldberg and Humayun, 2010). Weathering profiles on a given lithology, in warmer, more humid environments also transition from fresh to weathered material over shorter distances, while these transitions in the cooler and drier environments are more gradual (e.g., White et al., 2001; Hewawasam et al., 2013; Schaffhauser, 2013; Schaffhauser et al., 2014; Buss et al., 2017). Conversely, fresh bedrock is reached at shallower depths at sites where weathering is more intense (Fig. 2.7).

Variations in bedrock porosity and permeability can also determine weathering profile morphology. A more permeable bedrock would expose greater volumes of minerals to reactive fluids. The permeability of the Panola bedrock is lower than that of Davis Run, which exhibits less intense, but deeper weathering (Table 2.1; White et al., 2001). The greater permeability at Davis Run relative to Panola (hydraulic conductivity = >4 x 10^{-3} m yr^{-1} and 1 x 10^{-3} m yr^{-1}, respectively)

may allow weathering to penetrate further into the bedrock (White et al., 2001). Similarly, the Río Icacos bedrock has low permeability (primary porosity < 0.03 %; Buss et al., 2008), with secondary porosity generated largely through reaction-driven fracturing (Fletcher et al., 2006), followed by dissolution and micro-cracking (Buss et al., 2008). Advective flow of reactive fluids through fractures promotes rapid weathering at Río Icacos, where regolith is deeper where the bedrock is more fractured (Orlando et al., 2016; Hynek et al., 2017).

Comparisons between the profiles above strongly indicate that weathering fronts become sharper within warmer and more humid climates, with the weathering front in the Río Icacos transitioning from fresh to near-totally weathered material over a distance of 1 m. The parameters affecting weathering processes within this transition zone are thus critical for understanding controls on weathering and its long-term impact on global climate. Below we further assess the parameters affecting weathering to determine the extent to which individual parameters determine weathering rates and profile morphology.

2.4.3. Controls on Weathering Rates in Different Climate Regimes

Plagiolcase Composition

Plagioclase weathering rates are available for four of the profiles: Lysina, Davis Run, Panola, and Río Icacos (in order of increasing MAT and MAP; Tables 2.1 and 2.5; White et al., 2001, 2002; Buss et al., 2008). In all four profiles, plagioclase weathers faster than K-feldspar or micas, with plagioclase rates ranging from log R = -16.4 mol m^{-2} s^{-1} at Davis Run to -13.0 in the Río Icacos profile (Eq. 2.5; Table 2.5). The plagioclase of both Lysina and Davis Run is predominately albite, while the Panola and Río Icacos plagioclases contain more Ca: An_{23} and An_{48}, respectively (White et al., 2001; Buss et al., 2008). Ca-rich plagioclase is typically more reactive than Na-rich plagioclase (e.g., Bandstra et al., 2008). Lysina has significantly higher plagioclase weathering rates (log R = -16.1 mol m^{-2} s^{-1}) than Davis Run (log R = -16.4 m^{-2} s^{-1}), despite mean annual temperatures that are 5 °C warmer at Davis Run. MAP values are similar between the two sites, with less than 10% difference. Plagioclase weathering rates are slightly faster at Panola (Log R = -15.7 mol m^{-2} s^{-1}) than Lysina, but more than 2 orders of magnitude slower than at Río Icacos (Log R = -13.0 mol m^{-2} s^{-1}). MAT differs by 5 °C between Panola and Río Icacos (17 °C and 22 °C, respectively), and between Lysina and Davis Run (5 °C and 10 °C, respectively), but weathering rates differ significantly between the two warmer sites (1.4 – 2.7 orders of magnitude), and comparatively little at the two cooler sites ($<$ 1 order of magnitude). Within this dataset, precipitation appears to have a strong influence on plagioclase weathering rates, while the influence of temperature appears to be weaker (Fig. 2.10A).

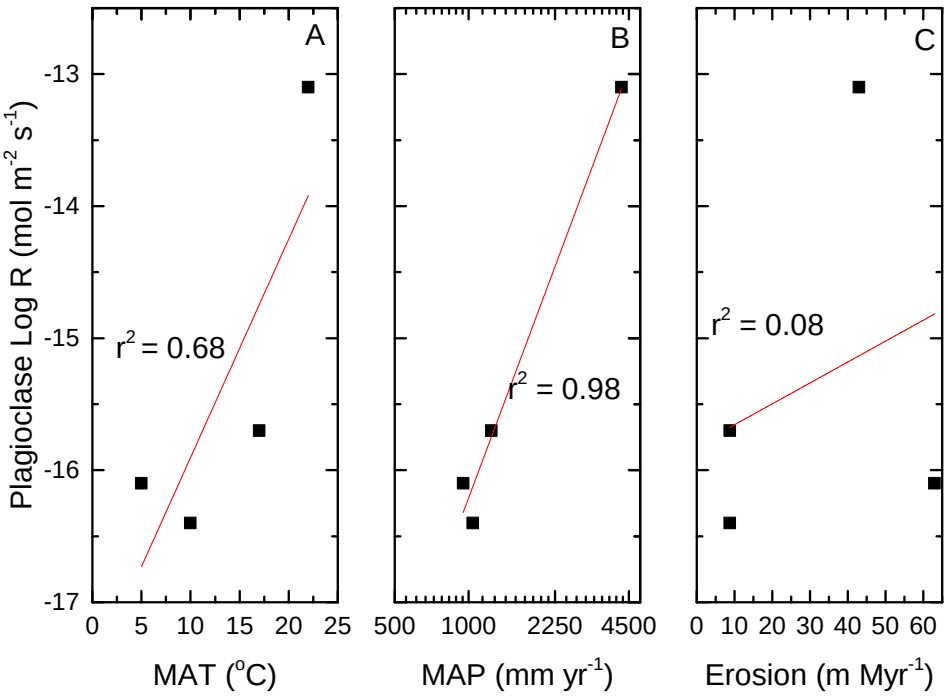

Figure 2.10: Log plagioclase weathering rates from the four primary sites plotted against (A) mean annual temperature, (B) mean annual precipitation, and (C) erosion rates (Tables 1 and 5). Plagioclase rates show a stronger correlation with MAP (r^2 = 0.98, p = 0.009) than MAT (r^2 = 0.68, p = 0.18) which shows inconsistent changes in rates over similar values (i.e., a decrease in rates over a 5 °C increase between Lysina and Davis Run, and three orders of magnitude increase over a 5 °C increase between Panola and Río Icacos). Erosion rates show no clear correlation with plagioclase weathering rates in this sample. Due to the low sample size, confidence in these correlations is very low.

Although differences in composition will have some impact on plagioclase weathering rates, it is unlikely that they explain the scale of the differences in rates seen between the four sites. A comparison of laboratory-derived rates shows only around 1 order of magnitude difference in weathering rates between albite and andesine (Bandstra et al., 2008). Furthermore, recent studies have indicated that differences in mineral stoichiometry may have less impact on weathering rates than previously thought; a study covering a range of plagioclase compositions (An_{21} – An_{50}) found differences of only a tenth of an order of magnitude in dissolution rates (White et al., 2017). As such, it is unlikely that the variations in plagioclase compositions significantly influence the differences in weathering rates seen in our dataset and suggests that other factors such as tectonic and climatic influences must be considered.

Erosion and Tectonics

A number of studies have argued that erosion (and thus tectonic activity) is a strong control on weathering rates (e.g., Berner et al., 1983; Raymo and Ruddiman, 1992; Riebe et al., 2001;

Dixon and von Blanckenburg, 2012). Erosion can promote weathering by exposing fresh mineral surfaces and reducing soil and regolith accumulation, whereas the accumulation of thick weathered regolith can reduce the exposure of weatherable mineral surfaces to reactive fluids. Ratios of $^{10}Be/^{9}Be$ indicate that Lysina experiences approximately 63 m Myr^{-1} of erosion, accounting for approximately 90% of the total denudation (Dannhaus et al., 2018). Similarly high erosion rates (20-100 m Myr^{-1}) have been observed at several other highland catchments in Europe, although the causes of these high rates remain unclear (Schaller et al., 2001). Low surface erosion rates likely account for the thicker regolith at Davis Run and Panola (11 m and 5 m, respectively) relative to Lysina and Río Icacos (2.6 m and 5 m, respectively; Table 2.1; Bacon et al., 2012; Brantley et al., 2017). Erosion in Río Icacos is dominated by landslides along slopes, but the regolith-mantled ridgetops are remarkably stable (Larsen and Torres-Sanchez, 1998; Brocard et al., 2015). Ridgetop weathering profiles in Río Icacos are believed to be in steady state (erosion rates = weathering rates, with regolith thickness stable through time), and denudation rates of ˜43 m Myr^{-1} have been derived using both ^{10}Be and U/Th methods (Brown et al., 1995; Chabaux et al., 2013) , considerably higher than erosion rates at Davis Run and Panola (4.5-13 m Myr^{-1} at both sites) (Pavich, 1985; Brantley et al., 2017).

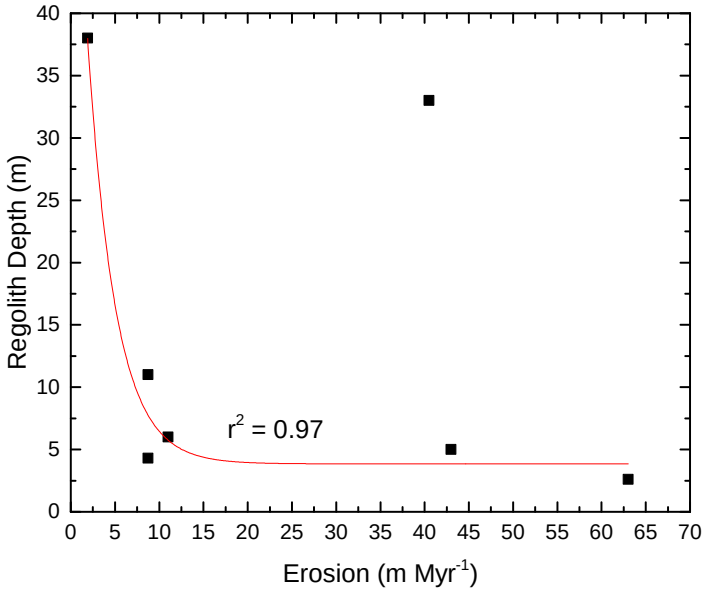

Figure 2.11: Regolith depth plotted against erosion rates for all sites (Table 1). Regolith depth shows a general decrease where erosion rates are highest, although Curacavi (Erosion Rate = 40.5 m Myr^{-1}, Depth = 33 m) is an outlier in this trend. An exponential trendline returns a correlation of r^2=0.97 (significant at the 95% confidence level) if the outlier (Curacavi) is excluded. The correlation has a low power of 0.13 however.

Crucially, although Río Icacos and Lysina experience a similar long-term average rate of erosion (43 m Myr^{-1} and 63 m Myr^{-1}, respectively), plagioclase weathering rates at Río Icacos are

nearly three orders of magnitude higher than those at Lysina. (Tables 1 and 5). It is possible that chemical weathering responses to erosion are site specific, as indicated by other studies (Ferrier and West, 2017). Thinner regolith may promote more rapid chemical weathering by allowing greater quantities of reactive fluids to make contact with minerals in the bedrock (Fletcher et al., 2006; Gabet and Mudd, 2009). Such a process may explain why plagioclase weathering rates are faster at Lysina than Davis Run and Panola, despite a cooler and slightly drier climate. Lysina's relatively thin regolith layer (2-3 m) contrasts with the deeper regolith of Davis Run (11 m), and albite mass loss increases significantly above Lysina's regolith-bedrock boundary (Table 2.3). There is no clear trend of faster mineral weathering rates at sites with higher erosion rates in this limited dataset (Fig. 2.10C). Regolith depth does appear to have a relationship with erosion rates however, especially when considering the larger dataset of sites (Table 2.1), with the thinnest regolith generally found at the sites with the highest erosion rates (Fig. 2.11).

Although mineral specific weathering rates exhibit only a limited response to higher erosion rates, whole-rock chemical weathering rates (CWR) from other sites could be used to argue for a stronger erosional influence. The humid tropical sites of Nsimi in Cameroon, and Hakgala in Sri Lanka, both experience low CWR, despite high precipitation and warm MAT (Table 2.1). In the case of Hakgala, the low CWR is attributed to the very low erosion rate, leading to a low supply rate of fresh material to the weathering environment (Hewawasam et al., 2013). At the humid site of Nsimi, deep (38 m), highly weathered regolith has been produced, likely as a result of the low erosion rate (Braun et al., 2005, 2012). In contrast, the arid site of Curacavi in Chile experiences comparable erosion rates (40.5 m Myr^{-1}) to Lysina and Río Icacos, but exhibits only limited weathering (Table 2.1; Vázquez et al., 2016). As such, data from the sites presented here show no clear trend between erosion and CWR, in contrast to results from previous studies (Riebe et al., 2004; West et al., 2005). However, Río Icacos, which has the highest CWR of our sites, has both a high erosion rate and high MAP (Table 2.1). Therefore, erosion rates may exert a significant control on CWR in environments where other variables, such as precipitation, do not restrict weathering. This effect is consistent with observations from previous compilations (West et al., 2005) and modeling studies that suggest that erosion is a control on weathering *regimes* (Lebedeva et al., 2010), where the balance between erosion and water infiltration determines whether a profile is "transport limited" or "weathering limited".

Climate and the Subsurface

In the absence of strong lithological and erosional controls on chemical weathering rates, climatic differences likely explain much of the variation in mineral and whole-rock weathering rates amongst the four key sites studied here (Tables 2.1 and 2.5). A relationship between climate and chemical weathering has been long established (Strakhov, 1967), although debate continues as to the relative influences of temperature and precipitation (e.g., White et al., 1999; Maher, 2010; Ibarra et al., 2016) . The sharpness of weathering fronts (weathering gradients) in granitic

profiles shows a strong correlation with MAP and a weak correlation with MAT (r^2 = 0.86 and 0.29, respectively). Figure 2.12 shows the Na weathering gradients (as a proxy for plagioclase weathering) of the sites (Table 2.1) plotted against MAT and MAP. The strong correlation between the Na gradient and MAP indicates that as MAP increases, Na becomes depleted in profiles over smaller distances, thus leading to sharper weathering fronts. These results are in line with those indicated by correlations between plagioclase weathering rates and climate variables (Fig. 2.10), as well as correlations between climate variables and whole-rock chemical weathering rates , both of which show a strong correlation with MAP (Fig. 2.14; Oliva et al., 2003; Maher, 2010; Ibarra et al., 2016). The Na gradient appears to be only weakly influenced by MAT, while erosion has essentially no impact on Na gradient values (Fig.12C). The similarity of the response of Na gradients, CWR, and plagioclase weathering rates to MAP suggests that water fluxes to the profile determines both the sharpness of the weathering front and whole-rock chemical weathering rates.

In environments where both precipitation and infiltration rates are high (i.e., high effective precipitation), groundwater residence times are shorter and weathering products are more easily removed from the profile, thus lowering the geochemical saturation state of the groundwater, with respect to weatherable minerals, and favoring faster mineral weathering rates. The link between groundwater geochemical saturation states and fluid residence times within weathering profiles, has been proposed as a strong control on weathering rates (Maher, 2010). In cases where high effective precipitation keeps pore water thermodynamically undersaturated, effective precipitation would be the dominant control on chemical weathering rates and weathering gradients, with high weathering rates causing rapid depletion of minerals from the profile, resulting in sharper gradients. This scenario was demonstrated by reactive transport models that indicated that the highest plagioclase weathering rates were only achieved under high water flow rates and rapid fluid transit times, allowing groundwater to be further from equilibrium and permitting more rapid weathering reactions (Maher and Druhan, 2014). Similar observations have been made in studies of laboratory derived weathering rates, which are frequently 2-4 orders of magnitude more rapid than field derived rates (White and Brantley, 2003; Riebe et al., 2004). This difference in rates has been attributed to, in part, the far from equilibrium laboratory conditions in most experiments, rather than the nearer to equilibrium conditions found in natural settings.

If water fluxes and fluid residence times are key controls on weathering gradients and rates, the structure of the subsurface and its impact on these factors must be considered. Greater secondary porosity should promote fluid transport through the regolith, increasing flow rates and reducing residence times (Maher and Druhan, 2014). Furthermore, even slight weathering may still result in drastic changes in the secondary porosity of the bedrock, allowing new weathering pathways to be produced (St Clair et al., 2015; Goodfellow et al., 2016). Within the Lysina core, samples from fractured zones show slightly higher CIA values than those from less fractured zones (Fig. 2.5; Štědrá et al., 2016). Fractured samples within this study typically show more evidence of weathering in the form of higher CIA values than samples from Štědrá et al. (2016) and greater

secondary clay content than those with fewer fractures (Table 2.3). While these differences in weathering are very small, representing only a change in CIA values of 2-3, these remain outside the range of calculated uncertainty (Fig. 2.5). It is possible that fractures promote water movement in the Lysina core, leading to greater weathering in fractured zones. A more extreme version of this process may be occurring in the Río Icacos catchment. Much of the variation in regolith depth between profiles at Río Icacos has been attributed to differences in the extent of fracturing, with fractures allowing for more efficient transport of water and weathering products (Orlando et al., 2016).

Such examples highlight the potential impact of subsurface architecture on both weathering rates and weathering gradients, as well as the key role of secondary porosity development on exposing fresh minerals to reactive fluids. The dataset compiled here (Table 2.1) reveals a trend of weathering deep into the bedrock in cooler and drier environments such as Lysina and Davis Run, where weathering is sufficiently slow to allow fluids to penetrate the bedrock but insufficiently rapid to produce regolith. These slower weathering rates produce deep profiles with gentle transitions between fresh and highly weathered material over 10s of metres. In contrast, the bedrock in warm and humid environments such as Panola, Hakgala, and Río Icacos is largely unweathered, with sharp weathering transitions between the bedrock and regolith over small distances (˜1 m). Such sharp transitions may represent weathering "hotspots", where chemical weathering occurs rapidly, producing thin weathering fronts (Buss et al., 2017) and high fluxes of inorganic nutrients and energy sources for subsurface biota (Buss et al., 2005, 2010).

Extensive, weathering-relevant datasets from deep critical zone boreholes are relatively few in number, and although compelling trends were identified in this study, conclusively determining the impact of subsurface architecture on weathering rates may not be possible from field data alone. Recent advances in topographic stress modeling and geophysical analysis of the critical zone could, however, provide a way to predict catchment-scale subsurface architecture with fewer deep boreholes (Moon et al., 2017). Reactive transport models also provide a method of determining the impact of subsurface architecture, independent of climate conditions (e.g., Maher and Druhan, 2014).

Although higher erosion rates could promote more rapid chemical weathering rates within our dataset (as evidenced by the more rapid weathering at Lysina relative to Davis Run), comparison with additional sites and studies suggest the effects of erosion are highly site specific (Ferrier and West, 2017). Importantly, they do not appear to significantly increase weathering rates at sites where precipitation is limited, as evidenced by the high erosion/low precipitation site of Curacavi (Table 2.1, Fig. 2.9). However, where high erosion rates combine with warm and humid conditions (e.g., tectonically active tropical mountain belts or volcanic islands (e.g., Rad et al., 2007), chemical weathering rates have the potential to be very high, as seen in Río Icacos. The steep slopes in mountainous environments may also promote more effective water transport,

reducing fluid residence times (Maher, 2010).

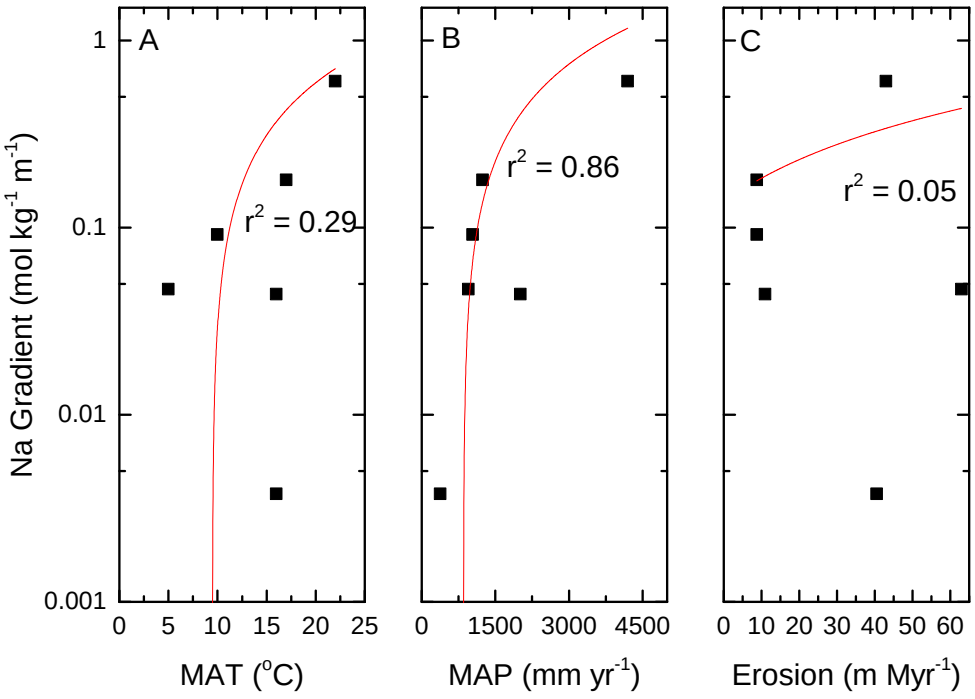

Figure 2.12: Na weathering gradients (as a proxy for plagioclase weathering) correlated against (A) MAT, (B) MAT, and (C) erosion rates at six of the field sites (Table 1). Nsimi is excluded due to non-continuous sampling of that profile preventing the calculation of a gradient value. Na weathering gradients strongly correlate with MAP (r^2 = 0.86, p = 0.007), while correlations are much weaker for MAT and erosion rates. These correlations have statistical powers of 0.99, 0.66, and 0.70, respectively.

Despite CWR and weathering front sharpness both being strongly influenced by MAP, CWRs may be decoupled from weathering front sharpness. While a sharp weathering front indicates that a profile becomes depleted in weatherable minerals over a short distance, the CWR of a profile will be primarily determined by the rate of weathering front advance. However, a front that advances slowly will result in low CWR in a profile. As such, a sharp weathering front in a profile where weathering advance rates are high will likely produce high CWR, but a sharp weathering front is not necessarily indicative of high CWR. The dependence of CWR on weathering advance rates likely explains the stronger erosion control on CWR (Fig. 2.13C) relative to weathering gradients (Fig. 2.12C).

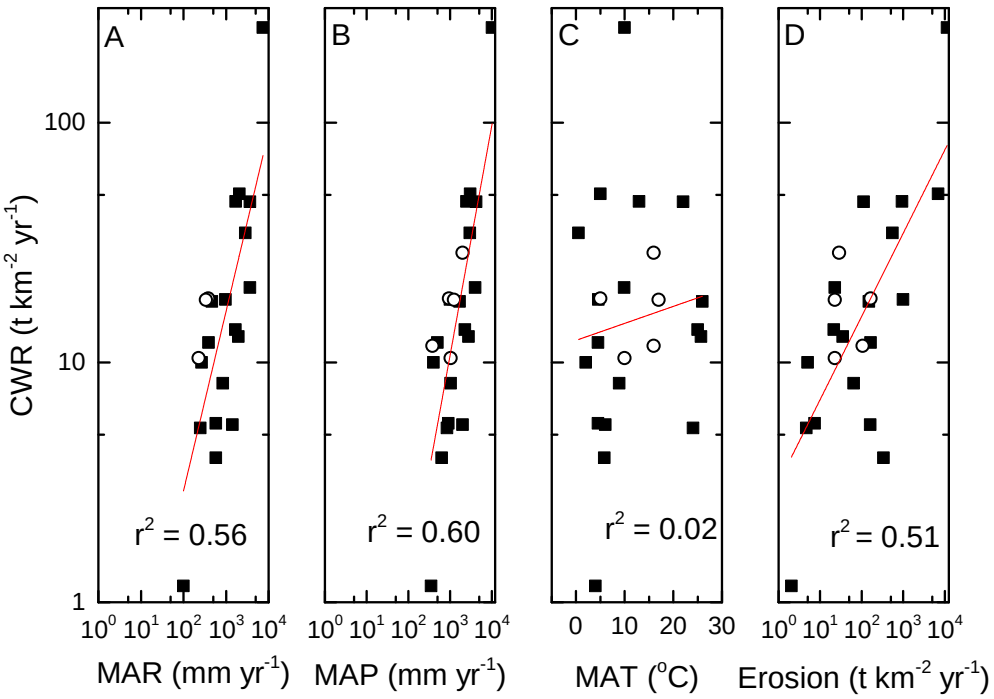

Figure 2.13: Chemical weathering rates (CWR) from 18 sites plotted against (A) mean annual runoff (MAR), (B) mean annual precipitation, (C) mean annual temperatures (MAT), and (D) erosion rates, using data compiled by West et al. (2005) (black squares) and sites from this study (open circles) where data are available. Note that the Nsimi and Río Icacos catchments are included within the West et al. (2005) dataset. The strongest correlations are between CWR and MAP/MAR, with a slightly weaker correlation between CWR and erosion rates. MAT shows no significant correlation with CWR, suggesting that MAR, MAP and erosion are much stronger controls on CWR. The majority of the sites are granitic or granitic/metamorphic, along with four sites with purely metamorphic lithologies.

Our analysis indicates that precipitation represents a primary environmental control on granitic weathering rates, presumably by increasing water fluxes and lowering geochemical saturation within weathering profiles. Similarly, the sharpness of weathering fronts are also likely determined by water fluxes and geochemical saturation states. Sharp weathering fronts (fresh to highly weathered material over distances of a few metres) occur when the profile is further from saturation with respect to weatherable minerals. Temperature appears to exert a minimal influence on most of the profiles within this study, although the impact of temperature may be amplified under more humid conditions (Oliva et al., 2003). These findings are consistent with West et al. (2005), who showed that chemical weathering rates correlate most strongly with mean annual runoff and had no significant correlation with temperature (Fig. 2.13), but extends those findings to the deep subsurface. The latitudinal trends in weathering profiles identified by Strakhov (1967) suggest that climate has a stronger influence on weathering front morphology than lithology or subsurface architecture (which is the result of the parent lithology and weathering). The effects of subsurface

architecture may be more significant at the local scale (profile to watershed) where variations in climate are more limited. However, the potential for subsurface architecture to affect weathering fronts lies in its control on water flow, thus, together, these parameters appear to be more important than temperature in establishing weathering fronts and rates.

2.5. Conclusions

We presented new geochemical analyses of a granitic weathering profile in a temperate forest, Lysina, from which we calculated mineral specific weathering rates and identified key weathering processes. We then compared weathering intensities (CIA), mineral-specific weathering rates and weathering front morphology with additional granitic profiles from the literature from different climatic regimes to identify dominant weathering controls.

Lysina exhibits thin regolith overlying a weathered bedrock extending down at least 15 m and likely beyond 30 m, suggesting deep infiltration of meteoric water. SEM observations, EDS phase analyses, and mass loss calculations indicate that the fastest mineral to weather in the Lysina profile is albite (log R = -16.1 mol m^{-2} s^{-1}), while K-Feldspar and Li-Micas weather more slowly.

Comparison with three additional granitic profiles showed a wide array of weathering front morphologies, ranging from 10s of metres of slightly weathered bedrock at Lysina to the sharp, 1 m transition of fresh bedrock to highly weathered regolith at Río Icacos. Plagioclase weathering rates vary by over three orders of magnitude among these four sites, with the most rapid rates occurring at the tropical Río Icacos and the slowest rates occurring at the temperate Davis Run catchment. In contrast to some earlier studies (e.g., White and Blum, 1995; White et al., 1999; Riebe et al., 2004), weathering rates in our dataset indicated a weaker association with temperature and erosion and a stronger association with precipitation. This relationship likely stems from the higher water fluxes and shorter water residence times within regolith in high-precipitation environments, allowing for lower geochemical saturation in the subsurface, which promotes faster weathering rates, consistent with Maher (2010). Comparison with additional sites suggested that precipitation is the primary limiting factor on whole-rock weathering rates (CWR), with erosion playing a secondary role. These limiting effects could be highly significant for weathering and climate interactions over geological time and indicate the potential importance of rapidly eroding sites in warm and humid environments on long-term atmospheric CO_2 concentrations. Such environments would then disproportionately contribute to the global drawdown of atmospheric CO_2 via the 'weathering thermostat'; by extension, the geographical distributions of such environments could control the efficacy of that thermostat.

The structure, or *architecture*, of the subsurface likely plays a key role in determining water flow rates and geochemical saturation states through weathering profiles. A high degree of variability in secondary porosity exists between sites, even amongst similar lithologies. High

secondary porosity likely promotes high water fluxes and reduced residence times in the subsurface environment. These variations are difficult to predict at the watershed scale, but can lead to significant differences in structure between profiles within individual catchments, especially in intense weathering environments. Structures that promote more rapid water flow, such as fractures, could result in weathering "hotspots", especially at depth. Furthermore, deep fractures may lead to decoupling between the weathering zone and the surface environment by allowing weathering reactions to occur further from the surface. Furthermore, the interplay of subsurface architecture and precipitation in controlling water flow and thus weathering rates means that the nature of precipitation is important, i.e., intense, episodic precipitation leads to high runoff and poor infiltration but high erosion. Additional field site data from more critical zone profiles and reactive transport modeling will allow us to better understand the impacts of episodic precipitation and mechanisms of shallow and deep weathering processes on profile morphology and weathering rates on various spatial and time scales.

Chapter 3

Investigating Controls on Granitic Weathering Profile Morpholgy: A Reactive Transport Modelling Approach

Author contributions and declaration: Reactive transport modelling in this chapter was performed and devised by Nicholas Hayes with assistance and guidance from Oliver Moore, Jennifer Druhan, and Heather Buss. Field site data were gathered from literature sources with the exception of Lysina, which uses data generated for chapter 2 of this thesis.

3.1. Introduction

Chapter 2 identified a strong hydrological control on the morphology of granitic weathering profiles, and further supported theories that hydrology is a dominant control on chemical weathering rates (Maher, 2010, 2011; Maher and Druhan, 2014). As such, precipitation, as the main source of water within weathering profiles, is likely the primary limiting factor on granitic weathering rates and profile morphology. Higher erosion (physical) also promotes weathering rates and is believed to reduce the thickness of regolith, while temperature only increases weathering rates significantly in humid and high erosion environments (e.g., Fig. 2.13). However, the relatively small number of well-sampled granitic profiles prevents the drawing of more robust conclusions from the dataset used in Chapter 2. Furthermore, Chapter 2 identified a possible geochemical saturation control on weathering rates and gradients within profiles, as well as a potential role of subsurface architecture (i.e., primary and secondary porosity, permeability) in determining water flow rates within the subsurface, however there was insufficient data on these factors to draw meaningful conclusions from the available field data. Conditions further from geochemical saturation with respect to weatherable minerals are believed to promote faster weathering (Maher, 2010; Maher and Druhan, 2014) as well as sharper weathering gradients (Fig. 2.12), with higher water flow rates believed to promote geochemically unsaturated conditions within profile.

Using a one-dimensional reactive transport modelling approach, in addition to further field data from less well-sampled sites, this chapter will build upon and further support the findings of Chapter 2. Reactive Transport Models (RTMs) provide an alternative to field studies, as well as a means to experimentally test the independent impact of factors such as temperature, water flow rates, and erosion on chemical weathering rates and profile morphology. In particular, an RTM approach will enable simulations of subsurface architecture and geochemical saturation states to examine their potential impact on weathering processes, which is not practical using field data. The modelling approach will also elucidate relationships between climate and environmental boundary conditions (i.e., temperature, precipitation, erosion) and the evolution of conditions within the subsurface, such as geochemical saturation and secondary porosity development. This chapter aims to identify mechanistic processes that affect the depth of the weathering front, weathering front morphology, and weathering intensity on granitic lithologies, and compare modelled results with data from a range of field sites.

3.2. Methods

This study uses two model simulations created in the RTM Crunchflow (Steefel et al., 2014). One is a model of a simplified granitic profile, which is used to investigate the different profile morphologies and weathering rates produced under a range of climate and erosion regimes and to explore the mechanisms leading to such morphologies. The other is a model of the Río Icacos profile (Chapter 2, Fig. 2.7), which is used to "ground-truth" the simple model design, such that

the key features of a well-known weathering profile (weathering front morphology and weathering intensity) are simulated.

3.2.1. Crunchflow

Crunchflow is a multi-component reactive transport model, primarily intended for modelling chemical processes in porous media (Steefel et al., 2014). Crunchflow has been used to model a range of chemical weathering processes (e.g., primary mineral dissolution, secondary mineral precipitation, geochemical saturation controls on weathering fluxes, secondary porosity development) in the critical zone (e.g., Steefel and Maher, 2009; Maher, 2010; Navarre-Sitchler et al., 2011; Maher and Druhan, 2014). Crunchflow simulates both chemical and physical changes within heterogeneous porous media, making it ideal for studying the interactions of porosity development and flow rate changes on weathering rates and profile morphology. Minerals, their stoichiometries, and equilibrium constants are provided in Crunchflow by a database derived from the EQ3/EQ6 database (Steefel et al., 2014).

3.2.2. Configuration of the Simplified Granite Model

Table 3.1: Río Icacos Model Initial Conditions

Temperature (°C)	22
Initial Pressure (Pa)[a]	60
pH[b]	4.0
Profile Depth (m)	30
Initial Lithology (vol %)[c]	Quartz (25)
	Plagioclase[e] (57)
	Biotite (8)
	Mg-hornblende (7)
	Halloysite (0.0001)
	Goethite (2)
Rate Constants	Quartz (-40.0)
(mol m^{-2} s^{-1})[d]	Andesine (-13.0)
	Biotite (-14.5)
	Mg-hornblende (-12.2)
	Halloysite (-15.0)
	Goethite (-25.0)

[a] Initial pressure was specified at a value that resulted in a flow rate of approximately 1 m yr^{-1} after 150-200 Kyr (Hynek et al., 2017). [b] White et al. (1998). [c] Turner et al. (2003). [d] Buss et al. (2008). [e] Andesine was used for the plagioclase phase as this is most similiar to the plagioclase composition in Río Icacos.

The simplified model simulates the infiltration of water through a one dimensional 30 m "block" of a simplified granite consisting of quartz (50 vol %) and albite (49 vol %) with 1 vol % porosity, weathering to halloysite (Table 3.1). This simplified granite was used to model the impact of different climate regimes and changes in subsurface architecture on granitic profiles. Additionally, using a simplified lithology improves model stability and reduces run time.

Table 3.2: Temperature, Initial Pressure, and Water Flow Conditions for a Simplified Granitic Model

Climate Regime	Temperature (°C)	Initial Pressure (Pa)	Flow Rate at 200 Kyr (m yr^{-1})[a]
Cool-Arid	5	1	0.01
Cool-Humid	5	15	1
Warm-Arid	25	1	0.01
Warm-Humid	25	15	1

[a] Initial pressures were specified in order to produce flow rates of approximately 0.01 and 1 m yr^{-1} under arid and humid conditions, respectively. The flow rate in the saprolite of the LGW-1 core, Río Icacos, Puerto Rico (1 m yr^{-1}) was used as the model humid flow rate. The arid environment was assumed to have a flow rate approximately 2 orders of magnitude lower than the humid environment. 200 Kyr is the approximate age of the LGW-1 weathering profile.

Four diverse climate regimes were created with different temperatures and water availability, represented by specifying a pressure gradient between the surface and the base of the model profile (Table 3.2). This approach allows water flow rates to be recalculated as porosity and permeability evolve during the course of the model simulation.

An initial water pressure of 15 Pa was specified in the humid models to produce flow rates similar to those measured in the Río Icacos saprolite (˜1 m yr^{-1}) (Hynek et al., 2017), while arid regimes used an initial pressure of 1 Pa, to produce a flow rate approximately 2 orders of magnitude lower than the humid environment. Cool regimes were set at a temperature of 5°C and warm regimes were set to a temperature of 25°C. The flow rate is determined by the initial permeability of the modelled profile and the initial pressure. We also alter the initial permeability value by an order of magnitude to test the impact of varying subsurface architecture (represented here as permeability) on water flow and weathering rates and the resulting impact on profile morphology.

Simulations using the simplified model were also run with an erosion component. In natural settings, weathering profiles often enter a steady-state where the rate of regolith production is approximately equal to the rate of regolith removal through erosion (e.g., Lebedeva et al., 2010). The depth of regolith may significantly affect weathering rates by reducing the exposure of fresh bedrock to reactive fluids where deep regolith is present (e.g., Gabet and Mudd, 2009; West, 2012; Viers et al., 2014). However data from field studies suggest that individual profiles may have inconsistent responses to erosion, with some sites showing faster weathering under high erosion rates while others show slower weathering (Ferrier and West, 2017). Within Crunchflow, erosion is modelled simply as the removal of material from the ground surface and addition of fresh material to the deepest node at a specified rate (Steefel et al., 2014). The four climate regimes were re-run with the erosion component under three erosion regimes of 10 m Myr^{-1}, 25 m Myr^{-1}, and 100 m Myr^{-1}, chosen to reflect low, moderate, and high erosion environments, respectively.

The model was run for a total of 2000 Kyr to investigate the continued development of the weathering profile, with 2000 Kyr representing the upper age limit of the profiles investigated

within this study (Vázquez et al., 2016). The modelled profiles from the simplified model are examined at 200 Kyr, a similar timeframe to the calibration model.

3.2.3. Río Icacos Model Configuration

A representation of the Río Icacos LGW-1 (Buss et al., 2017, Chapter 2.2.2.) profile was created in Crunchflow (Table 3.1). Within Crunchflow, the LGW-1 profile was modelled as a one-dimensional 30 m "block" of the Río Blanco Quartz Diorite, which was then subjected to environmental conditions present within the catchment (White et al., 1998; Turner et al., 2003). The Río Icacos catchment has been extensively studied (e.g., Brown et al., 1995; White et al., 1998; Turner et al., 2003; Buss et al., 2017; Lara et al., 2017), and thus the geochemistry and environmental conditions are relatively well constrained. Furthermore, mineral specific reaction rates are available (Buss et al., 2008), and the age of the profile has been calculated independently using ^{10}Be (Brown et al., 1995) and U/Th disequilibria (Chabaux et al., 2013) as approximately 200 Ka.

The model was run for 165 Kyr, the approximate time taken to produce a 7-8 m profile from a weathering advance rate of 43 m Myr^{-1} as derived by Brown et al. (1995) and Chabaux et al. (2013). The model was directed to output data at four additional timesteps during the model runs (1 Kyr, 10 Kyr, 50 Kyr, 100 Kyr).

3.2.4. Field Sites

Table 3.3: Conditions at a Range of Granitic Profiles from the Literature

Site	Location	Lithology	Climate	MAT (^oC)	MAP (mm yr^{-1})	Erosion (m Myr^{-1})
Boulder Creek [a,b]	Colorado, USA	Granitic/Gneiss	Cool Alpine	5.1	519	nd
Cheras [c]	Malaysia	Granite	Tropical	26.8	2444	nd
Curacavi [d]	Chile	Granodiorite	Semi-arid	16	380	40.5
Davis Run [e,f]	Virginia, USA	Granodiorite	Temperate	10	1040	8.75
Hakgala [g]	Sri Lanka	Granitic/Gneiss	Humid Subtropical	16	2013	11
Longnan [h,i,j]	SE China	Granite	Humid Subtropical	18.9	1600	7.46*
Lysina [k,l,m]	Czech Republic	Leucogranite	Temperate	5	950	63
Panola [e,f]	Georgia, USA	Granodiorite	Subtropical	17	1240	8.75
Rawang [c]	Malaysia	Granite	Tropical	27.3	2623	nd
Ringelbach [n,o]	France	Granite	Temperate	7.5	1250	nd
Río Icacos [p,q,r,s]	Puerto Rico	Tonalite	Tropical	22	4200	43

[a] Eldam (2016) [b] Dethier and Lazarus (2006) [c] Yusoff et al. (2013) [d] Vázquez et al. (2016) [e] White et al. (2001) [f] Brantley et al. (2017), [g] Hewawasam et al. (2013) [h] Zhang et al. (2015) [j] Liu et al. (2016), [k] Krám et al. (2012), [l] Štědrá et al. (2016), [m] Dannhaus et al. (2018), [n] Schaffhauser (2013) [o] Schaffhauser et al. (2014) [p] Turner et al. (2003) [q] Buss et al. (2008) [r] Buss et al. (2017) [s] Brown et al. (1995).* Converted from g m^{-1} yr^{-1} using average soil density of 1.34 g cm^{-3}.

Geochemical data were gathered from 11 studies of granitic weathering profiles from a range of climate regimes around the world (Table 3.3). Mean annual temperature (MAT) values at the

field sites ranged from 5-27.3°C, approximately the same temperature range as in the simplified weathering model. Mean annual precipitation (MAP) values ranged from 380-4200 mm yr^{-1} . Mass transfer coefficients (Brimhall and Dietrich, 1987) (Equation 2.1) and the Chemical Index of Alteration (CIA) (Nesbitt and Young, 1982) (Equation 2.2) were calculated for all profiles. Cw values of the base cations (Ca, K, Mg, Na) were calculated (Equation 2.4) for each profile to estimate the total masses of mobile elements lost during weathering. Mass transfer coefficients (Equation 2.1) of these total masses were used to identify weathering fronts within the profiles, and weathering gradients (Equation 2.5) were calculated by taking a linear regression line through each elemental weathering front (Appendix B). Sum totals of mobile mass loss gradients were calculated using Equation 3.1:

$$b_{sum} = b_{Ca} + b_K + b_{Mg} + b_{Na} \tag{3.1}$$

where b_{sum} is the sum of the mass loss gradients of four cations that are mobile during weathering: b_{Ca}, b_K, b_{Mg}, and b_{Na} in mol kg^{-1} m^{-1}. Weathering fronts were defined as the zone of predominant mass loss for each mobile cation; where incomplete profiles were observed, the front was defined as the area from the onset of weathering to the surface (Appendix B). Where available, mineral abundance data were used to better estimate the size and location of weathering fronts. These gradients were then correlated with the MAT and MAP values of the 11 sites to identify any climate controls on the steepness of the weathering gradients, which we relate to weathering front morphology.

3.3. Results

3.4. Field Site Correlations

Correlations between summed mass loss gradients (b_{sum}) (Equation 3.1) and site MAP (Table 3.3) produced an r^2 value of 0.81, statistically significant at the 95% confidence level (Table 3.4; Figure 3.1). Although lower, the r^2 value remains high (0.70), even when excluding Río Icacos, which has an unusually high MAP (4200 mm yr^{-1}). In contrast, the correlation between b_{sum} and MAT is somewhat weaker (r^2 = 0.65).

While b_{sum} values show strong correlations with MAP and weaker correlations with MAT, individual element gradients (b_{Ca}, b_K, b_{Mg}, b_{Na}) (Appendix B) exhibit differences in the strength of the correlations with climate variables (Table 3.4). Sodium exhibits a slightly weaker correlation with MAP (r^2 = 0.55) than the other mobile elements (r^2 = 0.59-0.72). In contrast, Ca and Mg both have much lower r^2 values (0.14 and 0.19) with MAT than K and Na (0.55 and 0.74), with only K and Na being statistically significant at the 95% level.

Table 3.4: Element Specific and Sum Mass Loss Gradients from 11 Granitic Weatheirng Profiles[a]

Site	Ca Gradient mol kg^{-1} m^{-1}	K Gradient mol kg^{-1} m^{-1}	Mg Gradient mol kg^{-1} m^{-1}	Na Gradient mol kg^{-1} m^{-1}	Sum Gradient mol kg^{-1} m^{-1}
Boulder Creek	4.06×10^{-2}	1.37×10^{-2}	2.36×10^{-2}	4.35×10^{-2}	1.21×10^{-1}
Cheras	2.26×10^{-2}	8.75×10^{-2}	2.95×10^{-2}	7.98×10^{-1}	9.38×10^{-1}
Curacavi	2.81×10^{-3}	2.42×10^{-4}	2.03×10^{-3}	3.78×10^{-3}	8.86×10^{-3}
Davis Run	3.76×10^{-2}	3.67×10^{-2}	1.53×10^{-2}	9.19×10^{-2}	1.82×10^{-1}
Hakgala	1.14×10^{-2}	1.45×10^{-1}	1.79×10^{-2}	4.41×10^{-2}	2.18×10^{-1}
Longnan	$5.4\,6x\,10^{-2}$	1.83×10^{-1}	1.69×10^{-2}	2.75×10^{-1}	5.30×10^{-1}
Lysina	4.47×10^{-3}	3.31×10^{-2}	5.86×10^{-4}	4.69×10^{-2}	8.50×10^{-2}
Panola	1.12×10^{-1}	8.07×10^{-2}	3.63×10^{-2}	1.80×10^{-1}	4.09×10^{-1}
Rawang	1.03×10^{-1}	2.83×10^{-1}	1.01×10^{-1}	9.74×10^{-1}	1.46
Ringelbach	1.60×10^{-3}	3.04×10^{-3}	-1.28×10^{-5}	2.15×10^{-3}	6.78×10^{-3}
Río Icacos	5.17×10^{-1}	1.18×10^{-1}	3.44×10^{-1}	6.07×10^{-1}	1.59

[a] See appendix B for original C_w values and weathering front locations used to calculate gradient values.

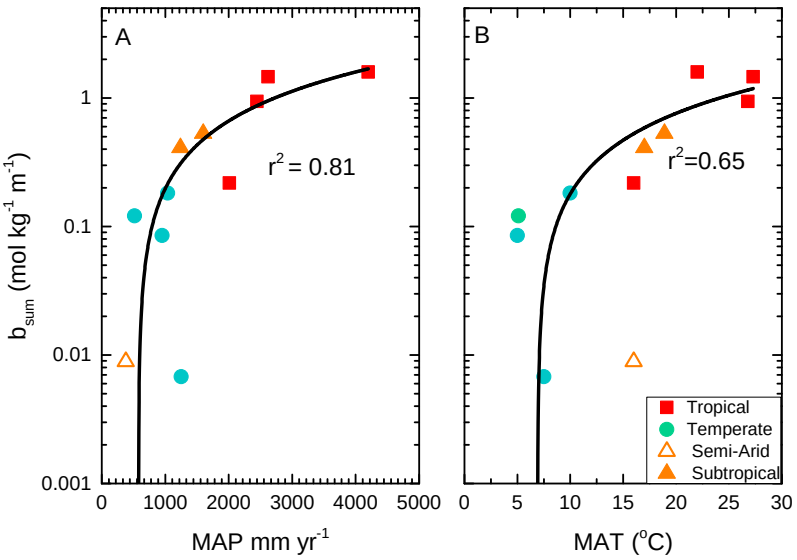

Figure 3.1: Linear correlations between the sum mass loss gradients of mobile elements (b_{sum}) (Ca, K, Mg, Na) in 11 granitic weathering profiles and site MAP (A) and MAT (B). Sum gradients show a strong correlation with MAP ($r^2 = 0.81$) but a weaker correlation with MAT ($r^2 = 0.65$). Note the logarithmic Y axis to show the large range of sum gradient values.

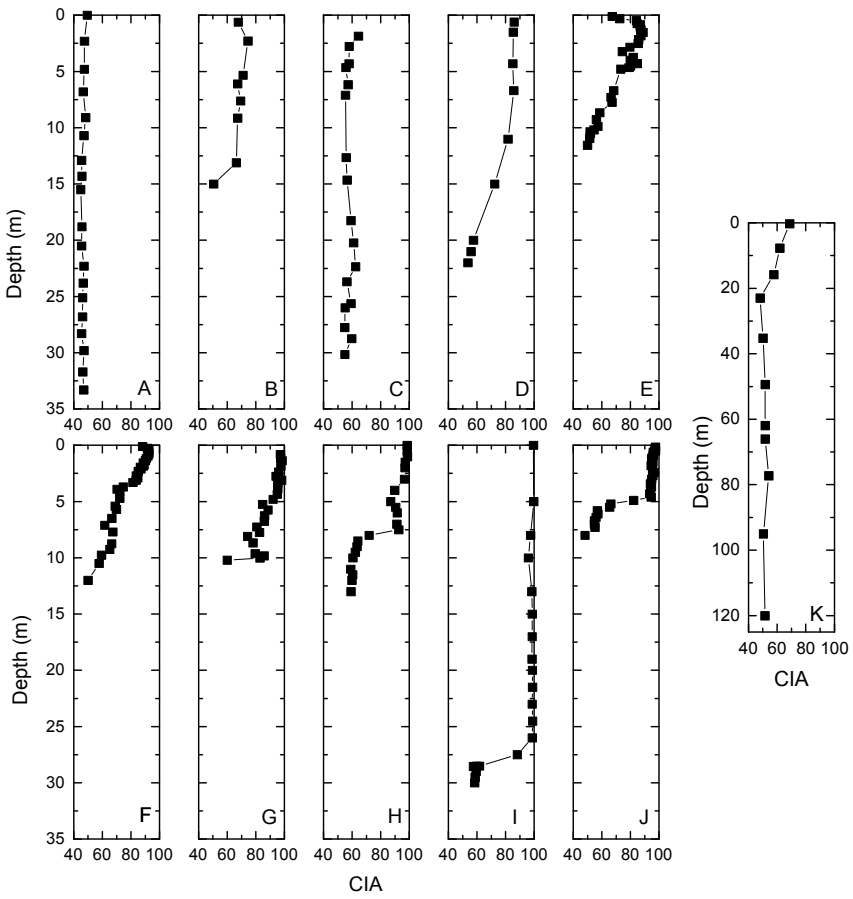

Figure 3.2: CIA profiles of the field sites in order of increasing MAP, (A) Curacavi, (B) Boulder Creek, (C) Lysina, (D) Davis Run, (E) Panola, (F) Longnan, (G) Hakgala, (H) Cheras, (I) Rawang, and (J) Río Icacos. The Ringelbach profile (K) is shown separately to due to its anomalously deep profile ($>$ 120 m). Ringelbach has a MAP value (1250 mm yr^{-1}) between those of Panola (E) and Longnan (F). These profiles show a trend of steepening weathering gradients and higher weathering intensity with increasing MAP.

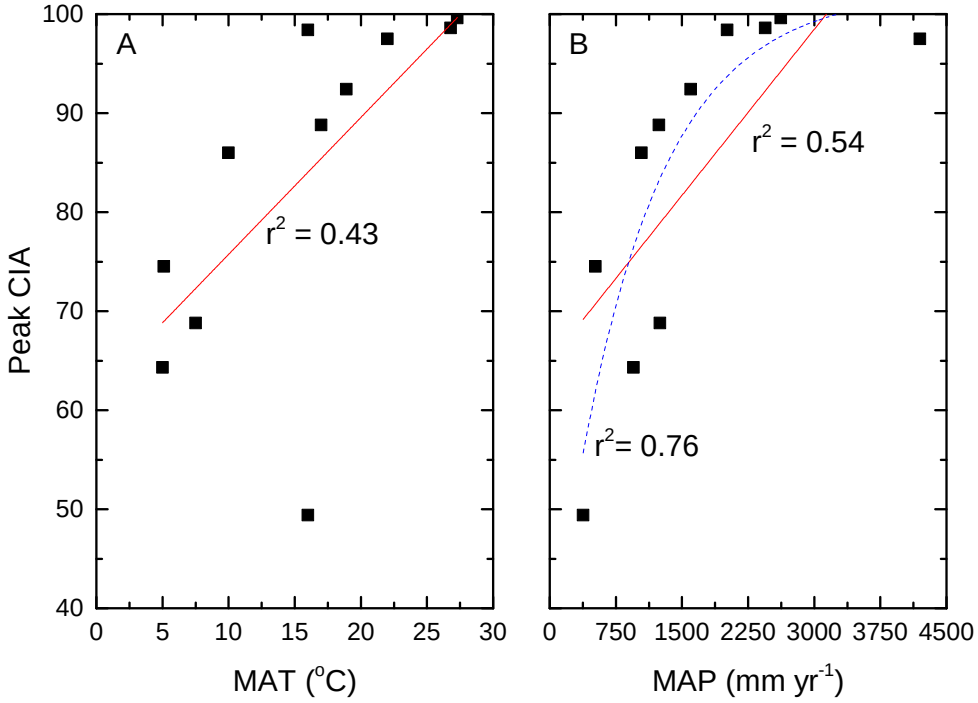

Figure 3.3: Peak weathering intensity (CIA) values from each field site profile plotted and correlated against (A) MAT and (B) MAP. Linear regressions (solid red lines) show a stronger correlation between peak weathering intensity and MAP rather than MAT (r^2 = 0.54 and r^2 = 0.43, respectively). MAP vs weathering intensity may be better approximated by an exponential regression (dashed blue line) which shows a stronger correlation of 0.76.

The highest CIA values (Equation 1.12) from each site correlate linearly with both MAT and MAP values at the 95% confidence level, with MAP having a stronger correlation (r^2 = 0.43 and 0.54, respectively; Figures 3.2 and 3.3). Using an exponential regression results in a stronger correlation between MAP and CIA (r^2 = 0.76). An exponential regression may be more appropriate for MAP as CIA values begin to plateau at higher MAP values and field data indicate that whole-rock weathering rates increase exponentially under more humid conditions (West et al., 2005, Figure 3.3B, Chapter 2). The warm, humid sites show the highest weathering intensities with peak CIA values in the high 90s, while the cooler and drier sites have considerably lower peak CIA values (60-70). The semi-arid Curacavi site has the lowest peak CIA value of 49. Warm, humid sites in the dataset in this study typically show sharp transitions from fresh to highly weathered material, as reflected by the higher weathering gradient values (Figure 3.2; Table 3.4).

3.4.1. Río Icacos Model

Initial experiments with the Río Icacos model produced unrealistically rapid weathering rates of the hornblende and biotite components, resulting in several metres of complete depletion by the first timestep (1 Kyr). In reality, biotite lingers in the Río Icacos saprolite, weathering slowly relative

to the plagioclase phase (Murphy et al., 1998; White et al., 1998; Buss et al., 2008). Furthermore, the biotite and hornblende phases in the Crunchflow database, phlogopite and Mg-hornblende, respectively, have different stoichiometries than the biotite and hornblende in the Río Icacos bedrock. To address these discrepancies, the biotite and hornblende mineral equilibrium constants (log K) in the Crunchflow database were adjusted to be comparable to similar mica and Fe -Mg chain silicate phases. Biotite log Ks were changed to values intermediate between muscovite and annite, whereas hornblende log Ks were changed to those of augite (see appendix B for values); the adjusted equilibrium constants produced weathering fronts similar to field observations (Buss et al., 2008, 2017). Mineral stoichiometries in the Crunchflow database were modified to better approximate those derived from microprobe analysis of samples from Río Icacos (Buss et al., 2008). Using more precise stoichiometries allows for more accurate modelling of interactions between the geochemical saturation of the reactive fluids with minerals.

After adjusting the mineralogical parameters as described above, the Río Icacos model replicated data from the field site well (Figure 3.4). Both the model and the field data show approximately the same weathering front depth and similar weathering front morphology, namely a sharp transition from fresh (rock) to highly-weathered material (saprolite; Figure 3.4). Mass transfers (τ, normalised to Si; Equation 2.1) calculated from the model outputs closely match the Ca, Mg, and Na profiles from the field data (Figure 3.4). The modelled Ca profile produces a slightly sharper weathering gradient than the field data, while the modelled Mg mass transfer shows a shallower gradient that penetrates further into the bedrock. The modelled K profile shows slightly more depleted τ values than the field data and depletion extends further into the bedrock (Figures 3.4B and 3.5B).

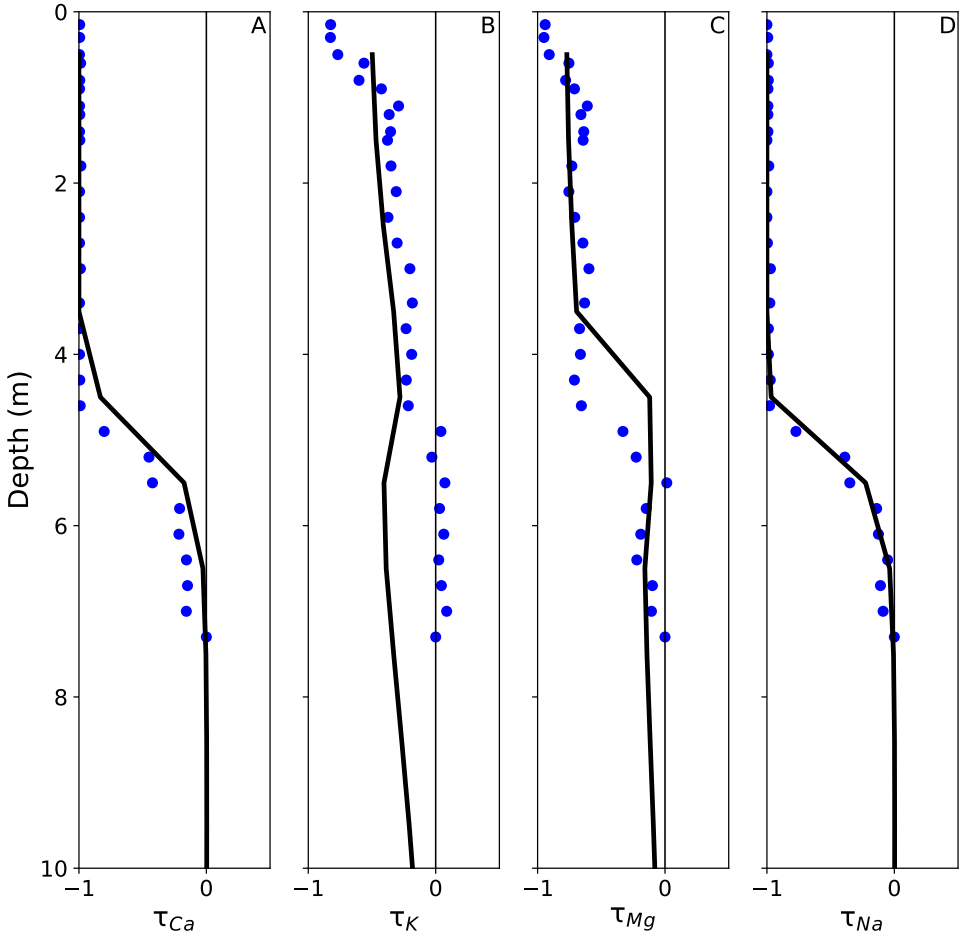

Figure 3.4: Modelled mass transfers for mobile elements (A) Ca, (B) K, (C) Mg, and (D) Na normalised to Si after 165 kyr (black squares and lines) plotted against mass transfers normalised to Si from the field data (blue circles). Modelled mass transfers generally agree well with those from the field, although the model produces a slightly sharper Ca gradient and a shallower Mg weathering front. The model K profile is depleted relative to the field data. The model Na profile shows excellent agreement with the field data.

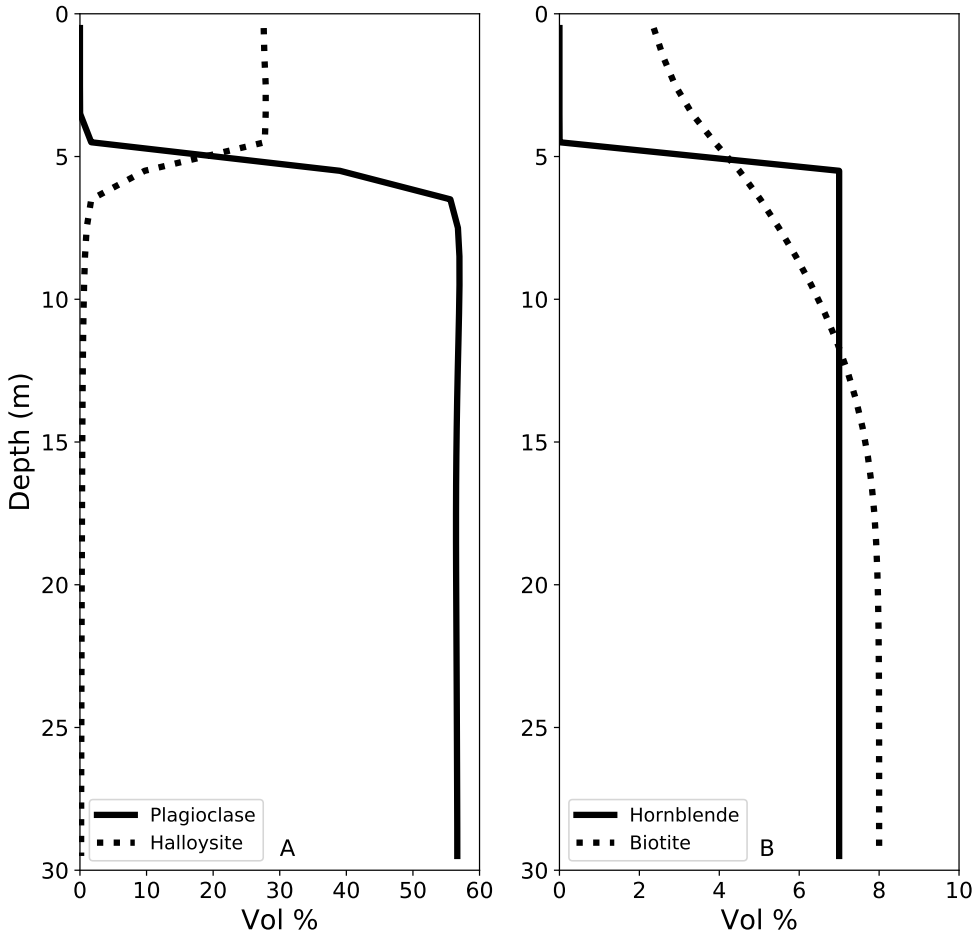

Figure 3.5: Mineral volumes within the Río Icacos model profile after 165 kyr. Major minerals (A) are plagioclase (solid line) weathering to halloysite (dotted line). Minor minerals (B) are hornblende (solid line) and biotite (dotted line). Plagioclase and hornblende are sharply depleted between 5 and 7 m depth, reflected by an increase in halloysite concentrations in the same zone. Biotite shows a more gradual weathering trend beginning deeper in the bedrock but remains present at the surface. Note different x axes between panels due to differing mineral abundances.

Consistent with field data (Buss et al., 2008), the Río Icacos model shows that plagioclase and hornblende are lost rapidly at the bedrock-regolith boundary and are altered to halloysite, which increases significantly in concentration in the same zone (Figure 3.5). Biotite weathers considerably slower and remains present at the surface in small amounts (˜2 vol %). Quartz and goethite show little change in abundance through the profile. Such a result is expected given the very low rate constants specified for these minerals.

3.4.2. Simplified Granite Model

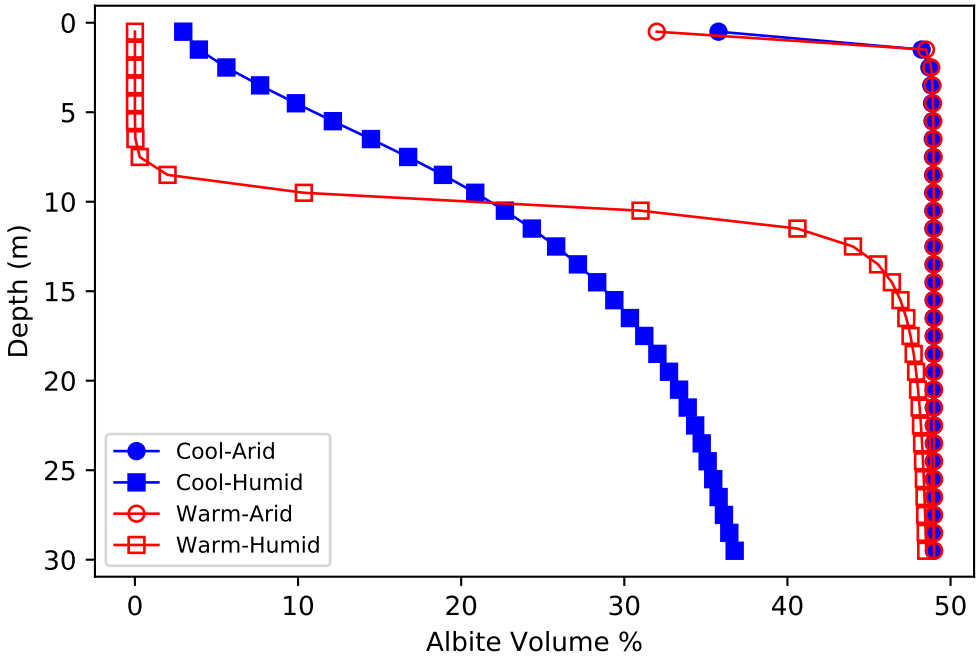

Figure 3.6: Simplified model albite volume profiles after 200kyr under cool-arid (closed blue circles), cool-humid (closed blue squares), warm-arid (open red circles), and warm-humid (open red squares) climate regimes. Both arid profiles show only limited weathering, with the warm-arid environment showing slightly more intense weathering at the surface. The cool-humid profile shows moderate weathering extending to the bottom of the model profile, but albite remains present in small quantities at the surface. The warm-humid model produces a sharp albite weathering front between 8 to 12 m but weathering is limited below 12 m.

The four climate regimes in the model resulted in significant differences in weathering intensity and profile morphology after 200 Kyr (Figure 3.6). These differences were most pronounced when the flow rate was altered. The arid model runs resulted in only minimal weathering after 200 Kyr, with the only significant weathering occurring in the top 1 m of the model profile. The warm-arid model produced only slightly more weathering in the top 1 m than the cool-arid model. As might be expected, albite weathering rates were slightly faster in the top 1 m for the warm-arid model, but weathering rates deeper in the profile were faster for the cool-arid model (Figure 3.7).

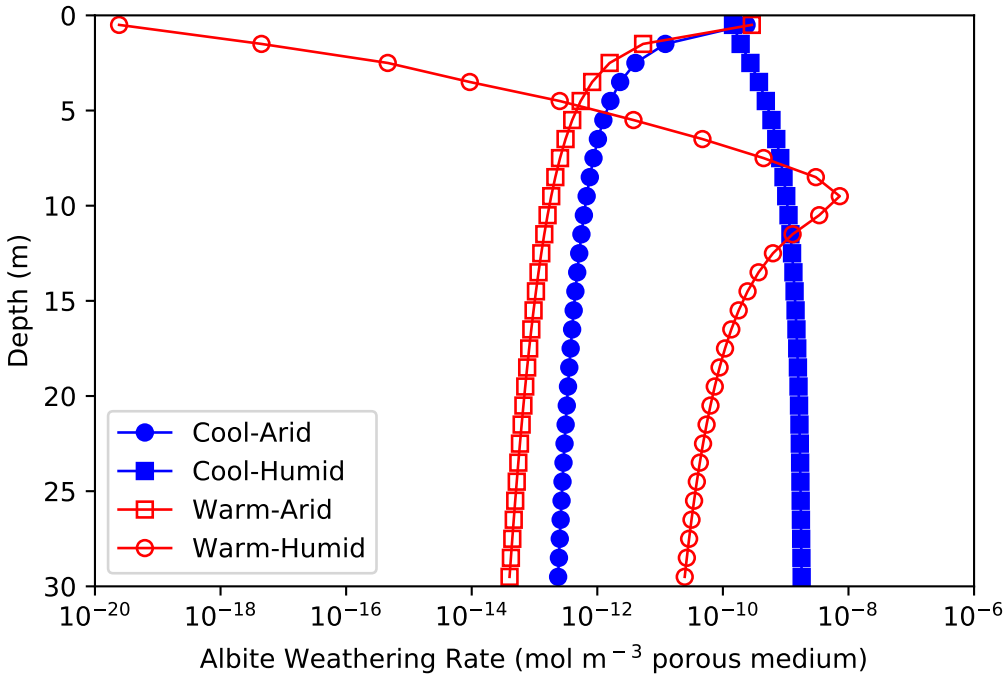

Figure 3.7: Albite weathering rates under cool-arid (closed blue circles), cool-humid (closed blue squares), warm-arid (open red circles), and warm-humid (open red squares) climate regimes. The slowest weathering rates are present in the arid profiles. The warm-arid profile shows the most rapid rates at the surface, but rates are slower throughout the rest of the profile relative to the cool-arid profile. The warm-humid model shows a narrow zone at approximately 8 m depth with the most rapid weathering rates, but below this depth weathering rates are slower than those in the cool-humid profile. The reduction in weathering rates towards the surface in the warm-humid model likely reflects the very low abundance of albite in the weathered regolith.

In contrast, both the cool-humid and warm-humid models resulted in significant weathering and produced differing weathering profile morphologies (Figure 3.6). The cool-humid model produced a very deep weathering profile (˜30 m) with moderate weathering intensity. Albite remains present in all parts of the profile, ranging from 4 vol% at the surface to 37 vol% at the deepest point (30 m). Albite weathering rates (Figure 3.7) in the humid models are 3-4 orders of magnitude higher than those in the arid models , especially within the deeper parts of the profile ($>$ 5 m). Albite weathering rates decrease towards the surface as albite become less abundant.

The warm-humid profile shows intense weathering between 8-10 m depth where albite abundance decreases from $>$40 vol% to near zero (Figure 3.6). This sharp decrease in albite abundance is reflected by very rapid albite weathering rates between 8-10 m depth, the most rapid rates produced by any of the four models (Figure 3.7). Due to the near-total depletion of albite above 8 m, albite weathering rates decrease significantly towards the surface.

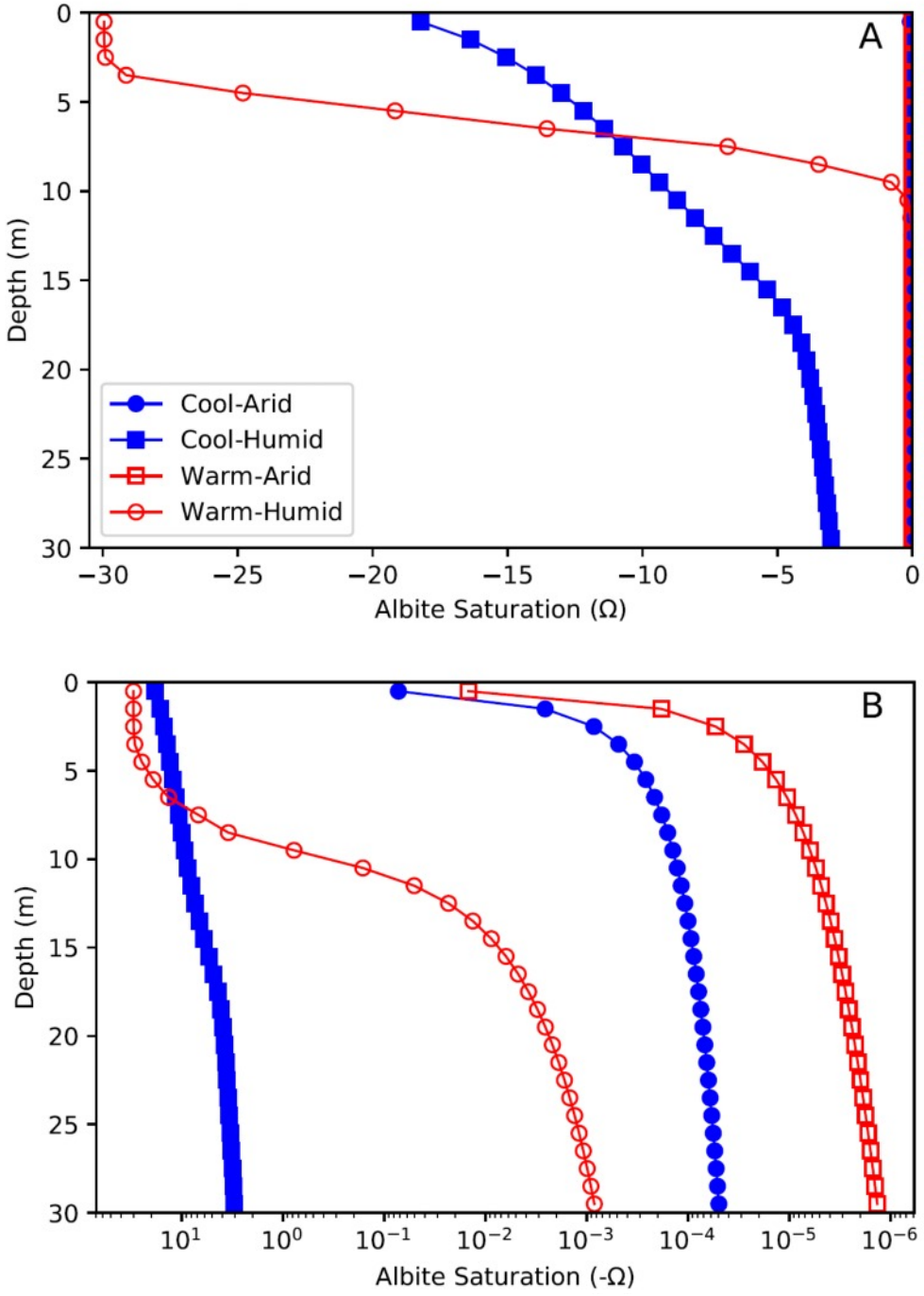

Figure 3.8: (A) Albite saturation indices under cool-arid (closed blue circles), cool-humid (closed blue squares), warm-arid (open red circles), and warm-humid (open red squares) climate regimes. Both arid profiles remain at or near saturation throughout the entire 30 m profile. The cool-humid profile is undersaturated throughout, but is less so at the base of the profile. In contrast, the warm-humid profile is extremely undersaturated near the surface, but reaches near- saturation (Ω = -10^{-2} – -10^{3}) just below the weathering boundary.(B) presents the same data with a logarithmic x axis to display variability in albite saturation state near Ω = 0. Saturation data have been converted to positive values to allow plotting with a logarithmic scale.

The saturation indices (Ω) with respect to albite with depth in the four model profiles reflect the weathering regimes present (Figure 3.8). In the arid models, albite remains close to saturation (Ω 0) throughout the entire profile. The cool-humid model remains undersaturated in albite throughout the entire profile, but undersaturation increases towards the surface. In contrast, the warm-humid model is highly undersaturated near the surface (Ω = -30), but sharply transitions to saturated or near-saturated conditions across the weathering front (8-10 m depth).

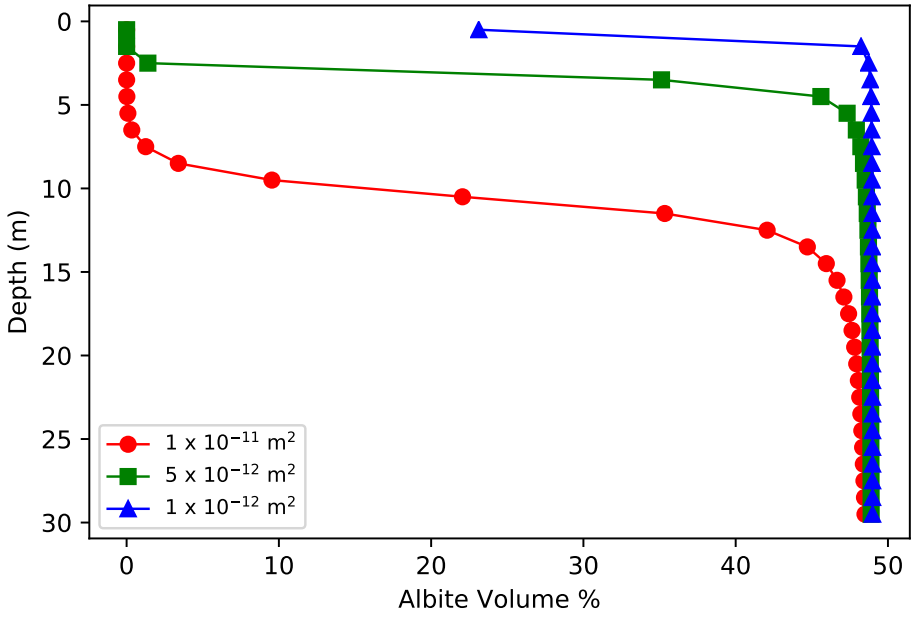

Figure 3.9: Three modelled albite profiles produced under a warm-humid climate with different permeabilities after 200 kyr. The highest permeability (red circles) results in the deepest profile. Profiles become shallower with decreasing permeability.

Increasing the initial permeability of the bedrock resulted in enhanced weathering and deeper weathering fronts (Figure 3.9). Water flow rates increased non-linearly when initial permeability was increased (Figure 3.10). Increasing the permeability from 1 x 10^{-12} m^2 to 5 x 10^{12} m^2 resulted in an increase in water flow rates from 0.018 m yr^{-1} to 0.14 m yr^{-1}, while the same magnitude increase in permeability (5 x 10^{-12} m^2 to 1 x 10^{-11} m^2) increased flow rates to 0.89 m yr^{-1} .

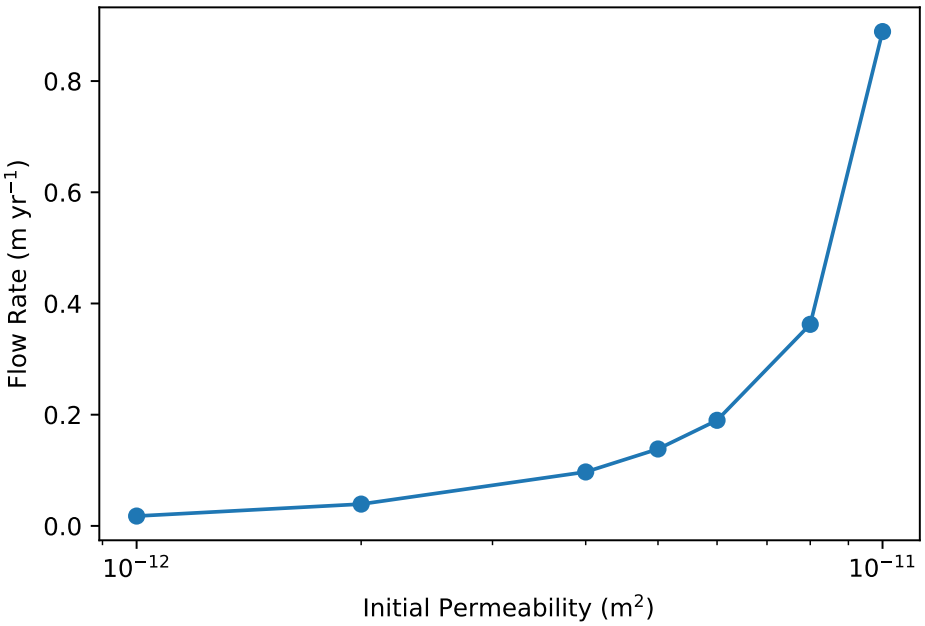

Figure 3.10: Model flow rates under a warm-humid climate with three differing permeabilities. Flow rates are highest when permeability is highest and increases non-linearly as permeability is increased.

The addition of erosion to the simplified model resulted in shallower profiles under all climate conditions (Figures 3.11 and 3.12). The shallowest profiles were produced under an erosion rate of 100 m Myr^{-1} while erosion effects on the profiles at 10 m Myr^{-1} were minor relative to the non-eroding model. In the cool-humid model, even the lowest erosion rate of 10 m Myr^{-1} resulted in a much steeper and shallower profile than the non-eroding model (Figures 3.11C and 3.12C). The highest erosion rate of 100 m Myr^{-1} resulted in the warm-humid model producing an incomplete weathering profile as albite is retained at the surface. Higher erosion rates resulted in less than an order of magnitude slower albite weathering rates in all modelled profiles (Figure 3.13). Similarly, increasing erosion rates resulted in all profiles becoming more saturated with respect to albite (Figure 3.14). At an erosion rate of 100 m Myr^{-1}, the warm-humid profile became almost entirely saturated (i.e., reached equilibrium; Figure 3.14D).

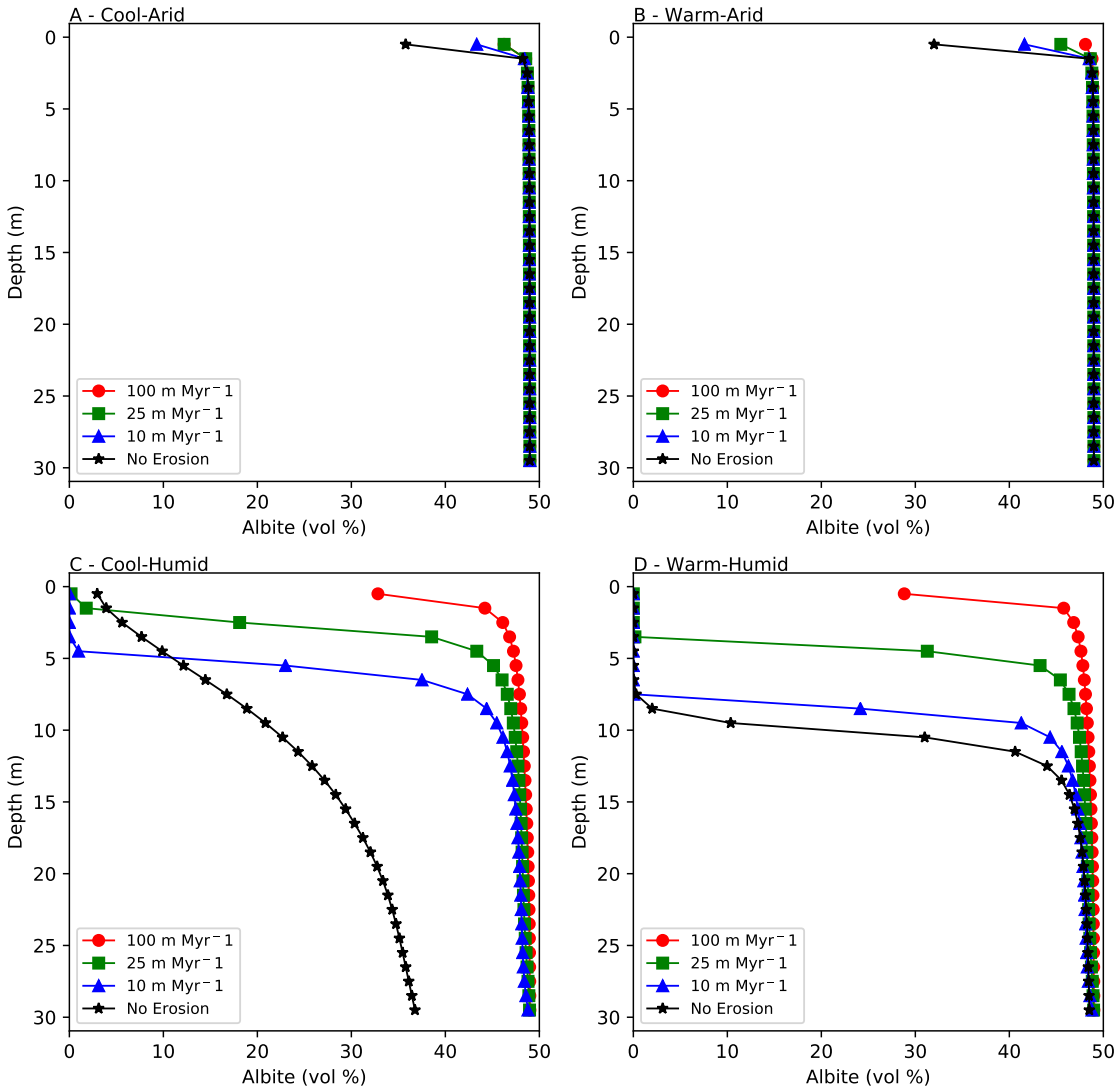

Figure 3.11: Modelled albite profiles produced under different erosion rates in (A) cool-arid, (B) warm-arid, (C) cool-humid, and (D) warm-humid climates. Increasing erosion rates resulted in shallower profiles under all climate conditions. The cool-humid profile (C) shows a notable sharpening of the profile even under the lowest erosion rates relative to the non-eroding model (black stars).

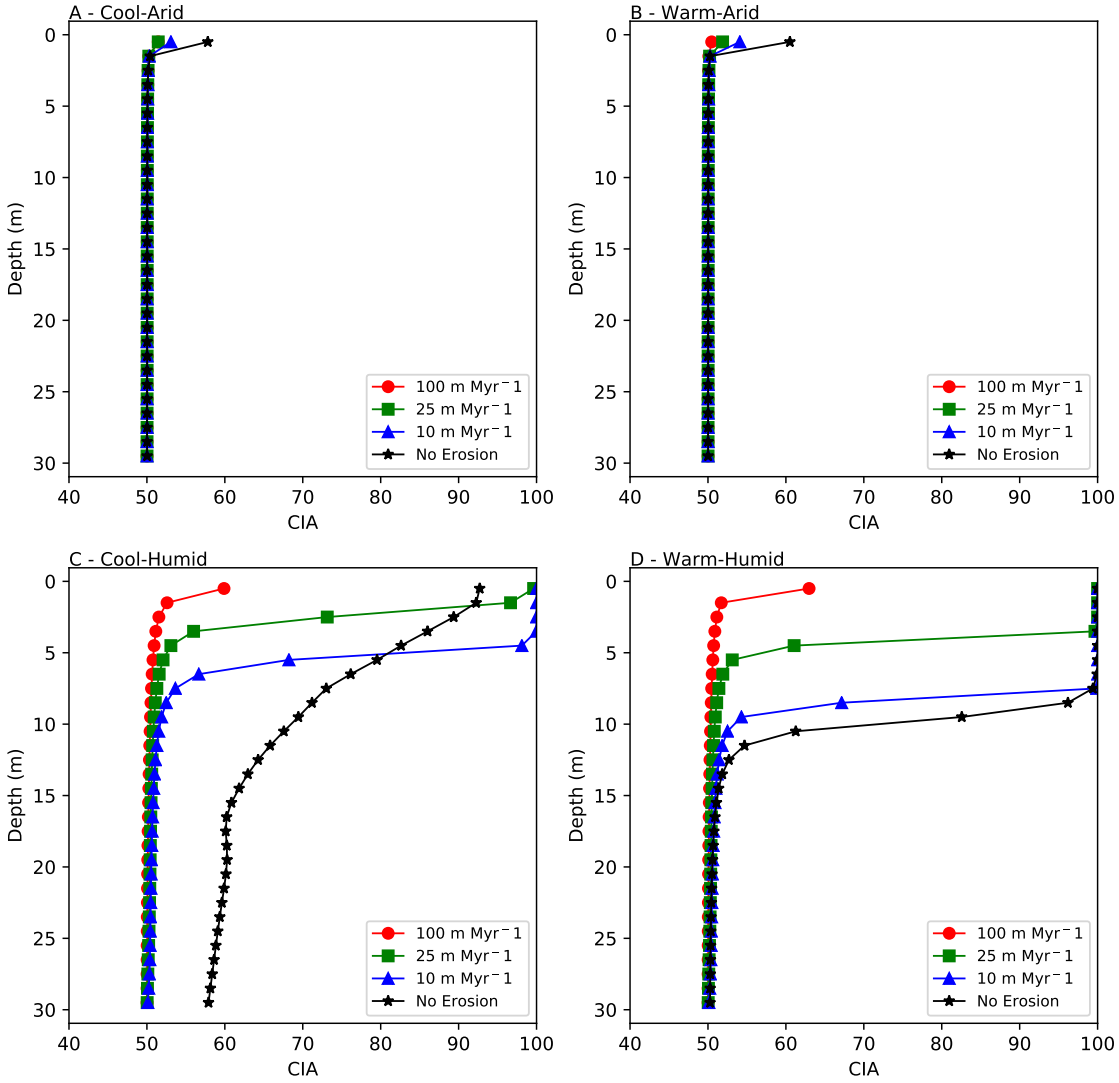

Figure 3.12: Modelled CIA profiles (Equation 1.3) produced under four erosion regimes in (A) cool-arid, (B) warm-arid, (C) cool-humid, and (D) warm-humid profiles. The modelled CIA profiles are very similar to the modelled albite volume profiles, although the non-eroding cool-humid profile (C) shows a slight reduction in CIA values between 15 and 20 m depth, while the corresponding albite volume profile (Figure 3.11C) shows no reversal in albite volumes at the same depth.

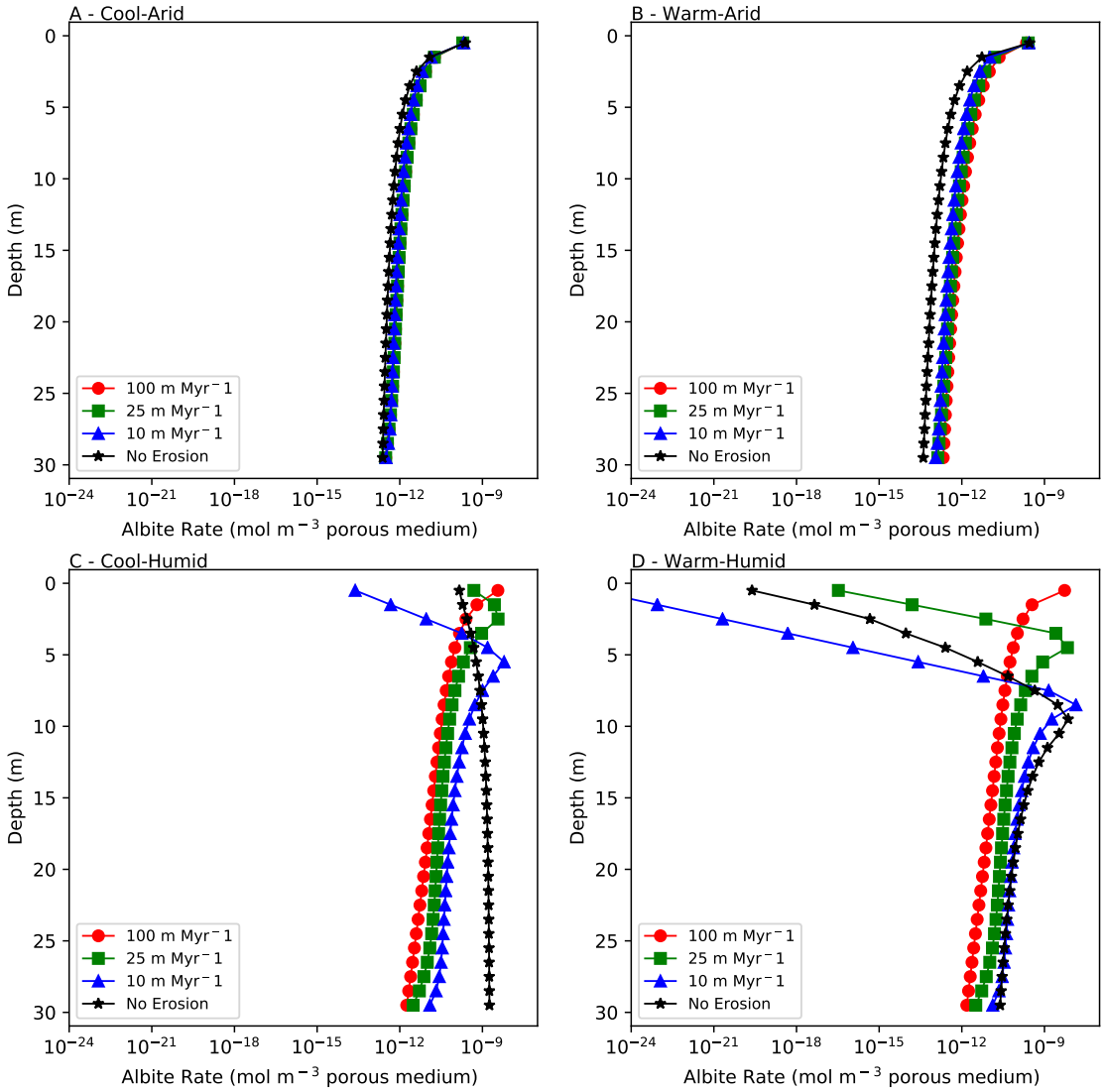

Figure 3.13: Modelled albite weathering rates produced under different erosion rates in (A) cool-arid, (B) warm-arid, (C) cool-humid, and (D) warm-humid climates. Increasing erosion rates reduces weathering rates in all profiles, although these effects are minimal in the arid climates.

Erosion rates appear to affect the time taken for the profile to reach a quasi-steady-state where albite volumes show limited changes between timesteps and the depth of the weathering front remains relatively constant (Lichtner, 1988). In the warm-humid model under erosion rates of 10 m Myr^{-1} and 25 m Myr^{-1}, the depth of the weathering front remains relatively stable between 200-500 Kyr, and only comparatively small changes in albite volumes occur after 1000 Kyr and 2000 Kyr (Figures 3.15A and B). Under an erosion rate of 100 m Myr^{-1}, albite volumes in the profile remain relatively stable between 500 Kyr and 1000 Kyr, with a quasi-steady-state being reached by 2000 Kyr (Figure 3.15C). Under the 10 m Myr^{-1} and 25 m Myr^{-1} erosion regimes, a steady-state weathering front depth is reached around 29-30 m in the warm-humid profile. In contrast the 100 m Myr^{-1} regime results in a steady-state weathering front depth of only 1-2 m.

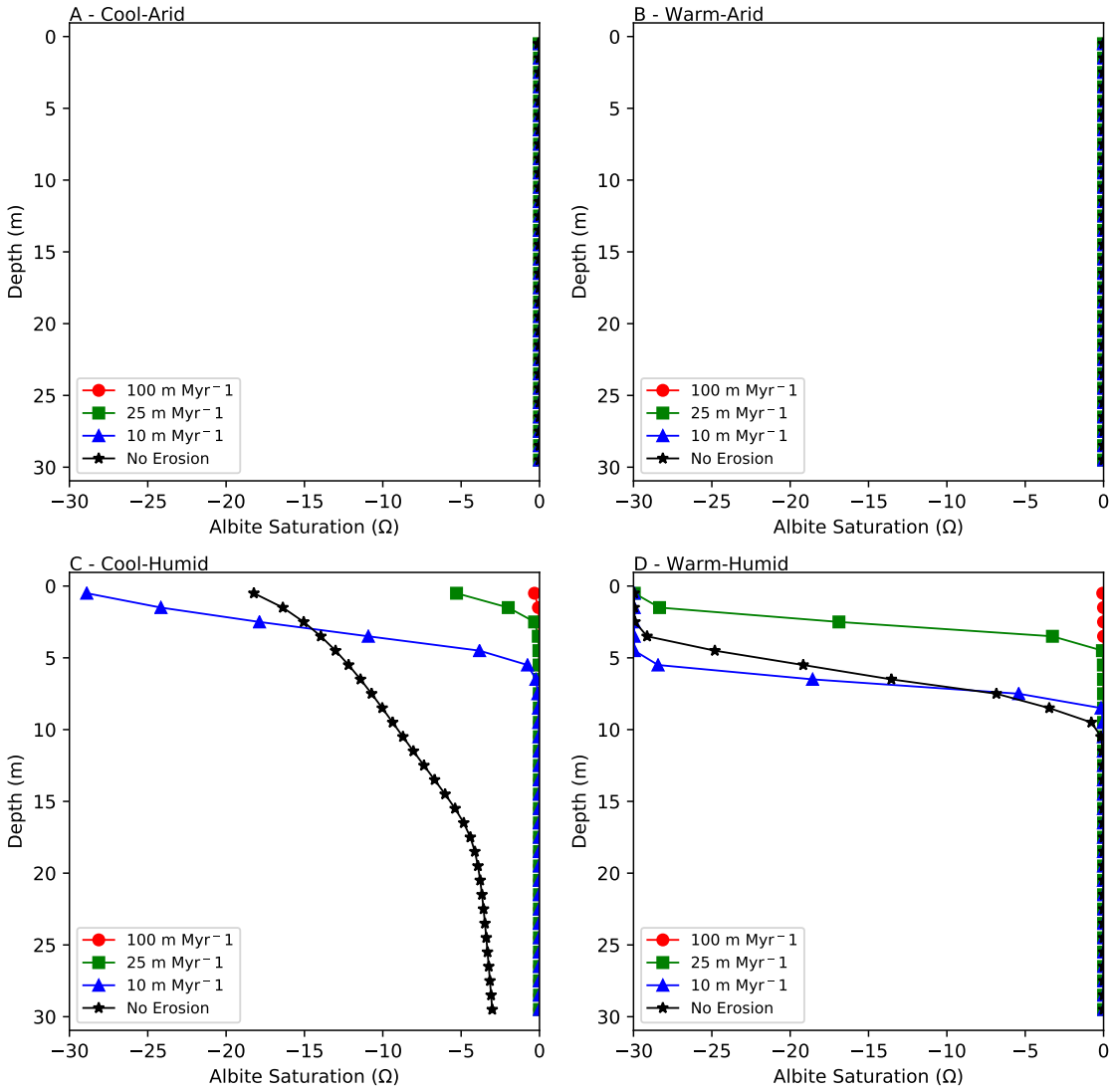

Figure 3.14: Modelled albite saturation states under three different erosion regimes in (A) cool-arid, (B) warm-arid, (C) cool-humid, and (D) warm-humid climates. Increasing erosion rates push all profiles closer towards saturation, although under humid conditions the low erosion profiles (10 m Myr^{-1}) show sharper transitions from undersaturated to saturated conditions. At erosion rates of 100 m Myr^{-1} (red circles), all profiles are saturated with respect to albite.

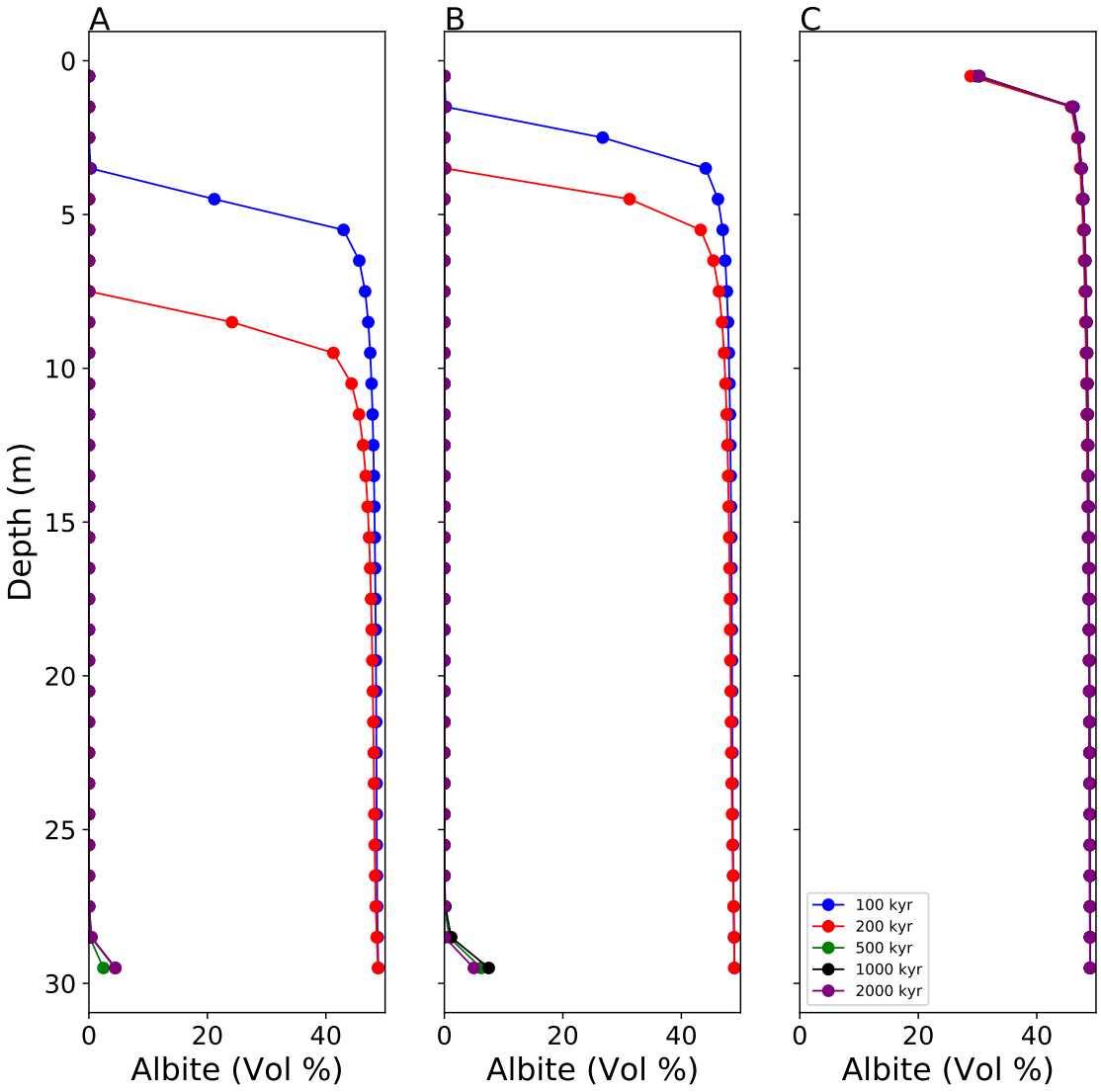

Figure 3.15: Modelled albite weathering profiles from 100 kyr - 2000 kyr in a warm-humid climate under three erosion rates, (A) 10 m Myr^{-1}, (B) 25 m Myr^{-1}, (C) 100 m Myr^{-1}. The modelled profiles reach steady state more rapidly under higher erosion rates. At rates of 10-25 m Myr^{-1} the profile reaches steady state between 500 kyr and 1000 kyr, while at a rate of 100 m Myr^{-1} the profile reaches steady state between 200 and 500 kyr.

3.5. Discussion

3.5.1. Comparison of Modelled Profiles with Field Data

The models produce similar weathering profiles to those seen in the field under similar climate regimes. Similar to the temperate Lysina and Davis run sites, the cool-humid models produce slight to moderate weathering extending 20-30 metres into the bedrock (Figure 3.2C-D; Figure 3.7 ; Figure 2.7 Chapter 2). Weathering intensity in the cool-humid model is somewhat higher than at Lysina or Davis Run, which may be due to the flow rate used (1 m yr^{-1}) (flow rate data are not available for Lysina and Davis Run). However, a simple runoff-infiltration balance for the Lysina profile based on hydrological data calculated in Buzek et al. (1995) suggests a flow rate in the range of 0.4 - 0.5 m yr^{-1}. As precipitation values for Davis Run are only slightly higher than Lysina (1040 mm yr^{-1} and 950 mm yr^{-1}, respectively) flow rates at Davis Run may be comparable to those at Lysina.

While there is no analogue for the cool-arid profile in our field data compilation, the warm-arid profile is quite similar to the Curacavi profile (Figure 3.2A; Figure 3.6), showing very limited weathering. The modelled warm-arid profile shows some weathering in the top 0.5 m which is not seen at Curacavi, however this may be explained by the lack of erosion in the modelled profile (discussed further in Section 3.4.3). Erosion rates are reasonably high at Curacavi (40.5 m Myr^{-1}) and given the much slower weathering rate (4.5 m Myr^{-1}) (Vázquez et al., 2016) of the profile, any weathered material near the surface would likely be quickly eroded away.

The warm-humid profile is similar to those of the warm-humid sites from our field data compilation (Cheras, Hakgala, Rawang, and Río Icacos) (Figure 3.2G-J; Figure 3.6; Figure 3.12), with all four sites showing sharp transitions from fresh bedrock to highly weathered material over 1-2 metres. The depth of the weathering boundary in the warm-humid model is approximately 8-10 m, similar to Cheras and Hakgala, but deeper than Río Icacos (˜7 m) and considerably shallower than Rawang (˜28 m). As with the warm-arid model and Curacavi, the lack of erosion in this version of the simplified model may explain some of these differences (discussed further in Section 3.4.3.), especially as erosion rates are quite high at Río Icacos (43 m Myr^{-1}). Local variability in subsurface architecture, such as permeability and porosity, may also be a factor. Although such data are unavailable for Cheras, Hakgala, and Rawang, the bedrock and regolith structure at Río Icacos have been well studied. Regolith depth varies in Río Icacos, which has been attributed to the variable fracturing of the local bedrock (Hynek et al., 2017; Orlando et al., 2016). The deepest profiles have approximately 30 m of regolith and occur where the bedrock is more fractured. Our simplified model assumes a uniform initial porosity and permeability, and thus does not capture the natural variability present in the Río Icacos bedrock. Additionally, fracture generation at Río Icacos is driven by oxidative expansion of Fe in biotite (Fletcher et al., 2006; Buss et al., 2008). Biotite is not included as a phase within the simplified model and Crunchflow is not currently capable

of modelling expansion fracturing (although it can simulate secondary porosity produced by the dissolution of minerals) . The simplified mineralogy of the model (e.g., no biotite) may affect the saturation state of the profile, which may in turn affect the depth of weathering, as the Río Icacos model produced weathering depths similar to field data (Figure 3.2J; Figure 3.4). Despite these differences, the warm-humid model successfully reproduces the dominant features of the warm-humid field profiles: sharp weathering gradients and high weathering intensity (Figures 3.2G-J, Figure 3.6).

The eroding simplified model produced effects similar to those indicated from field data and theoretical models (West, 2012, Chapter 2) where higher erosion rates result in shallower weathering profiles and regolith depth, but had no significant impact on the sharpness of the weathering front (Figures 3.11 and 3.12). One notable exception is the cool-humid profile in which the weathering front morphology dramatically sharpened when erosion was added (Figure 3.12C).

Both the cool-humid and warm-arid CIA profiles (Figures 3.12C and 3.12B, respectively) under high erosion (100 m Myr^{-1}) reflect the shape and depth of the Lysina and Curacavi weathering profiles (erosion rates of 63 m Myr^{-1} and 40.5 m Myr^{-1}, respectively) (Table 3.3; Figures 3.2A and C). The cool-humid profile has a sharp, but incomplete weathering front near the surface, suggesting a thin zone where weathering rates are higher than in the bedrock, much as at Lysina (regolith depth = 2-3 m). Similarly, when erosion rates are high in the warm-arid model (Figure 3.12B), the weathering intensity at the surface is significantly lower relative to the non-eroding model, making it more similar to the Curacavi profile (Figure 3.2A). The warm-humid profile (Figure 3.12D) remains similar to Río Icacos (Figure 3.2J) under erosion rates of 10 m Myr^{-1} and 25 m Myr^{-1}, but at 100 m Myr^{-1}, erosion is approximately double the rate of weathering (43 m Myr^{-1}) (Brown et al., 1995; Chabaux et al., 2013) resulting in an incomplete profile.

3.5.2. Impact of Climate Variables on Modelled Profiles

Both the field data (Chapter 2) and the modelled profiles (Figure 3.2; Figures 3.6-12) indicate that water flow rates have a significant impact on the resulting weathering profile. The modelled profiles under humid conditions both produced significantly deeper profiles than the arid models, indicating that higher water flow rates result in weathering penetrating deeper into the bedrock (Figure 3.6). Higher water flow rates appear to amplify the effects of temperature on chemical weathering. Under humid conditions, higher temperatures resulted in significantly increased weathering intensity, while under arid conditions, higher temperatures resulted in only modestly increased weathering intensity. Similarly, higher temperatures resulted in a much sharper weathering front in the warm humid model relative to the cool-humid, but the depth of the weathering front was considerably shallower in the warm-humid model (Figure 3.6).

It is likely that the shallower, and sharper, weathering front in the warm-humid model is linked to the faster weathering rates within that profile. The warm-humid model reaches near-saturation (Ω=

-10^{-2} - -10^{-3}) with respect to albite just below the weathering front (Figure 3.8). The most rapid albite weathering rates occur at the bottom of the weathering front (Figure 3.7), where permeability changes, allowing the abundant bedrock albite to be exposed to the undersaturated, high-flow, infiltrating water. In contrast, the cool-humid model remains undersaturated with respect to albite throughout the profile, but the maximum albite weathering rate is slower than in the warm-humid model. The higher temperatures in the warm-humid model result in a faster maximum weathering rate, but such rapid weathering saturates the pore water with respect to albite, resulting in negligible weathering just below this maximum weathering zone (Figures 3.7 and 3.8). In contrast, the slower weathering rates of the cool-humid model produce more gradual weathering which does not result in the profile approaching saturation, allowing weathering to penetrate deeper into the bedrock but at a lower intensity relative to the shallower, but higher intensity weathering in the warm-humid profile. However, at depth ($>$ 12m), weathering is more intense in the cool-humid profile relative to the warm-humid profile.

The effects of the geochemical saturation state of the profile with respect to weatherable minerals can also be seen in the arid models. Both arid models remain near- saturation with respect to albite throughout their profiles regardless of temperature, indicating that water flow rates are a strong control on the geochemical saturation state of the profile (Figure 3.8). Both arid models also only produced shallow weathering (˜0.5 m), because the low water flow is insufficient to flush out weathering products fast enough to maintain undersaturation with respect to albite, thus preventing weathering from penetrating deeper into the profile (Figure 3.8). These models indicate that water fluxes and their subsequent impacts on geochemical saturation states are a strong control on both weathering profile morphology and weathering intensity. Higher MAT (expressed in the models as higher temperature) results in increased weathering intensity, but the impacts of MAT are supressed under low water flow rates (Figure 3.6).

If saturation state is strongly controlled by water flow rates in the subsurface, then the structure of the subsurface, or the subsurface architecture (e.g., permeability and connected porosity, depth and morphology of the bedrock-regolith interface), must also be considered. Subsurface architectures that favour greater water flow rates through a profile reduce water residence times and thus lower the saturation states (Maher and Druhan, 2014). The modelled profiles with higher permeabilities allow water to move more freely through the weathering profile (Figure 3.9; Figure 3.10). Lower permeabilities result in a non-linear increase in water flow rates through the profile, with flow rates that increase exponentially as permeability increases. Although the simplified models use a simple representation of subsurface architecture by varying initial permeability, such a result suggests that even relatively small changes ($<$1 order of magnitude) in permeability will result in large changes in water flow rates within the profile. Increases in water flow rates will also reduce the geochemical saturation state of the profile, promoting more rapid weathering.

3.5.3. Impact of Varying Erosion Rates on Profiles

Theoretically, a profile should become more undersaturated with respect to weatherable minerals in response to higher erosion rates, as erosion will remove material from the surface increasing the accessibility of fresh minerals to reactive fluids (e.g., Viers et al., 2014). Reactive fluids will have less contact time with weathering products in a shallower profile and thus have a lower saturation state, promoting higher weathering rates.

While our modelled profiles have thinner regolith under high erosion (Figure 3.12), they are also closer to saturation with respect to albite under higher erosion rates (Figure 3.14) and have supressed weathering rates (Figure 3.13). Such a result is contrary to both theoretical predictions and field studies, which typically indicate that erosion should increase chemical weathering rates by exposing a greater area of fresh minerals to weathering (White, 2002; Riebe et al., 2004). The counterintuitive result stems from the decrease in water flow rates with increasing erosion rates in the modelled profiles (Figure 3.16). This relationship is caused by erosion removing higher permeability weathered material (regolith) from the surface, thus increasing the proportion of lower permeability, less-weathered and un-weathered material (e.g., bedrock) within the modelled profiles. The lower permeability hinders water flow through the profile, leading to more geochemically saturated conditions and lower weathering rates. When the water flow rate of the model was directed to remain at a constant value (i.e., no change in velocity due to the development of secondary porosity) the difference in weathering rates under different erosion regimes was significantly less (Figure 3.17) and all profiles were further from equilibrium with respect to albite (Figure 3.18). As a result, under the constant flow configuration, significantly deeper profiles were produced under all erosion regimes (Figure 3.19).

Regardless of the unexpected relationship between erosion and weathering rates, the resulting profiles from both the non-eroding and the eroding simplified models agree well with the field data in that higher erosion rates reduce regolith thickness (Table 3.3; Figure 3.2), and highlights the role of water flow rates in controlling weathering rates and shaping profile morphology. Our model data also suggests there may be a "tipping point" in the balance between weathering fluxes and erosion, where erosion rates are sufficiently high to overwhelm weathering rates resulting in incomplete weathering profiles (Figure 3.12). Such a tipping point can be linked to different "limiting regimes" for weathering within a profile (West et al., 2005; Lebedeva et al., 2010), suggesting that the balance between weathering rates and erosion rates will determine if weathering fluxes are limited by erosion (i.e., supply limited) or the chemical reaction rates of mineral dissolution (i.e., kinetically limited).

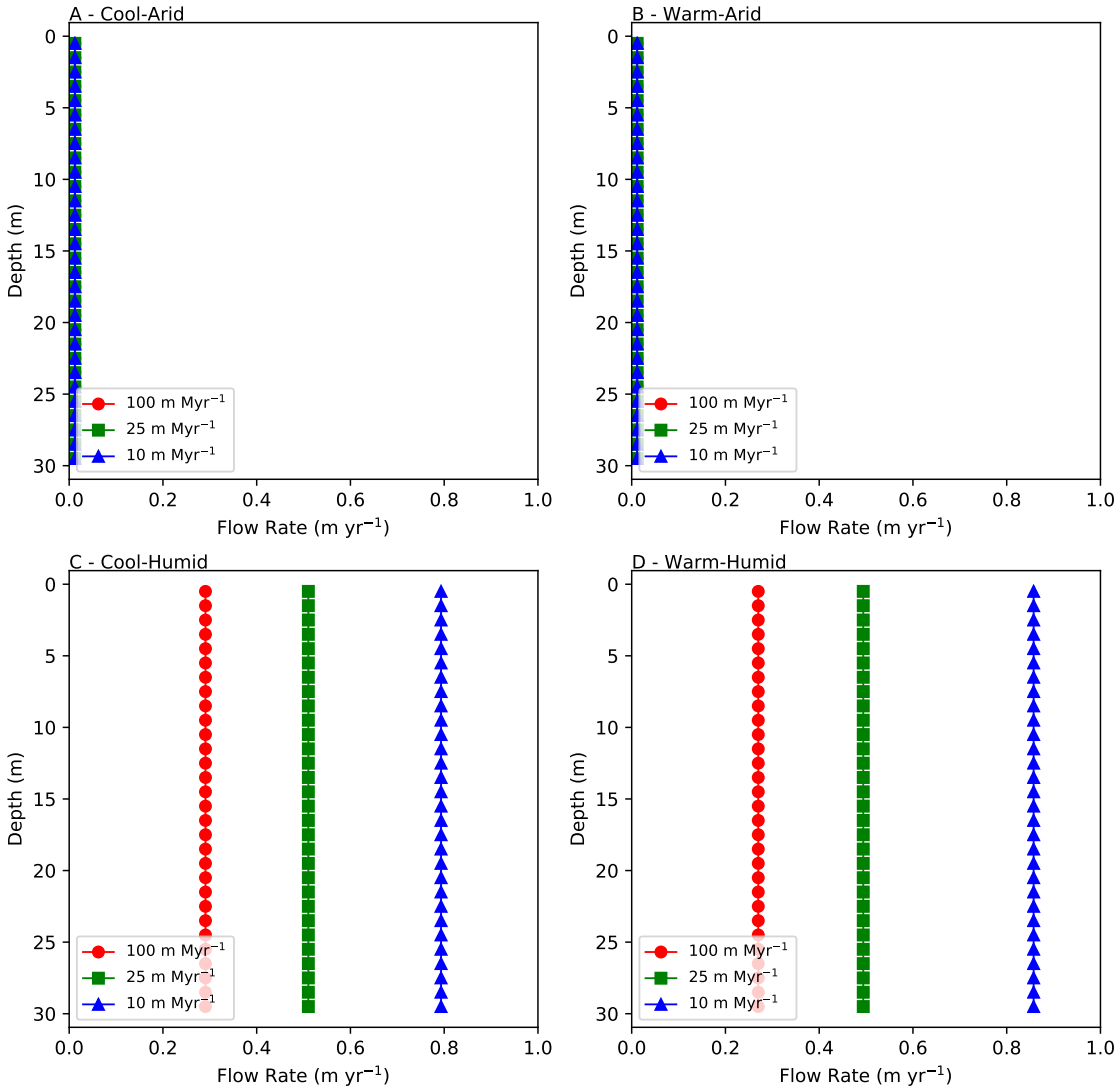

Figure 3.16: Modelled flow rates under three erosion rates in (A) cool-arid, (B) warm-arid, (C) cool-humid, and (D) warm-humid climates. Erosion results in lower average flow rates in all profiles, although these effects are most pronounced in the humid climates. Under arid conditions, variation in average flow rates under all erosion rates is minimal. The reduction in average flow rate is likely due to erosion removing more permeable material from the profile, causing the model to lower flow rates in response.

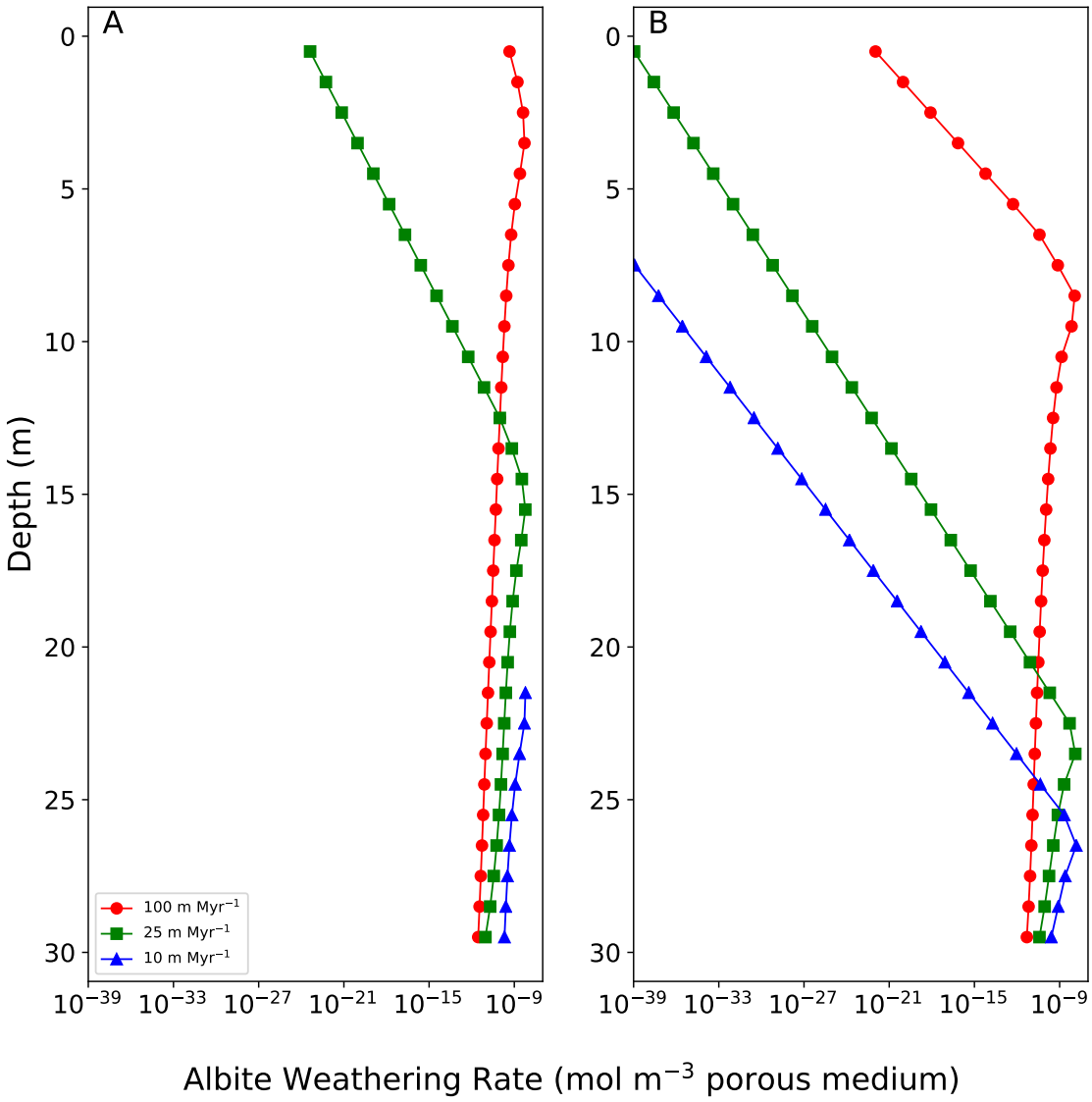

Figure 3.17: Albite weathering rates at a constant flow rate of 1 m yr^{-1} under three different erosion rates at (A) 5°C and (B) 25°C. Under constant flow conditions, increasing erosion results in only slight reductions of weathering rates. Thus, it is likely that the reduction in weathering rates seen in the variable flow model are the result of changing flow rates under different erosion rates. The low erosion rate simulation in Panel A (10 m Myr^{-1}) produces albite weathering rates of zero above ~22 m, and thus cannot be plotted on the logarithmic scale used here.

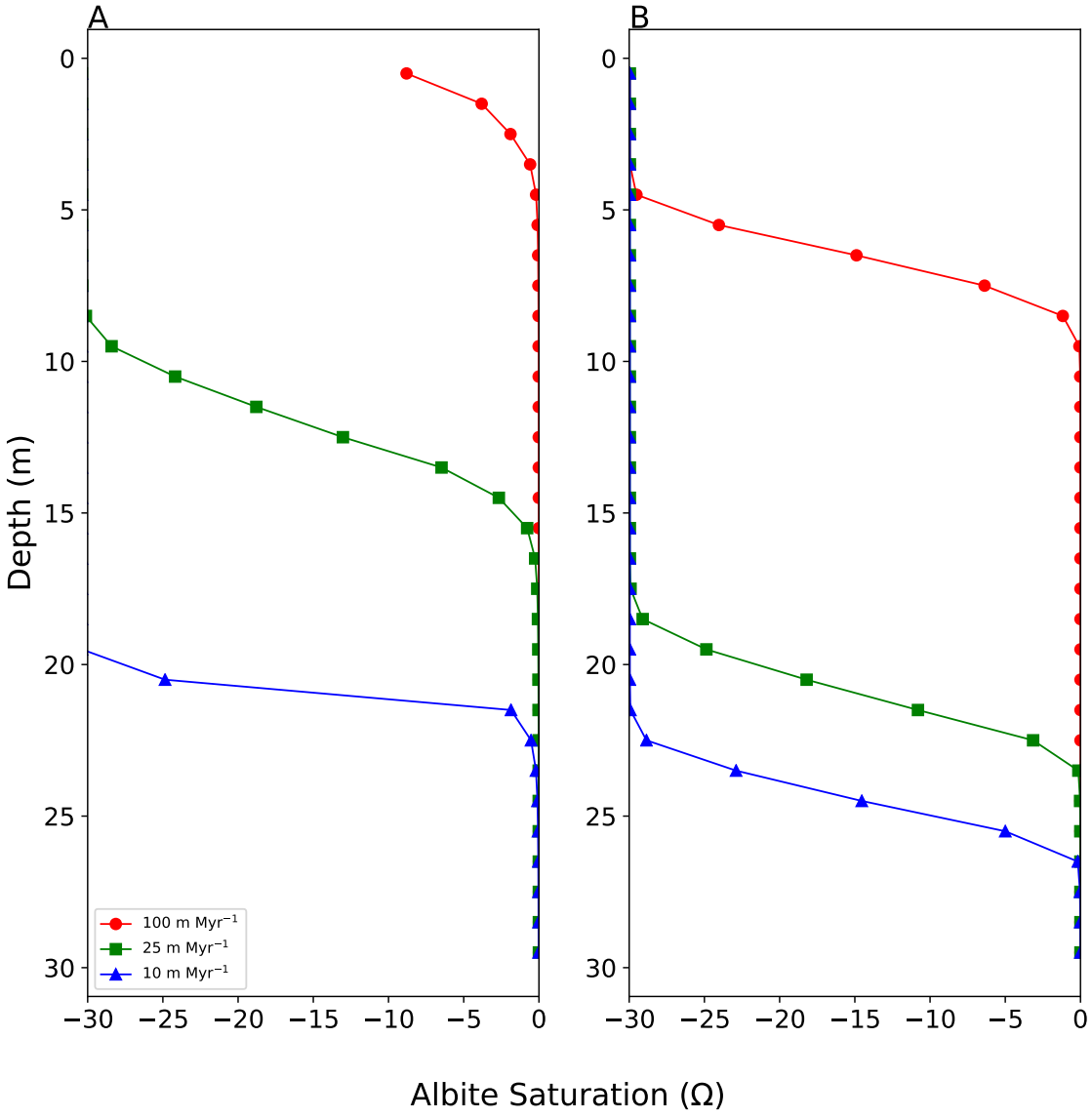

Figure 3.18: Modelled albite saturation states using a constant flow of 1 m yr^{-1} under three erosion regimes at (A) 5°C and (B) 25°C. Compared to the variable flow model, albite saturation states do not show any significant difference, although the depth of the weathering boundary reduces as erosion rates increase.

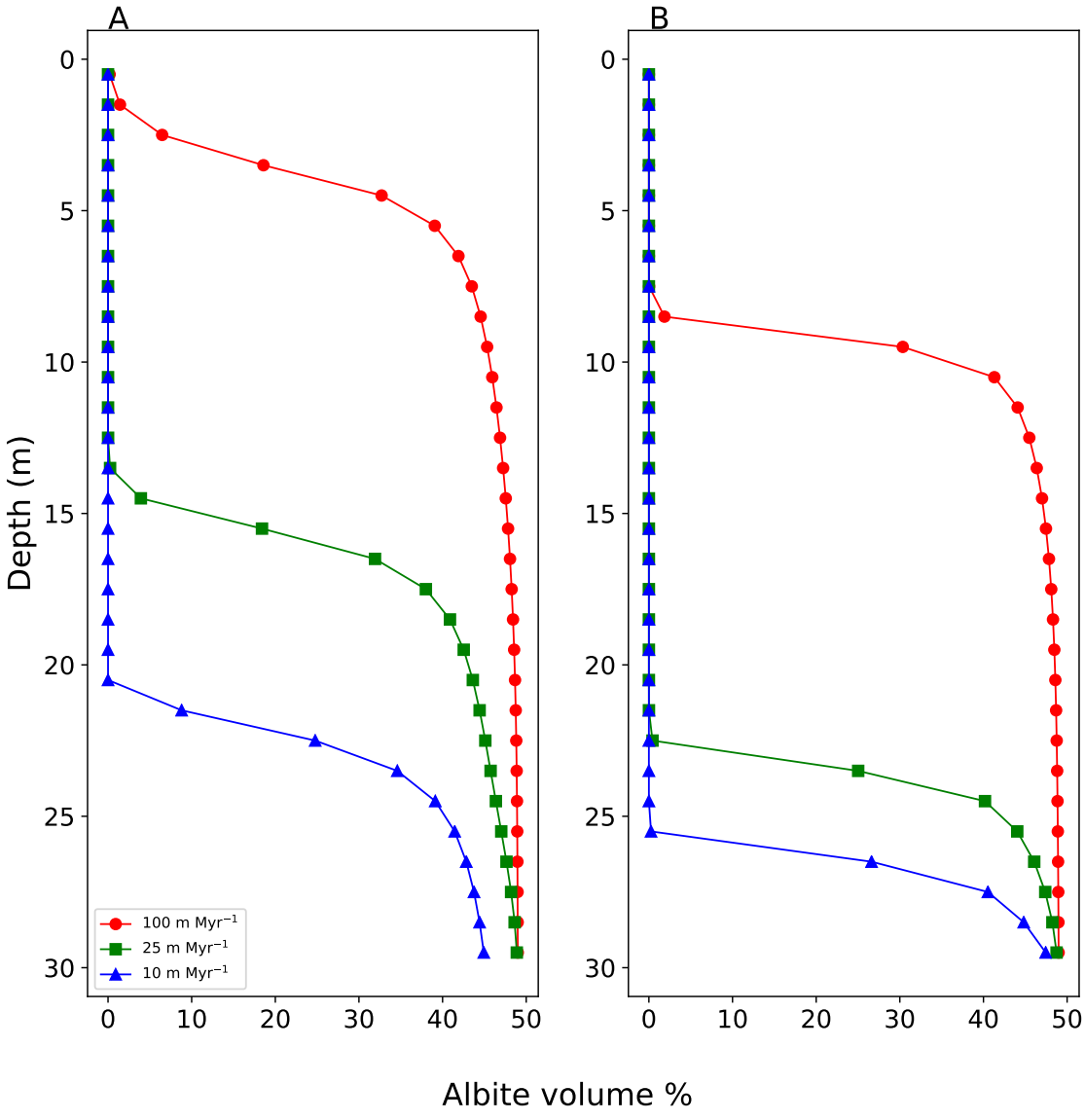

Figure 3.19: Modelled albite volumes at a constant flow rate of 1 m yr^{-1} under three erosion regimes at (A) 5°C and (B) 25°C. As with the variable flow model, increasing erosion results in a shallower weathering front and reduced regolith depth, however weathering penetrates deeper into the bedrock as albite weathering rates are not supressed as a result of the reduced flow rate in the variable model.

3.5.4. Implications for Wider-Scale Weathering-Climate Interactions

Although relatively simple, the models used in this study largely agree with field observations (Figures 3.2, 3.6, and 3.12). As such, it is likely that our models represent large-scale processes that affect weathering rates and morphology (e.g., climate) reasonably well and suggests that small-scale (watershed-profile scale) parameters (e.g., minor mineral components, mechanisms of secondary porosity development) are less important in determining weathering profile morphology at the global scale.

Much of the variations within the modelled profiles are the result of climate parameters, especially water flow rates (governed primarily by precipitation and runoff). Mechanistically, water flow rates control weathering rates by determining the geochemical saturation state of the subsurface, with greater water fluxes lowering the saturation state of a profile with respect to weatherable minerals. The geochemical saturation state of a profile is lowered under high water flow rates due to the efficient removal of weathering products. Our results are consistent with earlier modelling studies that demonstrated that weathering rates are strongly controlled by the geochemical saturation state of the profile and groundwater with respect to weatherable minerals (Maher, 2010; Maher and Druhan, 2014).

If water flow rates are the primary control on weathering rates and weathering front morphology (i.e., sharpness), then the implications for weathering processes are twofold. Firstly, water flow rates are primarily determined by precipitation rates at a given site, as precipitation is the primary source of water for most weathering profiles (e.g., Giardino and Houser, 2015). As such, it is likely that there is a very strong climate control on weathering rates and front morphology, but that the climate control is largely determined by the humidity regime of any given site rather than the temperature regime. While early modelling studies of global weathering rates through geological time (e.g., Berner et al., 1983; Berner and Kothavala, 2001) suggested that weathering rates were determined by the Arrhenius relationship, more recent studies have struggled to link the weathering patterns of individual profiles to the Arrhenius relationship (Maher, 2011). Additionally, further studies now indicate other factors such as precipitation/runoff (e.g., Oliva et al., 2003; Goddéris et al., 2017) or erosion (e.g., Riebe et al., 2004; West et al., 2005) have a stronger control on global weathering rates than temperature.

Although temperature may not be the primary control on weathering rates, data from this study strongly suggest that the impact of temperature is amplified when weathering is not limited by low water flow rates. In the non-eroding model, the warm-humid profile has a considerably sharper and shallower weathering front, and considerably faster weathering rates, than the cool-humid profile. In contrast, the warm-arid and cool-arid profiles are almost identical, despite a 20°C temperature difference (Figure 3.6). As such, the results of this study indicate that water flow rates, strongly influenced by precipitation rates, are likely the primary control on weathering front morphology

and the primary limiting factor on weathering rates within a profile.

The second implication of water flow rates being the primary control on weathering rates and weathering front morphology is that the subsurface architecture is a significant contributing factor. The results of this study show that water flow rates are strongly influenced by permeability, and increase non-linearly as permeability increases (Figures 3.9 and 3.10). It is therefore likely that even relatively small changes in rock structure, such as the development of secondary porosity (either through chemical weathering or physical processes) can result in significant differences in weathering rates as flow rates evolve over time.

Although our models only represent subsurface architecture in the simplest way (i.e., a homogenous bedrock structure, constant initial permeability and porosity through the entire profile, and a simplified lithology), they still capture the dominant features of the weathering profiles seen in the field. This result indicates that despite its potential to affect flow rates, subsurface architecture is actually a relatively minor component in determining weathering gradients and weathering intensity. There is some evidence from the field to support subsurface architecture being less significant than climate in terms of weathering profile morphology. Weathering studies (e.g., Strakhov, 1967) have noted broad latitudinal trends in weathering profile morphology. Were subsurface architecture a stronger control than climate in determining profile morphology, it seems unlikely that a clear latitudinal trend would be observed.

While the models in this study replicate existing weathering gradients and intensities reasonably well, significant variations in the depth of weathering fronts and profiles are observed in the field even under similar climates (Braun et al., 2012; Bazilevskaya et al., 2013; Hewawasam et al., 2013; Yusoff et al., 2013; Orlando et al., 2016) and such variations are not clearly observed in our model results. Some of the variation can be explained by differing erosion rates between sites, such as the deeper profiles at the slowly eroding Nsimi and Hakgala catchments compared to the shallower profile at the more rapidly eroding Río Icacos catchment (Table 3.3; Braun et al., 2012).Under different erosion regimes the eroding model shows considerable variation in weathering profile depth (Figures 3.11, 3.12, and 3.15).

If factors such as climate and erosion rates remain relatively constant within a catchment, it is difficult to explain variations in weathering profile depth between profiles. It is likely that local variations in weathering depth may stem partly from variations in bedrock structure (porosity, fracturing). In the Río Icacos catchment, profile depths range from 5 to 30 m and this wide range has been attributed to variable degrees of fracturing present within the local bedrock, with the deeper profiles occurring over more highly fractured bedrock (Hynek et al., 2017). The more highly fractured bedrock allows reactive fluids to penetrate further into the bedrock and provides a more efficient pathway for the removal of weathering products (Orlando et al., 2016). However, as previously noted, it is unlikely that such variations in local bedrock structure will have a significant impact on weathering rates at the global scale, which are much more likely to be determined

by broad scale parameters such as climate factors. Understanding small-scale processes, such as secondary porosity development, will however be significant for understanding variability in weathering within individual catchments.

3.5.5. Future Research

This study demonstrates that much of the variability in weathering front morphology and weathering rates can be explained by variations in climate, with erosion playing a lesser but still significant role. There remain a number of future avenues to explore in further studies. Model limitations prevented exploration of some of these avenues within this study. When erosion was added to the simplified model, the modelled flow regime unexpectedly lowered weathering rates under higher erosion rates, as the model interpreted the removal of material as decreasing the average permeability throughout the profile, thus reducing flow rates. In reality, flow rates would be highly variable through the profile depending on heterogeneities in permeability and porosity (e.g., fractures and other preferential flow paths), which were not captured by the simple models presented here. The models also assumed saturated conditions and a constant water supply and recalculated the flow rate as weathering occurred, whereas in nature, water supply would vary through time, and saturation would decrease as secondary porosity develops. Due to model limitations, infiltration was modelled as a pressure gradient between the surface and the bedrock. Ideally, infiltration would be modelled as a constant water flux at the model boundary, with flow rates through the profile updated as porosity and permeability evolve, which would likely provide a more accurate representation of water flow rates from precipitation.

Currently, it is difficult to model the effects of seasonally variable precipitation on weathering over long timescales (>1000 years). The model assumes that infiltration remains constant throughout the model run, while in some environments, such as monsoon climates, precipitation is highly seasonal in nature. Highly seasonal precipitation may have significant impacts on factors such as water flow rates and the hydrological saturation state within the regolith. Currently, the temporal resolution of most reactive transport models is too coarse to resolve seasonal variation when modelling long-term weathering. Additionally, many reactive transport models do not have the ability to alter boundary conditions during the course of individual simulations, which would prohibit a seasonal precipitation configuration in a model. Nevertheless, given the importance of water flow rates in affecting weathering, modelling the impact of seasonality on weathering processes should be further investigated.

3.6. Conclusions

Using Reactive Transport Model simulations of a simplified granitic profile, a range of weathering profiles observed in the field under diverse climate conditions were successfully recreated. These simulations demonstrated that water flow rates (primarily controlled by precipitation) have a

dominant impact on both chemical weathering rates and weathering profile morphology. Water flow rates determine chemical weathering rates by controlling the geochemical saturation state of the profile with respect to weatherable minerals by removing weathering products from the profile, thus keeping the profile further from equilibrium. The geochemical saturation state of the profile also influences profile morphology. Profiles generated under arid conditions are typically near saturation due to low water flow rates, and as a result produce only limited and shallow weathering ($<$1 m). In contrast, profiles generated under humid conditions result in much deeper and more intensely weathered profiles ($>$10 m). Interestingly, the deepest profile was produced under cool-humid conditions, where moderate weathering was present to at least 20 m depth with a gradual transition between fresh and more heavily weathered material over that distance. In contrast, the warm-humid profile produced a shallower (˜10 m), but much more intensely weathered, profile with a sharp transition between fresh bedrock and totally depleted material. Model results indicate that there is a thin band (0.5 m) of extremely high albite weathering rates within the warm-humid profile, below which the profile becomes geochemically saturated with respect to albite. Extremely rapid weathering within the warm-humid profile results in the weathering boundary becoming geochemically saturated with respect to weatherable minerals, preventing weathering from penetrating deeper into the bedrock. In contrast, the cool-humid profile maintains slower weathering rates, but the profile remains geochemically undersaturated, allowing weathering to penetrate deeper into the bedrock. These profiles are in good agreement with those observed in the field under similar climate conditions.

Model outputs show that temperature has a much weaker impact on weathering rates and profile morphology relative to water flow rates, however the impact of temperature is amplified under humid conditions. The modelled cool-arid and warm-arid profiles are nearly identical in terms of profile morphology and weathering rates, despite a temperature difference of 20°C. In contrast, the humid profiles show highly diverse morphologies and weathering rates. Under humid conditions, higher temperatures allow for considerably faster weathering.

As water flow rates were shown to have a significant impact on weathering profiles, the impact of subsurface architecture was also investigated, which would also influence water flow rates through a profile. Lower permeabilities resulted in lower flow rates and weathering rates. However, it was found that as permeabilities increased, water flow rates increased exponentially, suggesting that even relatively small changes in secondary porosity may have large impacts on water flow rates. Localised variations in porosity and permeability may explain the variability seen between different profiles in the same watershed, but such variations appear to be insignificant at the global scale, where climate factors appear to be dominant in determining profile morphology.

The impact of erosion rates on weathering profiles was also investigated. Model data suggested that higher erosion rates result in shallower profiles due to the increased removal of weathered material, which agrees with field observations. Model data also indicated that higher erosion rates

also resulted in lower weathering rates, likely due to an unanticipated interaction between erosion and the water flow regime in the model, where greater erosion decreased the average permeability of the profile resulting in lower water flow and weathering rates. Indeed, under an alternative flow regime where flow rates were held constant, weathering rates showed less variability with erosion rates.

A number of avenues for future research have also been highlighted. Further investigation is needed into the interaction between erosion rates and water fluxes to determine if the effects seen in this study are an artifact of the model configuration or an accurate representation of natural processes. Additional alternatives to the water flow configuration could also be explored, especially alternatives that include variable hydrological saturation states within the model, as the model in this study assumes saturation, and struggles to function under lower saturation conditions. Additional modelling using more complex subsurface architecture configurations would also further constrain the impact of subsurface architecture on weathering rates and its potential interaction with climate factors.

Chapter 4

Modelling the Impact of Palaeogeographical Changes on Potential Weathering During the Cretaceous-Eocene Period

Author contributions and declaration: The GEOCLIM simulations presented in this chapter were performed by Nicholas Hayes with instruction and assistance from Yves Goddéris and Dan Lunt. Input data for these simulations were provided by Yves Goddéris (FOAM) and Dan Lunt (HadCM3L), with additional input data produced from these datasets by Nicholas Hayes.

Summary

The previous two chapters of this thesis have focused on mm scale and weathering profile-scale investigations of controls on silicate weathering rates. Both chapters demonstrated that water flow rates through the subsurface (primarily determined by precipitation and runoff rates) are the primary control on weathering rates within granitic profiles, thus suggesting that the hydrological cycle may be a powerful control on long-term atmospheric CO_2 concentrations. However, it is unknown to what extent mm and profile-scale controls on weathering may apply at the global scale. This chapter will investigate the control the hydrological cycle exerts on weathering rates at the global scale, and whether such a control remains consistent through geological time.

In this chapter, the role of changing climate (associated with changing palaeogeography) on global chemical weathering fluxes, and thus long-term atmospheric CO_2 changes, will be investigated using a global geochemical model (GEOCLIM) and climate input data from the HadCM3L GCM. The "weatherability" (i.e., potential weathering fluxes) of the Earth's surface will vary over geological time in response to changing continental land area, climate variables (specifically precipitation/runoff and temperature) and changing lithology. Global climates are primarily determined by the position of continental landmasses, topographic and bathymetric features and ocean gateways (all of which affect ocean/atmospheric circulation patterns), and atmospheric CO_2 concentrations. GEOCLIM has previously been used to test the impact of continental configurations on long-term CO_2 concentrations, but using relatively low spatial resolution climate data (7.5° x 4.5°) and temporal (˜1 simulation per 25 Myr) resolution.

Outputs (climate data and palaeogeography) from 19 HadCM3L climate model simulations of the Cretaceous-Eocene period will be used to evaluate the impact of changing weatherability on long-term CO_2 concentrations under constant degassing rates. These simulations are considerably higher spatial resolution (3.65x) and provide a higher temporal resolution (˜ 1 simulation per 6 Myr) than previous GEOCLIM studies. These higher resolution simulations will allow for more robust modelling of regional changes in weathering fluxes (which are highly variable from site to site), identification of key factors affecting global weathering rates, and the impact of relatively gradual palaeogeographical changes on long-term CO_2 concentrations. The resulting steady-state CO_2 concentrations will then be compared with CO_2 curves from proxy data to examine to what extent changes in weatherability under constant degassing rates can explain the observed past evolution of atmospheric CO_2, and whether the CO_2 changes are suitably large on geologically short timescales ($<$ 10 Myr) to have significant climate impacts.

As GEOCLIM studies have not previously used HadCM3L climate inputs, this chapter also examines the impact of using climate inputs from different models, in particular providing an evaluation of some key assumptions that are made in the methodology .

4.1. Introduction

Chemical weathering rates of silicate minerals are known to be sensitive to climate variables such as temperature and precipitation in addition to intrinsic factors such as lithology (Strakhov, 1967; Walker et al., 1981; Berner et al., 1983; White and Blum, 1995; Oliva et al., 2003; West et al., 2005; Ibarra et al., 2016). While there is evidence from individual sites that weathering is accelerated under warm, humid conditions (e.g., White and Blum, 1995), and this thesis has shown in Chapters 2 and 3 that the hydrological cycle plays a key role at a local scale, it is unclear whether these trends can be applied at the global scale. Evidence from field and modelling studies of weathering profiles suggests a stronger precipitation or runoff-based control on weathering rates than temperature (Oliva et al., 2003; Maher, 2010; Ibarra et al., 2016), while global models (e.g., GEOCARB and derivates) have often invoked temperature as a stronger control (Berner et al., 1983; Berner and Kothavala, 2001). Other global models, including GEOCLIM, have suggested that runoff may be a more significant control on weathering rates and thus long-term climate (Goddéris et al., 2014). General Circulation Models (GCMs) have been used extensively over the past few decades to model climates in geological time (e.g., Tobis, 1997; Jost et al., 2005; Huber, 2008; Haywood et al., 2010; Lunt et al., 2012, 2017). These models have been evaluated using records from proxies such as stable isotope ratios (e.g., Lunt et al., 2012). Although GCM simulations do not always produce results that agree with proxy data (e.g., Huber and Caballero, 2011; Keating-Bitonti et al., 2011; Lunt et al., 2012; Jagniecki et al., 2015), they have greatly expanded the spatial availability of climate data, whereas proxy data have been gathered from a comparatively limited number of sites (e.g., Huber and Caballero, 2011). Furthermore, proxy data often produce conflicting reconstructions, such as differing atmospheric CO_2 levels (e.g., Jagniecki et al., 2015) or significantly different temperature and precipitation reconstructions (e.g., Keating-Bitonti et al., 2011). GCMs can be used to reconstruct global climates based on different proxy records and compare the results with other proxy data (Huber and Caballero, 2011; Lunt et al., 2012, 2016). Thus, GCMs have become a powerful tool in reconstructing palaeoclimates.

The large quantities of climate outputs created by GCMs have been incorporated into global geochemical models over the last 10-15 years (e.g., Berner and Kothavala, 2001; Donnadieu et al., 2004), enabling these models to provide estimates of global weathering rates under different climate and palaeogeographic configurations. However, as noted above, these datasets can vary significantly in their climate reconstructions, depending on the model configuration and the boundary conditions used.

4.1.1. Late Mesozoic-Early Cenozoic Climate

The late Mesozoic to early Cenozoic period (145-34 Ma) was a period of warm climate conditions (e.g., Huber and Sloan, 2001; Huber and Caballero, 2011; Littler et al., 2011; Inglis et al., 2017), associated with atmospheric CO_2 concentrations considerably higher than today (e.g., Hay and

Floegel, 2012). This period also saw the continued breakup of Pangaea, resulting in the opening of the Atlantic Ocean and a transition towards the modern continental configuration by the end of the Eocene (Donnadieu et al., 2006; Lunt et al., 2016). The Earth's climate state shifted during the Eocene-Oligocene boundary in response to declining CO_2 concentrations towards icehouse conditions (DeConto and Pollard, 2003; Pagani et al., 2005; Lear et al., 2008), initiating the glaciation of Antarctica and ending the long-term greenhouse climate that had been prevalent during the Mesozoic (Zachos, 2001).

"Greenhouse" conditions (i.e., globally widespread warm temperatures) were present during the early Cretaceous, with CO_2 proxy data indicating high atmospheric CO_2 levels ($>$1000 ppm) (Foster et al., 2017). At the start of the Cretaceous (145 Ma) the continents were still in a broadly supercontinental configuration (Scotese, 2004), although the breakup of the southern landmass of Gondwana had begun by this time. The converged continental configuration resulted in large areas of arid environments, especially in the northern hemisphere (Hay and Floegel, 2012). In addition, the gradual warming of the sun (Gough, 1981) also represents a forcing factor on global climate during this period. In contrast, CO_2 levels decreased from the early Cretaceous into the mid-late Cretaceous. Towards the end of the Cretaceous, CO_2 and global temperatures continued to decrease (Foster et al., 2017).

The early Cenozoic saw a temporary halt to the long-term global cooling that began during the Cretaceous. Several geologically brief "hyperthermals" occurred during the late Palaeocene and the Eocene, resulting in rapid warming where global temperatures increased by 4-8°C over 50-200 kyr (Thomas and Zachos, 2000; Galeotti et al., 2010), identifiable in ocean sediment records as an abrupt carbon isotope excursion (Thomas and Zachos, 2000; Lourens et al., 2005). During the Palaeocene-Eocene Thermal Maximum (PETM; ˜56 Ma), the most extreme of these hyperthermals, conditions were sufficiently warm to support a subtropical-like climate at the poles with warm temperatures (Sluijs et al., 2006), plentiful precipitation, and tropical flora and fauna such as palm trees and alligators (Eberle and Greenwood, 2011). Less extreme hyperthermals occurred into the Eocene, such as ETM-2 (Eocene Thermal Maximum 2)(Lourens et al., 2005). A curious facet of the Palaeocene-Eocene climate suggested by proxy data was a reduced temperature gradient between the poles and the equator that GCMs have struggled to recreate (Huber and Sloan, 2001; Sluijs et al., 2006; Greenwood et al., 2010; Sagoo et al., 2013; West et al., 2015). The climate of the early Eocene was the warmest period in the Cenozoic, known as the Early Eocene Climatic Optimum (EECO; 56-48 Ma) (Zachos, 2001; Huber and Caballero, 2011). Global cooling resumed during the mid-Eocene but was temporarily halted by the Middle Eocene Climatic Optimum (MECO ; 41-40 Ma), another period of prolonged warmth (e.g., Edgar et al., 2010). CO_2 concentrations and global temperatures continued to decline towards the Eocene-Oligocene boundary (34 Ma) (Pagani et al., 2005), eventually dropping sufficiently to allow a permanent ice cap to form in Antarctica (Zachos, 2001; Zachos and Kump, 2005).

4.1.2. Controls on Mesozoic-Cenozoic Climate

In the longest-term, climates during the Mesozoic and Cenozoic were affected by a gradual increase in solar forcing and by a gradual decrease in CO_2 forcing (Foster et al., 2017). A number of theories have been advanced to explain changes in atmospheric CO_2, and thus climate, over 1-10 Myr timescales. The gradual breakup of Pangaea and associated rifting likely resulted in increased volcanic degassing fluxes (Tajika, 1998). Additionally, at least two large igneous provinces were formed during the late Mesozoic-early Cenozoic period. The Deccan traps in India were active in the late Cretaceous (Jaeger et al., 1989), while the North Atlantic Igneous Province (NAIP) formed during the opening of the Atlantic in the early Cenozoic (Meyer et al., 2007). The late Cretaceous and the Cenozoic saw a period of mountain building associated with the latter stages of the break-up of Pangaea. The Laramide orogeny began approximately 70 Ma (Humphreys et al., 2003) and the development of the Northern Andes and Himalaya occurred during the early Cenozoic (Schellart, 2008). The development of new mountain ranges, particularly Himalaya, has been implicated in the reduction of CO_2 concentrations during the Cenozoic by increasing silicate weathering rates and thus increasing CO_2 drawdown (Raymo and Ruddiman, 1992). Changes in weathering rates have been linked to a number of climate shifts in the Earth's past, including the Hirnantian glaciation and global cooling during the Carboniferous (e.g., Lenton et al., 2012; Goddéris et al., 2014, 2017).

Significant ice sheets were not believed to be present during this period, so it is unlikely that albedo changes represent a major climate forcing in the late Mesozoic-early Cenozoic (e.g., Lefebvre et al., 2013), although recent studies have challenged this assumption (Ladant and Donnadieu, 2016). Another direct forcing is that of palaeogeography, and although it has been shown that this can have substantial local effects (Lunt et al., 2016), on a global scale these changes are relatively small. As such, the potential silicate weathering flux, or 'weatherability' of the continents is likely to represent a key climate forcing during the late Mesozoic-early Cenozoic and forms the focus of this chapter.

At steady-state, silicate weathering fluxes are equal to emissions from volcanic degassing (e.g., Walker et al., 1981; Berner et al., 1983; Goddéris et al., 2014). However, a distinction should be drawn between weathering and "weatherability". In the long-term, weathering will balance volcanic degassing, however weatherability is decoupled from volcanic degassing. Thus, although weathering may moderate atmospheric CO_2, the steady-state concentration of CO_2 will vary through time due to changes in global weatherability, i.e., the amount of weathering for a fixed CO_2 concentration (ppm) (Goddéris et al., 2014).

Key controls on weatherability are temperature, water fluxes (precipitation and infiltration) , erosion rates (as a function of uplift and slope), and lithology (Dessert et al., 2003; Oliva et al., 2003; West et al., 2005; Maher, 2010; West, 2012; Bazilevskaya et al., 2013; Ibarra et al., 2016),

although work in this thesis indicates higher temperatures do not always result in higher weathering rates (Chapters 2 and 3). Global palaeolithologies are poorly constrained and become less well constrained further back into the geological record. Similarly, factors such as topography and uplift rates, which affect erosion rates (e.g., Riebe et al., 2004; West et al., 2005; Gabet and Mudd, 2009, Chapter 3), are also poorly constrained into geological time. In contrast, broad scale climate parameters like temperature and precipitation patterns are comparatively well constrained through proxy data and GCM studies. Climate states are in turn strongly controlled by the positioning of the continents, which can affect oceanic and atmospheric circulation patterns (e.g., Gyllenhaal et al., 1991; Von der Heydt and Dijkstra, 2006). The positioning of the continents also affects weatherability by determining the land area in intense weathering environments, such as the tropics (e.g., Goddéris et al., 2014).

In contrast to palaeo degassing rates, palaeogeographies are relatively well constrained. Thus, there is scope to investigate the impact of changing weatherability on long-term CO_2 concentrations. Early studies using zero-dimensional global models such as GEOCARB used estimations of global MAT and runoff values, but no geographical constraints, to estimate global weathering fluxes and steady-state CO_2 concentrations in geological time (Berner, 1991). Further studies refined the GEOCARB approach by including palaeogeographical reconstructions, both conceptual (e.g., 'ringworld' configurations) and realistic, which demonstrated that continental configurations had significant impact on steady-state CO_2 concentrations (e.g., Barron et al., 1989) and that palaeogeography and climate interact to determine steady-state CO_2 concentrations (Otto-Bliesner, 1995). Further model developments provided spatial patterns in climate forcing data, demonstrating that regional changes in weatherability can have global climate impacts (Donnadieu et al., 2004). More recently, such models have shown that the positioning of the continents also affects weatherability by determining the land area in intense weathering environments, such as the tropics (e.g., Goddéris et al., 2014).

The impact of changing weatherability as a result of changes in palaeogeography during the Phanerozoic has previously been investigated by (Goddéris et al., 2014) using the GEOCLIM model with climate inputs from the FOAM GCM, which found that the formation of supercontinents resulted in a continental configuration favourable for high atmospheric CO_2 concentrations (10-25 x PAL), as the converged continental configuration resulted in arid continental interiors and reduced weatherability. Conversely, dispersed continental configurations were more favourable to lower atmospheric CO_2 concentrations (1-8 x PAL) by favouring higher continental runoff and weatherability. Furthermore, Goddéris et al. (2014) found that continents or even smaller landmasses crossing warm-humid climate belts can result in significant draw drown of atmospheric CO_2. For example, during the late-Triassic, the gradual northward drift of Pangaea brought larger areas of landmass into more humid zones. In response, CO_2 concentrations fell sharply over ~20 Myr from 19 x PAL to 3 x PAL (Goddéris et al., 2014).

Goddéris et al. (2014) had a relatively low temporal resolution of 22 simulations over the last ~520 Myr (approximately 1 simulation per 20-30 Myr). In contrast, this study will use 19 simulations over the Cretaceous-Eocene period (145-36 Ma) in addition to higher resolution (3.65x) palaeogeography and climate inputs. The higher temporal resolution will allow for the investigation of the impacts of higher temporal resolution changes (~5 Myr) in palaeogeography on weatherability, while the higher spatial resolution will better constrain regional variability in weatherability relative to Goddéris et al. (2014). The use of climate inputs produced by the more complex HadCM3L model in this study (relative to the FOAM inputs used by Goddéris et al. (2014)) also represents an improvement.

4.1.3. Research Questions

1): What is the effect of using different climate and palaeogeographical inputs from different GCMs in GEOCLIM simulations? How do differing reconstructions affect steady-state CO_2 concentrations and which parameters are responsible for any such changes?

2): What is the impact on weatherability of changing palaeogeographic configuration during the Cretaceous-Eocene? Furthermore, which factors (i.e. continental land area, runoff, temperature) if any, have stronger influences on weatherability, and does the strength of any influence change during the course of the modelled period?

3): What is the impact of changes in weatherability on atmospheric CO_2 during the Cretaceous-Eocene period (assuming a constant degassing rate), and are these changes of significant magnitude to have potentially affected the long-term climate?

4.2. Methodology

This chapter will investigate the impact of varying climate and paleogeography from the Early Cretaceous to the Late Eocene on weatherability, using a global climate and geochemical model, GEOCLIM. The climatic reconstructions are derived from the HadCM3L model, while previous GEOCLIM used the Fast Ocean Atmosphere Model (FOAM) (Goddéris et al., 2014). Prior to investigating the impacts of palaeogeography, this study will first investigate the impact of transitioning to the use of HadCM3L inputs in GEOCLIM and test the methodology of extrapolating climate inputs from data at 2 CO_2 concentrations. HadCM3L has not been used with GEOCLIM before and many of the inputs require some modification for use within GEOCLIM. Transitioning between the two GCMs will also provide an opportunity to perform a sensitivity study of weathering rates to changes in global and regional variables, as well as assessing the potential impact of modifying the HadCM3L inputs for use in GEOCLIM.

4.2.1. FOAM

The Fast Ocean Atmosphere Model (FOAM) began development in the early 1990s to provide a coupled ocean-atmosphere model with low runtime demands at an acceptable resolution (Tobis, 1997). The low runtime is intended to facilitate long-term climate simulations,(Jacob et al., 2001). FOAM uses a relatively coarse grid resolution of 48x40 (7.5° x 4.5°), which was found to be the minimum resolution necessary to accurately model ocean circulation interactions with the atmosphere (Tobis, 1997). Since its development, FOAM has been used in a number of studies of past, present, and future climate at a variety of temporal scales, ranging from annual-decadal to geological timescales (e.g., Masson-Delmotte et al., 2006; Notaro et al., 2006). Most importantly for this study, FOAM outputs have been extensively used in previous GEOCLIM simulation studies (Donnadieu et al., 2006, 2009; Lefebvre et al., 2013; Goddéris et al., 2014, 2017).

4.2.2. HadCM3L

HadCM3L is part of the HadCM3 "family" of coupled GCMs originally developed by the UK Met Office (Gordon et al., 2000; Valdes et al., 2017). The HadCM3 family of models have been in use for over 15 years, with various modifications to the configuration of the original HadCM3 model being made in that time. HadCM3L is a version of HadCM3 using a "low-resolution" ocean, where ocean and atmosphere share the same 96x73 (3.75° x 2.5°) resolution (Valdes et al., 2017). Although described as "low-resolution", 96x73 is nonetheless 3.65 times higher resolution than FOAM. However, like FOAM, HadCM3L is used for long term simulations where higher resolution models would be too time intensive to be practical. To that end, HadCM3L has been used extensively in pre-quaternary climate studies, where long term climate simulations are required (e.g., Lunt et al., 2010, 2011, 2012; Kennedy et al., 2015; Lunt et al., 2016; Carmichael et al., 2017; Valdes et al., 2017), although HadCM3L has never been used to model chemical weathering processes.

4.2.3. GCM Input Simulation Comparison

Climate data from existing FOAM and HadCM3L simulations of the early Eocene (52 Ma) were used to investigate the sensitivity of GEOCLIM to changing model inputs and methodologies (Lunt et al., 2012; Goddéris et al., 2014). Under Eocene conditions, the FOAM and HadCM3L model simulations have comparable global MAT (21.6°C and 21.4°C, respectively) and continental MAR (41.3 cm yr^{-1} and 44.0 cm yr^{-1}, respectively, hereafter referred to as global MAR) values at 1120 ppm of CO_2.

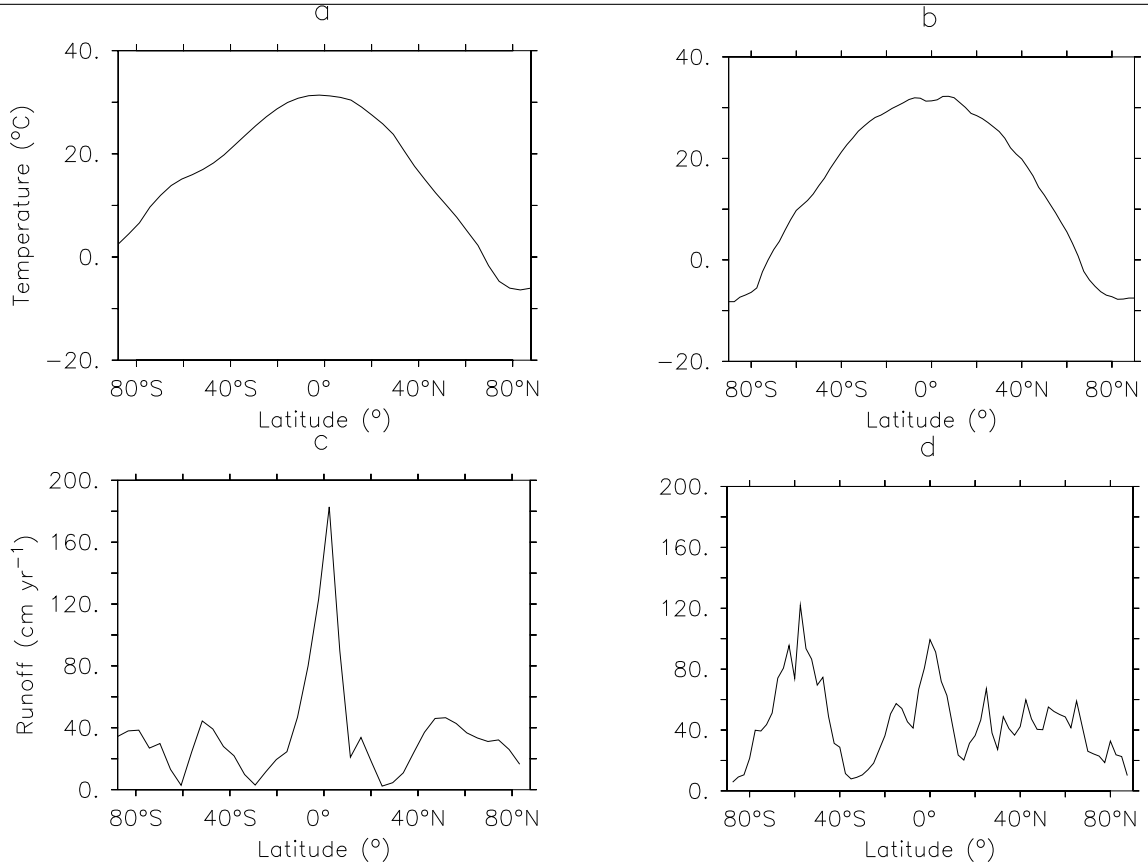

Figure 4.1: Zonal means for GEOCLIM simulations with FOAM (A) and HadCM3L (B) mean annual temperatures (°C) and FOAM (C) and HadCM3L (D) mean annual runoff values (cm yr^{-1}). Both FOAM and HadCM3L simulations have similar MAT zonal means, while zonal mean runoff varies significantly. FOAM shows a pronounced equatorial peak in runoff, while in HadCM3L peaks in runoff are more widely distributed.

In contrast, zonal means show significant differences in the global distribution of continental temperature and runoff between the two models. While both models have similar tropical continental MAT values (30-32°C), FOAM has a weaker equator to polar temperature gradient, with southern polar continental MAT remaining above freezing (Figure 4.1A and B, Figure 4.2E). Both poles in the HadCM3L model remain below freezing, slightly above -10°C. In this regard, FOAM likely provides a better representation of the low equator-pole temperature gradient present during the Eocene (Lunt et al., 2012). HadCM3L shows a more pronounced temperature difference between continental and ocean air temperatures, with the tropical and subtropical landmasses being significantly warmer than ocean areas at similar latitudes (Figure 4.1B and 4.2F). Mean annual runoff is divergent between the two simulations. In the FOAM simulation runoff is strongly concentrated at the equator with zonal means exceeding 175 cm yr^{-1}, while elsewhere MAR does not exceed 50 cm yr^{-1} (Figure 4.1C, 4.2C). In contrast, zonal MAR in the HadCM3L model is highest in the southern mid-latitudes (120 cm yr^{-1}), with a secondary peak at the equator of approximately 100 cm yr^{-1} (Figure 4.1D). Zonal MAR in the HadCM3L model shows pronounced peaks associated with mountain ranges, particularly the Laramides and the Appalachians, which

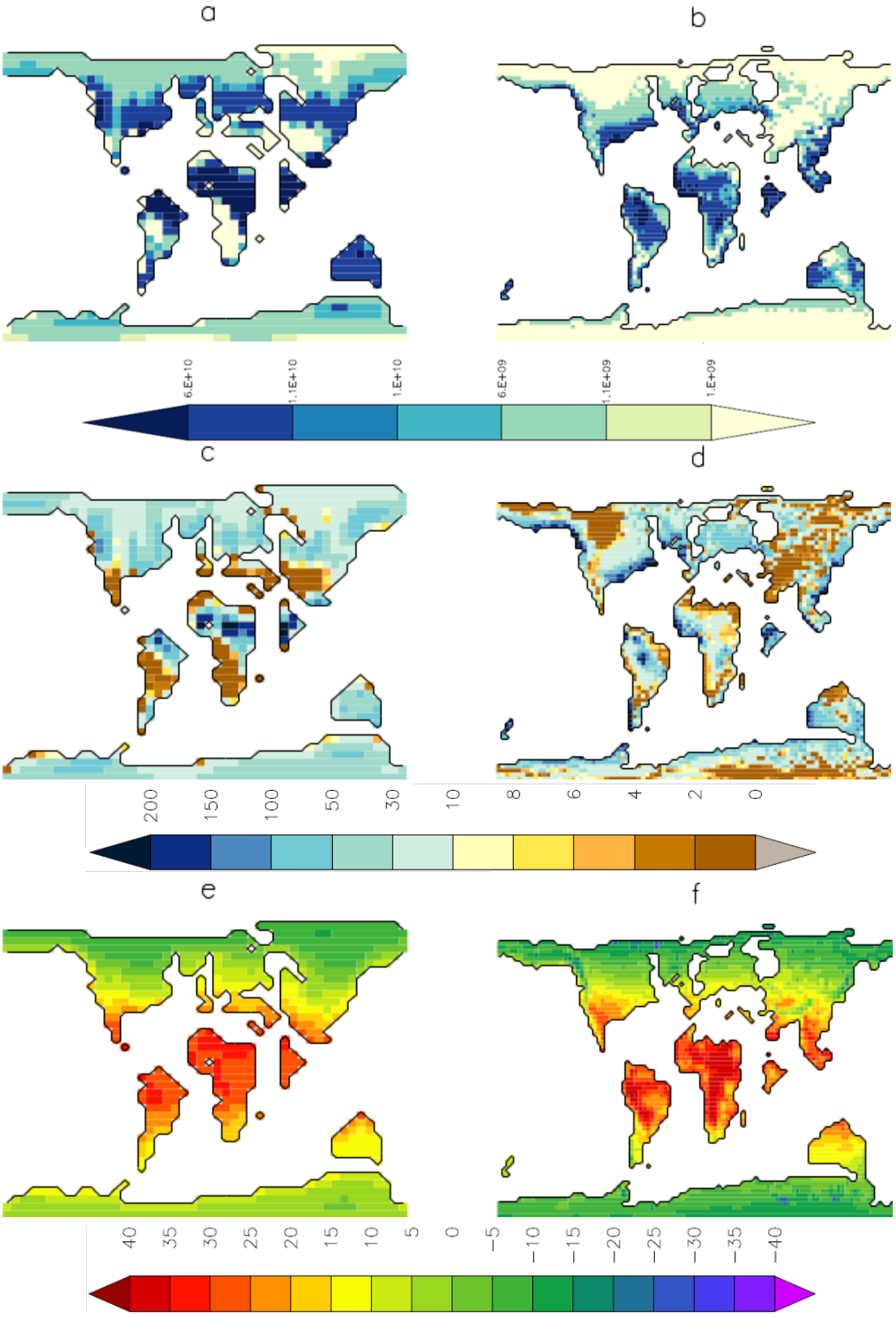

Figure 4.2: Maps comparing initial weathering fluxes (mol C yr^{-1}), runoff (cm yr^{-1}), and temperature (°C) conditions for (a,c,e) FOAM and (b,d,f) HadCM3L. FOAM displays considerably higher runoff fluxes in Saharan Africa and Central Asia relative to HadCM3L, which is in general more arid. HadCM3L displays higher temperatures in continental South America and Africa, but cooler temperatures in the Arctic and Antarctica relative to FOAM.

are resolvable at the higher resolution used in this model (Figure 4.1D, 4.2D). Precipitation in HadCM3L is likely a better approximation of real-world conditions during the Eocene, and precipitation within HadCM3L is similar to other models of the Eocene (Carmichael et al., 2017).

4.2.4. GEOCLIM

GEOCLIM is a coupled global climate and biogeochemical model developed in the early 2000's and has been used to investigate interactions between climate and geochemistry in deep time settings on geological timescales (Donnadieu et al., 2004). GEOCLIM uses climate inputs from GCMs, initially using CLIMBER inputs (Donnadieu et al., 2004), but more recent studies have used FOAM inputs (Lefebvre et al., 2013; Goddéris et al., 2014, 2017). GEOCLIM also includes a geochemical model, COMBINE.

COMBINE

Geochemical cycles within GEOCLIM are modelled by COMBINE (COupled Model of Biogeochemical cycles aNd climatE). The COMBINE model is coupled offline to GCM output data to reduce computational demands as fully coupling COMBINE to a GCM would result in impractical model runtimes given the timescales involved in climate-weathering interactions (Donnadieu et al., 2004).

The primary structure of COMBINE consists of 10 reservoirs, 9 of which are ocean reservoirs with the remaining reservoir representing the atmosphere. The ocean reservoirs are separated based on latitude and depth (Figure 4.3). Continental and ocean areas are specified by land-sea mask and global surface area data. Deep ocean sediments are not represented by a reservoir but burial fluxes between the oceans and sediments are calculated within COMBINE. COMBINE models 18 primary geochemical variables including C, O, P, and S, with this study focusing on the carbon cycle.

Inputs of carbon into COMBINE are represented by specified constant volcanic (F_{Vol}) and mid ocean ridge (F_{MOR}) degassing fluxes. Volcanic degassing occurs directly into the atmospheric reservoir while mid ocean ridge degassing occurs in the deep mid-latitude ocean box (Figure 4.3). Within COMBINE, a number of fluxes transport carbon between reservoirs, such as weathering fluxes and ocean-atmosphere exchange . On the continents, silicate weathering (granite and basalt) acts as a carbon sink while carbonate weathering acts as a source. The calculations involved in these weathering reactions are discussed in further detail later. Carbon is also exchanged between the surface ocean boxes and the atmosphere. Thus, changes in atmospheric CO_2 in GEOCLIM are determined by the balance of volcanic degassing, weathering fluxes, and atmosphere-ocean exchanges. COMBINE provides further options for enabling volcanic traps although these options are not utilised in this study.

Weathering within COMBINE uses separate equations to calculate weathering fluxes of granite

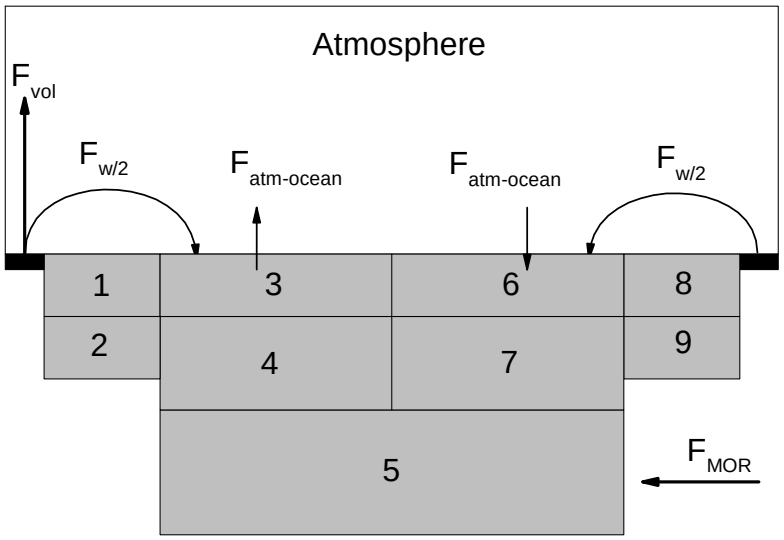

Figure 4.3: Diagram of the geochemical reservoirs (defined as 'boxes') within GEOCLIM, consisting of nine ocean reservoirs (split into four surface (1,3,6,8) and five deep reservoirs (2,4,5,7,9)) and one atmospheric reservoir. Dark rectangles indicate continental landmasses. Volcanic degassing (F_{vol}) occurs directly into the atmospheric reservoir while mid-ocean ridge degassing (F_{mor}) occurs directly into the deep ocean reservoir. Weathering fluxes ($F_{w/2}$) draw CO_2 from the atmosphere and transport weathering products all surface ocean reservoirs. Atmosphere-ocean ($F_{atm-ocean}$) exchange occurs between the atmosphere and the surface ocean reservoirs.

(referred to as silicates in the model), basalt, and carbonate. These equations combine geochemical constants, climate variables, and grid cell area parameters to produce weathering fluxes in each cell and a global weathering value. In the absence of well-constrained palaeogeological reconstructions, each grid cell contains an equal proportion of the three rock types used in COMBINE, with basalt weathering representing 30% of the total silicate weathering flux (granite + basalt) (Dessert et al., 2003).

$$facgra = (\frac{-48200}{Rgas}) * (\frac{1}{T_j + 273.15} - \frac{1}{288.15}) \tag{4.1}$$

The term *facgra* (dimensonless) represents the granitic dependence on dissolution based on air temperature, which uses the activation energy for granite defined by Oliva et al. (2003) and the air

temperature in a given grid cell, T_j (Equation 4.1). This value can then be applied in Equation 4.2.

$$F_{sil}(t) = k_{sil} * (area_j(t) * runoff_j(t) * exp(facgra)) \tag{4.2}$$

Equation 4.2 calculates the silicate weathering flux in moles of C per year at a timestep *(t)* in a given grid cell, $F_{sil}(t)$, k_{sil} is the silicate weathering constant, $area_j(t)$ is the area of a grid cell (10^6 km^2), $runoff_j(t)$ is the runoff value of that grid cell (cm yr^{-1}). The silicate weathering flux of each grid cell are summed to provide a global silicate weathering flux at a given timestep, $F_{silw}(t)$. Similar processes are applied for the basalt weathering constant (Equation 4.3) and weathering fluxes of basalt and carbonate (Equations 4.4 and 4.5)

$$facbas = (\frac{-42300}{Rgas}) * (\frac{1}{T_j + 273.15} - \frac{1}{288.15}) \tag{4.3}$$

$$F_{bas}(t) = k_{bas} * (area_j(t) * runoff_j(t) * exp(facbas)) \tag{4.4}$$

$$F_{carb} = 1.86 * 10^{10} * \sqrt{runoff_j(t)} * area_j(t) \tag{4.5}$$

As GEOCLIM is not directly coupled to a GCM, climate change is determined by linearly interpolating between input variable values (such as MAT, runoff) from model simulations previously carried out at specified CO_2 concentrations. GEOCLIM cannot extrapolate beyond the range of specified CO_2 concentrations, and if CO_2 falls outside of the specified range, the model will cease updating climate variables and use the lowest or highest values within this range.

4.2.5. Data Extrapolation

Because GEOCLIM interpolates climate variables based on climate data at specified CO_2 levels, it was necessary to ensure that both the FOAM and HadCM3L input data had consistent CO_2 concentrations. FOAM was previously run at 11 CO_2 levels between 160 and 1400 ppm, while HadCM3L was previously run only at 560 and 1120 ppm. For consistency, a methodology was developed to produce "synthetic" model output from HadCM3L at the same CO_2 concentrations as for FOAM. This was deemed particularly important because GEOCLIM model runs with Ypresian FOAM inputs have previously produced CO_2 concentrations below 560 ppm (Lefebvre et al., 2013).

To address these issues, the HadCM3L climate inputs were extrapolated to the same 11 CO_2 concentrations to cover the same range as the FOAM data. Two separate extrapolation methods were used to calculate the temperature and runoff to better reflect their sensitivity to CO_2 level changes in observed data. The HadCM3L temperature *(T_x)* for a CO_2 concentration of CO_{2x}, was approximated as:

$$T_x = T_{560} + (T_{diff} * \frac{ln\frac{CO_{2x}}{280}}{ln2} - 1) \tag{4.6}$$

Temperature values were extrapolated based on absolute differences between the 560 and 1120 ppm temperature outputs (Equation 4.6).T_x is the temperature value at any given CO_2 concentration, where T_{560} is the temperature at 560 ppm, T_{diff} is the difference in temperature between 1120 and 560 ppm, and CO_{2x} is a specific concentration of atmospheric CO_2 (ppm).

Runoff was extrapolated in a similar fashion to temperature, except that a constant ratio rather than a constant absolute difference was assumed per CO_2 doubling, because this relationship is found in the model results and absolute value changes would result in large areas of negative runoff and excessive aridity at lower CO_2 concentrations which were deemed to be unrealistic:

$$R_x = R_{560} * exp((\frac{CO_{2x} - 560}{560} * ln(R_{diff}) \tag{4.7}$$

Equation 4.7 was used to extrapolate runoff rates (cm yr^{-1}), R_x, at any given CO_2 concentration. R_{560} represents the runoff rate at 560 ppm, while R_{diff} is the magnitude difference between runoff values at 1120 and 560 ppm. Section 4.3 shows how this method of extrapolation would likely affect the results, by applying the synthetic methodology to the FOAM outputs.

When transitioning between FOAM and HadCM3L palaeogeography inputs, FOAM runoff and temperature values were laid over the HadCM3L palaeogeography. These inputs were then extrapolated to "fill" land areas which were not present in the FOAM palaeogeography inputs. As non-land areas in GEOCLIM are given a runoff value of zero, this step was necessary to avoid large areas of "artificial deserts".

As weathering flux calculations in GEOCLIM are area-sensitive, it was necessary ensure that both the FOAM and HadCM3L palaeogeographies had identical total global area values (i.e., continental and ocean area). The existing FOAM inputs provided a fractional land-sea mask for each grid cell, plus a total area of each grid cell, while the HadCM3L model inputs provided a binary land-sea mask (land = 1, ocean = 0) with no associated area values. To produce grid cell areas for the HadCM3L palaeogeography, areas were calculated for each grid cell at 96x73 resolution as a fraction of total global area, multiplied by the total global area value for the FOAM

simulation. These values were then multiplied by a correction factor (represented by the FOAM total global area divided by the HadCM3L total global area) to ensure that the total global area of both the FOAM and HadCM3L reconstructions were identical. To produce the continental grid cell area array for HadCM3L, the binary land-sea mask array was multiplied by the global grid cell area array.

4.2.6. GEOCLIM Simulation Configuration

For this study, GEOCLIM was set to model the impact of varying environmental factors (MAT, runoff, and palaeogeography) on chemical weathering rates during the Ypresian period of the early Eocene (˜52 Ma). New high spatial resolution reconstructions from HadCM3L were adapted for use in GEOCLIM as described above. All models were run using a constant volcanic degassing rate of 6.8 x 10^{12} mol C yr^{-1} and identical initial CO_2 concentrations (798 ppm or 2.85 PAL).

Table 4.1: GEOCLIM Sensitivity Simulation Sequence

	CLIMATE		**GRID**		**EXTRAPOLATED**		
Run Name	**Runoff**	**Temp**	**Resolution**[c]	**LSM**	**Oceans**	**Runoff Extrapolation**	**Temp Extrapolation**
Run_01	F[a]	F	F	F	O[d]	-	-[g]
Run_02	F	F	F	F	O	-	Y
Run_03	F	F	F	F	O	Y[f]	Y
Run_04	F	F	F	F	C[e]	Y	Y
Run_05	F	F	F	M	C	Y	Y
Run_06	F	F	M	M	C	Y	Y
Run_07	F	M	M	M	C	Y	Y
Run_08	M[b]	M	M	M	C	Y	Y

Run_01 was performed using only FOAM inputs and Run_08 was performed using only HadCM3L inputs. [a]F = FOAM inputs. [b]M = HadCM3L inputs. [c]For resolution F = 48 x 40, M = 96 x 73 [d]O = original ocean configuration. [e]C = corrected ocean configuration (see section 2). [f]Y = climate variables have been extrapolated to 11 CO_2 concentrations using the processes described in the methods. [g] – indicates no extrapolation process has been applied to variables. LSM = land-sea mask.

Initially, a simulation using the FOAM inputs from Goddéris et al. (2014) was carried out, and the results of this simulation were compared with a simulation using HadCM3L inputs (run_01 and run_08, respectively; Table 4.1). To investigate the role of individual factors (e.g., runoff, temperature) between the two simulations on the resulting differences, and the role of methodological differences between the two models (e.g., resolution and extrapolation), further simulations were run where factors were changed incrementally from FOAM inputs to HadCM3L inputs (Table 4.1)

A minor change to the ocean configuration was made for some of the simulations in this study. Initially, GEOCLIM was set up such that the polar oceans represented the southernmost and

northernmost 1/6 of the Earth's ocean surface. However, given that the number of latitude bands in HadCM3 does not divide exactly by 6, this configuration results in anomalies when using the HadCM3L resolution. The boundaries of the polar oceans are specified as 60°S and 60°N (specified using grid cell numbers) to amend this issue.

4.3. Results - Sensitivity Study

4.3.1. GEOCLIM FOAM-HadCM3L Comparison

Runs of GEOCLIM using the FOAM and HadCM3L inputs (runs 01 and 08) resulted in significant differences in steady-state CO_2 concentrations (after 1 Myr) and spatial weathering patterns at 5 kyr, used here as a representation of "weatherability"(Table 4.2; Figures 4.2 and 4.4-6 panels a and h). Weathering flux data (and climate data) are examined at the first timestep (5 kyr) as the weathering data provide an estimate of the global weatherability under a given climate and palaeogeographical configuration. CO_2 concentrations are examined at 1 Myr to determine the steady-state CO_2 concentration produced as a result of differences in weatherability.

Table 4.2: Steady-State CO_2 and Silicate Weathering Fluxes of GEOCLIM Sensitivity Simulations

Run Name	Steady-State CO_2 (ppm)[a]	Difference from Previous Run (ppm)	Difference from Run_01 (ppm)	Initial Global Silicate Weathering Flux (mol C yr^{-1})[b]
Run_01	299	n/a	n/a	2.45 x 10^{13}
Run_02	308	9	9	2.45 x 10^{13}
Run_03	274	-34	-25	2.43 x 10^{13}
Run_04	272	-2	-27	2.43 x 10^{13}
Run_05	228	-44	-71	2.52 x 10^{13}
Run_06	332	104	33	2.30 x 10^{13}
Run_07	310	-22	11	2.46 x 10^{13}
Run_08	505	195	206	2.14 x 10^{13}

[a] at final output timestep of 1 Myr. [b] at first output timestep of 5 kyr.

Using FOAM inputs resulted in a steady-state CO_2 concentration of 299 ppm after 1 Myr. Such a value is relatively low compared to proxy reconstructions of Eocene CO_2 concentrations (Jagniecki et al., 2015; Anagnostou et al., 2016; Foster et al., 2017), but similar to levels produced by previous GEOCLIM simulations (Lefebvre et al., 2013). In contrast, using HadCM3L inputs produced a considerably higher steady-state CO_2 concentration of 505 ppm. However, given that we have prescribed a fairly arbitrary volcanic emissions rate, such comparison is not particularly meaningful. For both models, an emissions rate could be estimated that gave a CO_2 concentration agreement with the proxy evidence.

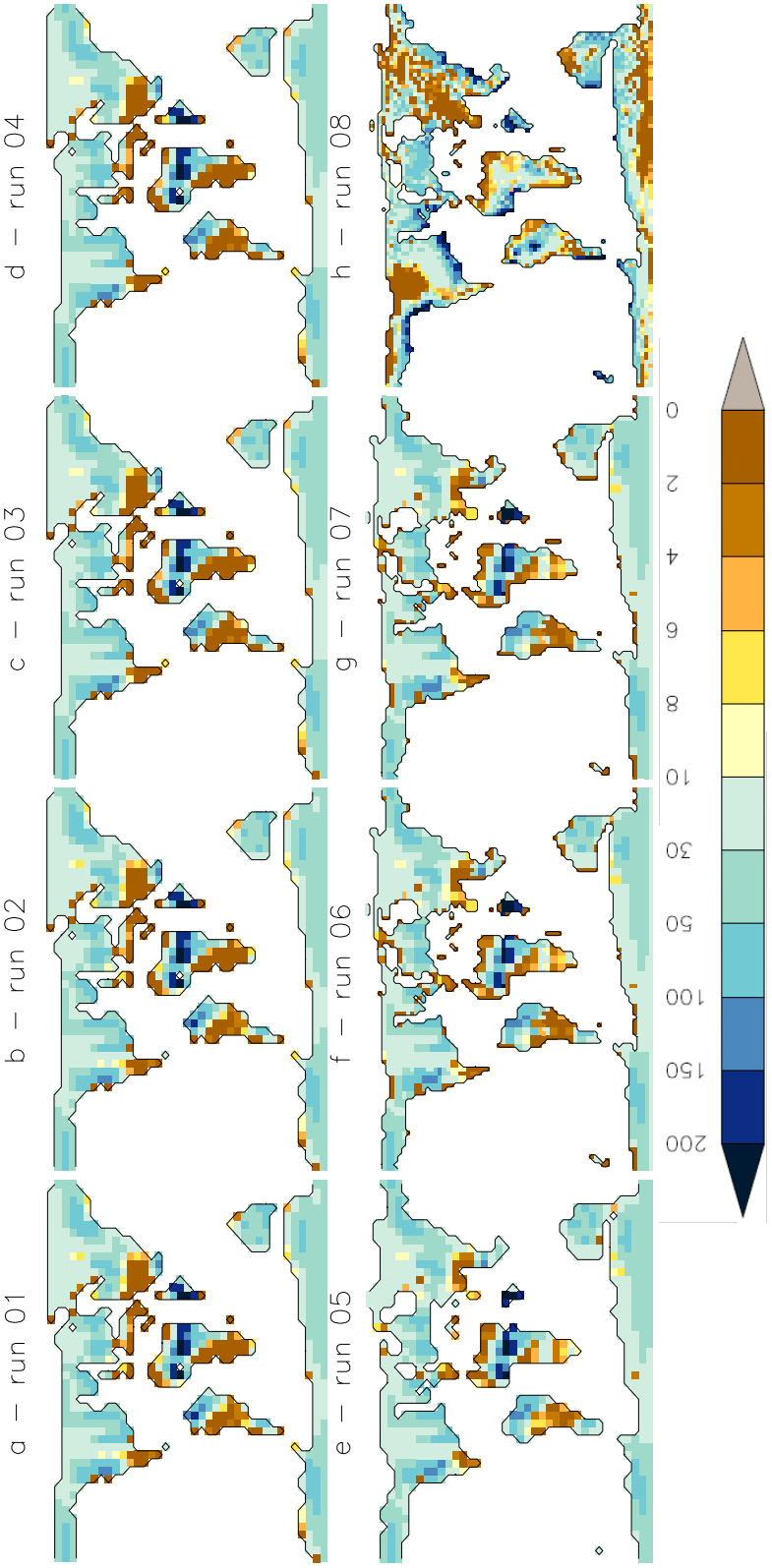

Figure 4.4: Mean annual runoff (cm yr^{-1} output maps after 5 kyr for GEOCLIM sensitivity runs 01-08 (a-h)(Table 4.1).

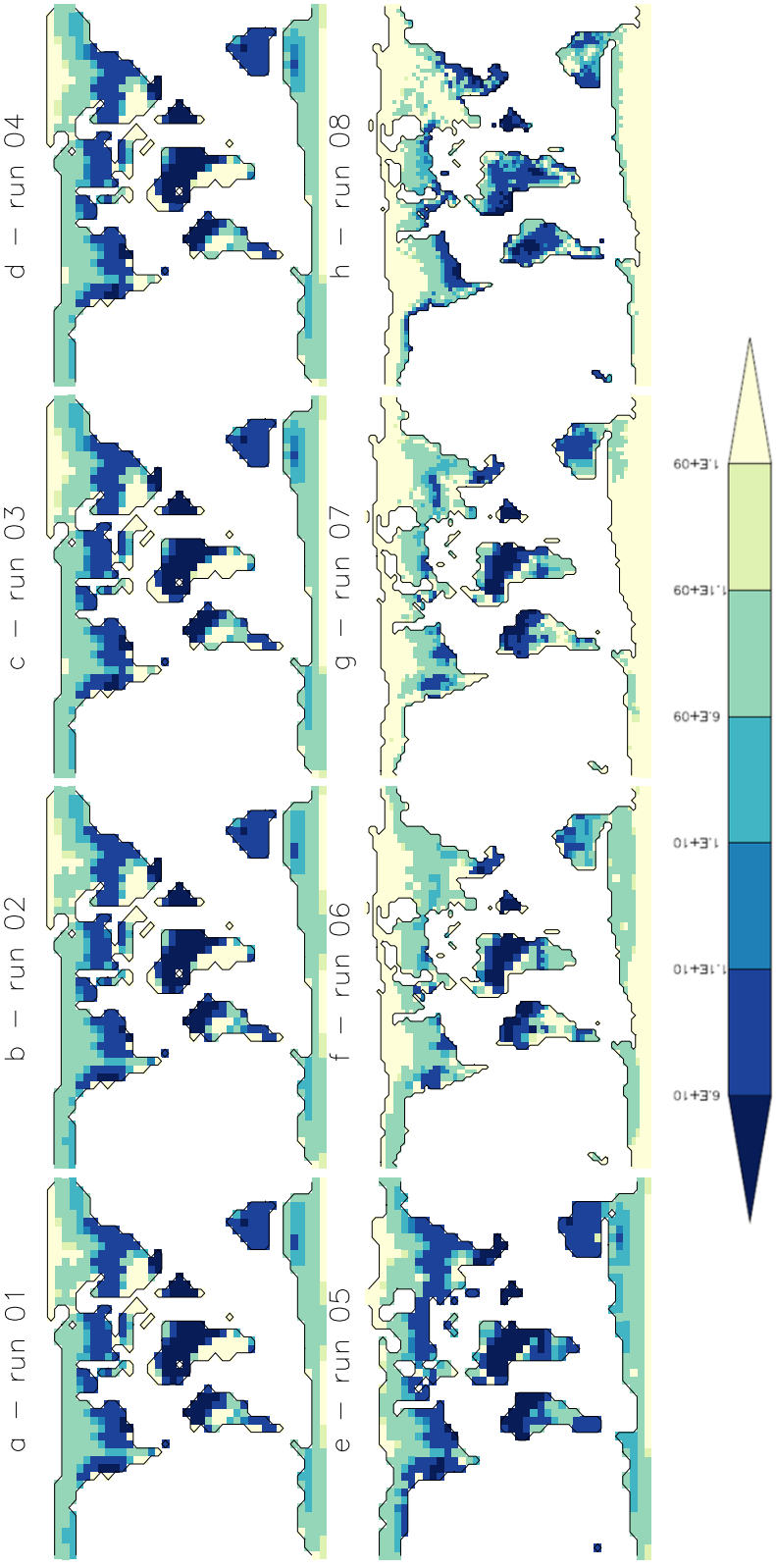

Figure 4.5: Silicate weathering flux (mol C yr^{-1}) maps after 5 kyr for GEOCLIM sensitivity runs 01-08 (a-h)(Table 4.1).

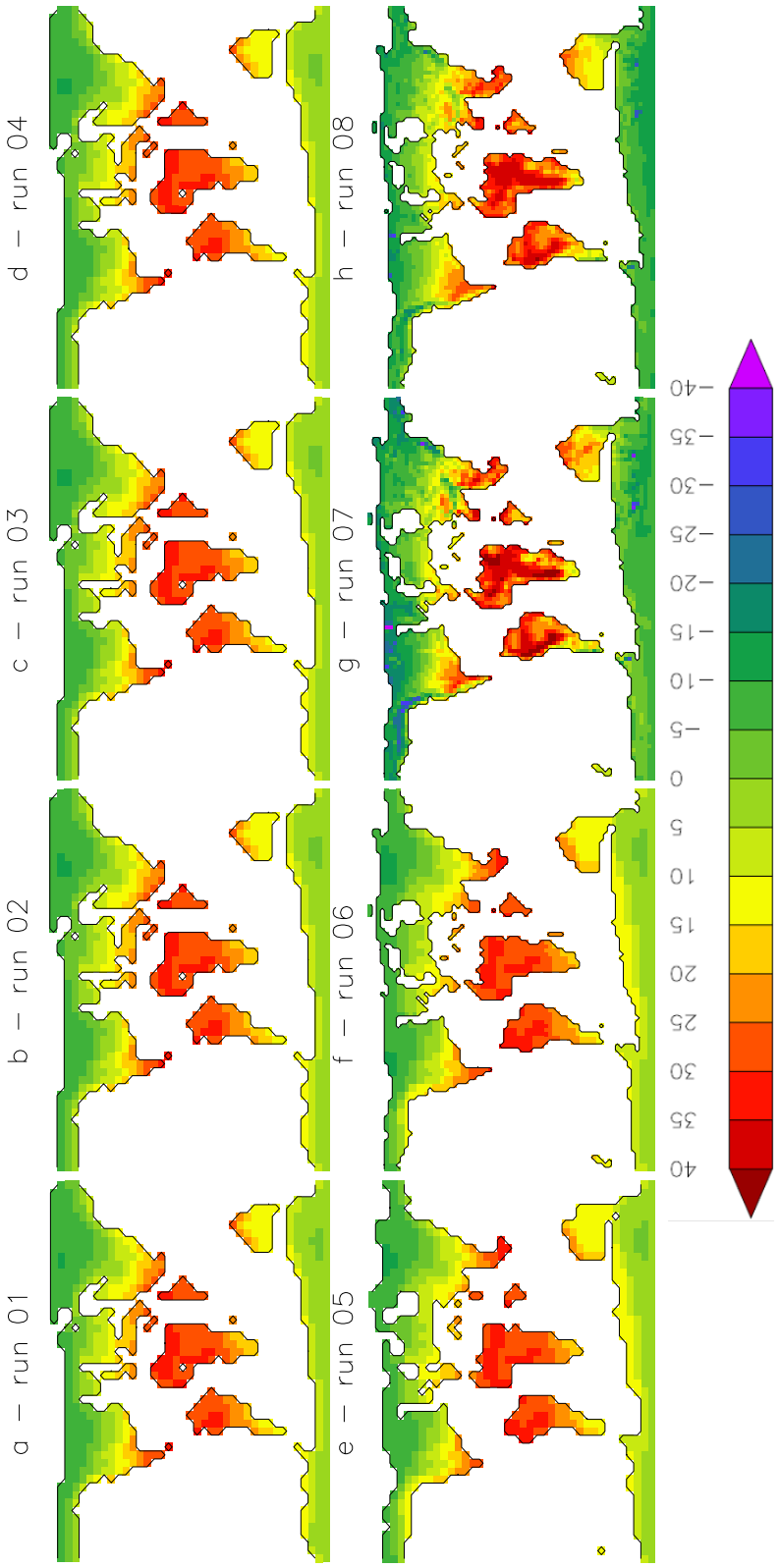

Figure 4.6: Mean annual temperature (°C) output maps after 5 kyr for GEOCLIM sensitivity runs 01-08 (a-h)(Table 4.1).

At the first output timestep (5 kyr), the total global silicate weathering flux (as a representation of weatherability) in the FOAM run was 2.45 x 10^{13} mol C yr^{-1} , while the HadCM3L run produced a global flux of 2.14 x 10^{13} mol C yr^{-1} (Table 4.2). Thus, the global silicate weathering flux after 5 kyr is approximately 12% higher in the FOAM run versus the HadCM3L run . In the FOAM run, bands of intense weathering are present across the equator, with the highest values covering much of northern Africa, India, and northernmost South America (Figure 4.4A). Bands of substantial, but less intense weathering are present across the temperate mid-latitudes. A few zones of negligible weathering occur in southwest Africa, Siberia, and southern Asia. The HadCM3L run shows a greater degree of spatial variability in weathering fluxes with a less distinct latitudinal trend relative to the FOAM run (Figure 4.2B, 4.4H). Like the FOAM run, the HadCM3L run results in intense weathering in India and South America but produces more intense weathering in south-east Asia. The HadCM3L run also exhibits far larger areas of low or negligible weathering, with much of inland Asia, Antarctica, and North America having low weathering fluxes.

4.3.2. Effects of FOAM-HadCM3L Transition

Why do FOAM and HadCM3L give such different estimates of weatherability and steady-state CO_2 concentration? In order to answer this question, inputs are moved incrementally from FOAM to HadCM3L, changing one variable or methodology at a time. Here, it is hoped that the difference in climate variable (e.g., temperature or runoff) rather than method (e.g., extrapolation of GCM fields) is the most significant factor, as this will demonstrate that the extrapolation method is robust and can be applied to other climate datasets.

As part of the sensitivity study, FOAM data were interpolated to 96x73 resolution, providing an intermediate step in transitioning between FOAM and HadCM3L inputs. A nearest-neighbour interpolation method was favoured over a bilinear interpolation method for such a step, as the nearest-neighbour method preserves local values rather than global means. As weathering rates are highly variable from site to site (Chapter 2), preserving local values was deemed more appropriate in this study than preserving global means.

The GEOCLIM simulation sequence begins with the "original" unmodified FOAM inputs, then the extrapolated temperature inputs are used, followed by the extrapolated runoff inputs . These steps allow for the testing of the impact of the extrapolation process on the results relative to the unmodified FOAM inputs. A 48x40 resolution HadCM3L land-sea mask is then introduced to test the impact of changing palaeogeography while retaining the FOAM climate inputs. The resolution of the model is then increased to 96x73. As 96x73 is not a direct multiple of 48x40, and give the highly non-linear characteristics of weathering processes, there may be impacts on the climate inputs as a result of the interpolation process. The HadCM3L temperature inputs are then introduced followed by the HadCM3L runoff inputs.

The effect on steady-state CO_2 and weathering fluxes of the incremental transition from FOAM

to HadCM3L is shown in Table 4.2. Using extrapolated FOAM temperature inputs (run 02, see methods described in section 4.2.1) resulted a slight increase in steady-state CO_2 and the extrapolated runoff inputs (run 03) caused a decrease (to 308 and 274 ppm, while initial weathering fluxes were 2.45 x 10^{13} and 2.43 x 10^{13} mol C yr^{-1}, for runs 02 and 03, respectively). Using the HadCM3L land sea mask at 48x40 resolution (run 05) resulted in a significant drop in steady-state CO_2 to 228 ppm (initial weathering flux = 2.52 x 10^{13} mol C yr^{-1}) likely due to changes in continental land area, while changing to the 96x73 resolution land-sea mask (run 06) increased CO_2 to 332 ppm from 228 ppm in run 05 (weathering flux = 2.30 x 10^{13} mol C yr^{-1}). The most significant impact on steady-state CO_2 occurred as a result of using the HadCM3L runoff (run 08) which increased steady-state CO_2 to 505 ppm (weathering flux = 2.14 x 10^{13}), while incorporating the HadCM3L temperature (run 07) had a less significant impact (CO_2 decreased by 22 ppm relative to run 06; Table 4.2).

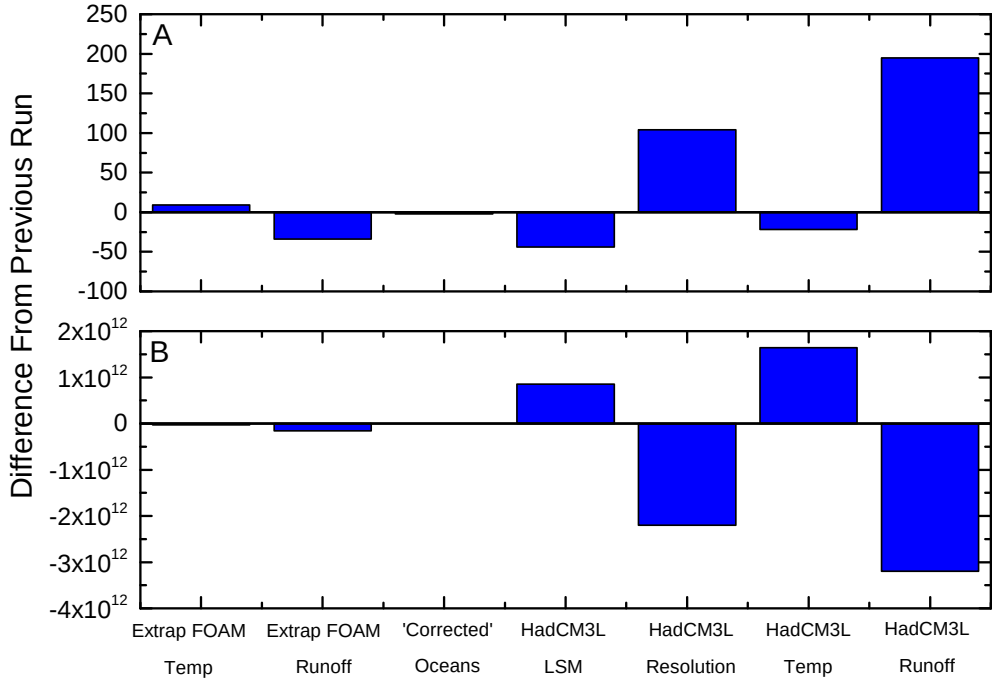

Figure 4.7: (A) Changes in modelled steady-state CO_2 in ppm (after 1 Myr) for runs 02-08 relative to the previous run and (B) changes in initial global silicate weathering fluxes (mol C yr^{-1}) relative to the previous run. The variable changed in each run is shown as the x-axis (Table 1). Changes in weathering fluxes are essentially an inverse of the pattern of changes in steady-state CO_2.

As expected, changes in initial global silicate weathering fluxes (i.e., weatherability) across the FOAM-HadCM3L transition were broadly the inverse of the final equilibrium CO_2 changes (Figure 4.7). The transition to the HadCM3L runoff, resolution, and temperature produced the greatest changes in weathering fluxes, both between runs and relative to the first run with FOAM inputs.

As with CO_2, changing to the HadCM3L runoff had the strongest effect on global weathering fluxes.

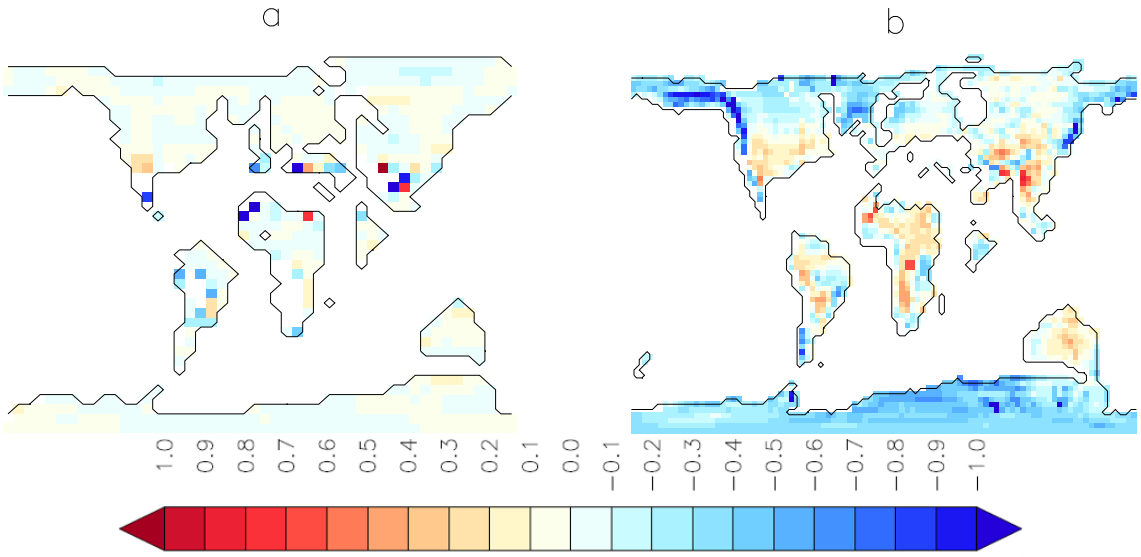

Figure 4.8: Maps showing magnitude changes in initial weathering fluxes (after 5 kyr) between (A) run 02 and 03 and (B) run 06 and 07. (A) displays the impact of using extrapolated FOAM runoff inputs causes very large and localised regional changes in weathering fluxes ($>$ 1 order of magnitude). (B) displays that the impact of using HadCM3L temperature inputs has lower magnitude changes (0.5-0.8) but such changes are more widespread.

Some of the FOAM-HadCM3L transition stages (02 and 04) resulted in only minor changes to regional weathering fluxes (Figure 4.4). Incorporating the extrapolated FOAM runoff resulted in a general increase in regional weathering fluxes, but some tropical areas show very strong changes ($>$ 1 order of magnitude) in weathering fluxes (Figure 4.8A). Using the HadCM3L temperature inputs also resulted in strong changes in weathering fluxes within continental interiors (0.5-0.8 orders of magnitude; Figure 4.8B), such as Africa, Australia, and Asia (Figure 4.4). Coastal areas, such as north America and northeastern Asia revealed significantly reduced weathering fluxes. Maps of weathering fluxes are strongly similar to runoff maps, but less similar to temperature maps (Figures 4.4-6).

Overall, given that the largest differences between FOAM and HadCM3L are the runoff climatologies, rather than methodological differences associated with the extrapolation of GCM simulations, provides some some confidence that HadCM3L can be used in a more detailed study.

4.4. Discussion - Sensitivity Study

4.4.1. Sensitivity of GEOCLIM to GCM Inputs

The results of the sensitivity study (Section 4.3) indicate that changing to the extrapolated FOAM inputs from the original FOAM inputs has only a minor impact for temperature but a stronger impact for runoff (Table 4.2). The effects of this can be seen in runs 02 and 03, where the original FOAM climate inputs are replaced with extrapolated versions of the temperature and runoff data, respectively. Run 2 shows an increase in steady-state CO_2 of only 9 ppm relative to run 01 (change in methodology for temperature), while run 03 shows a drop of 25 ppm (change in methodology for runoff). Still, the relatively small changes in steady-state CO_2 seen suggest that the extrapolation process still provides a reasonable estimate of climate conditions relative to the non-extrapolated inputs. As such, it is likely that the extrapolation process will also provide a good estimate for HadCM3L inputs outside of 560-1120 ppm range.

Interestingly, the transition to 96x73 resolution (run 06) produced a significant increase in steady-state CO_2 relative to the same inputs at 48x40 resolution (run 05). It is likely that this change is the result of the interpolation process used to "increase" the resolution of the FOAM inputs. 96x73 is not a direct multiple of 48x40, and thus the interpolation process will result in the averaging of some values where cells overlap under the higher resolution grid. As shown by runs 02 and 03, GEOCLIM is highly sensitive to even relatively small changes in input values (likely due to exponential functions within silicate weathering equations), and the averaging of climate input values could be significant enough to result in relatively large steady-state CO_2 changes between model runs.

The transition process shows that the model is much more sensitive to changes in runoff than in temperature when changing from FOAM to HadCM3L inputs, with the change to the HadCM3L runoff inputs producing the largest change in steady-state CO_2, both relative to the previous run and the first run (Table 4.2). The change to HadCM3L temperature inputs had comparatively little impact on CO_2. Similarly, the change to extrapolated FOAM runoff from the original inputs had a more significant impact than the extrapolated temperature inputs.

The pattern of the initial global silicate weathering fluxes between runs is the inverse of the CO_2 changes (Figure 4.7), indicating that silicate weathering fluxes are the main source of CO_2 changes between runs in GEOCLIM. As such, the changes in the inputs are affecting steady-state CO_2 concentrations by impacting silicate weathering fluxes. As the largest changes in CO_2 concentrations were caused by changing runoff inputs, runoff is also the strongest control on silicate weathering rates in the sensitivity model.

Spatial patterns of silicate weathering fluxes closely match those of runoff in both the FOAM and HadCM3L runs (runs 01 and 08) (Figures 4.2 and 4.4), likely due to the non-linear dependence of

silicate weathering rates on runoff (Equations 4.2 and 4.4) Silicate weathering fluxes are limited in areas of low runoff. Correlations between silicate weathering fluxes and regional runoff are stronger under the FOAM inputs than the HadCM3L inputs (r = 0.91 and 0.69, respectively), although the FOAM dataset is considerably smaller due to the lower resolution. Correlations are weaker against temperature than runoff in both datasets with a value of r = 0.38 for the FOAM inputs and r = 0.39 for the HadCM3L inputs.

4.5. Methodology - Palaeogeography Study

4.5.1. HadCM3L Inputs

The palaeogeography aspect of this study uses 19 HadCM3L simulations of the Cretaceous-Eocene period at intervals of 3-13 Ma (Farnsworth et al., In revisions). As with the inputs used in the sensitivity study these simulations were run with CO_2 concentrations at 560 ppm and 1120. In contrast to the HadCM3L simulation used in the sensitivity study, these simulations had a significantly increased spin-up time (˜10400 compared with 1,400 years).

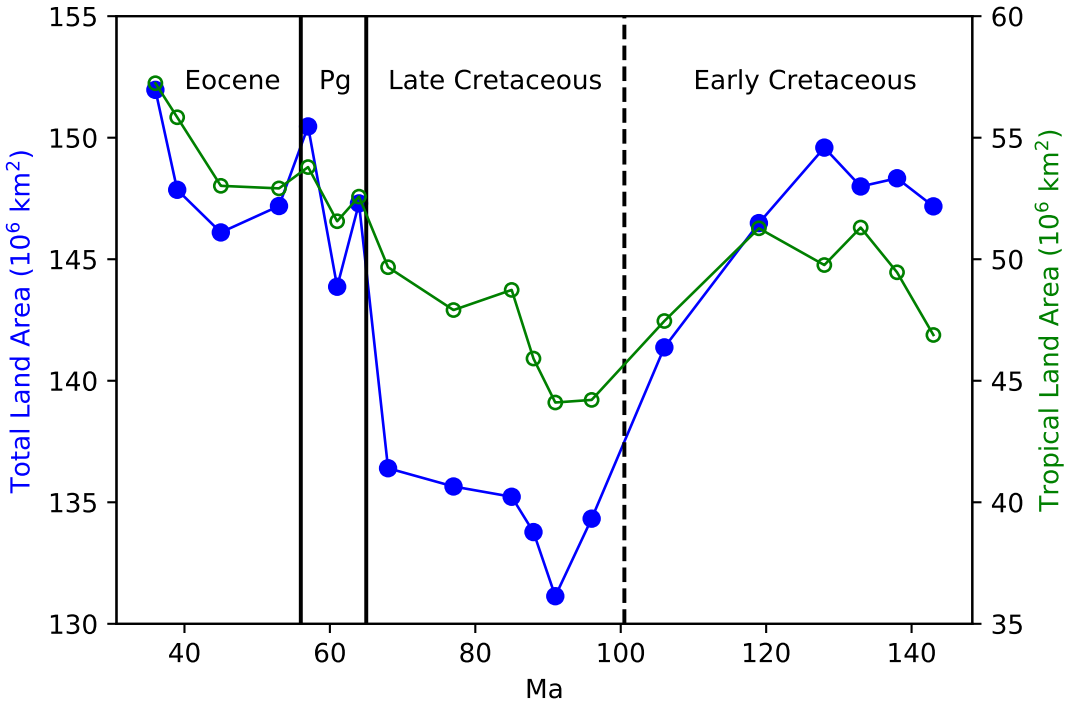

Figure 4.9: Changes in total land area (blue circles) and tropical (0-30° N/S) land area (open green circles) in HadCM3L simulations of the Cretaceous-Eocene period. Both total land and tropical land areas show a u-shaped pattern through the modelled period, with land areas decreasing towards the mid-late Cretaceous and increasing into the Cenozoic. Total land areas show a greater decrease than tropical land areas, indicating that much of the change in land area is occurring outside of the tropics.

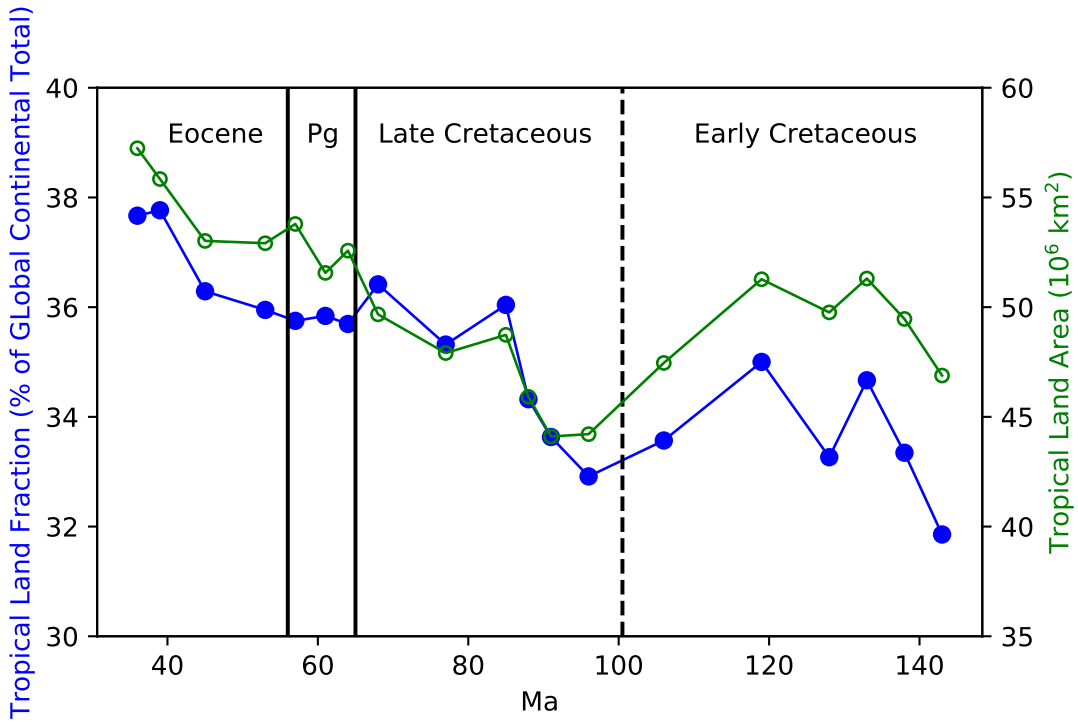

Figure 4.10: Tropical land area as a percentage of total global land area (blue circles) and tropical land areas (open green circles) from HadCM3L simulations of the Cretaceous-Eocene period. Tropical land fraction is variable during the early-mid Cretaceous, but shows an increasing trend into the Cenozoic, concurrent with an increase in total tropical land areas.

The palaeogeographic configuration through the modelled time period shows a pattern of decreasing global continental areas from the early Cretaceous to the mid Cretaceous, falling from 150 x 10^6 km^2 at 128 Ma to approximately 130 x 10^6 km^2 at 91 Ma (Figure 4.9). Global continental areas rise sharply towards the end of the Cretaceous and continue to increase to the end of the Eocene, exceeding 150 x 10^6 km^2 at 36 Ma. The continental area in the tropics (30°N – 30°S) show a similar trend, both in total area and as a fraction of the global continental area (Figure 4.10).

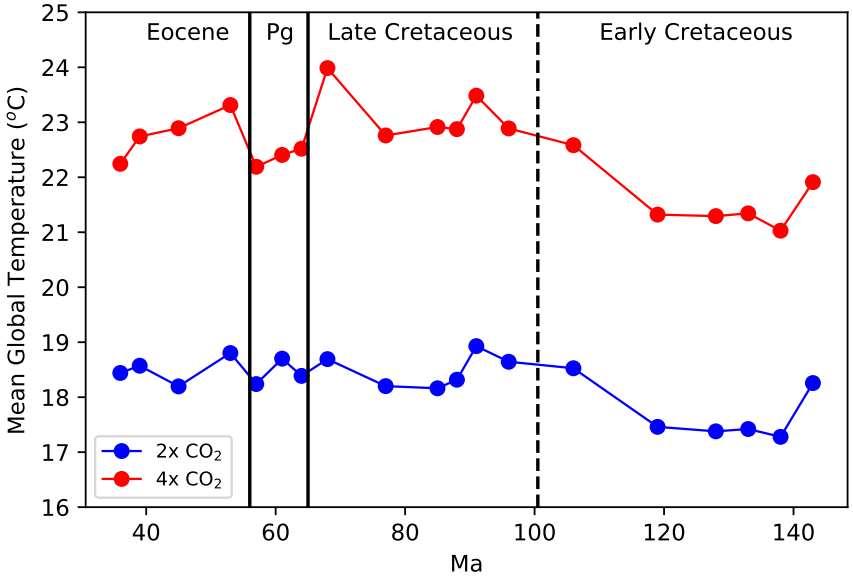

Figure 4.11: Global Mean annual temperatures from HadCM3L simulations of the Cretaceous-Eocene period at 2x and 4x PAL CO_2 (Farnsworth et al., In revisions). MAT values remain relatively stable during the modelled period, although there is a slight increase in MAT into the late-Cretaceous. MAT at 4x CO_2 displays greater variability than MAT at 2x CO_2.

Mean global temperatures across the 19 simulations are relatively constant, with only 2-3°C of variability through the Cretaceous-Eocene period (Figure 4.11). Mean global temperatures show greater variability at 1120 ppm relative to 560 ppm. Although variability is limited, modelled global temperatures increase through the early Cretaceous, peaking in the mid to late Cretaceous. The highest modelled global temperature is reached under the 1120 ppm simulation shortly before the K-Pg boundary, where high ocean area (reducing global albedo) and solar luminosity, combined with a switch in ocean circulation at high CO_2, result in increased climate sensitivity (Farnsworth et al., In revisions). Mean global temperatures show a gradual reduction into the Cenozoic.

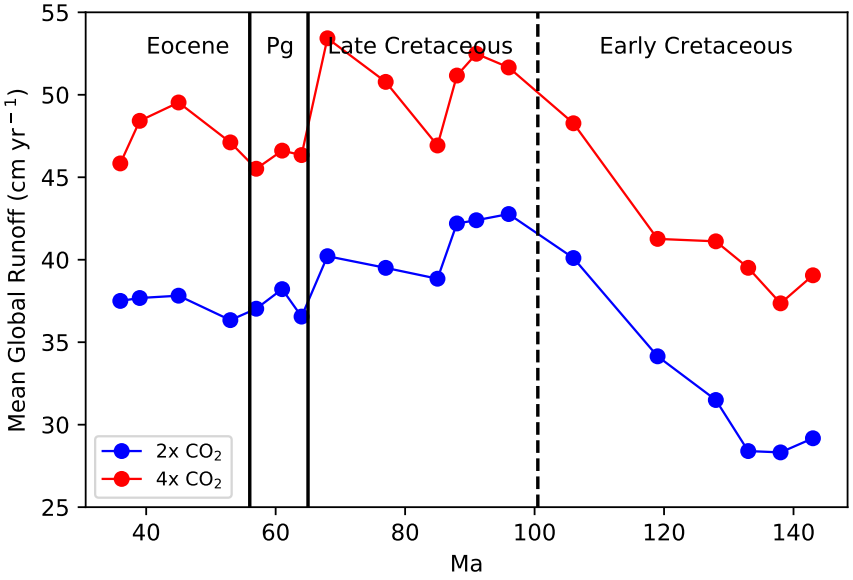

Figure 4.12: Global mean annual runoff from HadCM3L simulations of the Cretaceous-Eocene period at 4x and 2x PAL CO_2 (Farnsworth et al., In revisions). MAR increases significantly from the early-Cretaceous to the late-Cretaceous before falling into the Cenozoic. As with MAT, MAR at 4x CO_2 displays greater variability than at 2x CO_2.

Mean global runoff patterns exhibit more variability between simulations than the temperature record, with a pronounced aridity present in the early Cretaceous. The mid-Cretaceous sees a dramatic rise in mean global runoff, with values nearly doubling relative to the early-Cretaceous (Figure 4.12). Global runoff remains high throughout the rest of the Cretaceous followed by a slight reduction into the Cenozoic.

4.5.2. GEOCLIM Configuration

The HadCM3L input data were converted to GEOCLIM format using the methods detailed in section 4.2.5. and each GEOCLIM simulation was run for 1 Myr. The sensitivity study resulted in steady-state CO_2 concentrations under the modern degassing rate (6.8 x 10^{12} mol C yr^{-1}) which were somewhat lower than those indicated by proxy data for the early Eocene . The more spun-up 52 Ma Eocene HadCM3L simulation (Farnsworth et al., In revisions) produced steady-state CO_2 concentrations that were lower than those of the simulation used in the sensitivity study (486 ppm and 505 ppm, respectively). The more spun-up simulation displays higher climate sensitivity between 2x and 4x CO_2 concentrations than the sensitivity simulation, with similar 2x temperature and runoff but higher 4x temperature and runoff, and results in lower steady-state CO_2 concentrations. Thus, the degassing rate for the paleogeography simulations was increased to 1 x 10^{13} mol C yr^{-1}. A similar approach was taken in previous GEOCLIM studies (Lefebvre et al., 2013), and a value of 1 x 10^{13} mol C yr^{-1} is within the range of estimates (˜1.2 – 2 times

modern) for degassing rates during the Cretaceous-Eocene period (Van Der Meer et al., 2014).

4.6. Results - Palaeogeography Study

4.6.1. Global Trends

The GEOCLIM simulations of the 19 time slices resulted in a range of CO_2 concentrations, with the lowest value of ˜650 ppm at the end of the Eocene and the highest value of ˜1100 ppm during the early Cretaceous (Figure 4.13). Atmospheric CO_2 exceeds 1000 ppm during the early Cretaceous but declines significantly to ˜700 ppm by the mid-Cretaceous. There is a brief increase in CO_2 around 85 Ma to ˜900 ppm, followed by a gradual decrease into the Cenozoic and through to the end of the Eocene.

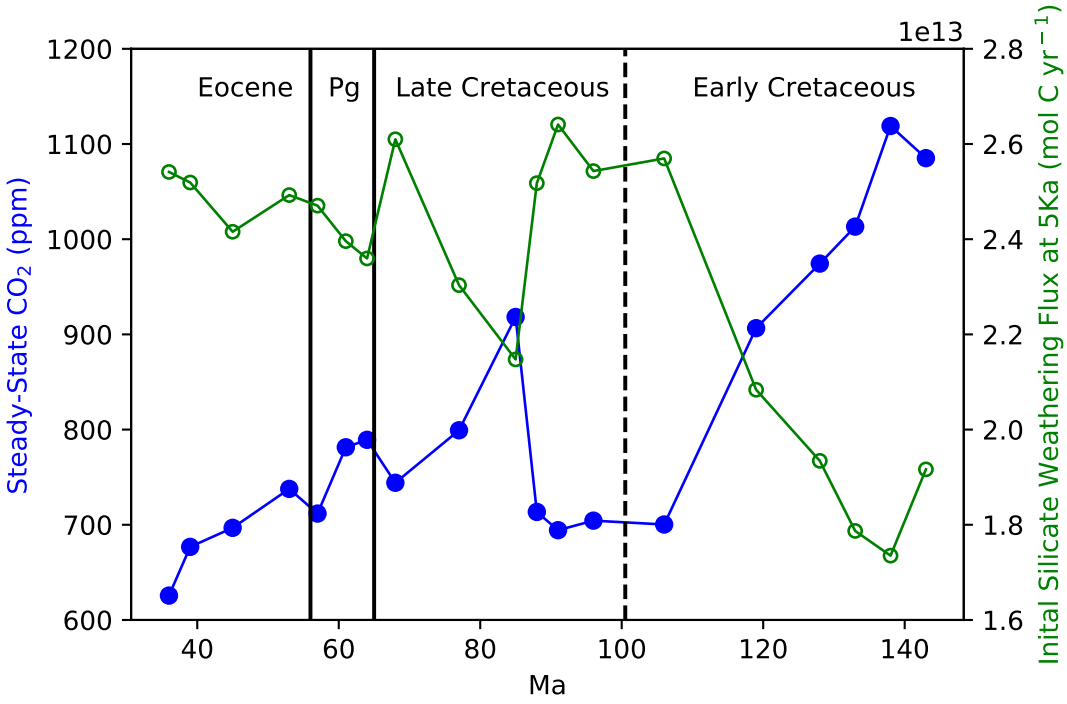

Figure 4.13: Modelled steady-state CO_2 and initial silicate weathering fluxes produced from GEOCLIM simulations during the Cretaceous-Eocene period. Steady-state CO_2 is high in the early-Cretaceous but falls sharply towards the mid-Cretaceous. A brief rise in CO_2 occurs in the late-Cretaceous, but otherwise CO_2 concentrations decrease into the Cenozoic. Steady-state CO_2 displays an inverse pattern relative to initial silicate weathering fluxes, with high steady-state CO_2 values occurring when silicate weathering fluxes are lower.

As expected, the initial global silicate weathering flux (at 5 kyr) is inversely related to steady-state CO_2 (Figure 4.13). The early Cretaceous is marked by low silicate weathering fluxes, although fluxes increase significantly towards the mid Cretaceous and peaks at approximately 91 Myr. A brief, but sharp decrease occurs until 85 Myr, followed by a similarly rapid recovery at the end

Cretaceous to a similar level of weathering seen at 91 Myr. Another brief decrease occurs into the Palaeocene, followed by a gradual rise through the Eocene.

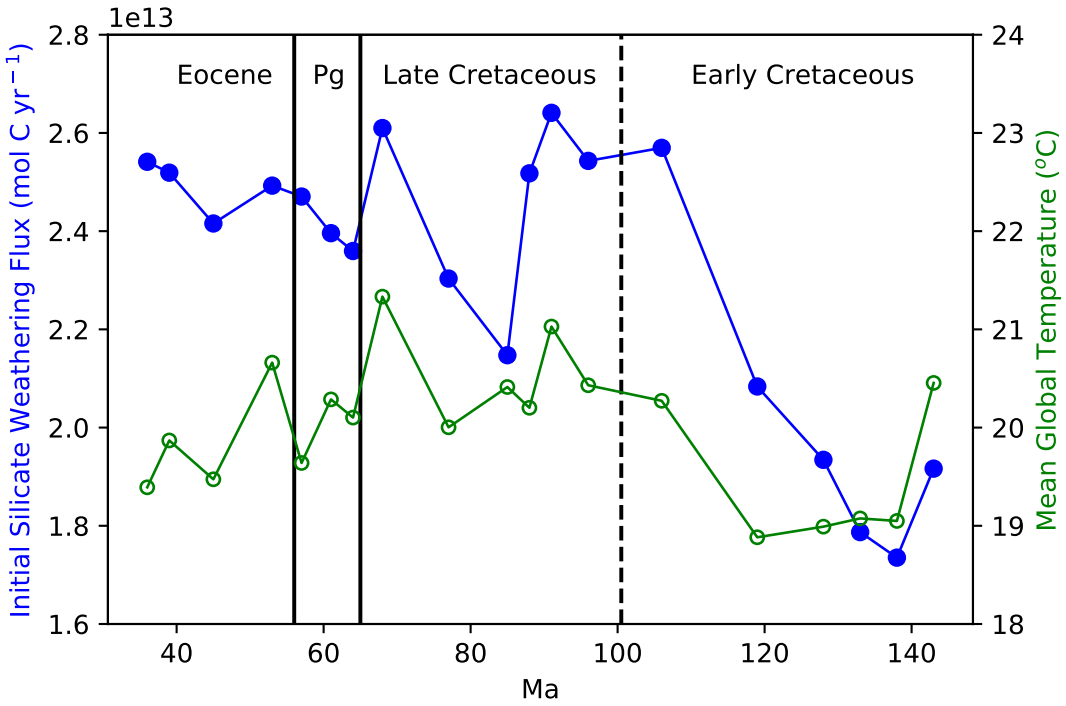

Figure 4.14: Modelled initial silicate weathering fluxes plotted against initial global mean annual temperatures during the Cretaceous-Eocene period. Silicate weathering fluxes show a superficially similar pattern to MAT, with some similarity between the two curves in the Cretaceous, however, the two curves show little similarity during the Cenozoic.

The modelled initial climate state (MAT, MAR) (at 5 kyr) for all time periods is determined to a large extent by the initial prescribed atmospheric CO_2 concentration of *2.85 PAL .This CO_2 concentration is intermediate between the 560 and 1120 ppm HadCM3L climate inputs (Figures 4.11-12 and 4.14-15). Initial global mean temperature varies little throughout the Cretaceous-Eocene period, although a period of warming occurs in the mid-late Cretaceous, followed by gradual cooling into the Cenozoic. Initial mean global runoff increases significantly into the mid-Cretaceous, followed by a brief decrease around 85 Ma, and then an increase again towards the end-Cretaceous. Runoff drops sharply at the start of the Palaeocene and remains mostly stable through the Eocene.

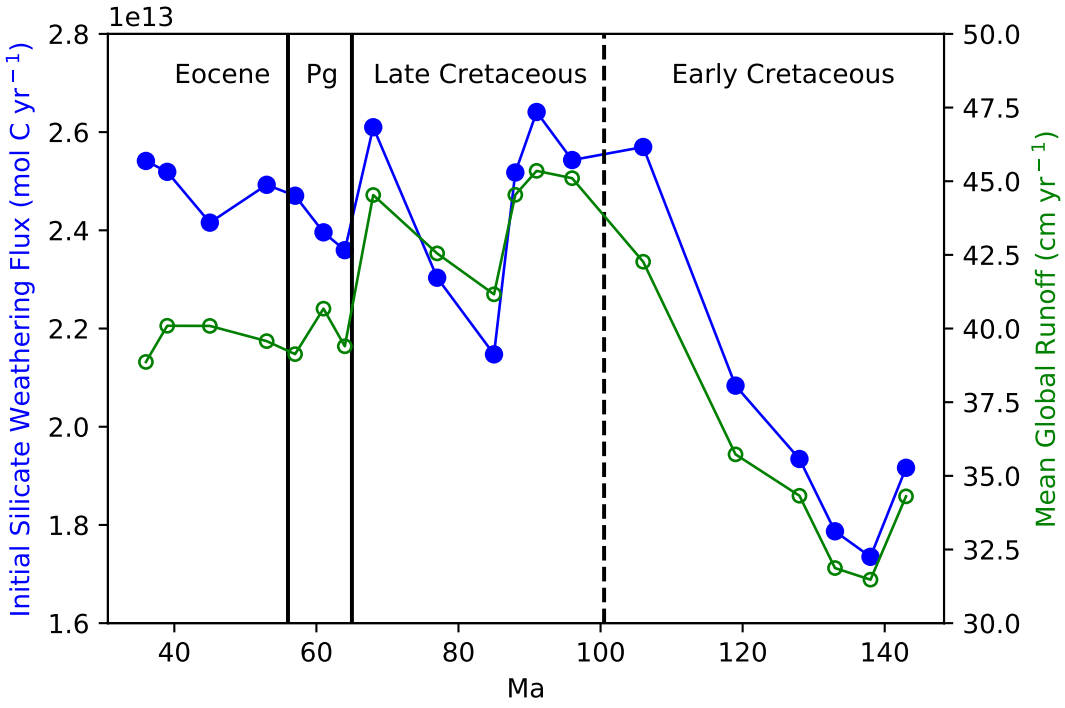

Figure 4.15: Modelled initial silicate weathering fluxes and initial continental mean annual runoff (referred to as mean annual runoff (MAR)) during the Cretaceous-Eocene period. Silicate weathering fluxes show a strong relationship with MAR during the modelled period with higher weathering fluxes occurring with higher MAR, although in the late-Eocene silicate weathering fluxes increase while MAR falls.

4.6.2. Regional Trends

Initial regional silicate weathering fluxes vary significantly during the Cretaceous-Eocene period (Figures 4.16 and 4.17). During the earliest-Cretaceous, intense weathering (i.e., high weatherability) is confined mainly to the northern coasts of Gondwana and the southern coast of Laurasia, with generally low weathering fluxes within the continental interiors. Weathering fluxes increase slightly in the tropics and the southern mid-latitudes over the next 25 Myr. Weathering fluxes at the equator increase drastically at 106 Ma over north Africa and the Amazon as the southern Atlantic begins to open. Equatorial weathering fluxes remain high until 91 Ma, after which time fluxes begin to fall. At the end-Cretaceous, an area of high weathering fluxes extends northwards from the equator (Figures 4.16 and 4.17). Into the Eocene, weathering fluxes peak at the equator during the mid-Cretaceous, but rather are high over in low-latitudes zones, such as India, North Africa, and South America (Figures 4.16 and 4.17). High weathering fluxes also occur on the Atlantic Coast of north America (Figure 4.15). The distribution of weathering changes little during the Eocene but increases in magnitude towards the end of the Eocene.

Temperature distribution (at 5 kyr) does not change significantly during the Cretaceous-Eocene period, with the highest temperature consistently found over south America, Africa, and south-

east Asia (Figure 4.18). India becomes progressively warmer as it moves northwards towards lower-latitudes. There are occasional "cold-spots" likely associated with small areas of snow near the poles during the Cretaceous, but such areas do not persist for long (<10 Myr).

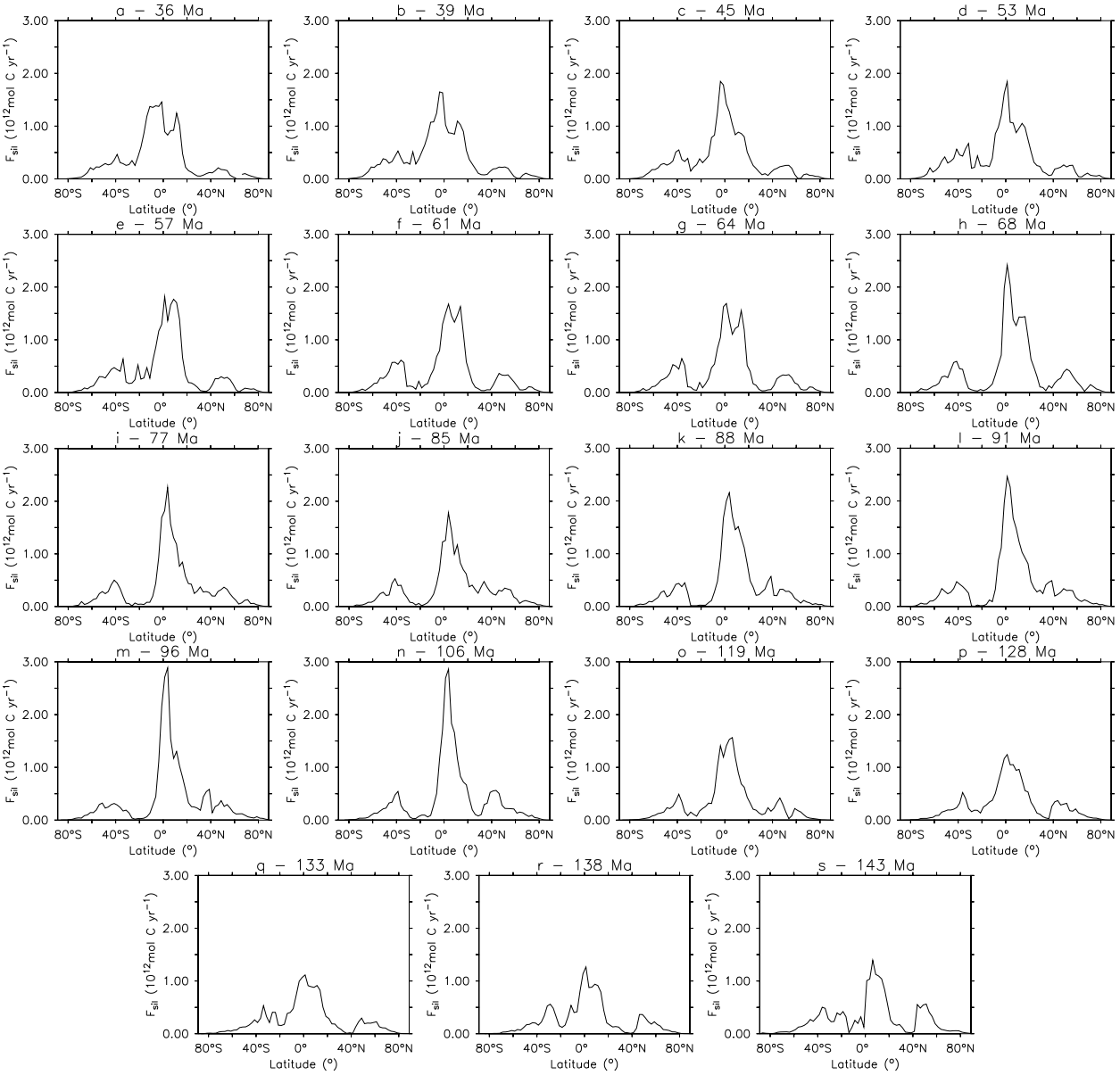

Figure 4.16: Modelled zonal sum weathering fluxes (F_{sil}) from the earliest-Cretaceous (s) to the latest-Eocene (A). Weathering fluxes are limited in the early-Cretaceous (s-p) but equatorial weathering fluxes increase dramatically into the mid-Cretaceous (o-l). Into the late-Cretaceous and the Cenozoic, equatorial weathering fluxes weaken, but high weathering fluxes are present over a wider area in the tropics (h-a).

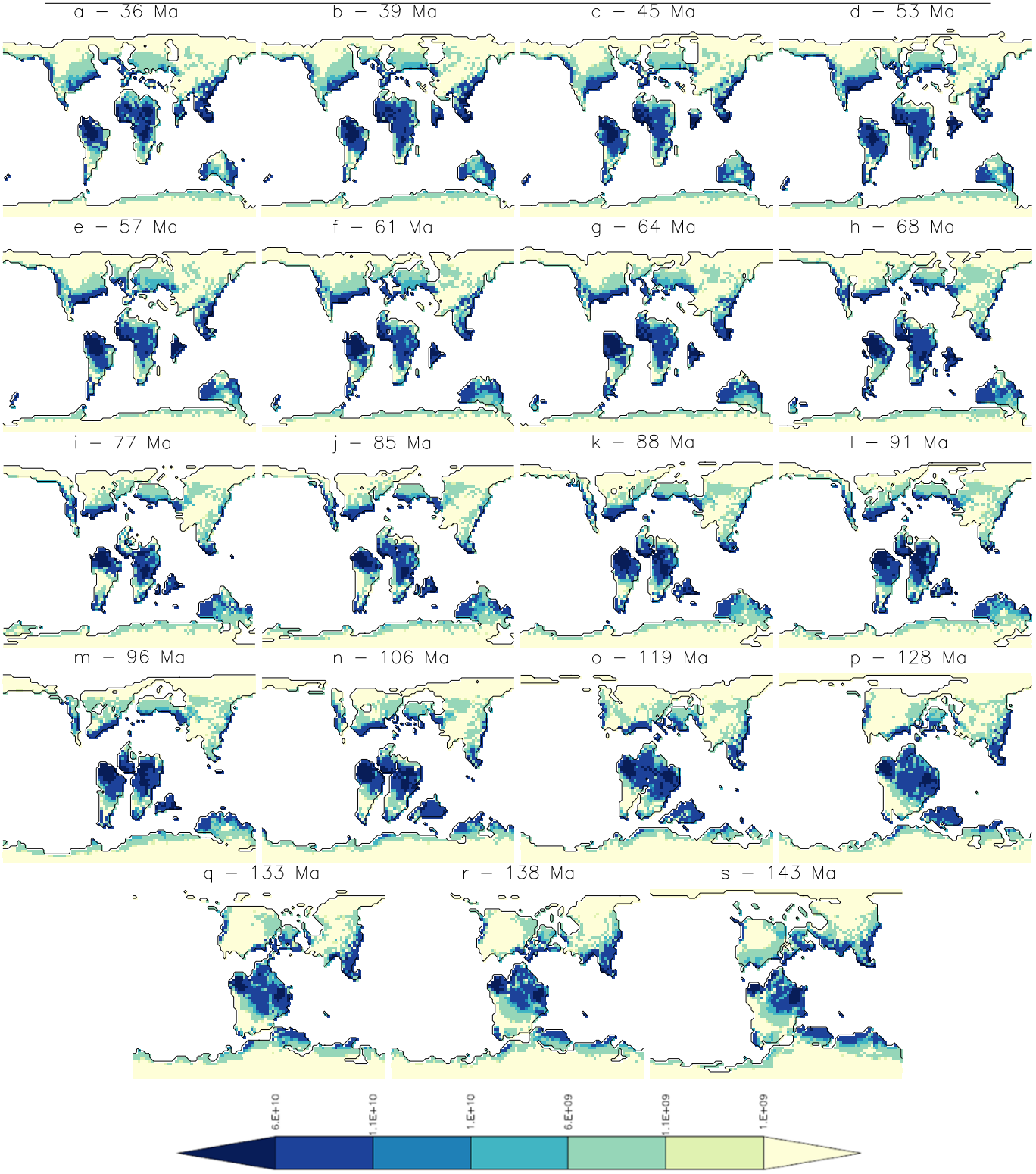

Figure 4.17: Regional weathering flux (mol C yr^{-1}) maps from the earliest-Cretaceous (s) to the latest-Eocene (A). During the Cretaceous-Eocene period, weathering fluxes increase in continental interiors, particularly North America. Intense weathering remains present near the equator (especially South America and Africa) throughout the model period.

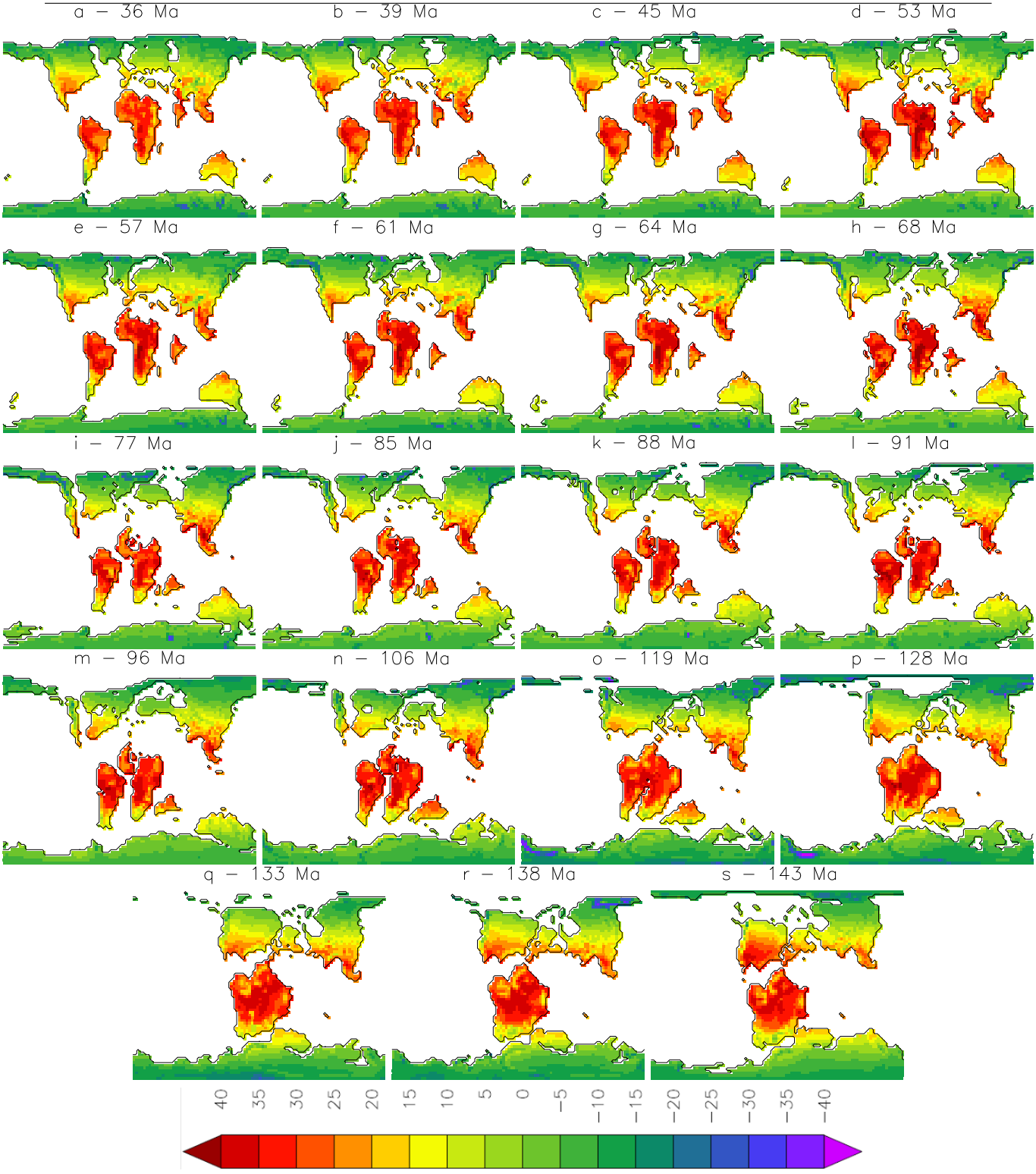

Figure 4.18: Regional mean annual temperature (°C) maps from the earliest-Cretaceous (s) to the latest-Eocene (A). During the Cretaceous-Eocene, temperatures are globally high, with few areas of significant cold (such as Antarctica in panels p and o). Equatorial areas such as South America and Africa remain hot during through the entire period, cooling slightly in the Cenozoic (panels g-a). The interior of North America is hot during the early-Cretaceous, but cools towards the mid-Cretaceous as sea levels rise and its land area diminishes.

In contrast to temperature, the distribution of initial runoff changes significantly during the Cretaceous-Eocene period (Figures 4.19 and 4.20). During the early Cretaceous, large areas of North America, South America, Asia, and Antarctica have low or zero runoff. There are some areas of high runoff, such as the northern coast of Gondwana, along with parts of the western Amazon and east Africa. Into the mid-late Cretaceous, North America and Antarctica become much more humid while Asia becomes more arid. The Amazon remains persistently humid, while the Atlantic coast of North America has high runoff . The west coast of North America has especially high runoff , with zonal means indicating that runoff here is greater than at the equator, although runoff falls towards the late Cretaceous. Into the Cenozoic, areas such as India and western Australia have a significant increase in runoff. Towards the end of the Eocene, areas such as North America and Asia become more arid, while runoff in the southern mid-latitudes increases slightly. Much of the world however becomes more arid, reflecting the global drop in runoff at the end of the Eocene.

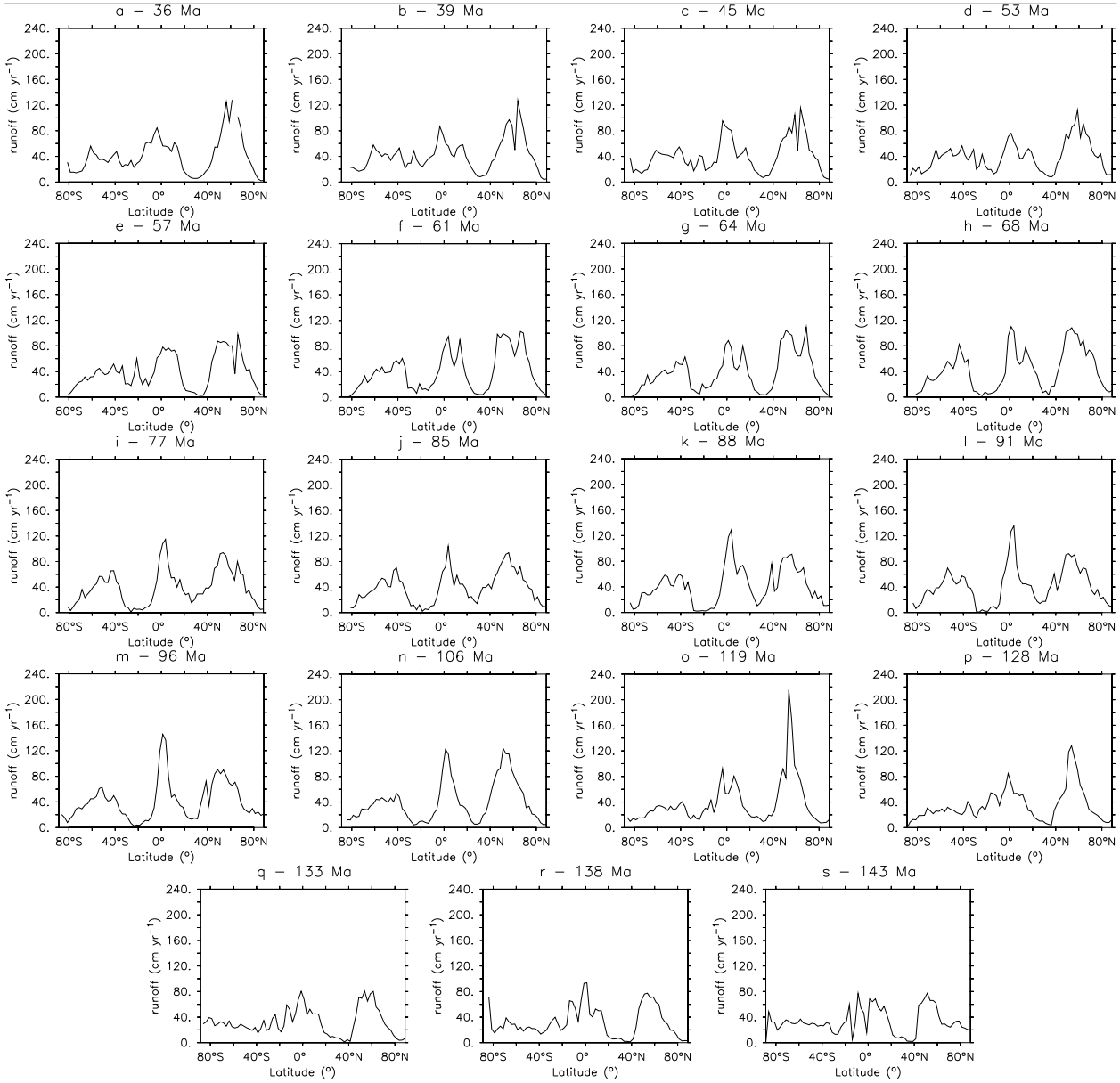

Figure 4.19: Modelled zonal mean runoff (cm yr^{-1}) from the earliest-Cretaceous (s) to the latest-Eocene (A). Zonal runoff means are low in the early-Cretaceous (s-p), but increase significantly into the mid-Cretaceous, especially in the northern mid-latitudes (o-k). Zonal mean runoff falls slightly into the late-Cretaceous, but there is an intensification in equatorial mean zonal runoff (j-h). In the Cenozoic, zonal runoff intensifies again (g-e) but begins to weaken again during the Eocene (d-a).

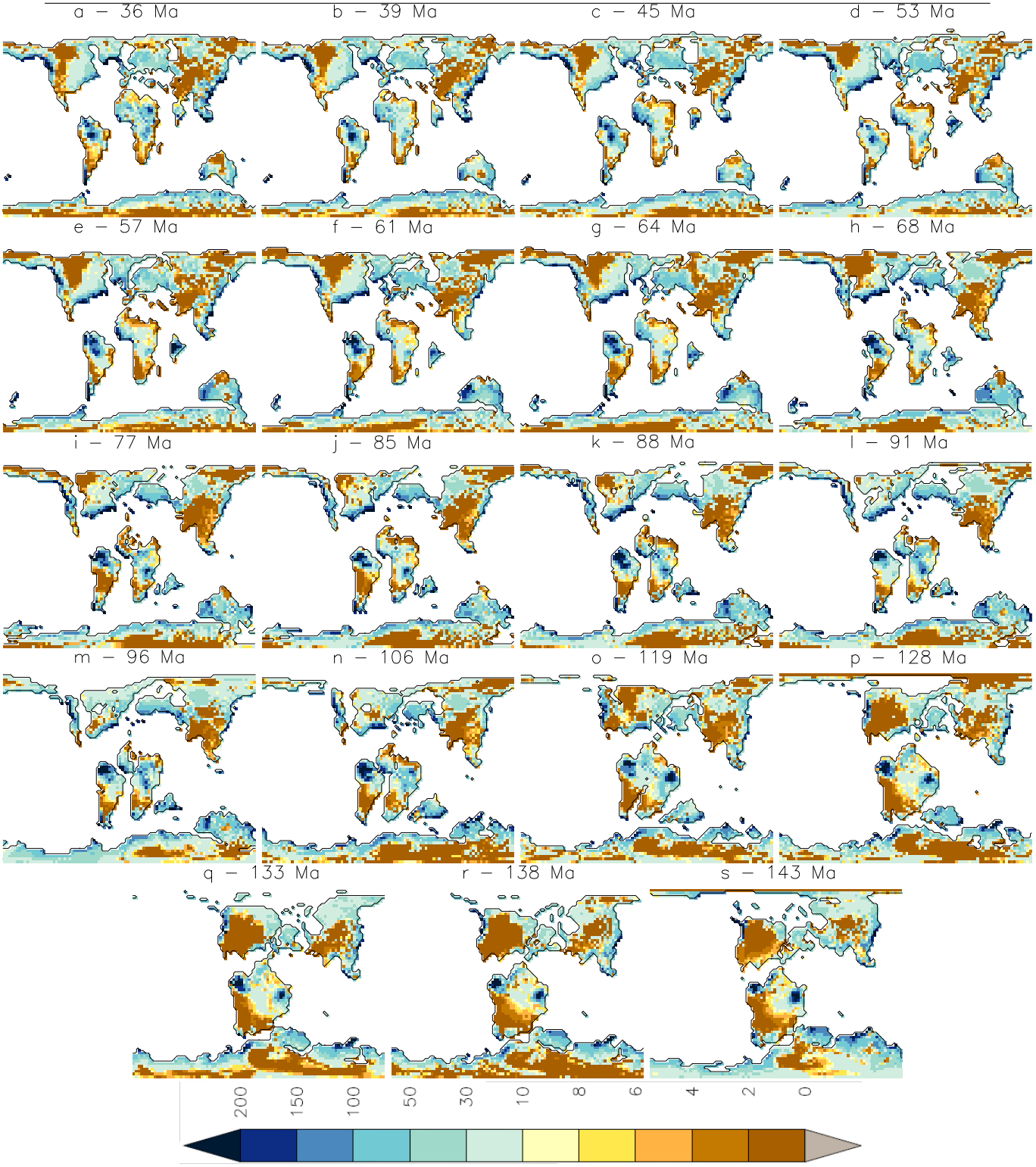

Figure 4.20: Regional mean annual runoff (cm yr^{-1} maps from the earliest-Cretaceous (s) to the latest-Eocene (A). An arid climate prevails during the early-Cretaceous (s-o), particularly in the continental interior of North America. Runoff increases significantly from the mid-Cretaceous, with very high runoff rates present in Amazonia (m-k). High runoff totals are present in India during the latest-Cretaceous and the Palaeocene as it crosses the equator (h-e). The world becomes slightly more arid through the Eocene (d-a).

4.7. Discussion

4.7.1. Effect of Palaeogeographical Change on Cretaceous-Eocene Weathering Rates

Global and Regional Correlations Between Climate Variables and Weathering Fluxes

Global initial silicate weathering fluxes (as a proxy for weatherability) show a very strong inverse correlation (r = -0.96) with steady-state CO_2 concentrations during the modelled period (Figure 4.21). Such a result matches with those seen in the sensitivity study, where silicate weathering fluxes were the strongest control on steady-state CO_2 concentrations. In turn, global silicate fluxes show a strong positive correlation with both global mean runoff and total global runoff (r = 0.88 and r = 0.89, respectively; Figure 4.22), once again reflecting the results of the sensitivity study. Mean global temperatures are more weakly correlated with silicate weathering fluxes and steady-state CO_2 concentrations (r = 0.61 and -0.38, respectively; Figure 4.23), however warmer climates in the modelled period typically have higher runoff rates (Figures 4.11 and 4.12). Such a correlation indicates that warmer initial climates likely have higher weathering fluxes by increasing runoff rates, rather than higher temperatures directly increasing weathering fluxes.

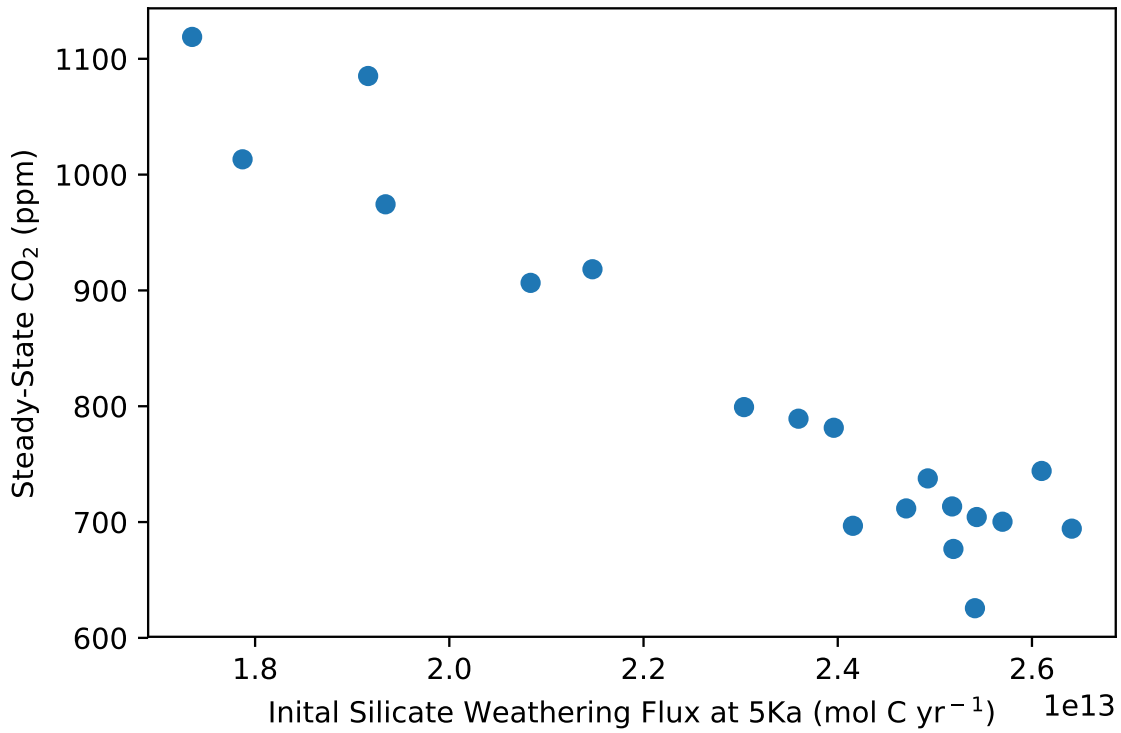

Figure 4.21: Initial silicate weathering fluxes plotted against steady-state CO_2 concentrations during the modelled period. Steady-state CO_2 displays a strong negative correlation (r = -0.96, p = < 0.01) with initial silicate weathering fluxes.

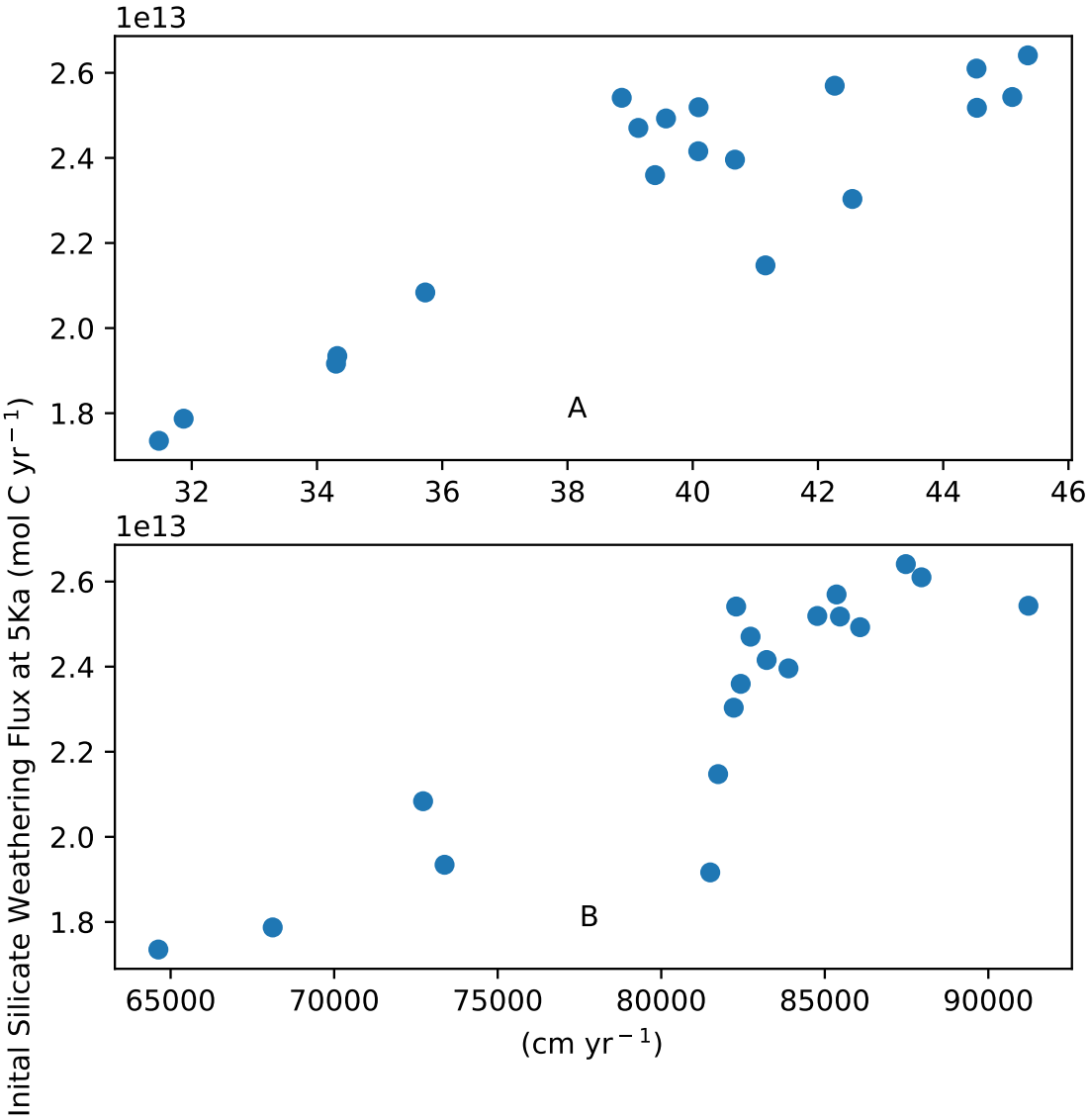

Figure 4.22: Initial silicate weathering fluxes during the modelled period plotted against (A) global mean annual runoff and (B) global total annual runoff. Both runoff variables display strong positive correlations with silicate weathering fluxes (r = 0.88 and 0.89, respectively, and p values = < 0.01).

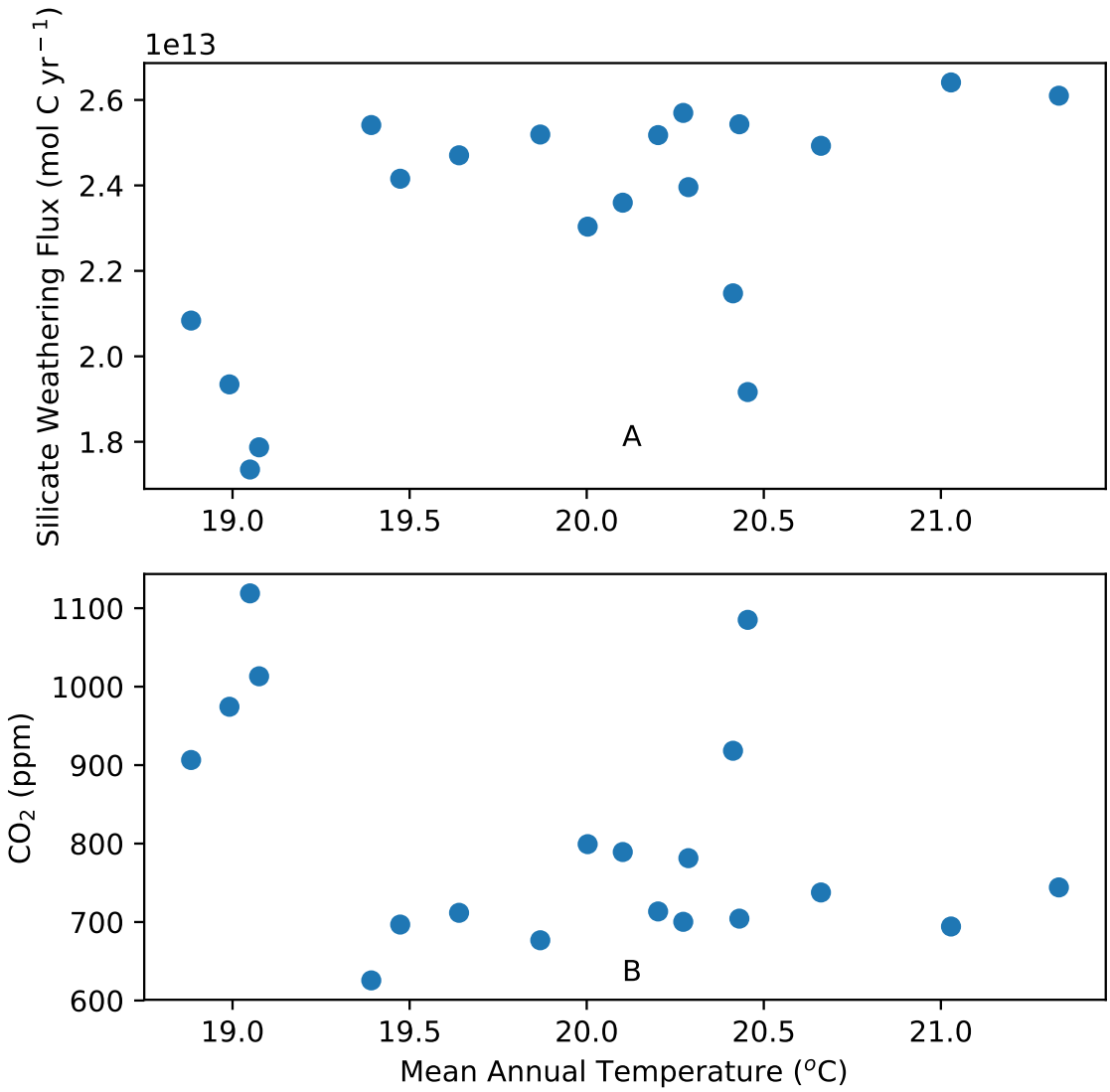

Figure 4.23: Global mean annual temperatures plotted against (A) initial silicate weathering fluxes and (B) steady-state CO_2 concentrations during the modelled period. Both variables show weaker correlations with MAT than MAR (r = 0.61 and -0.38, and p values = $<$ 0.01 and 0.10, respectively).

To confirm the strong relationship between silicate weathering fluxes and runoff, several simulations from the modelled time-period were re-run using runoff inputs from a different time period (Table 4.3.). The selected simulations were from periods with significant changes in steady-state CO_2 concentrations between simulations (79, 85, and 88 Ma (I, J, and K) and 106-119 Ma (N and O)) (Figures 4.13 and 4.20). Runoff inputs were interpolated onto different palaegeographies using methods described in Section 4.2.5. Runoff inputs were "swapped" between consecutive simulations (i.e., 85 Ma to 88 Ma) to reduce the impact of palaeogeographical changes and to minimise errors from interpolated runoff data. These "swapped" simulations indicate that the

resulting steady-state CO_2 is predominantly determined by the runoff input used, rather than temperature or palaeogeographical configuration (Table 4.3).

Table 4.3: GEOCLIM Simulations With Exchanged Runoff Inputs

Original Simulation	**CO_2 (ppm) (1 Myr)**	**Palaeogeography Input**	**Runoff Input**	**CO_2 (ppm) (1 Myr)**
77 Ma	799	77 Ma	85 Ma	907
85 Ma	918	85 Ma	77 Ma	788
			88 Ma[a]	699
88 Ma	713	88 Ma	85 Ma	870
106 Ma	700	106 Ma	119 Ma	808
119 Ma	907	119 Ma	106 Ma	567

[a] Uses palaeogeography inputs from 85 Ma simulation.

While global weathering fluxes will be important for determining steady-state CO_2, field data of silicate weathering shows that weathering is highly variable from site to site (e.g., Dessert et al., 2003; Oliva et al., 2003; West et al., 2005; Orlando et al., 2016, Chapter 2). Furthermore, the sensitivity study shows that weathering fluxes in GEOCLIM are highly sensitive to even small changes in climate conditions (Table 4.2). Thus, it may be more pertinent to examine the regional relationships between climate conditions and weathering fluxes.

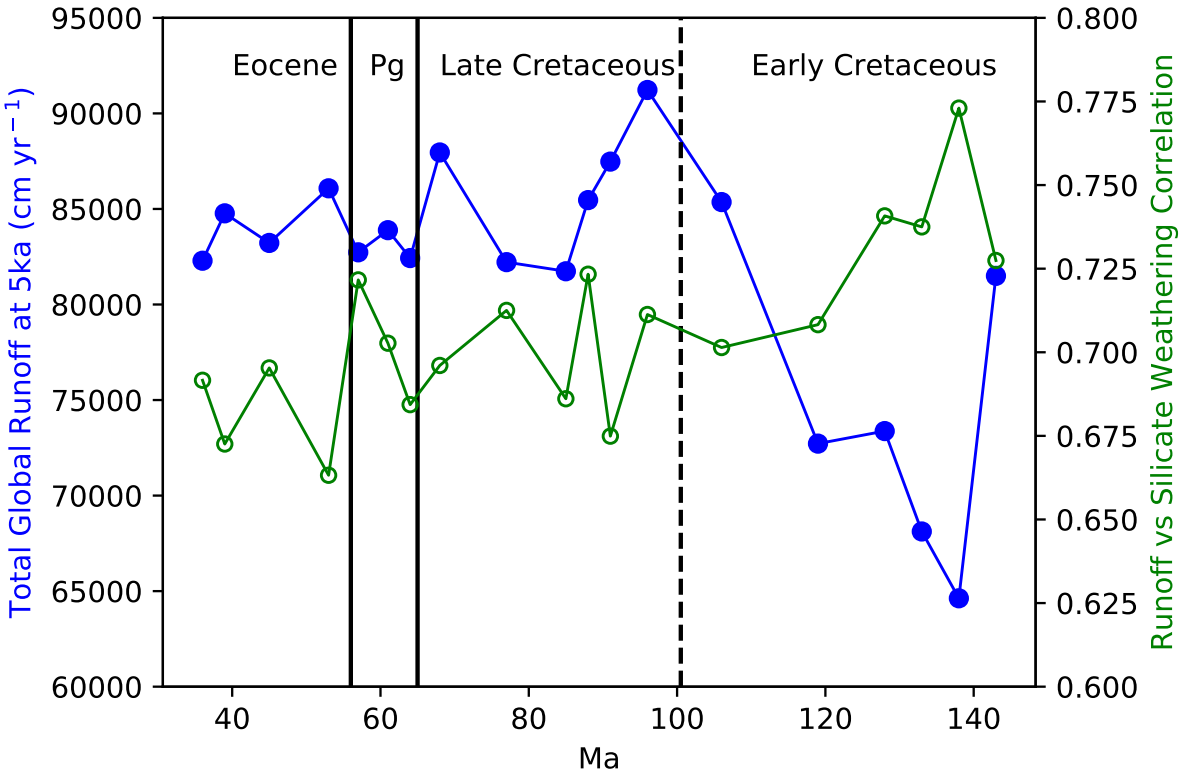

Figure 4.24: Total global runoff plotted against pearson correlation values between regional runoff and regional initial silicate weathering fluxes during the modelled period. Correlation values show a generally inverse pattern to total global runoff, with the strongest correlations occurring when total global runoff is lowest, which may indicate that silicate weathering fluxes are more sensitive to changes in runoff when the global climate is more arid.

Correlations of runoff and weathering fluxes between each cell of each simulation show that the strength of the correlation varies through the modelled period, ranging from r = 0.67-0.77 (Figure 4.24). These correlations are weaker than those at the global level, which may indicate varying weathering flux sensitivity to runoff at the regional scale relative to the global scale. The strongest correlations are found during the early-Cretaceous where global runoff rates are relatively low, while the correlations generally become slightly weaker into the Cenozoic when runoff is generally higher.

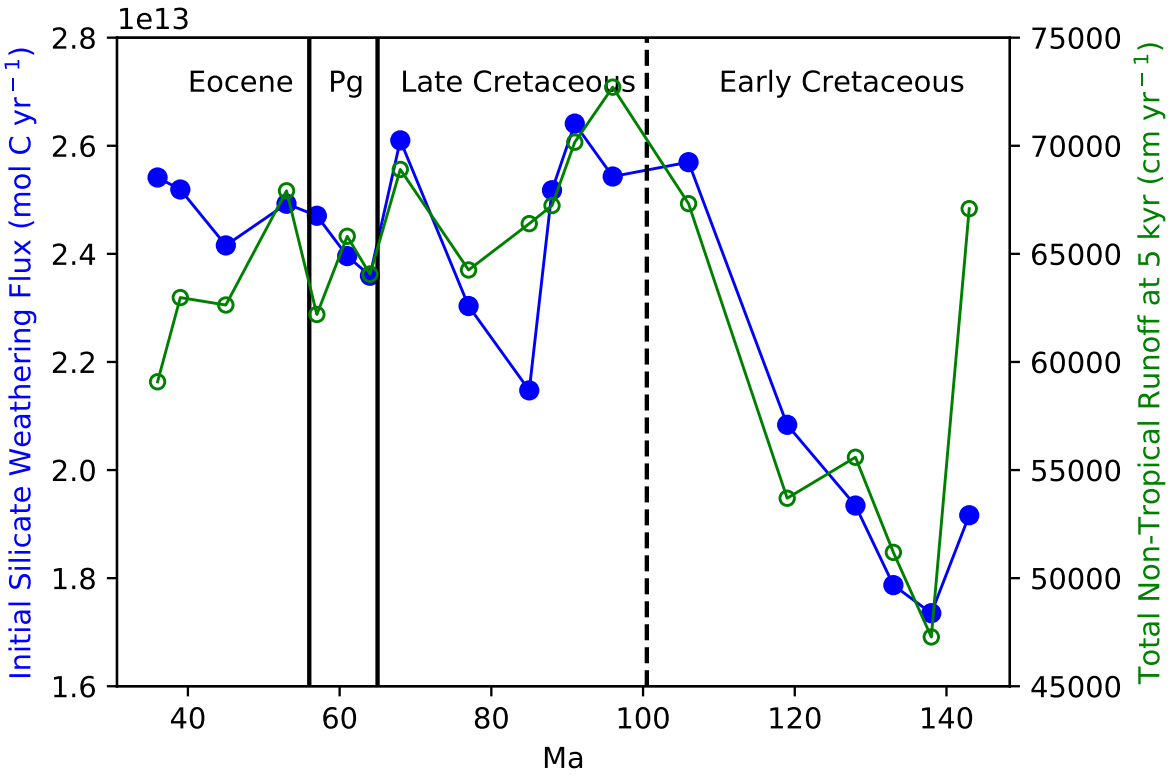

Figure 4.25: Initial silicate weathering fluxes plotted against total non-tropical runoff (>30°C N/S) during the modelled period. Initial silicate weathering fluxes show a very similar pattern to total non-tropical runoff during the early-Cretaceous, but an inverse pattern during the Cenozoic. As such, during the early-Cretaceous, increase weathering fluxes may have been driven by increasing runoff in the mid-latitudes.

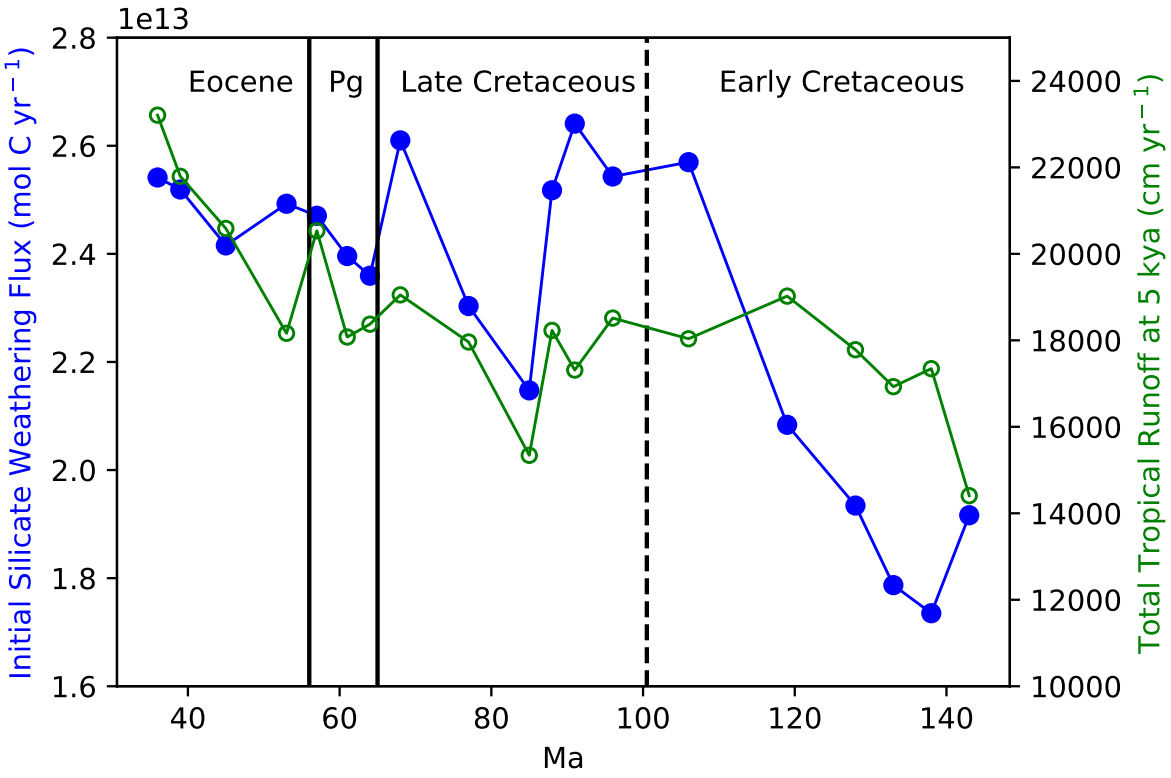

Figure 4.26: Initial silicate weathering fluxes plotted against total tropical runoff (0-30° N/S) during the modelled period. Silicate weathering fluxes and total tropical runoff display an inverse of the pattern seen between weathering fluxes and non-tropical runoff, with changes in tropical runoff appearing to have little impact on silicate weathering flues during the Cretaceous (with the exception of a brief period in the late-Cretaceous), while an increase in weathering fluxes during the Eocene coincides with a sharp rise in tropical runoff.

During the Eocene, both mean and total global initial runoff falls but silicate weathering fluxes rise, an inverse of the pattern seen during the Cretaceous where initial runoff rates and initial weathering fluxes show identical patterns (Figures 4.13, 15, 25 and 26). During the early-Cretaceous, silicate weathering fluxes are strongly controlled by non-tropical runoff (>30°N/S), showing an almost identical pattern until the mid-Cretaceous (Figure 4.25). This pattern weakens somewhat around 86 Ma, but strengthens by the end of the Cretaceous. Into the Cenozoic, the pattern weakens again and silicate weathering fluxes become anti-phased to non-tropical runoff. In contrast, silicate weathering fluxes in the Eocene seem to be more strongly controlled by runoff rates in the tropics (Figure 4.26). Similarly, tropical runoff changes in the Cretaceous does not appear to have a significant impact on silicate weathering fluxes, with the exception of a brief period during the late-Cretaceous (86 Ma). Correlations reflect the shift seen in the data, with r values of total non-tropical runoff and tropical runoff with silicate weathering fluxes during the Cenozoic being -0.41 and 0.66, respectively, although these values do not meet the 95% confidence level. The inverse of this relationship is seen during the Cretaceous, with a much stronger correlation with non-tropical runoff relative to tropical runoff (r = 0.93 and 0.38, respectively), although only the

non-tropical runoff correlation exceeds the 95% confidence level. Although confidence is low in these correlations, likely due to the small number of samples (n = 6) during the Cenozoic period, there does seem to be a noticeable weakening of the influence of non-tropical runoff on weathering fluxes from the Cretaceous to the Cenozoic.

The shift from non-tropical to tropical runoff controlled weathering appears to represent a regime change in the long-term climate pattern seen during the modelled period. Theoretically, a continental configuration with a greater land area in the low-latitudes, where precipitation is generally highest, would favour lower global CO_2 concentrations by increasing silicate weathering rates (Gibbs and Kump, 1994; Otto-Bliesner, 1995; Goddéris et al., 2014). However, changes in continental positioning will alter ocean circulation and evaporation patterns, which would then alter climate patterns, especially runoff (Barron et al., 1989; Lunt et al., 2012). Furthermore, runoff patterns will also be affected by whether continents are in a dispersed or converged (i.e., supercontinental) configuration.

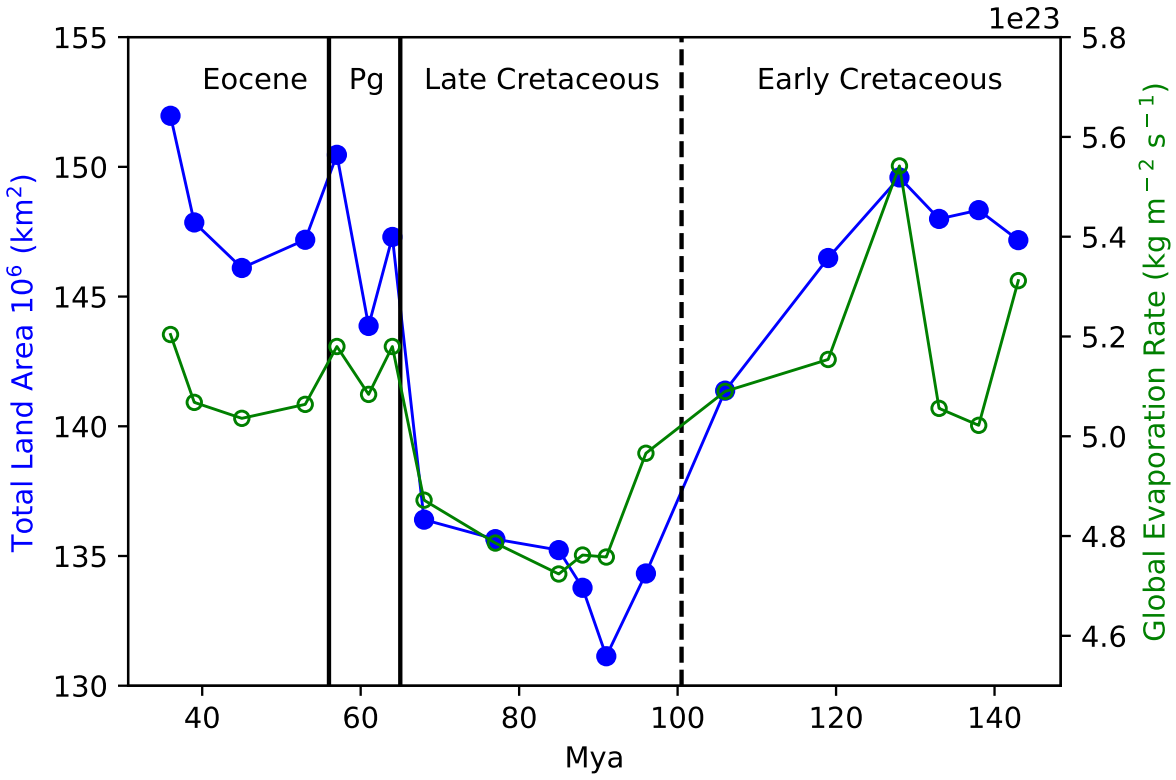

Figure 4.27: Total land area plotted against mean global evaporation rates at 4x CO_2 during the modelled period. Mean global evaporation rates increase when land area decreases, suggesting that a reduction in land area increases evaporation rates by increasing ocean surface areas.

As seen in the HadCM3L simulations of the early-Cretaceous, runoff rates are low in the continental interiors of Gondwana and Laurasia, but runoff rates in these regions increased as Pangaea broke up (Figure 4.20), suggesting that the runoff increase is due to continental positioning

altering climate processes, rather than the continents moving into more humid zones. Similarly, global land areas decreased as Pangaea broke up and sea levels rose, resulting in a greater ocean area which should produce greater evaporation rates. Indeed, this appears to be the case during the Cretaceous, where the highest mean global evaporation rates occur during a fall in total land area associated with rising sea levels (Figure 4.27). Similarly, mean global evaporation correlates positively with silicate weathering fluxes (r = 0.81, p = $<$ 0.01), which would further indicate that the changes in silicate weathering are being driven by climate changes rather than the continents moving into a position more favourable to weathering. However, in the Cenozoic, silicate weathering fluxes appear to become anti-phased to changes in global evaporation (Figure 4.28), providing further evidence that controls on silicate weathering undergo a shift into the Cenozoic.

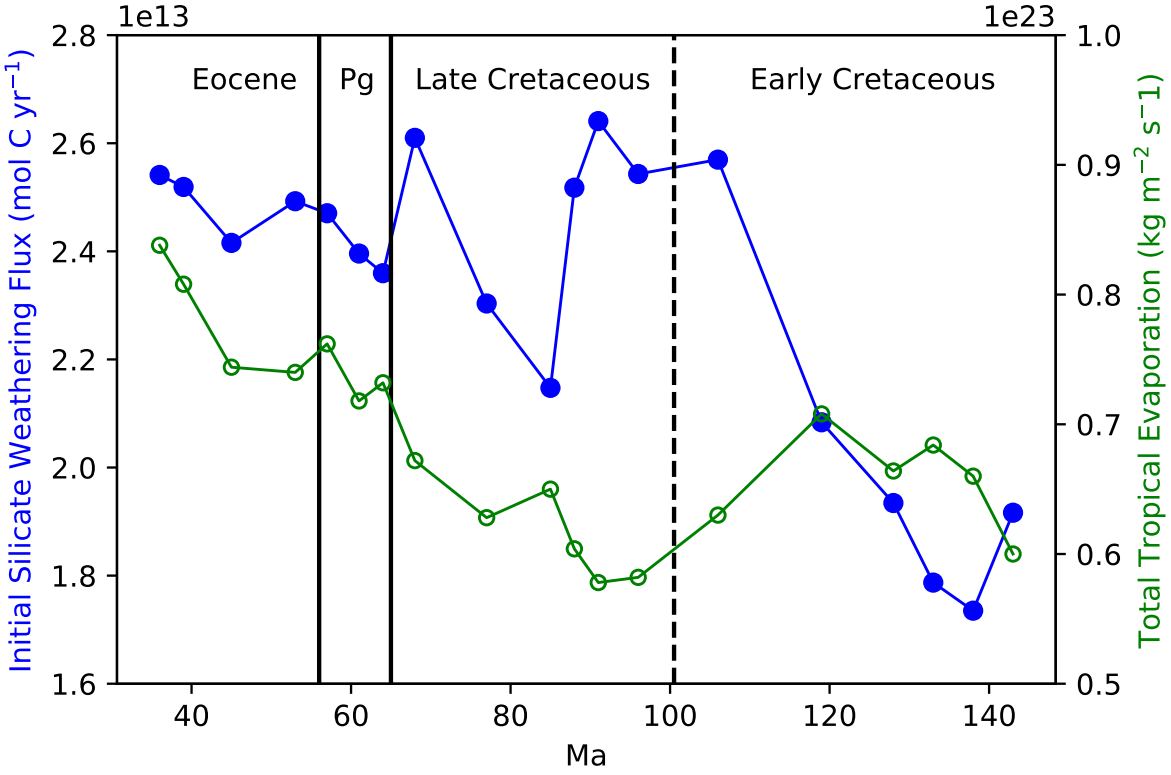

Figure 4.28: Initial silicate weathering fluxes plotted against mean global evaporation rates at 4x CO_2 during the modelled period. Mean global evaporation rates display a similar pattern to silicate weathering fluxes. As silicate weathering is strongly correlated to runoff rates, it is likely that the increase in runoff rates seen during the early-Cretaceous was driven by enhanced evaporation. A notable exception occurs in the late-Eocene, where evaporation rates fall but silicate weathering increases suggesting a different process is at work during this time.

The shift in weathering controls seen in the GEOCLIM simulations may be the result of a change in the effects of palaeogeography on weathering fluxes. During the Cretaceous, the models suggest that increased weathering occurred as a result of the climate becoming more humid due

to the break-up of Pangaea. The break-up of Pangaea promoted higher weathering fluxes through evaporation by increased ocean area and more favourable moisture transport to the continental interiors. In contrast, during the Cenozoic both total land areas and tropical land areas increased (Figure 4.9). During the same period, modelled total global runoff falls, but tropical runoff increases, resulting in both a greater weatherable area and a more intense weathering environment in the tropics. As such, the shift in weathering controls in the Cenozoic from non-tropical to tropical runoff may be the result of the continents moving into more favourable positions, while during the Cretaceous changes in weathering fluxes were largely caused by climate changes induced by the break-up of Pangaea which increased runoff in the previously arid continental interiors.

4.7.2. Comparison to Previous GEOCLIM Palaeogeography Study

The model outputs presented in this study demonstrate that the long-term climate (under constant degassing rates) is strongly controlled by silicate weathering fluxes, which in turn are predominately controlled by runoff rates. Palaeogeographical changes are likely to have had significant impacts on both the intensity and distribution of runoff. These findings are in line with those of Goddéris et al. (2014) , which found a strong direct palaeogeographical influence on runoff, and thus weathering rates and long-term atmospheric CO_2. Both Goddéris et al. (2014) and this study found a general decreasing trend in atmospheric CO_2 from the Cretaceous to the early Cenozoic, although this study has a higher temporal resolution during that period (19 simulations vs 5). Goddéris et al. (2014) noted a number of potential climate impacts from palaeogeographical changes, based on their GEOCLIM study with FOAM inputs.

Goddéris et al. (2014) found that a converged, or supercontinental, arrangement inhibited weathering fluxes leading to high CO_2 concentrations. In contrast, a dispersed continental configuration favours higher weathering fluxes. While the time period in this study does not cover the formation of Pangaea, during the earliest Cretaceous the continents were still in a converged configuration (Figures 4.17,4.18, and 4.20) and coincided with the highest CO_2 concentrations and lowest weathering fluxes in the modelled period. Goddéris et al. (2014) showed significant rises and falls in CO_2 (up to 20x PAL) within ˜10 Myr occurring during the formation and subsequent break-up of Panagea associated with changes in weathering fluxes. Similarly, this study indicates rapid changes in CO_2 (200-300 ppm within 5 Myr) as Gondwana and Laurasia break apart, indicating the potential for geologically rapid CO_2 changes as a result of palaeogeographical changes.

Goddéris et al. (2014) also noted the potential climate impact of high weathering rates on small continental landmasses in tropical areas. During the Rhaetian period of the Triassic, south China crossed the tropics and contributed 17% of the global CO_2 drawdown despite a small land area relative to Pangaea (Goddéris et al., 2014). This disproportionate CO_2 drawdown may be the

result of a generally arid climate during the Triassic, as a similar result is not seen in this study (Figure 4.13), despite the passage of India across the tropics during the Cretaceous-Eocene. While weathering rates on the Indian subcontinent increase significantly as it crosses the tropics, its passage does not appear to be associated with a significant drop in atmospheric CO_2 (Figure 4.13). Global weathering rates do rise however as India crosses the tropics, but this rise occurs just after a global drop in runoff rates and weathering fluxes. Thus, while the passage of India through the tropics raises global weathering fluxes significantly, the effect of this rise is counteracted by the fall in global weathering fluxes as a result of increasing aridity. As such, the influence of small continental landmasses on long-term CO_2 concentrations appears to be variable and largely dependent on the prevailing global climate state, with CO_2 concentrations more sensitive to change under a more arid global climate. In this study, a stronger influence on long-term weathering rates occurs as the result of a continental configuration that favours either increased evaporation from the oceans and moisture transport to continental interiors or a general increase in tropical land areas.

A notable advance made by this study on the work of Goddéris et al. (2014) is the higher resolution GCM and palaeogeography inputs. Previous studies (both from field and model data) have suggested that a significant proportion of global weathering fluxes may be the result of so-called "hot-spots", i.e., small land areas with high weathering fluxes such as volcanic islands and mountain ranges (e.g., Rad et al., 2007; Kent and Muttoni, 2013). These regions are similar to locations with very sharp weathering fronts identified in Chapters 2 and 3 (i.e., warm-humid upland areas). While FOAM inputs show areas of higher runoff associated with mountain ranges, the higher resolution of the HadCM3L inputs relative to FOAM inputs may be sufficient to more accurately resolve weathering hot spots. Furthermore, given that weathering fluxes are highly spatially variable, the HadCM3L likely better constrains such features and thus provides a better estimate of global weathering fluxes. This study indicates a number of areas of high weathering fluxes, particularly outside of the tropics, associated with areas of high relief in the GCM simulations, particularly the Laramides and Appalachians (north America) and the southern Andes (Figures 4.16 and 4.17). In the original HadCM3L simulations these areas have high runoff rates, likely associated with orographic intensification of rainfall. Thus, the GEOCLIM simulations in this study may provide a better spatial estimate of weathering fluxes than those using FOAM inputs. These regions may be partly responsible for the sharp rise in non-tropical runoff in the early-Cretaceous (Figure 4.25), and further support the role of active mountain ranges in influencing CO_2 drawdown (Raymo and Ruddiman, 1992; Riebe et al., 2004; West et al., 2005; Goddéris et al., 2017).

4.7.3. Comparison to Proxy Data and Implications for Palaeoclimates

While the GEOCLIM simulations in this study represent an improvement over previous studies due to their higher spatial-temporal resolution and better constrained palaeogeography, they are nonetheless an obvious simplification relative to both pure GCM studies (which provide more

realistic modelling of climate change processes rather than the linear interpolation used here) and real-world settings. As the primary aim of this study is to assess the impact of palaeogeographic changes on potential global "weatherability", simplifications such as a constant degassing rate and uniform palaeolithologies were used in the absence of well-constrained data for such fields. Still, it is naturally of interest to compare the CO_2 curve produced in this study with those derived from previous modelling studies and proxy data. Such a comparison may provide an indication of the potential impact of changing weatherability on long-term CO_2 concentrations through the Cretaceous-Eocene period (assuming constant emission rates). Further GEOCLIM simulations were performed using variable degassing rates based on those in Van Der Meer et al. (2014) to assess the potential impact of the constant degassing rate used in this study on the resulting CO_2 curve.

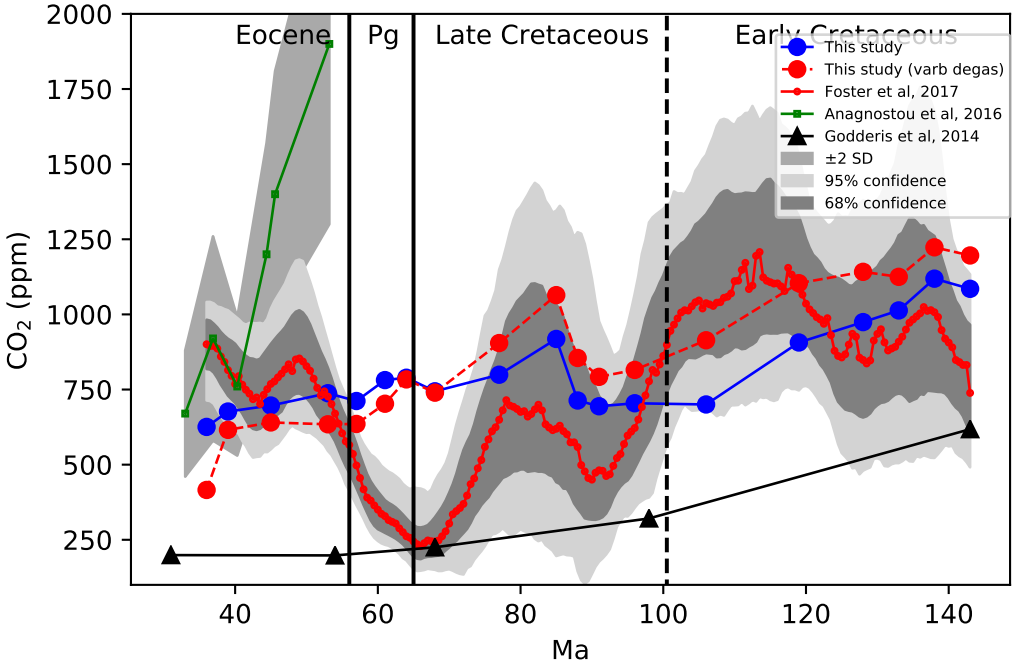

Figure 4.29: Steady-state CO_2 as modelled by GEOCLIM plotted against two CO_2 proxy curves from the literature. Also shown is the simulated curve from Goddéris et al. (2014) where each simulation was run at a different degassing rate. The GEOCLIM curve displays some agreement with the curve from Foster et al. (2017), particularly during the early-Cretaceous where CO_2 concentrations are comparably high, the late-Cretaceous where a brief rise in CO_2 is displayed by both curves, and during the late-Eocene. The curve from Anagnostou et al. (2016) displays considerably higher CO_2 concentrations during the early-Eocene than those in the GEOCLIM and Foster curves, but shows better agreement with both curves towards the mid and late Eocene. A second GEOCLIM curve (dashed red) displays the results of running GEOCLIM simulations using variable degassing rates calculated in Van Der Meer et al. (2014). The variable degassing curve displays a similar pattern to the simulations using a fixed degassing rate, however CO_2 concentrations are typically higher in the early Cretaceous under variable degassing, and significantly lower in the latest-Eocene.

Figure 4.29 presents the CO_2 curve produced in this study plotted (henceforth referred to as the GEOCLIM curve) against two CO_2 curves derived from proxy data (Anagnostou et al., 2016; Foster et al., 2017) and the 145-34 Ma portion of the curve from Goddéris et al. (2014).. Through the Cretaceous-Eocene period, there are three periods in which the trends in the GEOCLIM curve agrees with the two proxy curves: the early-Cretaceous, the late Cretaceous, and the mid-Eocene.

Periods of Agreement in the CO_2 Curves

Both the GEOCLIM curve and the curve from Foster et al. (2017) indicates relatively high (>800 ppm) CO_2 concentrations in the earliest-Cretaceous, followed by a general decreasing trend until 125 Ma. The high CO_2 concentrations in the early-Cretaceous are likely the result of the converged continental configuration which is unfavourable for high weathering fluxes. Both curves indicate a rise in CO_2 just after the earliest-Cretaceous (138 Ma, although only one GEOCLIM simulation is available between 140 and 135 Ma) . At this time, the continental interiors become more arid, as reflected by global runoff falling from ˜82 x 10^3 cm yr^{-1} to ˜64 x 10^3 cm yr^{-1} over a period of 5 Myr (Figures 4.15 and 4.20). The fall in global runoff leads to a reduction of silicate weathering fluxes, resulting in a CO_2 increase.

A rise in CO_2 during the late-Cretaceous (˜85 Ma) occurs in both the GEOCLIM curve and the curve from Foster et al. (2017). During the same period, a drop in global weathering fluxes (especially in the tropics) and a fall in total tropical runoff occurs (Figure 4.26). In both curves, the rise in CO_2 is relatively brief (10-20 Myr) and of approximately the same magnitude (˜200 ppm).

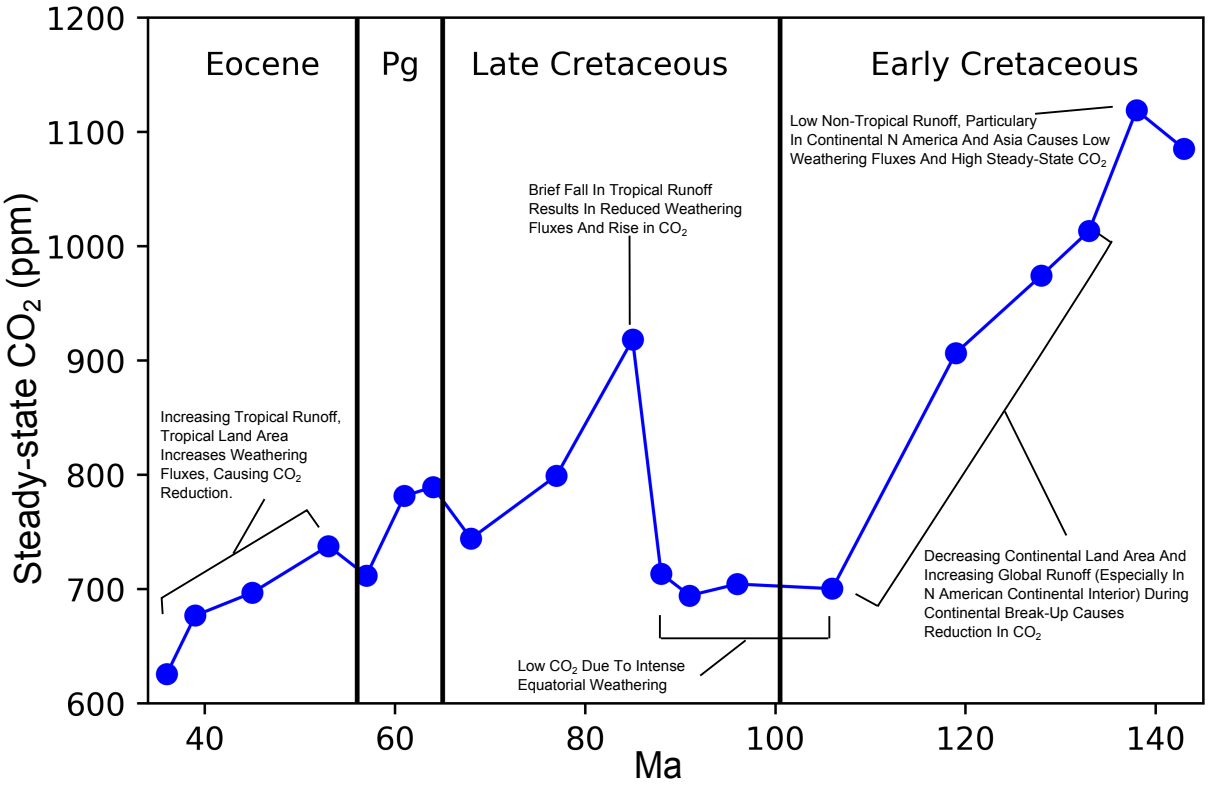

Figure 4.30: GEOCLIM steady-state CO_2 curve with annotations showing major controls on steady-state CO_2 concentrations.Significant changes in steady-state CO_2 are typically due to changes in runoff and continental land areas.

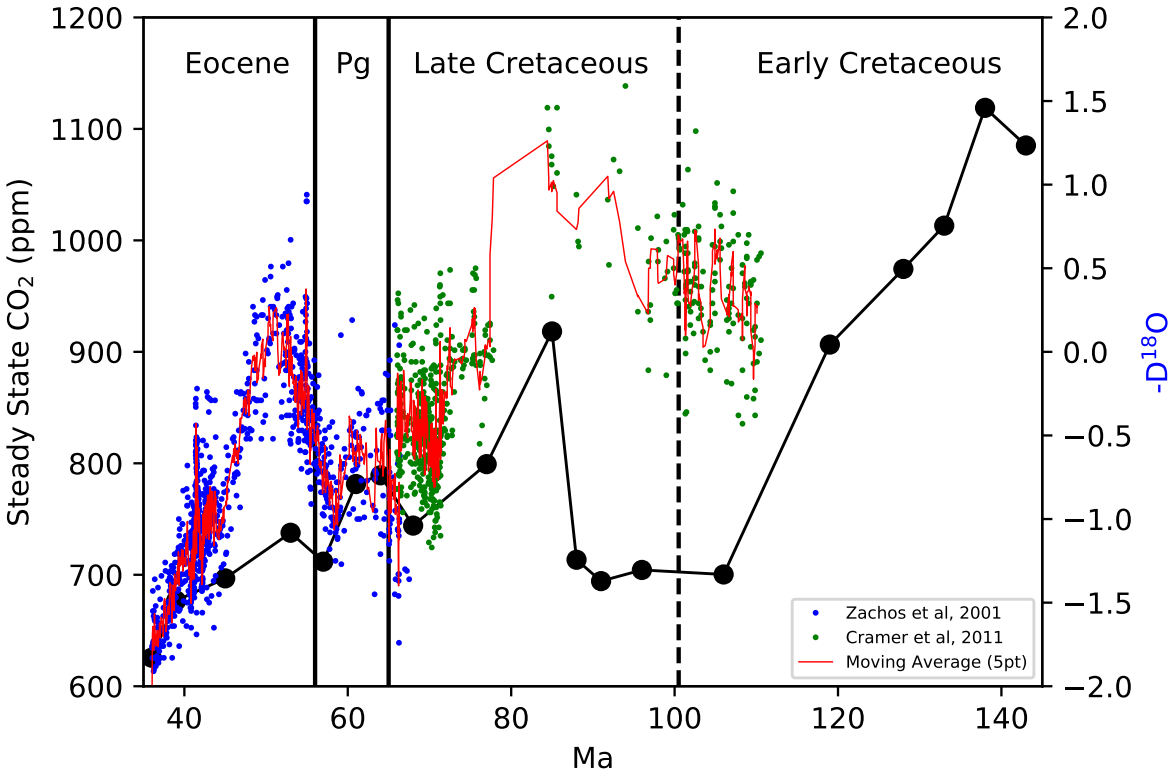

Figure 4.31: GEOCLIM steady-state CO_2 curve plotted against the $D^{18}O$ records of Zachos (2001) and Cramer et al. (2011).^{18}O values are plotted negatively to correlate with trends in atmospheric CO_2. The ^{18}O records show some similar trends, namely warmer conditions associated with high CO_2 in the early-Cretaceous and a trend towards cooler conditions into the Cenozoic.

All three curves indicate a drop in CO_2 of varying magnitudes towards the mid-Eocene, with the GEOCLIM curve showing the smallest drop in CO_2 (< 100 ppm) while the curve from Anagnostou et al. (2016) indicates a much larger drop of around 600 ppm. A fall in CO_2 from the early to mid-Eocene is often attributed to increased silicate weathering (e.g., Raymo and Ruddiman, 1992). Indeed, modelled weathering fluxes from this study during the Eocene are generally high and with a general rising trend towards the end of the Eocene, which coincides with falling CO_2 concentrations (Figure 4.29, 4.30). Zonal weathering plots indicate a wider area of high weathering fluxes in the tropics at this time relative to other time periods (e.g. mid-Cretaceous) in this study (30° N/S). Weathering fluxes intensify particularly over South-east Asia and India, but weathering fluxes in the Tibetan region remain relatively low (Figure 4.17).

Impact of Variable Degassing Rate

Further GEOCLIM simulations were performed using variable degassing rates ranging from a low value of 7.82 x 10^{12} mol C yr^{-1} in the latest-Eocene to a high of 1.23 x 10^{13} mol C yr^{-1} in the early-Cretaceous, based on rates calculated from subduction arc lengths in Van Der Meer et al. (2014). Degassing rates peak in the early-Cretaceous and fall gradually through the late-

Cretaceous and Cenozoic periods. The variable degassing simulations produced a curve similar to the GEOCLIM simulations using a fixed degassing rate of 1 x 10^{13} mol C yr^{-1}, likely due to the similarity of such a value to the range of degassing rates calculated by Van Der Meer et al. (2014). In general, the varaible degassing simulations produced slightly higher steady-state CO_2 concentrations during the Cretaceous, but slightly lower steady-state concentrations during the Cenozoic (Figure 4.29). Steady-state CO_2 concentrations fall sharply in the latest-Eocene in response to a decrease in degassing rates.

Implications

The GEOCLIM CO_2 curve presented in this study reflects the changes in global "weatherability" through the Cretaceous-Eocene period, indicating a general trend towards increased global weatherability during that time, punctuated by a decrease at ˜80 Ma. Although comparison with CO_2 curves from proxy data suggest that not all changes in long-term CO_2 can be ascribed to changes in global weatherability, the three curves indicate that changes in global weatherability have sufficiently powerful impacts on geologically short timescales (˜10 Myr) to be expressed in long term CO_2 curves, further supported by periods of agreement between the curves. These changes in weatherability are primarily associated with the break-up of Pangaea during the early-Cretaceous, and changes in tropical land areas and runoff rates in the mid-Cretaceous and the Eocene, respectively. Based on these findings, the implications for palaeoclimates are twofold.

Firstly, this study reinforces the conclusions of previous studies that continental configuration is a strong control on long-term CO_2 concentrations by influencing runoff (Otto-Bliesner, 1995; Donnadieu et al., 2004; Goddéris et al., 2014). Supercontinental configurations reduce global weatherability and favour high CO_2 concentrations by limiting global runoff, while dispersed configurations increase global weatherability and favour lower CO_2 concentrations as the dispersed configuration favours moisture transport to continental interiors.

Secondly, this study demonstrates the potential for relatively localised changes in weatherability to have global impacts and that in fact, changes in regional conditions may be a stronger control on long-term CO_2 than globally averaged values. This effect is demonstrated by the GEOCLIM CO_2 curve in the Eocene. For much of the modelled period, global runoff correlates with the initial silicate weathering flux, which is in turn inversely correlated to CO_2. However, during the Eocene, global runoff becomes inversely correlated to silicate weathering fluxes and global weathering fluxes increase despite a decrease in global runoff (Figure 4.30). During the Eocene, non-tropical runoff totals fall substantially but tropical runoff increases significantly, likely associated with an increase in tropical land areas at the same time. Similarly, during the mid-Cretaceous, tropical runoff totals remain stable but non-tropical rainfall increases. The increase in non-tropical rainfall is sufficient to increase silicate weathering fluxes and lower atmospheric CO_2 concentrations by 200 ppm over 13 Myr.

4.7.4. Future Work

There are a number of improvements that could be made to the GEOCLIM model that would help confirm, or perhaps challenge, the findings of this study. Many of these improvements are currently being implemented into the code but the improved version is not yet available for general use.

GEOCLIM has previously been run with the locations of various basaltic large igneous provinces specified, rather than the uniform lithology used in this model (Lefebvre et al., 2013). These large igneous provinces may significantly increase weathering fluxes if they pass through humid zones. In the absence of well constrained global datasets of palaeolithologies, including the locations of large igneous provinces in GEOCLIM may provide a better estimate of the effects of regional variations in lithology on long-term CO_2 concentrations.

The GEOCLIM simulations in this study show that silicate weathering rates are strongly determined by runoff. In some natural tropical settings however (e.g., Africa, South America), deep regolith layers can be produced which will inhibit weathering rates (Braun et al., 2005; Gabet and Mudd, 2009; West, 2012). A study using a modified version of the GEOCLIM model estimated the effects of deep regolith layers on weathering fluxes using a "shielding factor," where weathering fluxes decreased when deep regolith layers were produced (Goddéris et al., 2017). That study showed that the unmodified version of GEOCLIM may overestimate weathering fluxes in low-altitude tropical areas where slope gradients were low. In contrast, the modified version of the model showed that some high-altitude areas, which likely experience higher erosion rates which would prevent the development of deep regolith layers, had weathering fluxes that were higher than in the unmodified version of GEOCLIM. The study by Goddéris et al. (2017) demonstrates the potential role of topography on weathering fluxes, which is not captured by the version of the GEOCLIM model used in this study. While many of the high-runoff areas identified in this study are associated with mountain belts, there are some (such as Africa and The Amazon) which are not, and thus the version of GEOCLIM used in this study may overestimate weathering fluxes from such areas. A version of GEOCLIM is currently in development that can model potential regolith depths and their impact on weathering rates, based on the erosion-weathering rate laws described by Gabet and Mudd (2009). The Gabet and Mudd rate laws would provide a more robust method for estimating the effect of regolith depth on weathering rates, and allow for comparison with profiles and weathering rates from reactive transport models (Chapter 3). Furthermore, modelled regolith depths would allow for comparison between modern weathering fronts and those produced under conditions during the Cretaceous-Eocene, permitting further examination of the role of weathering front morphologies on long-term CO_2 concentrations. Additionally, given that some have theorised that the high CO_2 concentrations of the Eocene may have been due to low levels of relief (Froelich, 2014), it would be prudent to run the inputs from this study in the improved GEOCLIM model when it becomes available.

4.8. Conclusions

This study presents both a sensitivity analysis of the GEOCLIM model to inputs from different GCMs from the early-Eocene and an analysis of the potential impact of changing "weatherability" during the Cretaceous-Eocene period on long-term CO_2 concentrations. This study used higher resolution climate and palaeogeography inputs from the HadCM3L model, which provide a more robust dataset than the pre-existing FOAM inputs used in previous GEOCLIM studies. Data from the HadCM3L model were modified to the appropriate format for use in GEOCLIM.

The sensitivity analysis indicates that weathering in GEOCLIM is highly sensitive to changes in inputs, with runoff having the most significant impact on weathering fluxes. The HadCM3L inputs resulted in considerably higher steady-state CO_2 concentrations after 1 Myr relative to the original FOAM inputs (505 ppm and 299 ppm, respectively) due to lower mean global runoff. The sensitivity study also showed that care must be taken when converting data from one resolution to another as different interpolation methods produced considerable variation in results, despite identical initial data. The nearest-neighbour interpolation method was found to be the most appropriate method as it preserves local values, which in turn demonstrates the ability for regional climate values to have global impacts. However, the extrapolation technique used for producing 11 CO_2 concentrations from 2 levels appears to be robust.

The palaeogeography analysis showed that "weatherability" changed significantly through the Cretaceous-Eocene period as Pangaea broke up and the continents entered a more dispersed configuration. Changes in weatherability as a result of palaeogeographical change may be due to two processes. The first process is increased evaporation and more favourable moisture transport as continents became more dispersed, which occured during the early-Cretaceous. The second process is due to continents moving into more humid zones, which occured during the late-Eocene.

Steady-state CO_2 concentrations were initially high in the early-Cretaceous due to low total global runoff inhibiting weathering fluxes. As Pangaea broke up, evaporation from the ocean increased and improved moisture transport to the continental interiors, increasing runoff rates and weathering fluxes, resulting in lower steady-state CO_2 concentrations. Into the Cenozoic however, global weatherability appears to "switch" regimes. During the Mesozoic, weatherability changes are largely caused by changes in moisture fluxes to the continents as a result of increased evaporation from the oceans. In the Cenozoic, weatherability appears to be determined by increases in tropical land area, allowing for greater weathering in the tropics. Furthermore, global runoff fell in the late Eocene but silicate weathering fluxes continued to increase. The increase in silicate weathering is due to an increase in total tropical runoff as land areas in the tropics increased, which is sufficient to allow global weathering fluxes to increase despite a fall in total global runoff.

While the aim of this study was to investigate the role of palaeogeography on weatherability, the CO_2 curve produced by GEOCLIM was also compared with two proxy derived curves from the

literature to determine if changes in weatherability are expressed in long-term climate patterns. Three periods were identified when the GEOCLIM curve agreed with the proxy CO_2 curves and thus suggest that changes in weatherability were perhaps influencing global climate: the early-Cretaceous, the late-Cretaceous, and the mid-Eocene. High CO_2 concentrations in the early Cretaceous are likely due to the arid nature of the continental interior. A brief (10-20 Myr) rise in CO_2 during the late-Cretaceous appears to be the result of falling tropical runoff, causing global weathering fluxes to fall. Finally, a falling trend in CO_2 during the mid-Eocene appears to be linked to increased global weathering fluxes as tropical land areas increase. However, due to the assumption of constant degassing used in this study, care must be taken in interpreting both agreements and disagreements between the model and data.

The periods of agreement in the three CO_2 curves indicate that weatherability changes were sufficient in magnitude to affect the long-term climate of the Cretaceous-Eocene period. Furthermore, this study shows the potential for regional changes (e.g. localised changes in tropical runoff and land area) to have global impacts, and that such regional changes may be more significant than global averages for determining long-term climate.

Chapter 5

Conclusions and Directions for Future Work

5.1. Introduction

This chapter will summarise the findings of Chapters 2-4 and the implications of these findings for Critical Zone studies and long-term weathering rates. The direction for potential future studies (discussed in Chapters 3 and 4) will also be summarised.

5.2. Controls on Granitic Weathering Gradients, Morphology, and Rates as Indicated by Field Data

Chapter 2 presented new geochemical and mineralogical data (supplemented with existing data) from the temperate Lysina granitic weathering profile in the Czech Republic. These data were compared with existing geochemical data from other studies of granitic weathering profiles produced under different climate regimes with the goal of identifying controls on weathering gradients in granitic profiles and evaluating weathering processes at Lysina in the context of global weathering patterns.

The temperate Lysina profile exhibits a shallow regolith layer (2.6 m) above $>$ 30 m of weakly weathered bedrock. The primary weathering reaction in the Lysina profile is the dissolution of albite at a rate of -16.1 log mol m^2 s^{-1}, while other weathering reactions, such as the dissolution of K-feldspar and Li-micas occur at a slower pace. Weathering of albite occurs throughout the profile, and the Lysina profile exhibits low-intensity weathering throughout.

An albite weathering rate of -16.1 log mol m^2 s^{-1} is more rapid than plagioclase weathering rates in other granitic weathering profiles formed under warmer and slightly more humid climate conditions (e.g., White et al., 2001), but slower than rates measured in profiles formed under

subtropical and tropical conditions (White et al., 2001; Buss et al., 2008). Correlations between plagioclase weathering rates and environmental variables (MAT, MAP, and erosion rates) revealed a very strong correlation with MAP (r^2 = 0.98) but weaker correlations with MAT (r^2 = 0.68) and erosion rates (r^2 = 0.08), although whole-rock chemical weathering rates were better correlated with erosion (r^2 = 0.51) than were plagioclase weathering rates. Higher erosion rates also typically resulted in shallower regolith depth.

Correlations between environmental variables and Na weathering gradients (as a proxy for plagioclase weathering) using further data from the literature produced sharper gradients (i.e. greater mass loss per unit depth) strongly correlated with higher MAP (r^2 = 0.86) and considerably weaker correlations with MAT and erosion rates (r^2 = 0.29 and 0.05, respectively; Chapter 2; Figure 2.12). The strong correlations between plagioclase weathering rates and gradients with MAP are likely the result of decreasing geochemical saturation states with respect to weatherable minerals due to enhanced water flow rates in the subsurface, as suggested by previous studies (Maher, 2010; Maher and Druhan, 2014).

The implications of these findings are as follows:

1) Long-term silicate weathering rates (and thus long-term CO_2 concentrations) are likely strongly controlled by precipitation regimes, and that water flow rates in the subsurface represent the primary limiting factor on granitic weathering rates. Similarly, higher water fluxes produce sharper weathering gradients. Thus, water fluxes govern the size of weathering fronts and impact the range of potential processes occurring within such fronts.

2) Where high temperatures and erosion rates occur in conjunction with high effective precipitation rates (i.e., high precipitation with high infiltration), such as active tropical mountain belts, chemical weathering rates may be extremely rapid. Thus, these regions may contribute disproportionately to CO_2 drawdown from silicate weathering, and the distribution and abundance of such regions may be more significant for long term CO_2 concentrations than the global mean climate state.

3) Warm and humid climates typically produce very sharp weathering gradients where the distance from fresh bedrock to totally weathered material may be as little as 1 m. As such, much of climate-significant weathering may occur within a very narrow zone of the Earth's surface. As such, physical, chemical, and biological processes occurring within this narrow zone could have drastic effects on the long-term climate of the Earth. These findings highlight the importance of understanding critical zone processes when interpreting or estimating weathering export fluxes.

4) If water flow rates are a key control on both weathering rates and gradients, the role of subsurface architecture (i.e. porosity, permeability) must also be considered. Subsurface architecture will likely strongly affect water flow rates through regolith and bedrock. Because accurately observing the subsurface is exceptionally difficult, it is not possible to determine a clear relationship between

subsurface architecture and weathering morphology using field data in this chapter.

5.3. Using Reactive Transport Models to Investigate Controls on Granitic Weathering Profile Morphology

Building on the findings of Chapter 2, reactive transport models (RTM) of granitic weathering profiles under different environmental conditions were created using Crunchflow (Steefel et al., 2014). Extensively sampled field sites with well constrained weathering profile extent, mineralogy, and geochemistry are relatively few in number ($<$ ˜20), hampering the ability to draw robust conclusions between environmental variables and weathering processes. The interconnectivity (and localised heterogeneity) of factors that affect weathering processes in natural settings further hamper such attempts. A modelling approach allows the impact of individual factors to be evaluated while keeping other values constant, thus overcoming one of the main disadvantages of field-based studies. The RTM simulations were run under four different climate and erosion regimes to evaluate the impact of temperature and water flow on resulting profile morphology, as well as the impact of physical erosion. Outputs from these simulations were compared with existing weathering intensity and mass transfer data from the literature (in addition to data from Chapter 2).

The model weathering profiles produced by the RTM agreed well, in terms of weathering depth and intensity, with profiles from field sites with similar climate and erosion conditions (Chapter 3.3). Profiles produced under arid conditions resulted in very limited and shallow ($<$ 0.5 m) weathering regardless of temperature, while those produced under humid conditions led to much deeper (10 to $>$ 30 m) and more intensely weathered profiles. The impact of temperature was amplified under humid conditions, with cool conditions leading to deep ($>$ 30 m) but less intense weathering. In contrast, warm conditions produced intense weathering but at shallower depths (10 m), with sharp transitions between highly weathered material and fresh bedrock over 1-2 m distances. Higher erosion rates had relatively limited impacts on weathering gradients but resulted in significantly shallower weathering profiles.

The primary control on weathering front morphology is geochemical saturation (with respect to weatherable minerals). More humid conditions lead to greater water flow rates within weathering profiles which lead to lower geochemical saturation states, permitting more rapid weathering and allowing weathering to penetrate further into the bedrock. However, higher temperatures (where water flow rates are high) will also enhance weathering rates. Under warm, humid conditions the models indicate that weathering is sufficiently rapid at the weathering-bedrock interface such that this zone becomes geochemically saturated, preventing weathering from penetrating deeper into the bedrock. This finding may explain why some tropical weathering profiles have relatively shallow weathering compared to cooler environments (Chapter 2).

Changing initial permeability within the model indicated that water flux rates increase non-linearly with increasing permeability, further highlighting the potential influence of subsurface architecture on weathering profile morphology. However, subsurface architecture appears to exert a less significant impact relative to climate factors on profile morphology.

The key findings of this chapter are as follows:

1) Water fluxes are the primary control on plagioclase weathering rates, profile morphology and gradients by determining the geochemical saturation state of the subsurface with respect to weatherable minerals. These findings reinforce the conclusions of Chapter 2, and are in agreement with previous studies (Maher, 2010; Maher and Druhan, 2014).

2) Climate variables appear to have a dominant role in determining profile morphology relative to subsurface architecture at the global scale. However, subsurface architecture may play a stronger role in determining profile morphology at the local level when climate conditions have limited variability.

3) Erosion does not appear to influence weathering gradient sharpness, but does significantly impact the depth of weathering profiles. There is no clear impact of erosion on weathering rates indicated by this chapter, but further investigation (ideally using further field sites) is needed to determine whether the lack of impact on weathering gradients is a real phenomenon or an artifact of model configuration.

5.4. Impact of Changing Palaeogeography on Global "Weatherability"

Previous chapters have focused on drawing relationships between climate and silicate weathering processes at the profile scale, and on comparatively short (1-2 Myr) geological timescales. Both Chapters 2 and 3 found a strong relationship between plagioclase weathering rates and water fluxes (i.e., precipitation, runoff, and subsurface flow rates) at the profile and watershed scales. Furthermore, the findings of these chapters strongly suggested that global precipitation and runoff patterns are a dominant control on long-term atmospheric CO_2 concentrations. To address these findings, , Chapter 4 focuses on the impact of climate and silicate weathering feedbacks at the global scale over much longer ($>$ 100 Myr) timescales, building on the insights gained from Chapters 2 and 3.

In the long-term, silicate weathering fluxes balance volcanic degassing rates and atmospheric CO_2 concentrations reach a steady-state (Berner et al., 1983). However, the potential CO_2 drawdown from silicate weathering at a given CO_2 concentration (termed 'weatherability') can vary significantly based on climate, lithology, and palaeogeography. Palaeogeographical configuration can strongly affect global climate states by affecting atmospheric and ocean circulation patterns,

and as the previous chapters have demonstrated, climate is a very strong control on silicate weathering fluxes. As such, Chapter 4 investigates the potential role of changing palaeogeography on the weatherability of the Earth during the Cretaceous-Eocene period, where Pangaea broke apart and the continents approached their modern configurations.

Changes in global weatherability under a constant degassing rate were simulated using the global biogeochemical model GEOCLIM, with climate (MAT (mean annual temperature), MAR (mean annual runoff) and palaeogeography inputs provided from 19 simulations in the HadCM3L General Circulation Model (GCM), with simulations run for 1 Myr to allow atmospheric CO_2 concentrations to reach a steady-state. GEOCLIM has been used previously to investigate changes in weathering fluxes through geological time (Donnadieu et al., 2004, 2009; Lefebvre et al., 2013), including as a result of palaeogeography (Goddéris et al., 2014). However, the simulations in Goddéris et al. (2014) were performed at a relatively low temporal resolution (1 simulation per 25 Myr) and low spatial resolution (48 x 40) using the relatively old FOAM GCM. In contrast, in Chapter 4 a much higher temporal (1 simulation per 6 Myr) and spatial (96 x 73) resolution was used, a significant advancement over previous simulations. HadCM3L has not previously been used with GEOCLIM, nor has it been used for weathering studies, so a sensitivity study was performed in GEOCLIM where climate inputs were incrementally transitioned from FOAM to HadCM3L inputs, in order to compare and contrast the two models, and to evaluate our methodology.

The sensitivity study indicates that initial silicate weathering rates in GEOCLIM were more sensitive to changes in initial runoff than initial temperature between the FOAM and HadCM3L inputs, and that the two GCM simulations resulted in significantly different steady-state CO_2 concentrations (299 and 505 ppm, respectively) and initial global weathering fluxes (a proxy for weatherability) (2.45 x 10^{13} and 2.14 x 10^{13} mol C yr^{-1}, respectively). However, the sensitivity studies indicated that our methodology, in which the results of two HadCM3L simulations were extrapolated to 11 different CO_2 concentrations, was robust.

Similarly, the Cretaceous-Eocene simulations also revealed a strong relationship between runoff and initial silicate weathering fluxes (i.e., weatherability), where simulations with high global runoff values produced high initial global weathering fluxes and lower steady-state CO_2 concentrations.

The Cretaceous-Eocene simulations revealed an interesting "switch" in weathering regimes during the modelled period. In the early-mid Cretaceous, CO_2 concentrations fall sharply in response to increasing non-tropical ($> 30^\circ$ N/S) runoff, caused by the break-up of Pangaea enabling greater moisture transport to previously arid continental interiors. In contrast, during the Eocene, initial silicate weathering fluxes continue to increase as a result of increasing initial tropical runoff rates, despite global runoff rates falling. This regime change highlights the potential for regional changes in weatherability to have impacts at the global scale.

The steady-state CO_2 values from the 19 Cretaceous-Eocene GEOCLIM simulations were used to produce a CO_2 curve (referred to as the GEOCLIM curve), which was then compared with two additional CO_2 curves from the literature produced from proxy data (Anagnostou et al., 2016; Foster et al., 2017). While all three curves show distinct patterns, the GEOCLIM curve trends shows good agreement with the Foster curve during the early-Cretaceous, and good agreement with trends in both proxy curves in the Eocene . These periods of agreement are interpreted as times in Earth's history where changes in global weatherability were sufficiently large in magnitude to have long-term impacts on atmospheric CO_2 concentrations and thus climate. This chapter also supports the findings of Goddéris et al. (2014), which demonstrated that dispersed continental configurations (i.e., the modern configuration) favour increased weatherability and lower CO_2 concentrations, while converged configurations (i.e., supercontinents) reduce weatherability and result in higher CO_2 concentrations by modulating global moisture regimes.

5.5. Summary of Outcomes

5.5.1. A Strong Hydrological Control on Weathering Processes

This thesis demonstrates that weathering processes in the Critical Zone are dominated by the interaction of rocks with water. This outcome supports the findings of previous studies that have described water as being the common "thread" that links Critical Zone processes (Giardino and Houser, 2015), and studies that have shown a strong link between precipitation and runoff regimes with increased weathering rates within weathering profiles (Oliva et al., 2003; Maher, 2010; Maher and Druhan, 2014). Ultimately, silicate weathering rates are determined by the geochemical saturation state of the profile with respect to weatherable minerals (Chapter 3.4.4; Figures 3.7 and 3.8). However, the saturation state of the profile is strongly determined by the residence time of water within the profile. The residence time of water will depend on the flow rate within the profile, determined by water input (i.e., infiltration) and subsurface architecture, which will determine how easily water can move through the profile.

Thus, high water fluxes (as a result of high infiltration) can lead to rapid weathering within a profile, which in turn produces secondary porosity and allows water to move through the profile more easily. Figure 3.10 demonstrates that water flow rates increase exponentially with increasing permeability. As such, environments with high precipitation and infiltration can rapidly develop secondary porosity and produce high flow rates within a profile. Furthermore, Figure 3.9 highlights that even small changes ($<$1 orders of magnitude) in permeability and porosity can have significant impacts on weathering profile development by affecting water flow rates.

Chapters 2 and 3 demonstrate the strong link between precipitation/runoff regimes with weathering profile morphology, particularly the sharpness of the weathering gradient, with much sharper weathering gradients occurring in warm-humid environments. Such environments also typically

have the greatest weathering fluxes. As such, it is likely that much of climate significant CO_2 drawdown occurs within a very narrow zone of the Earth's surface, highlighting the need for further study of processes within this zone, as such (comparatively) small scale processes may have disproportionately large impacts at the global scale. In a similar vein, the large and deep weathering fronts in cool-humid environments should also be further investigated, as weathering processes within these environments are likely controlled by a wide range of processes that may vary with depth, leading to decoupling from the surface environment. Chapter 4 continues the 'water' thread linking weathering processes but applied at the global scale. Chapter 4 shows the powerful role of the hydrological cycle on controlling global weatherability, and the part played by continental configurations in affecting the hydrological cycle.

5.5.2. Changes in Regional Weatheirng Fluxes Have Global Impacts

Similar to Chapters 2 and 3, Chapter 4 highlights the importance of considering regional-scale changes in weatherability, as such changes can have disproportionate impacts at the global scale. Chapter 4 demonstrated, using GEOCLIM simulations, that changes in initial runoff fluxes in tropical regions have a significant enough impact on silicate weathering fluxes to produce notable ($>$ 100 ppm) changes in atmospheric CO_2 concentrations (Chapter 4.6; Figure 4.30). Changes of this magnitude are sufficient to cause changes in global climate, altering mean global temperatures and potentially affecting precipitation patterns. During the late-Eocene, increased runoff in the tropics is sufficient to cause a reduction in CO_2 concentrations, despite mean average global runoff falling, highlighting the potential for relatively small regional changes to affect, or even outstrip the impact of global changes in climate.

Similarly, during the early-Cretaceous, mean tropical runoff remained relatively stable, but the gradual northward drift of Laurasia, in addition to sea level rises, resulted in increased runoff in the continental interiors of North America and Asia. Runoff increased in these regions as evaporation rates increased and moisture transport to the continental interior became more favourable, resulting in increased weathering fluxes. In addition, the development of mountain ranges such as the Laramides and Appalachians increased runoff due to orographic forcing. Although increased runoff is largely confined to the northern mid-latitudes, GEOCLIM simulations of the early-Cretaceous showed a significant fall in CO_2 concentrations (400 ppm) over 40 Myr (Figure 4.30), further demonstrating the potential for global impacts from regional weathering flux changes.

Chapter 2 indicated that regions with high temperatures, runoff, and erosion rates (such as tropical mountain ranges) could have very high weathering rates, and that such regions could disproportionately contribute to CO_2 drawdown. Although GEOCLIM does not have an erosion component, Chapter 4 nonetheless identified high weathering rates in mountainous regions, due to their high runoff rates (Chapter 4.6.3; Figure 4.20). Runoff rates increased in these regions through the early-Cretaceous, and may be partly responsible for the decrease in atmospheric CO_2

during this time period. These findings, although not conclusive, strongly support the indications in Chapter 2 that weathering warm-humid mountain environments could disproportionately influence long-term CO_2 concentrations.

5.6. Directions for Future Work

Chapters 2 and 3 show the rich array of data that can be gathered from solid-state weathering profiles, which provide valuable information on weathering processes (such as initial mineral weathering reactions, and the depth of weathering fronts) that are not provided by more readily available stream-solute data. Such solid-state profiles are few in number, and if further profiles were sampled using geochemistry and mineralogy from thick outcrops and deep critical zone drill cores, the available dataset of weathering processes would be vastly improved. In Chapters 2 and 3, a data set of 12 field sites were used (Tables 2.1 and 3.3). Of these sites, there were 8 with any weathering or erosion rate estimates, 5 of which also had quantitative mineralogical data, and only 2 sites had subsurface water flow rate estimates. A larger dataset would allow for much greater confidence in relationships between factors drawn from field data. Furthmore, Chapters 2 and 3 indicate that weathering fronts are often deep below the surface ($>$ 10 m), which may place such fronts outside of the direct influence of vegetation, challenging assumptions that chemical weathering rates are enhanced by vegetation. Further investigation in the role of vegetation on weathering fronts at different depths could form the basis of future studies.

Although the relatively simplistic reactive transport modelling done in this study overcame some of the difficulties that arose due to the limited number of field sites, further work should be undertaken. The simulations presented in Chapter 3 used a simplified bedrock composition and structure (i.e., homogeneous mineral composition, initial permeability, porosity), while in natural settings significant variation in bedrock structure and composition exists, which may affect weathering processes. Similarly, the water infiltration configuration used in Chapter 3.2.2 could also be refined to better represent natural infiltration processes. Furthermore, although beyond the scope of this thesis, refinements to infiltration and erosion configuration within Crunchflow could allow for more robust conclusions about the role of erosion in affecting weathering gradients and rates. Examining in extensive detail the interactions between water flow rates and erosion within profiles using a wider array of model configurations could solidify, or challenge, the conclusions of Chapter 3.

The simulations presented in Chapter 4 utilised the highest spatial resolution data ever for a GEOCLIM study, the version of GEOCLIM used nonetheless has significant simplifications, such as a uniform lithology and no erosion component. Newer versions of GEOCLIM are currently under development that include dynamic soil profiles and erosion rate laws based on those of Gabet and Mudd (2009), although this version of GEOCLIM is not yet available for general use. Because erosion has been highlighted as a potential strong control on weathering rates (particularly

in tropical environments) (Riebe et al., 2004; West et al., 2005; West, 2012), it would be fascinating to re-run the simulations in Chapter 4 with the newer version to see if the addition of an erosion component alters the GEOCLIM CO_2 curve produced in this study. If a significantly different curve were produced, it may indicate that erosion rates (and thus tectonic processes) must also be considered as part of the "big picture" of long-term atmospheric CO_2 concentrations and global climate. Further analysis of regions with high weathering fluxes would also be necessary to examine any potential interplay between erosion and water fluxes on weathering processes. Using the newer version of GEOCLIM would allow for the impacts of mountain uplift on weathering rates, which some have attributed to significant CO_2 drawdown (e.g., Raymo and Ruddiman, 1992; Goddéris et al., 2017), to be assessed. The newer version of GEOCLIM would allow for the independent impacts of mountain uplift on weathering rates, namely increased runoff through orographic forcing and increased erosion, to be quantified.

5.7. Closing Remarks

Ultimately, this thesis has demonstrated that the hydrological cycle is inextricably linked to global climate and long-term atmospheric CO_2 concentrations. Investigations of field sites, reactive transport modelling, and global geochemical modelling indicate that warm-humid environments can produce extremely rapid weathering rates across a narrow band of the critical zone, and that such environments contribute disproportionately to CO_2 drawdown. As such, m to mm scale weathering processes occurring within the critical zone play a key role in ensuring the long-term habitability of the Earth, and this thesis highlights the need for further gathering of field data and modelling to investigate these critical processes at both the local and global scale.

References

Aagaard, P., Helgeson, H. C., 1982. Thermodynamic and kinetic constraints on reaction rates among minerals and aqueous solutions i. theoretical considerations. Amer. J. Science 282, 237–285.

Anagnostou, E., John, E. H., Edgar, K. M., Foster, G. L., Ridgwell, A., Inglis, G. N., Pancost, R. D., Lunt, D. J., Pearson, P. N., 2016. Changing atmospheric co2 concentration was the primary driver of early cenozoic climate. Nature 533 (7603), 380–4.
URL https://www.ncbi.nlm.nih.gov/pubmed/27111509

Anderson, S. P., Dietrich, W. E., Brimhall, G. H., 2002. Weathering profiles, mass-balance analysis, and rates of solute loss: Linkages between weathering and erosion in a small, steep catchment. Geological Society of America Bulletin 114, 1143–1158.

Bacon, A. R., Richter, D. d., Bierman, P. R., Rood, D. H., 2012. Coupling meteoric 10be with pedogenic losses of 9be to improve soil residence time estimates on an ancient north american interfluve. Geology 40 (9), 847–850.

Bahlburg, H., Dobrzinski, N., 2011. Chapter 6 a review of the chemical index of alteration (cia) and its application to the study of neoproterozoic glacial deposits and climate transitions. Geological Society, London, Memoirs 36 (1), 81–92.

Bandstra, J., Buss, H. L., Campen, R., Liermann, L., Moore, J., Hausrath, E., Navarre-Sitchler, A., Jang, J.-H., Brantley, S., 2008. Appendix: Compilation of Mineral Dissolution Rates. Springer, New York, pp. 737–823.

Banwart, S., Bernasconi, S., Blum, W., de Souza, D., Chabaux, F., Duffy, C., Kercheva, M., Krám, P., Lair, G., Menon, M., Nikolaidis, N., Novak, M., Panagos, P., Ragnarsdottir, K., Robinson, D., Rousseva, S., de Ruiter, P., van Gaans, P., Weng, L., White, T., Zhang, B., 2017. Chapter one - soil functions in earth's critical zone: Key results and conclusions. Advances in Agronomy 142, 1–27.

Banwart, S., Menon, M., Bernasconi, S. M., Bloem, J., Blum, W. E. H., Souza, D. M. d., Davidsdotir, B., Duffy, C., Lair, G. J., Kram, P., Lamacova, A., Lundin, L., Nikolaidis, N. P., Novak, M., Panagos, P., Ragnarsdottir, K. V., Reynolds, B., Robinson, D., Rousseva, S., de Ruiter, P., van Gaans, P., Weng, L., White, T., Zhang, B., 2012. Soil processes and functions across an international network of critical zone observatories: Introduction to experimental methods and initial results. Comptes Rendus Geoscience 344 (11-12), 758–772.

Barron, E. J., Hay, W. W., Thompson, S., 1989. The hydrologic cycle: A major variable during earth history. Palaeogeography, Palaeoclimatology, Palaeoecology 75 (3), 157–174.

Bazilevskaya, E., Lebedeva, M., Pavich, M., Rother, G., Parkinson, D. Y., Cole, D., Brantley, S. L., 2013. Where fast weathering creates thin regolith and slow weathering creates thick regolith. Earth Surface Processes and Landforms 38 (8), 847–858.

Berner, R. A., 1991. A model for atmospheric co2 over phanerozoic time. American Journal of Science 291 (4), 339–376.

URL <GotoISI>://WOS:A1991FF64800002

Berner, R. A., Kothavala, Z., 2001. Geocarb iii: A revised model of atmospheric co2 over phanerozoic time. American Journal of Science 301 (2), 182–204.
URL <GotoISI>://WOS:000169318900005

Berner, R. A., Lasaga, A. C., Garrels, R. M., 1983. The carbonate-silicate geochemical cycle and its effect on the atmospheric carbon dioxide over the past 100 million years. American Journal of Science 283, 641–683.

Blecha, V., Štemprok, M., 2012. Petrophysical and geochemical characteristics of late variscan granites in the karlovy vary massif (czech republic) - implications for gravity and magnetic interpretation in shallow depths. Journal of GEOsciences, 65–85.

Brantley, S., Mellott, N., 2000. Surface area and porosity of primary silicate minerals. American Mineralogist 85, 1767–1783.

Brantley, S. L., Bandstra, J., Moore, J., White, A. F., 2008. Modelling chemical depletion profiles in regolith. Geoderma 145 (3-4), 494–504.

Brantley, S. L., Goldhaber, M. B., Ragnarsdottir, K. V., 2007. Crossing disciplines and scales to understand the critical zone. Elements 3, 307–314.

Brantley, S. L., Lebedeva, M., 2011. Learning to read the chemistry of regolith to understand the critical zone. Annual Review of Earth and Planetary Sciences 39 (1), 387–416.

Brantley, S. L., Lebedeva, M., Bazilevskaya, E., 2014. Relating Weathering Fronts for Acid Neutralization and Oxidation to pCO2 and pO2. Elsevier Inc., pp. 327–352.

Brantley, S. L., Lebedeva, M. I., Balashov, V. N., Singha, K., Sullivan, P. L., Stinchcomb, G., 2017. Toward a conceptual model relating chemical reaction fronts to water flow paths in hills. Geomorphology 277, 100–117.

Braun, J.-J., Marechal, J.-C., Riotte, J., Boeglin, J.-L., Bedimo Bedimo, J.-P., Ndam Ngoupayou, J. R., Nyeck, B., Robain, H., Sekhar, M., Audry, S., Viers, J., 2012. Elemental weathering fluxes and saprolite production rate in a central african lateritic terrain (nsimi, south cameroon). Geochimica et Cosmochimica Acta 99, 243–270.

Braun, J.-J., Ngoupayou, J. R. N., Viers, J., Dupre, B., Bedimo Bedimo, J.-P., Boeglin, J.-L., Robain, H., Nyeck, B., Freydier, R., Nkamdjou, L. S., Rouiller, J., Muller, J.-P., 2005. Present weathering rates in a humid tropical watershed: Nsimi, south cameroon. Geochimica et Cosmochimica Acta 69 (2), 357–387.

Brimhall, G. H., Dietrich, W. E., 1987. Constitutive mass balance relations between chemical composition, volume, density, porosity, and strain in metasomatic hydrochemical systems: Results on weathering and pedogenesis. Geochim et Cosmochim. Acta 51, 567–587.

Brocard, G. Y., Willenbring, J. K., Scatena, F. N., Johnson, A. H., 2015. Effects of a tectonically-triggered wave of incision on riverine exports and soil mineralogy in the luquillo mountains of puerto rico. Applied Geochemistry 63, 586–598.

Brown, E., Stallard, R., Larsen, M., Raisbeck, G., Yiou, F., 1995. Denudation rates determined from the accumulation of in situ-produced 10be in the luquillo experimental forest, puerto rico. Earth and Planetary Science Letters 129, 193–202.

Buss, H. L., Bruns, M. A., Schultz, M. J., Mathur, C. F., Moore, J., Brantley, S. L., 2005. Microbial fe cycling in deep regolith. Geochimica Et Cosmochimica Acta 69 (10), A225–A225.
URL <GotoISI>://WOS:000229399700437

Buss, H. L., Lara, M. C., Moore, O. W., Kurtz, A. C., Schulz, M. S., White, A. F., 2017. Lithological influences

on contemporary and long-term regolith weathering at the luquillo critical zone observatory. Geochimica Et Cosmochimica Acta 196, 224–251.
URL <GotoISI>://WOS:000390959200013

Buss, H. L., Mathur, R., White, A., Brantley, S., 2010. Phosphorus and iron cycling in deep saprolite, luquillo mountains, puerto rico. Chemical Geology 269, 52–61.

Buss, H. L., Sak, P. B., Webb, S. M., Brantley, S. L., 2008. Weathering of the rio blanco quartz diorite, luquillo mountains, puerto rico: Coupling oxidation, dissolution, and fracturing. Geochimica Et Cosmochimica Acta 72 (18), 4488–4507.
URL <GotoISI>://WOS:000259107700004

Buzek, F., Hruska, J., Kram, P., 1995. Three component model of runoff generation, lysina catchment, czech republic. Water , Air and Soil Pollution 79, 391–408.

Calmels, D., Galy, A., Hovius, N., Bickle, M., West, A. J., Chen, M.-C., Chapman, H., 2011. Contribution of deep groundwater to the weathering budget in a rapidly eroding mountain belt, taiwan. Earth and Planetary Science Letters 303, 48–58.

Carmichael, M. J., Inglis, G. N., Badger, M. P. S., Naafs, B. D. A., Behrooz, L., Remmelzwaal, S., Monteiro, F. M., Rohrssen, M., Farnsworth, A., Buss, H. L., Dickson, A. J., Valdes, P. J., Lunt, D. J., Pancost, R. D., 2017. Hydrological and associated biogeochemical consequences of rapid global warming during the paleocene-eocene thermal maximum. Global and Planetary Change 157, 114–138.
URL <GotoISI>://WOS:000413612100010

Chabaux, F., Blaes, E., Stille, P., di Chiara, R. R., Dosseto, A., Pelt, E., Ma, L., Buss, H. L., Brantley, S. L., 2013. Regolith formation rate from u-series nuclides: Implications from the study of a spheroidal weathering profile in the rio icacos watershed (puerto rico). Geochimica et Cosmochimica Acta 100, 73–95.

Chadwick, O. A., Brimhall, G. H., Hendricks, D. M., 1990. From black box to a grey box: a mass balance interpretation of pedogenesis. Geomorphology 3, 369–390.

Cramer, B., Miller, K., Barret, P., Wright, J., 2011. Late cretaceous–neogene trends in deep ocean temperature and continental ice volume: Reconciling records of benthic foraminiferal geochemistry (d18o and mg/ca) with sea level history. Journal of Geophysical Research 116, 1–23.

Dannhaus, N., Wittmann, H., Krám, P., Christl, M., von Blanckenburg, F., 2018. Catchment-wide weathering and erosion rates of mafic, ultramafic, and granitic rock from cosmogenic meteoric 10be/9be ratios. Geochimica et Cosmochimica Acta 222, 618–641.

Darcy, H., 1856. Les fontaines publiques de la ville de Dijon: exposition et application. Victor Dalmont.

DeConto, R. M., Pollard, D., 2003. Rapid cenozoic glaciation of antarctica induced by declining atmospheric co2. Nature 421 (6920), 245–9.
URL https://www.ncbi.nlm.nih.gov/pubmed/12529638

Deer, W. A., Howie, R. A., Zussman, J., 2013. An Introduction to the Rock-Forming Minerals, 3rd Edition. The Mineralogical Society, London.

Dessert, C., Dupré, B., Gaillardet, J., François, L. M., Allègre, C. J., 2003. Basalt weathering laws and the impact of basalt weathering on the global carbon cycle. Chemical Geology 202 (3-4), 257–273.

Dethier, D. P., Lazarus, E. D., 2006. Geomorphic inferences from regolith thickness, chemical denudation and crn erosion rates near the glacial limit, boulder creek catchment and vicinity, colorado. Geomorphology 75 (3-4), 384–399.

Dixon, J. L., von Blanckenburg, F., 2012. Soils as pacemakers and limiters of global silicate weathering. Comptes Rendus Geoscience 344 (11-12), 597–609.

Donnadieu, Y., Godderis, Y., Bouttes, N., 2009. Exploring the climatic impact of the continental vegetation on the mezosoic atmospheric co2 and climate history. Climate of the Past 5 (1), 85–96.
URL <GotoISI>://WOS:000264740800007

Donnadieu, Y., Godderis, Y., Ramstein, G., Nedelec, A., Meert, J., 2004. A 'snowball earth' climate triggered by continental break-up through changes in runoff. Nature 428 (6980), 303–306.
URL <GotoISI>://WOS:000220250200039

Donnadieu, Y., Pierrehumbert, R., Jacob, R., Fluteau, F., 2006. Modelling the primary control of paleogeography on cretaceous climate. Earth and Planetary Science Letters 248 (1-2), 426–437.

Dosseto, A., Buss, H., Suresh, P. O., 2011. The delicate balance between soil production and erosion, and its role on landscape evolution. Applied Geochemistry, In Press.

Dosseto, A., Buss, H. L., Suresh, P. O., 2012. Rapid regolith formation over volcanic bedrock and implications for landscape evolution. Earth and Planetary Science Letters 337-338, 47–55.

Drever, J. I., 1994. The effect of land plants on weathering rates of silicate minerals. Geochimica Et Cosmochimica Acta 58 (10), 2325–2332.
URL <GotoISI>://WOS:A1994NQ01200013

Drever, J. I., Zobrist, J., 1992. Chemical-weathering of silicate rocks as a function of elevation in the southern swiss alps. Geochimica Et Cosmochimica Acta 56 (8), 3209–3216.
URL <GotoISI>://WOS:A1992JL90100017

Dupont-Nivet, G., Hoorn, C., Konert, M., 2008. Tibetan uplift prior to the eocene-oligocene climate transition: Evidence from pollen analysis of the xining basin. Geology 36 (12).

Ebelman, J., 1845. Sur les produits de la d ecomposition des especes min erals de la famille des silicates. Ann. des Mines 7, 3–66.

Eberle, J. J., Greenwood, D. R., 2011. Life at the top of the greenhouse eocene world–a review of the eocene flora and vertebrate fauna from canada's high arctic. Geological Society of America Bulletin 124 (1-2), 3–23.

Edgar, K. M., Wilson, P. A., Sexton, P. F., Gibbs, S. J., Roberts, A. P., Norris, R. D., 2010. New biostratigraphic, magnetostratigraphic and isotopic insights into the middle eocene climatic optimum in low latitudes. Palaeogeography, Palaeoclimatology, Palaeoecology 297 (3-4), 670–682.

Eldam, R., 2016. Evaluating control of slope aspect on geochemical weathering within boulder creek czo. Thesis, Colorado School of Mines.

Farnsworth, A., Lunt, D., O'Brien, C., Inglis, G. N., Foster, G. L., Markwick, P. J., Pancost, R. D., Robinson, S., In revisions. Climate sensitivity on geological timescales controlled by non-linear feedbacks and ocean circulation. Geophysical Research Letters.

Ferrier, K. L., West, N., 2017. Responses of chemical erosion rates to transient perturbations in physical erosion rates, and implications for relationships between chemical and physical erosion rates in regolith-mantled hillslopes. Earth and Planetary Science Letters 474, 447–456.

Fletcher, R. C., Buss, H. L., Brantley, S. L., 2006. A spheroidal weathering model coupling porewater chemistry to soil thicknesses during steady-state denudation. Earth and Planetary Science Letters 244 (1-2), 444–457.
URL <GotoISI>://WOS:000236991300031

Foster, G. L., Royer, D. L., Lunt, D. J., 2017. Future climate forcing potentially without precedent in the last 420 million years. Nat Commun 8, 14845.
URL https://www.ncbi.nlm.nih.gov/pubmed/28375201

Frey, B., Rieder, S. R., Brunner, I., Plotze, M., Koetzsch, S., Lapanje, A., Brandl, H., Furrer, G., 2010. Weathering-associated bacteria from the damma glacier forefield: physiological capabilities and impact on granite dissolution. Appl Environ Microbiol 76 (14), 4788–96.
URL https://www.ncbi.nlm.nih.gov/pubmed/20525872

Froelich, F., 2014. Was the late paleocene-early eocene hot because earth was flat? an ocean lithium isotope view of mountain building, continental weathering, carbon dioxide, and earth's cenozoic clima. Oceanography 27 (1), 36–49.

Gabet, E. J., Mudd, S. M., 2009. A theoretical model coupling chemical weathering rates with denudation rates. Geology 37 (2), 151–154.

Gaillardet, J., Rad, S., Rive, K., Louvat, P., Gorge, C., Allegre, C. J., Lajeunesse, E., 2012. Orography-driven chemical denudation in the lesser antilles: Evidence for a new feed-back mechanism stabilizing atmospheric co2. American Journal of Science 311 (10), 851–894.

Galeotti, S., Krishnan, S., Pagani, M., Lanci, L., Gaudio, A., Zachos, J. C., Monechi, S., Morelli, G., Lourens, L., 2010. Orbital chronology of early eocene hyperthermals from the contessa road section, central italy. Earth and Planetary Science Letters 290 (1-2), 192–200.

Gamache, K. R., Giardino, J. R., Regmi, N. R., Vitek, J. D., 2015. The Impact of Glacial Geomorphology on Critical Zone Processes. Developments in Earth Surface Processes. pp. 363–395.

Giardino, J. R., Houser, C., 2015. Introduction to the Critical Zone. Developments in Earth Surface Processes. pp. 1–13.

Gibbs, M. T., Kump, L. R., 1994. Global chemical erosion during the last glacial maximum and the present - sensitivity to changes in lithology and hydrology. Paleoceanography 9 (4), 529–543.
URL <GotoISI>://WOS:A1994PB33900003

Gislason, S. R., Oelkers, E. H., Snorrason, , 2006. Role of river-suspended material in the global carbon cycle. Geology 34 (1).

Goddéris, Y., Donnadieu, Y., Carretier, S., Aretz, M., Dera, G., Macouin, M., Regard, V., 2017. Onset and ending of the late palaeozoic ice age triggered by tectonically paced rock weathering. Nature Geoscience 10 (5), 382–386.

Goddéris, Y., Donnadieu, Y., Le Hir, G., Lefebvre, V., Nardin, E., 2014. The role of palaeogeography in the phanerozoic history of atmospheric co2 and climate. Earth-Science Reviews 128, 122–138.

Goddéris, Y., François, L. M., Probst, A., Schott, J., Moncoulon, D., Labat, D., Viville, D., 2006. Modelling weathering processes at the catchment scale: The witch numerical model. Geochimica et Cosmochimica Acta 70 (5), 1128–1147.

Goddéris, Y., Joachimski, M. M., 2004. Global change in the late devonian: modelling the frasnian–famennian short-term carbon isotope excursions. Palaeogeography, Palaeoclimatology, Palaeoecology 202 (3-4), 309–329.

Goldberg, K., Humayun, M., 2010. The applicability of the chemical index of alteration as a paleoclimatic indicator: An example from the permian of the paraná basin, brazil. Palaeogeography, Palaeoclimatology, Palaeoecology 293 (1-2), 175–183.

Goldich, S., 1938. A study of rock weathering. Journal of Geology 46, 17–58.

Goodfellow, B. W., Hilley, G. E., Webb, S. M., Sklar, L. S., Moon, S., Olson, C. A., 2016. The chemical, mechanical, and hydrological evolution of weathering granitoid. Journal of Geophysical Research-Earth Surface 121 (8), 1410–1435.
URL <GotoISI>://WOS:000384442100001

Gordon, C., Cooper, C., Senior, C. A., Banks, H., Gregory, J. M., Johns, T. C., Mitchell, J. F. B., Wood, R. A., 2000. The simulation of sst, sea ice extents and ocean heat transports in a version of the hadley centre coupled model without flux adjustments. Climate Dynamics 16 (2-3), 147–168.
URL <GotoISI>://WOS:000085374600005

Goudie, A. S., Viles, H. A., 2012. Weathering and the global carbon cycle: Geomorphological perspectives. Earth-Science Reviews 113 (1-2), 59–71.

Gough, D., 1981. Solar interior structure and luminosity variations. Solar Phyiscs 74, 21–34.

Greenwood, D. R., Basinger, J. F., Smith, R. Y., 2010. How wet was the arctic eocene rain forest? estimates of precipitation from paleogene arctic macrofloras. Geology 38 (1), 15–18.

Gyllenhaal, E., Engberts, C., Markwick, P., Smith, L., Patzkowsky, M., 1991. The fujia-ziegler model - a new semi-quantitative technique for estimating palaeoclimate from palaeogeographic maps. Palaeogeography, Palaeoclimatology, Palaeoecology 86, 41–66.

Hay, W. W., Floegel, S., 2012. New thoughts about the cretaceous climate and oceans. Earth-Science Reviews 115 (4), 262–272.

Haywood, A., Dowsett, H., Otto-Bliiesner, B., Chandler, M., Dolan, A., Hill, D., Lunt, D., Robinson, M., Rosenbloom, N., Salzmann, U., Sohl, L., 2010. Pliocene model intercomparison project (pliomip): experimental design and boundary conditions (experiment 1). Geoscientific Model Development 3, 227–242.

Hewawasam, T., von Blanckenburg, F., Bouchez, J., Dixon, J. L., Schuessler, J. A., Maekeler, R., 2013. Slow advance of the weathering front during deep, supply-limited saprolite formation in the tropical highlands of sri lanka. Geochimica et Cosmochimica Acta 118, 202–230.

Hilley, G. E., Porder, S., 2008. A framework for predicting global silicate weathering and co2 drawdown rates over geologic time-scales.pdf¿. Proceedings of the National Academy of Sciences of the United States of America 105, 116855–16859.

Hodson, M. E., 2002. Experimental evidence for the mobility of zr and other trace elements in soils. Geochimica Cosmochimica Acta 66, 819–828.

Hruska, J., Moldan, F., Kram, P., 2002. Recovery from acidification in central europe - observed and predicted changes of soil and streamwater chemistry in the lysina. catchment, czech republic. Environmental Pollution 120 (2), 261–274.
URL <GotoISI>://WOS:000178582800013

Huber, M., 2008. Climate change. a hotter greenhouse? Science 321 (5887), 353–4.
URL https://www.ncbi.nlm.nih.gov/pubmed/18635786

Huber, M., Caballero, R., 2011. The early eocene equable climate problem revisited. Climate of the Past 7 (2), 603–633.

Huber, M., Sloan, L. C., 2001. Heat transport, deep waters, and thermal gradients: Coupled simulation of an eocene greenhouse climate. Geophysical Research Letters 28 (18), 3481–3484.

Humphreys, E., Hessler, E., Dueker, K., Farmer, G. L., Erslev, E., Atwater, T., 2003. How laramide-age hydration

of north american lithosphere by the farallon slab controlled subsequent activity in the western united states. International Geology Review 45 (7), 575–595.

Hynek, S., Comas, X., Brantley, S. L., 2017. The effect of fractures on weathering of igneous and volcaniclastic sedimentary rocks in the puerto rican tropical rain forest. Procedia Earth and Planetary Science 17, 972–975.

Ibarra, D. E., Caves, J. K., Moon, S., Thomas, D. L., Hartmann, J., Chamberlain, C. P., Maher, K., 2016. Differential weathering of basaltic and granitic catchments from concentration–discharge relationships. Geochimica et Cosmochimica Acta 190, 265–293.

Inglis, G. N., Collinson, M. E., Riegel, W., Wilde, V., Farnsworth, A., Lunt, D. J., Valdes, P., Robson, B. E., Scott, A. C., Lenz, O. K., Naafs, B. D. A., Pancost, R. D., 2017. Mid-latitude continental temperatures through the early eocene in western europe. Earth and Planetary Science Letters 460, 86–96.

Jacob, R., Scahfer, C., Foster, I., Tobis, M., Anderson, J., 2001. Computational Design and Performance of the Fast Ocean Atmosphere Model, Version One. Vol. 2073. Springer, Berlin, Heidelberg.

Jaeger, J. J., Courtillot, V., Tapponnier, P., 1989. Paleontological view of the ages of the deccan traps, the cretaceous tertiary boundary, and the india-asia collision. Geology 17 (4), 316–319.
URL <GotoISI>://WOS:A1989U236900006

Jagniecki, E. A., Lowenstein, T. K., Jenkins, D. M., Demicco, R. V., 2015. Eocene atmospheric co2 from the nahcolite proxy. Geology.

Jost, A., Lunt, D., Kageyama, M., Abe-Ouchi, A., Peyron, O., Valdes, P. J., Ramstein, G., 2005. High-resolution simulations of the last glacial maximum climate over europe: a solution to discrepancies with continental palaeoclimatic reconstructions? Climate Dynamics 24 (6), 577–590.

Keating-Bitonti, C. R., Ivany, L. C., Affek, H. P., Douglas, P., Samson, S. D., 2011. Warm, not super-hot, temperatures in the early eocene subtropics. Geology 39 (8), 771–774.

Kennedy, A. T., Farnsworth, A., Lunt, D. J., Lear, C. H., Markwick, P. J., 2015. Atmospheric and oceanic impacts of antarctic glaciation across the eocene-oligocene transition. Philos Trans A Math Phys Eng Sci 373 (2054).
URL https://www.ncbi.nlm.nih.gov/pubmed/26438285

Kopacek, J., Hejzlar, J., Kram, P., Oulehle, F., Posch, M., 2016. Effect of industrial dust on precipitation chemistry in the czech republic (central europe) from 1850 to 2013. Water Res 103, 30–37.
URL https://www.ncbi.nlm.nih.gov/pubmed/27429352

Krám, P., Curik, J., Veselovsky, F., Myska, O., Hruska, J., Stedra, V., Jarchovsky, T., Buss, H. L., Chuman, T., 2017. Hydrochemical fluxes and bedrock chemistry in three contrasting catchments underlain by felsic, mafic and ultramafic rocks. Vol. 17 of Procedia Earth and Planetary Science. pp. 538–541.
URL <GotoISI>://WOS:000398020400136

Krám, P., Farkaš, J., Pereponova, A., Nwaogu, C., Štědrá, V., Hruška, J., 2014. Bedrock weathering and stream water chemistry in felsic and ultramafic forest catchments. Procedia Earth and Planetary Science 10, 52–55.

Krám, P., Hruska, J., Wenner, B. S., Driscoll, C. T., Johnson, C. E., 1997. The biogeochemistry of basic cations in two forest catchments with contrasting lithology in the czech republic. Biogeochemistry 37 (2), 173–202.
URL <GotoISI>://WOS:A1997WT07100005

Krám, P., Hruška, J., Shanley, J. B., 2012. Streamwater chemistry in three contrasting monolithologic czech catchments. Applied Geochemistry 27 (9), 1854–1863.

Krám, P., Santore, R. C., Driscoll, C. T., Aber, J. D., Hruska, J., 1999. Application of the forest-soil-water model

(pnet-bgc/chess) to the lysina catchment, czech republic. Ecological Modelling 120 (1), 9–30.
URL <GotoISI>://WOS:000081878900002

Ladant, J.-B., Donnadieu, Y., 2016. Palaeogeographic regulation of glacial events during the cretaceous supergreenhouse. Nature Communications 7, 1–9.

Lara, M. C., Buss, H. L., von Strandmann, P., Schuessler, J. A., Moore, O. W., 2017. The influence of critical zone processes on the mg isotope budget in a tropical, highly weathered andesitic catchment. Geochimica Et Cosmochimica Acta 202, 77–100.
URL <GotoISI>://WOS:000396794300005

Larsen, I. J., Almond, P. C., Eger, A., Stone, J. O., Montgomery, D. R., Malcolm, B., 2014. Rapid soil production and weathering in the southern alps, new zealand. Science 343 (6171), 637–40.
URL https://www.ncbi.nlm.nih.gov/pubmed/24436184

Larsen, M. C., Torres-Sanchez, A. J., 1998. The frequency and distribution of recent landslides in three montane tropical regions of puerto rico. Geomorphology 24 (4), 309–331.
URL http://www.sciencedirect.com/science/article/B6V93-3V5YTC3-19/2/85ad32bfc115f539a26de6b47e8b03c8

Lawrence, C., Harden, J., Maher, K., 2014. Modeling the influence of organic acids on soil weathering. Geochimica et Cosmochimica Acta 139, 487–507.

Lear, C. H., Bailey, T. R., Pearson, P. N., Coxall, H. K., Rosenthal, Y., 2008. Cooling and ice growth across the eocene-oligocene transition. Geology 36 (3), 251–254.
URL <GotoISI>://WOS:000253751000015

Lebedeva, M. I., Fletcher, R. C., Brantley, S. L., 2010. A mathematical model for steady-state regolith production at constant erosion rate. Earth Surface Processes and Landforms, n/a–n/a.

Lefebvre, V., Donnadieu, Y., Goddéris, Y., Fluteau, F., Hubert-Théou, L., 2013. Was the antarctic glaciation delayed by a high degassing rate during the early cenozoic? Earth and Planetary Science Letters 371-372, 203–211.

Lenton, T. M., Crouch, M., Johnson, M., Pires, N., Dolan, L., 2012. First plants cooled the ordovician. Nature Geoscience 5 (2), 86–89.

Li, L., Maher, K., Navarre-Sitchler, A., Druhan, J., Meile, C., Lawrence, C., Moore, J., Perdrial, J., Sullivan, P., Thompson, A., Jin, L., Bolton, E. W., Brantley, S. L., Dietrich, W. E., Mayer, K. U., Steefel, C. I., Valocchi, A., Zachara, J., Kocar, B., McIntosh, J., Tutolo, B. M., Kumar, M., Sonnenthal, E., Bao, C., Beisman, J., 2017. Expanding the role of reactive transport models in critical zone processes. Earth-Science Reviews 165, 280–301.

Lichtner, P. C., 1988. The quasi-stationary state approximation to coupled mass transport and fluid-rock interaction in a porous medium. Geochimica et Cosmochimica Acta 52, 143–165.

Littler, K., Robinson, S. A., Bown, P. R., Nederbragt, A. J., Pancost, R. D., 2011. High sea-surface temperatures during the early cretaceous epoch. Nature Geoscience 4 (3), 169–172.
URL <GotoISI>://WOS:000287802300016

Liu, W., Liu, C., Brantley, S. L., Xu, Z., Zhao, T., Liu, T., Yu, C., Xue, D., Zhao, Z., Cui, L., Zhang, Z., Fan, B., Gu, X., 2016. Deep weathering along a granite ridgeline in a subtropical climate. Chemical Geology 427, 17–34.

Lourens, L. J., Sluijs, A., Kroon, D., Zachos, J. C., Thomas, E., Rohl, U., Bowles, J., Raffi, I., 2005. Astronomical pacing of late palaeocene to early eocene global warming events. Nature 435 (7045), 1083–7.
URL https://www.ncbi.nlm.nih.gov/pubmed/15944716

Lunt, D. J., Dunkley Jones, T., Heinemann, M., Huber, M., LeGrande, A., Winguth, A., Loptson, C., Marotzke, J., Roberts, C. D., Tindall, J., Valdes, P., Winguth, C., 2012. A model–data comparison for a multi-model ensemble of early eocene atmosphere–ocean simulations: Eomip. Climate of the Past 8 (5), 1717–1736.

Lunt, D. J., Farnsworth, A., Loptson, C., Foster, G. L., Markwick, P., amp, apos, Brien, C. L., Pancost, R. D., Robinson, S. A., Wrobel, N., 2016. Palaeogeographic controls on climate and proxy interpretation. Climate of the Past 12 (5), 1181–1198.

Lunt, D. J., Huber, M., Anagnostou, E., Baatsen, M. L. J., Caballero, R., DeConto, R., Dijkstra, H. A., Donnadieu, Y., Evans, D., Feng, R., Foster, G. L., Gasson, E., von der Heydt, A. S., Hollis, C. J., Inglis, G. N., Jones, S. M., Kiehl, J., Kirtland Turner, S., Korty, R. L., Kozdon, R., Krishnan, S., Ladant, J.-B., Langebroek, P., Lear, C. H., LeGrande, A. N., Littler, K., Markwick, P., Otto-Bliesner, B., Pearson, P., Poulsen, J., C., Salzmann, U., Shields, C., Snell, K., Stärz, M., Super, J., Tabor, C., Tierney, J. E., Tourte, G. J. L., Tripati, A., Upchurch, G. R., Wade, B. S., Wing, S. L., Winguth, A. M. E., Wright, N. M., Zachos, James C. Zeebe, R. E., 2017. The deepmip contribution to pmip4: experimental design for model simulations of the eeco, petm, and pre-petm (version 1.0). Geoscientific Model Development 10, 889–901.

Lunt, D. J., Ridgwell, A., Sluijs, A., Zachos, J., Hunter, S., Haywood, A., 2011. A model for orbital pacing of methane hydrate destabilization during the palaeogene. Nature Geoscience 4 (11), 775–778.

Lunt, D. J., Valdes, P. J., Jones, T. D., Ridgwell, A., Haywood, A. M., Schmidt, D. N., Marsh, R., Maslin, M., 2010. Co2-driven ocean circulation changes as an amplifier of paleocene-eocene thermal maximum hydrate destabilization. Geology 38 (10), 875–878.

Ma, L., Jin, L., Brantley, S. L., 2011. How mineralogy and slope aspect affect ree release and fractionation during shale weathering in the susquehanna/shale hills critical zone observatory. Chemical Geology 290 (1-2), 31–49.

Maher, K., 2010. The dependence of chemical weathering rates on fluid residence time. Earth and Planetary Science Letters 294 (1-2), 101–110.

Maher, K., 2011. The role of fluid residence time and topographic scales in determining chemical fluxes from landscapes. Earth and Planetary Science Letters 312 (1-2), 48–58.

Maher, K., Druhan, J., 2014. Relationships between the transit time of water and the fluxes of weathered elements through the critical zone. Procedia Earth and Planetary Science 10, 16–22.

Masson-Delmotte, V., Kageyama, M., Branconnot, P., Charbit, S., Krinner, G., Ritz, C., Guilyardi, E., Jouzel, J., Abe-Ouchi, A., Crucifix, M., Gladstone, R., Hewitt, C., Kitoh, A., LeGrande, A., Marti, O., Merkel, U., Motoi, T., Ohgaito, R., Otto-Bliesner, B., Peltier, W., Ross, I., Valdes, P., Vettoretti, G., Weber, S., Wolk, F., Yu, Y., 2006. Past and future polar amplificiation of climate change - climate model intercomparisons and ice-core constraints. Climate Dynamics 26, 513–529.

McDowell, W. H., Asbury, C. E., 1994. Export of carbon, nitrogen, and major ions from three tropical montane watersheds. Limnology and Oceanography 39 (1), 111–125.

Melfi, A. J., Cerri, C. C., Kronberg, B. I., Fyfe, W. S., Mckinnon, B., 1983. Granitic weathering - a brazilian study. Journal of Soil Science 34 (4), 841–851.
URL <GotoISI>://WOS:A1983RW07300016

Meyer, R., van Wijk, J., Gernigon, L., 2007. The North Atlantic Igneous Province: A review of models for its formation. pp. 525–552.

Moon, S., Perron, J. T., Martel, S. J., Holbrook, W. S., St. Clair, J., 2017. A model of three-dimensional topographic stresses with implications for bedrock fractures, surface processes, and landscape evolution. Journal of Geophysical

Research: Earth Surface 122 (4), 823–846.

Moore, O., Buss, H., Dosseto, A., 2019. Incipient chemical weathering at bedrock fracture interfaces in a tropical critical zone, puerto rico. Geochimica et Cosmochimica Acta 252, 61–87.

Morris, J. L., Leake, J. R., Stein, W. E., Berry, C. M., Marshall, J. E. A., Wellman, C. H., Milton, J. A., Hillier, S., Mannolini, F., Quirk, J., Beerling, D. J., Lomax, B., 2015. Investigating devonian trees as geo-engineers of past climates: linking palaeosols to palaeobotany and experimental geobiology. Palaeontology 58 (5), 787–801.

Murphy, S. F., Brantley, S. L., Blum, A. E., White, A. F., Dong, H., 1998. Chemical weathering in a tropical watershed, luquillo mountains, puerto rico; ii. rate and mechanism of biotite weathering. Geochimica et Cosmochimica Acta 62 (2), 227–243.

Navarre-Sitchler, A., Steefel, C. I., Sak, P. B., Brantley, S. L., 2011. A reactive-transport model for weathering rind formation on basalt. Geochimica et Cosmochimica Acta 75 (23), 7644–7667.

Navrátil, T., 2000. Beryllium in waters of czech forested ecosystems and the release of beryllium from granites. GeoLines 12, 18–40.

Nesbitt, H. W., Young, G. M., 1982. Early proterozoic climates and plate motions inferred from major element chemistry of lutites. Nature 199, 715–717.

Notaro, M., Vavrus, S., Liu, Z., 2006. Global vegetation and climate change due to future increase in co2 as projected by a fully coupled model with dynamic vegetation. Journal of Climate 20, 70–90.

Nwaogu, C., 2014. Mobility and biogeochemical cycling of base cations (ca and mg) during weathering processes in a sensitive forest ecosystem, lysina, slavkov forest, czech republic. M.sc.

Oliva, P., Viers, J., Dupré, B., 2003. Chemical weathering in granitic environments. Chemical Geology 202 (3-4), 225–256.

Oliver, M. A., Gregory, P. J., 2015. Soil, food security and human health: a review. European Journal of Soil Science 66 (2), 257–276.

Orlando, J., Comas, X., Hynek, S. A., Buss, H. L., Brantley, S. L., 2016. Architecture of the deep critical zone in the rio icacos watershed (luquillo critical zone observatory, puerto rico) inferred from drilling and ground penetrating radar (gpr). Earth Surface Processes and Landforms 41 (13), 1826–1840.
URL <GotoISI>://WOS:000386027000002

Otto-Bliesner, B., 1995. Continental drift, runoff, and weathering feedbacks - implications from climate model experiments. Journal of Geophysical Research 100, 537–548.

Pagani, M., Caldeira, K., Berner, R., Beerling, D. J., 2009. The role of terrestrial plants in limiting atmospheric co(2) decline over the past 24 million years. Nature 460 (7251), 85–8.
URL https://www.ncbi.nlm.nih.gov/pubmed/19571882

Pagani, M., Zachos, J. C., Freeman, K. H., Tipple, B., Bohaty, S., 2005. Marked decline in atmospheric carbon dioxide concentrations during the paleogene. Science 309 (5734), 600–3.
URL https://www.ncbi.nlm.nih.gov/pubmed/15961630

Pavich, M., 1985. 10be analysis of a quaternary weathering profile in the virginia piedmont. Geology 13, 39–41.

Pavich, M. J., 1989. Regolith residence time and the concept of surface age of the piedmont peneplain. Geomorphology 2 (1-3), 181–196.

Phillips, J. D., 2010. The convenient fiction of steady-state soil thickness. Geoderma 156 (3-4), 389–398.

URL <GotoISI>://WOS:000277703200034

Pierson-Wickmann, A. C., Aquilina, L., Martin, C., Ruiz, L., Molénat, J., Jaffrézic, A., Gascuel-Odoux, C., 2009. High chemical weathering rates in first-order granitic catchments induced by agricultural stress. Chemical Geology 265 (3-4), 369–380.
URL http://www.sciencedirect.com/science/article/B6V5Y-4W6Y844-2/2/c3a14885350e8517c6932f25f18b90bb

Porada, P., Lenton, T. M., Pohl, A., Weber, B., Mander, L., Donnadieu, Y., Beer, C., Poschl, U., Kleidon, A., 2016. High potential for weathering and climate effects of non-vascular vegetation in the late ordovician. Nat Commun 7, 12113.
URL https://www.ncbi.nlm.nih.gov/pubmed/27385026

Porada, P., Weber, B., Elbert, W., Pöschl, U., Kleidon, A., 2014. Estimating impacts of lichens and bryophytes on global biogeochemical cycles. Global Biogeochemical Cycles 28 (2), 71–85.

Quirk, J., Leake, J. R., Johnson, D. A., Taylor, L. L., Saccone, L., Beerling, D. J., 2015. Constraining the role of early land plants in palaeozoic weathering and global cooling. Proc Biol Sci 282 (1813), 20151115.
URL https://www.ncbi.nlm.nih.gov/pubmed/26246550

Rad, S., Allegre, C., Louvat, P., 2007. Hidden erosion on volcanic islands. Earth and Planetary Science Letters 262 (1-2), 109–124.

Raymo, M., Ruddiman, W., 1992. Tectonic forcing of the late cenozoic climate. Nature 359, 117–122.

Riebe, C. S., Hahm, W. J., Brantley, S. L., 2017. Controls on deep critical zone architecture: a historical review and four testable hypotheses. Earth Surface Processes and Landforms 42 (1), 128–156.

Riebe, C. S., Kirchner, J. W., Finkel, R. C., 2004. Sharp decrease in long-term chemical weathering rates along an altitudinal transect. Earth and Planetary Science Letters 218, 421–434.

Riebe, C. S., Kirchner, J. W., Granger, D. E., Finkel, R. C., 2001. Strong tectonic and weak climatic control of long-term chemical weathering rates. Geology 29 (6), 511–514.

Ruddiman, W. F., 1997. Tectonic Uplift and Climate Change. Plenum Press, New York.

Sagoo, N., Valdes, P., Flecker, R., Gregoire, L. J., 2013. The early eocene equable climate problem: can perturbations of climate model parameters identify possible solutions? Philos Trans A Math Phys Eng Sci 371 (2001), 20130123.
URL https://www.ncbi.nlm.nih.gov/pubmed/24043872

Sak, P. B., Navarre-Sitchler, A., Miller, C., Daniel, C., Gaillardet, J., Buss, H. L., Lebedeva, M., Brantley, S., 2010. Controls on rind thickness on basaltic andesite clasts weathering in guadeloupe. Chem. Geol. 276, 129–143.

Schaffhauser, T., 2013. Tracage et modelisation des processus d'alteration, a l'echelle d'un petit bassin versant, le ringelbach (vosges). Thesis.

Schaffhauser, T., Chabaux, F., Ambroise, B., Lucas, Y., Stille, P., Reuschlé, T., Perrone, T., Fritz, B., 2014. Geochemical and isotopic (u, sr) tracing of water pathways in the granitic ringelbach catchment (vosges mountains, france). Chemical Geology 374-375, 117–127.

Schaller, M., von Blanckenburg, F., Hovius, N., Kubik, P. W., 2001. Large-scale erosion rates from in situ-produced cosmogenic nuclides in european river sediments. Earth and Planetary Science Letters 188 (3-4), 441–458.
URL <GotoISI>://WOS:000169449400011

Schellart, W. P., 2008. Overriding plate shortening and extension above subduction zones: A parametric study to explain formation of the andes mountains. Geological Society of America Bulletin 120 (11-12), 1441–1454.

Scotese, C., 2004. Cenozoic and Mesozoic Paleogeography - Changing Terrestrial Biogeographic Pathways. Sunderland, Massachusetts, pp. 9–26.

Seiders, V., 1971. Creatceous and lower tertiary stratigraphy of the gurabo and el yunque quadrangles, puerto rico. Geological Survey Bulletin.

Shuckburgh, E., Mitchell, D., Stott, P., 2017. Hurricanes harvey, irma, and maria: how natural were these 'natural disasters'? Weather 72 (11), 353–354.
URL https://www.ncbi.nlm.nih.gov/pubmed/28894211

Sluijs, A., Schouten, S., Pagani, M., Woltering, M., Brinkhuis, H., Damsté, J. S. S., Dickens, G. R., Huber, M., Reichart, G.-J., Stein, R., Matthiessen, J., Lourens, L. J., Pedentchouk, N., Backman, J., Moran, K., 2006. Subtropical arctic ocean temperatures during the palaeocene/eocene thermal maximum. Nature 441 (7093), 610–613.

St Clair, J., Moon, S., Holbrook, W. S., Perron, J. T., Riebe, C. S., Martel, S. J., Carr, B., Harman, C., Singha, K., Richter, D., 2015. Geophysical imaging reveals topographic stress control of bedrock weathering. Science 350 (6260), 534–8.
URL https://www.ncbi.nlm.nih.gov/pubmed/26516279

Steefel, C. I., Appelo, C. A. J., Arora, B., Jacques, D., Kalbacher, T., Kolditz, O., Lagneau, V., Lichtner, P. C., Mayer, K. U., Meeussen, J. C. L., Molins, S., Moulton, D., Shao, H., Šimůnek, J., Spycher, N., Yabusaki, S. B., Yeh, G. T., 2014. Reactive transport codes for subsurface environmental simulation. Computational Geosciences 19 (3), 445–478.

Steefel, C. I., Maher, K., 2009. Fluid-Rock Interaction: A Reactive Transport Approach. Vol. 70 of Reviews in Mineralogy & Geochemistry. pp. 485–532.
URL <GotoISI>://WOS:000268929000011

Strakhov, N. M., 1967. Principles of Lithogenesis, ist english Edition. Consultants Bureau, New York.

Sverdrup, K., Warfvinge, P., 1995. Estimating field weathering rates using laboratory kinetics. Vol. 31 of Reviews in Mineralogy. Mineralogical Society of America, Washington, D.C., pp. 485–542.

Tajika, E., 1998. Climate change during the last 150 million years: reconstruction from a carbon cycle model. Earth and Planetary Science Letters 160 (3-4), 695–707.
URL <GotoISI>://WOS:000075835000035

Taylor, L. L., Quirk, J., Thorley, R. M. S., Kharecha, P. A., Hansen, J., Ridgwell, A., Lomas, M. R., Banwart, S. A., Beerling, D. J., 2015. Enhanced weathering strategies for stabilizing climate and averting ocean acidification. Nature Climate Change 6 (4), 402–406.

Thomas, E., Zachos, J. C., 2000. Was the late paleocene thermal maximum a unique event? Gff 122 (1), 169–170.

Tobis, 1997. Foam - expanding the horizons of climate modelling.

Turner, B. F., Stallard, R. F., Brantley, S. L., 2003. Investigation of in situ weathering of quartz diorite bedrock in the rio icacos basin, luquillo experimental forest, puerto rico. Chemical Geology 202 (3-4), 313–341.

Valdes, P. J., Armstrong, E., Badger, M. P. S., Bradshaw, C. D., Bragg, F., Davies-Barnard, T., Day, J. J., Farnsworth, A., Hopcroft, P. O., Kennedy, A. T., Lord, N. S., Lunt, D. J., Marzocchi, A., Parry, L. M., Roberts, W. H. G., Stone, E. J., Tourte, G. J. L., Williams, J. H. T., 2017. The bridge hadcm3 family of climate models: Hadcm3@bristol v1.0. Geoscientific Model Development Discussions, 1–42.

Van Der Meer, D. G., Zeebe, R. E., van Hinsbergen, D. J., Sluijs, A., Spakman, W., Torsvik, T. H., 2014. Plate tectonic

controls on atmospheric co2 levels since the triassic. Proc Natl Acad Sci U S A 111 (12), 4380–5.
URL https://www.ncbi.nlm.nih.gov/pubmed/24616495

Viers, J., Oliva, P., Dandurand, J. L., Dupré, B., Gaillardet, J., 2014. Chemical Weathering Rates, CO2 Consumption, and Control Parameters Deduced from the Chemical Composition of Rivers. pp. 175–194.

Von der Heydt, A., Dijkstra, H., 2006. Effect of ocean gateways on global ocean circulation in the late oligocene and early miocene. Paleoceanography 21, 1–18.

Vylita, T., Žák, K., Cílek, V., Hercman, H., Mikšíková, L., 2007. Evolution of hot-spring travertine accumulation in karlovy vary/carlsbad (czech republic) and its significance for the evolution of teplá valley and ohře/eger rift. Zeitschrift für Geomorphologie 51 (4), 427–442.

Vázquez, M., Ramírez, S., Morata, D., Reich, M., Braun, J.-J., Carretier, S., 2016. Regolith production and chemical weathering of granitic rocks in central chile. Chemical Geology 446, 87–98.

Walker, J. C. G., Hays, P. B., Kasting, J. F., 1981. A negative feedback mechanism for the long-term stabilization of earth's surface temperature. Journal of Geophysical Research 86 (9776-9782).

West, A. J., 2012. Thickness of the chemical weathering zone and implications for erosional and climatic drivers of weathering and for carbon-cycle feedbacks. Geology 40 (9), 811–814.

West, A. J., Galy, A., Bickle, M., 2005. Tectonic and climatic controls on silicate weathering. Earth and Planetary Science Letters 235, 211–228.

West, C. K., Greenwood, D. R., Basinger, J. F., 2015. Was the arctic eocene 'rainforest' monsoonal? estimates of seasonal precipitation from early eocene megafloras from ellesmere island, nunavut. Earth and Planetary Science Letters 427, 18–30.

White, A., Blum, A. E., Stonestrom, D. A., Bullen, T. D., Schulz, M. S., Huntington, T. . G., Peters, N. E., 2001. Differential rates of feldspar weathering in granitic regolths. Geochimica Cosmochimica Acta in press.

White, A. F., 2002. Determining mineral weathering rates based on solid and soute weathering gradients and velocities: application to biotite weathering in saprolites. Chemical Geology 190, 69–89.

White, A. F., Blum, A. E., 1995. Effects of climate on chemical weathering rates in watersheds. Geochimica et Cosmochimica Acta 59, 1729–1747.

White, A. F., Blum, A. E., Bullen, T. D., Vivit, D. V., Schulz, M., Fitzpatrick, J., 1999. The effect of temperature on experimental and natural weathering rates of granitoid rocks. Geochimica Cosmochimica Acta 63 (19-20), 3277–3291.

White, A. F., Blum, A. E., Schulz, M. S., Huntington, T. G., Peters, N. E., Stonestrom, D. A., 2002. Chemical weathering of the Panola Granite: Solute and regolith elemental fluxes and the dissolution rate of biotite. Vol. Special Publ. no. 7. The Geochemical Society, pp. 37–59.

White, A. F., Blum, A. E., Schulz, M. S., Vivit, D. V., Stonestrom, D. A., Larsen, M., Murphy, S. F., Eberl, D., 1998. Chemical weathering in a tropical watershed, luquillo mountains, puerto rico: I. long-term versus short-term weathering fluxes. Geochimica et Cosmochimica Acta 62 (2), 209–226.

White, A. F., Brantley, S. L., 2003. The effect of time on the weathering of silicate minerals: why do weathering rates differ in the laboratory and field? Chemical Geology 202 (3-4), 479–506.

White, A. F., Buss, H. L., 2014. 7.4 - Natural Weathering Rates of Silicate Minerals. Elsevier, Oxford, pp. 115–155.
URL http://www.sciencedirect.com/science/article/pii/B9780080959757005040

White, A. F., Peterson, M. L., 1990. Role of reactive surface area characterization in geochemical models. Vol. 416. Am Chem Soc Symp Ser, pp. 461–475.

White, A. F., Schulz, M. S., Lawrence, C. R., Vivit, D. V., Stonestrom, D. A., 2017. Long-term flow-through column experiments and their relevance to natural granitoid weathering rates. Geochimica et Cosmochimica Acta 202, 190–214.

White, A. F., Schulz, M. S., Lowenstern, J. B., Vivit, D. V., Bullen, T. D., 2005. The ubiquitous nature of accessory calcite in granitoid rocks: Implications for weathering, solute evolution, and petrogenesis. Geochimica et Cosmochimica Acta 69 (6), 1455–1471.

White, T., Brantley, S., Banwart, S., Chorover, J., Dietrich, W., Derry, L., Lohse, K., Anderson, S., Aufdendkampe, A., Bales, R., Kumar, P., Richter, D., McDowell, B., 2015. The Role of Critical Zone Observatories in Critical Zone Science. Developments in Earth Surface Processes. pp. 15–78.

Yusoff, Z. M., Ngwenya, B. T., Parsons, I., 2013. Mobility and fractionation of rees during deep weathering of geochemically contrasting granites in a tropical setting, malaysia. Chemical Geology 349-350, 71–86.

Zachos, J., 2001. Trends, rhythms, and aberrations in global climate 65ma to present.

Zachos, J., Kump, L., 2005. Carbon cycle feedbacks and the initiation of antarctic glaciation in the earliest oligocene. Global and Planetary Change 47 (1), 51–66.

Zhang, Z.-J., Liu, C.-Q., Zhao, Z.-Q., Cui, L.-F., Liu, W.-J., Liu, T.-Z., Liu, B.-J., Fan, B.-L., 2015. Behavior of redox-sensitive elements during weathering of granite in subtropical area using x-ray absorption fine structure spectroscopy. Journal of Asian Earth Sciences 105, 418–429.

Štědrá, V., Jarchovský, T., Krám, P., 2016. Lithium-rich granite in the lysina-v1 borehole in the southern part of the slavkov forest, western bohemia. Geoscience Research Reports.

Štědrá, V., Krám, P., Farkaš, J., 2015. Petrology and whole-rock geochemistry of metabasites from borehole cores in the na zeleném and pluhův bor catchments in the slavkov forest, western bohemia. Geoscience Research Reports.

Appendices

Chapter 6

Appendix A

This appendix contains raw geochemical data and weathering indices from the sites used in this study. Where available, uncertainty values were propagated from detection limits of the geochemical analysis technique used (e.g., ICP-OES). Uncertainty values represent the potential range of geochemical values and weathering indices after taking detection limits into account.

Table 6.1: Lysina mass transfer (Equation 2.1)[a]

Depth (m)	Ca τTi	K τTi	Li τTi	Na τTi
0.15	-0.95 ± 0.21	-0.90 ± 0.17	-0.85 ± 0.16	-0.90 ± 0.17
0.30	-0.97 ± 0.23	-0.89 ± 0.15	-0.80 ± 0.14	-0.89 ± 0.14
0.45	-0.96 ± 0.22	-0.88 ± 0.16	-0.79 ± 0.14	-0.89 ± 0.16
0.60	-0.94 ± 0.18	-0.89 ± 0.15	-0.79 ± 0.14	-0.90 ± 0.15
0.75	-0.97 ± 0.21	-0.90 ± 0.15	-0.86 ± 0.14	-0.91 ± 0.15
0.90	-0.89 ± 0.19	-0.83 ± 0.17	-0.67 ± 0.14	-0.84 ± 0.17
1.05	-0.87 ± 0.18	-0.82 ± 0.16	-0.69 ± 0.14	-0.83 ± 0.16
1.20	-0.88 ± 0.17	-0.87 ± 0.16	-0.73 ± 0.13	-0.88 ± 0.16
1.35	-0.89 ± 0.19	-0.80 ± 0.16	-0.58 ± 0.12	-0.82 ± 0.16
1.50	-0.90 ± 0.19	-0.82 ± 0.16	-0.63 ± 0.12	-0.84 ± 0.16
1.65	-0.93 ± 0.22	-0.84 ± 0.18	-0.73 ± 0.15	-0.85 ± 0.18
1.80	-0.94 ± 0.23	-0.83 ± 017	-0.68 ± 0.14	-0.85 ± 0.17
1.85	-0.13 ± 0.04	-0.42 ± 0.13	-0.27 ± 0.09	-0.79 ± 0.25
2.10	-0.95 ± 0.22	-0.85 ± 0.16	-0.72 ± 0.13	-0.86 ± 0.16
2.40	-0.95 ± 0.23	-0.84 ± 0.23	-0.68 ± 0.16	-0.85 ± 0.16
2.65	-0.69 ± 0.19	-0.64 ± 0.17	-0.26 ± 0.07	-0.66 ± 0.18
2.77	-0.43 ± 0.16	-0.20 ± 0.07	-0.23 ± 0.08	-0.46 ± 0.16
3.10	-0.72 ± 0.23	-0.58 ± 0.18	-0.15 ± 0.05	-0.75 ± 0.23
3.40	-0.67 ± 0.21	-0.61 ± 0.19	-0.08 ± 0.03	-0.79 ± 0.25
3.68	-0.72 ± 0.22	-0.61 ± 0.18	-0.15 ± 0.04	-0.67 ± 0.20
4.20	-0.54 ± 0.17	-0.53 ± 0.17	-0.09 ± 0.03	-0.57 ± 0.18
4.30	-0.16 ± 0.06	-0.22 ± 0.08	-0.16 ± 0.06	-0.45 ± 0.16
4.65	-0.32 ± 0.10	-0.33 ± 0.11	-0.50 ± 0.16	-0.40 ± 0.13
4.70	-0.63 ± 0.19	-0.60 ± 0.18	-0.19 ± 0.06	-0.64 ± 0.19
5.20	-0.47 ± 0.18	-0.42 ± 0.16	0.12 ± 0.05	-0.47 ± 0.18
5.90	-0.48 ± 0.17	-0.46 ± 0.16	-0.02 ± 0.01	-0.52 ± 0.18
6.17	-0.09 ± 0.04	0.08 ± 0.03	0.08 ± 0.03	-0.22 ± 0.10
6.40	-0.61 ± 0.19	-0.55 ± 0.17	-0.02 ± 0.01	-0.63 ± 0.20
6.80	-0.59 ± 0.21	-0.43 ± 0.15	0.01 ± 0.005	-0.54 ± 0.19
7.10	-0.35 ± 0.12	-0.25 ± 0.09	-0.38 ± 0.13	-0.38 ± 0.13
7.45	-0.40 ± 0.14	-0.47 ± 0.16	0.14 ± 0.05	-0.50 ± 0.18
7.95	-0.44 ± 0.16	-0.50 ± 0.18	0.18 ± 0.06	-0.48 ± 0.17
8.45	-0.42 ± 0.21	-0.36 ± 0.18	0.43 ± 0.21	-0.40 ± 0.20
8.90	-0.31 ± 0.12	-0.42 ± 0.16	0.34 ± 0.13	-0.37 ± 0.15
9.40	-0.47 ± 0.16	-0.47 ± 0.16	0.32 ± 0.11	-0.51 ± 0.17
10.00	-0.48 ± 0.18	-0.46 ± 0.17	0.17 ± 0.06	-0.43 ± 0.16
10.40	-0.31 ± 0.12	-0.42 ± 0.16	0.27 ± 0.10	-0.40 ± 0.16
11.00	-0.24 ± 0.10	-0.42 ± 0.17	0.31 ± 0.13	-0.36 ± 0.15
11.45	-0.10 ± 0.04	-0.40 ± 0.17	0.28 ± 0.12	-0.37 ± 0.15
11.90	-0.35 ± 0.14	-0.44 ± 0.17	0.27 ± 0.11	-0.38 ± 0.15
12.45	-0.34 ± 0.13	-0.45 ± 0.17	0.33 ± 0.13	-0.44 ± 0.17
12.65	-0.02 ± 0.09	-0.35 ± 0.12	-0.42 ± 0.15	-0.36 ± 0.13
13.00	-0.06 ± 0.25	-0.38 ± 0.15	0.29 ± 0.12	-0.39 ± 0.16
13.45	-0.35 ± 0.13	-0.45 ± 0.17	0.28 ± 0.11	-0.40 ± 0.15
14.00	0.01 ± 0.01	-0.29 ± 0.13	0.56 ± 0.24	-0.24 ± 0.10
14.40	-0.50 ± 0.16	-0.56 ± 0.18	0.20 ± 0.06	-0.56 ± 0.18
14.64	0	0	0	0

[a]Uncertainty estimated and propagated from geochemical analytical technique detection limits. * Calculated using data from Štědrá et al. (2016).

Table 6.2: Davis Run mass transfer and CIA[a]

Depth (m)	Ca τTi	K τTi	Mg τTi	Na τTi	CIA
0.60	-0.99	-0.87	-0.72	-0.98	86
1.50	-0.99	-0.84	-0.61	-0.97	85.3
4.30	-0.94	-0.63	-0.11	-0.96	85
6.70	-0.99	-0.44	-0.1	-0.98	85.7
11.00	-0.99	-0.26	-0.11	-0.98	81.6
15.00	-0.82	-0.05	0.1	-0.66	72.4
20.00	-0.22	-0.07	0.01	-0.04	57.5
21.00	-0.08	-0.02	-0.01	-0.05	55.7
22.00	0	0	0	0	53.6

[a]Calculated from data in Pavich (1989).

Table 6.3: Panola mass transfer and CIA[a]

Depth (m)	Ca τTi	K τTi	Mg τTi	Na τTi	CIA
0.10	-0.97	-0.67	-0.9	-0.93	67.3
0.30	-0.97	-0.54	-0.82	-0.93	72.5
0.48	-0.97	-0.58	-0.68	-0.93	84.1
0.74	-0.97	-0.42	-0.68	-0.93	84.6
0.84	-0.98	-0.55	-0.68	-0.94	86.7
1.07	-0.98	-0.59	-0.65	-0.95	86.8
1.27	-0.98	-0.54	-0.63	-0.95	87.2
1.52	-0.98	-0.59	-0.63	-0.94	88.8
1.83	-0.98	-0.55	-0.71	-0.96	87.3
2.16	-0.98	-0.47	-0.61	-0.95	85.8
2.51	-0.98	-0.5	-0.5	-0.97	85.3
2.84	-0.98	-0.32	-0.46	-0.95	79.6
3.23	-0.98	-0.32	-0.3	-0.96	74.3
3.73	-0.98	-0.33	-0.23	-0.95	81.8
3.99	-0.98	-0.33	-0.31	-0.95	79.8
4.29	-0.98	-0.37	-0.2	-0.93	84.7
4.52	-0.98	-0.36	-0.36	-0.95	80.1
4.65	-0.98	-0.33	-0.23	-0.95	78.9
4.79	-0.97	0.04	-0.1	-0.87	73.2
6.69	-0.98	0.03	-0.03	-0.89	68.3
7.30	-0.97	-0.01	-0.02	-0.87	66.4
7.75	-0.95	-0.03	-0.05	-0.85	67.1
8.66	-0.6	0	-0.05	-0.31	58.5
9.27	-0.47	-0.04	-0.06	-0.29	56.2
9.88	-0.42	-0.03	-0.03	-0.36	57.3
10.18	-0.33	0.01	-0.06	-0.08	54.5
10.34	-0.08	0.01	-0.05	0.06	51.8
10.49	-0.09	0.07	-0.05	0.14	51.9
11	0	0	0	0	50.7

[a]Calculated from data in White et al. (2001).

Table 6.4: Río Icacos mass transfer and CIA[a]

Depth (m)	Ca τTi	K τTi	Mg τTi	Na τTi	CIA
0.15	-0.99 ± 0.33	-0.80 ± 0.04	-0.93 ± 0.08	-1.00 ± 1.00	97.5
0.30	-0.99 ± 0.33	-0.79 ± 0.04	-0.94 ± 0.09	-0.99 ± 0.50	97.1
0.50	-1.00 ± 0.50	-0.79 ± 0.03	-0.92 ± 0.05	-1.00 ± 1.00	97.5
0.60	-0.99 ± 0.17	-0.66 ± 0.02	-0.81 ± 0.02	-0.99 ± 0.33	96.0
0.80	-0.99 ± 0.33	-0.64 ± 0.02	-0.80 ± 0.03	-0.99 ± 0.33	96.0
0.90	-1.00 ± 0.50	-0.55 ± 0.01	-0.77 ± 0.02	-0.99 ± 0.50	96.0
1.10	-1.00 ± 0.50	-0.47 ± 0.01	-0.71 ± 0.02	-0.99 ± 0.50	95.1
1.20	-0.99 ± 0.33	-0.50 ± 0.01	-0.73 ± 0.02	-0.99 ± 0.50	94.9
1.40	-1.00 ± 0.50	-0.52 ± 0.01	-0.73 ± 0.02	-0.99 ± 0.50	95.4
1.50	-1.00 ± 0.33	-0.56 ± 0.01	-0.75 ± 0.02	-1.00 ± 1.00	95.6
1.80	-0.99 ± 0.14	-0.43 ± 0.01	-0.76 ± 0.02	-0.99 ± 0.25	94.4
2.10	-1.00 ± 0.50	-0.49 ± 0.01	-0.82 ± 0.02	-1.00 ± 1.00	95.4
2.40	-1.00 ± 0.50	-0.47 ± 0.01	-0.75 ± 0.03	-1.00 ± 1.00	96.6
2.70	-1.00 ± 0.50	-0.47 ± 0.01	-0.73 ± 0.02	-1.00 ± 1.00	95.6
3.00	-0.99 ± 0.20	-0.44 ± 0.01	-0.72 ± 0.02	-0.98 ± 0.14	94.8
3.40	-1.00 ± 0.50	-0.35 ± 0.01	-0.71 ± 0.02	-0.98 ± 0.17	94.0
3.70	-1.00 ± 0.50	-0.42 ± 0.01	-0.75 ± 0.02	-0.99 ± 0.33	94.6
4.00	-1.00 ± 0.50	-0.39 ± 0.01	-0.75 ± 0.02	-0.99 ± 0.33	94.0
4.30	-0.99 ± 0.33	-0.38 ± 0.01	-0.77 ± 0.02	-0.98 ± 0.14	93.4
4.60	-0.99 ± 0.25	-0.53 ± 0.01	-0.80 ± 0.02	-0.99 ± 0.20	94.4
4.90	-0.83 ± 0.02	-0.13 ± 0.003	-0.44 ± 0.01	-0.81 ± 0.02	82.2
5.20	-0.48 ± 0.01	-0.08 ± 0.002	-0.27 ± 0.01	-0.42 ± 0.01	66.2
5.50	-0.50 ± 0.01	-0.08 ± 0.002	-0.13 ± 0.003	-0.44 ± 0.01	65.4
5.80	-0.19 ± 0.01	0.06 ± 0.002	-0.12 ± 0.004	-0.11 ± 0.003	56.8
6.10	-0.21 ± 0.01	0.07 ± 0.002	-0.18 ± 0.01	-0.12 ± 0.003	57.3
6.40	-0.05 ± 0.002	0.15 ± 0.005	-0.12 ± 0.004	0.07 ± 0.002	55.9
6.70	-0.14 ± 0.004	0.05 ± 0.001	-0.09 ± 0.003	-0.10 ± 0.003	54.9
7.00	-0.14 ± 0.004	0.10 ± 0.003	-0.09 ± 0.003	-0.07 ± 0.002	54.8
7.30	0	0	0	0	55.2

[a]Calculated from data in Buss et al. (2017). Uncertainty estimated and propagated from geochemical analytical technique detection limits. Uncertainty values of 1 occur in samples where Na was below detection limit (0.01 wt %).

Table 6.5: Lysina CIA

Depth (m)	CIA
1.85	64.4 ± 1.10
2.77	58.0 ± 1.63
4.30	57.8 ± 1.21
4.65*	55.7 ± 1.13
6.17	57.1 ± 1.38
7.10*	55.3 ± 1.34
12.65*	55.9 ± 0.91
14.64	56.5 ± 1.33
18.25*	59.2 ± 0.55
20.22	61.0 ± 0.74
22.35*	62.4 ± 1.08
23.68	56.3 ± 0.69
25.63	59.2 ± 1.34
26.00*	55.0 ± 1.05
27.75*	54.8 ± 1.10
28.75	59.7 ± 1.09
30.15*	54.9 ± 1.20

*Calculated using data in Štědrá et al. (2016).

Table 6.6: Comparison of granite standard GSP-2 geochemistry with SGS analysis

	Al_2O_3 wt %	CaO wt %	Fe_{tot} wt %	K_2O wt %	MgO wt %	Na_2O wt %	P_2O_5 wt %	SiO_2 wt %	TiO_2 wt %
GSP-2[a]	14.9 ± 0.2	2.1 ± 0.06	4.9 ± 0.16	5.38 ± 0.14	0.96 ± 0.03	2.78 ± 0.09	0.29 ± 0.02	66.6 ± 0.8	0.66 ± 0.02
LYS-3061[b]	16.3	2.16	5.05	5.52	0.94	2.83	0.27	66.3	0.63

[a] USGS Silver Plume granite standard.[b] SGS ICP-OES analysis of GSP-2 standard.

Chapter 7

Appendix B

7.1. Crunchflow Mineral Database Entries

In Chapter 3, some of the mineral database entries were modified to make their stoichiometries more representative of those from Río Icacos. Below are the mineral names, molar volumes (cm^3 mol^{-1}), number of species, stoichiometric coefficients, equilibrium constants at 0°C, 25°C, 60°C, 100°C, 150°C, 200°C, 250°C, and 300°C, followed by the molecular weight of the mineral.

Original biotite entry (phlogopite)

'Phlogopite' 181.2000 7 -10. 'H+' 1. 'Al+++' 1. 'K+' 2. 'Mg++' 1. 'Fe++' 3. 'SiO2(aq)' 6. 'H2O' 42.0937 37.4400 31.5103 25.9003 20.3119 15.8204 12.0011 8.5120 417.2600

Updated biotite entry

'Biotite' 181.2000 9 -9.6500 'H+' 1.2800 'Al+++' 0.8900 'K+' 1.1900 'Mg++' 0.0200 'Mn++' 0.1800 'Ti(OH)4(aq)' 1.2500 'Fe++' 2.8800 'SiO2(aq)' 6. 'H2O' 25.2157 21.5276 16.6474 11.9018 7.0619 3.0594 -0.4503 -3.7494 480.7956

Original hornblende entry

'Mg hornblende' 335.9800 6 -14. 'H+' 2. 'Ca++' 3. 'Mg++' 2. 'Fe++' 8. 'H2O' 8. 'SiO2(aq)' 66.9228 61.2367 53.1713 45.2528 37.3013 30.9517 25.6087 20.7268 812.3665

Updated hornblende entry

Mg hornblende' 335.9800 6 -14. 'H+' 2. 'Ca++' 3. 'Mg++' 2. 'Fe++' 8. 'H2O' 8. 'SiO2(aq)' 12.5491 11.3269 9.7322 8.2108 6.6978 5.4953 4.4929 3.5985 812.3665

Table 7.1: Boulder Creek C_w Values[a]

Depth (m)	C_w Ca (mol kg^{-1})	C_w K (mol kg^{-1})	C_w Mg (mol kg^{-1})	C_w Na (mol kg^{-1})	Sum C_w (mol kg^{-1})
0.61	8.03 x 10^{-2}	4.84 x 10^{-1}	8.19 x 10^{-2}	5.91 x 10^{-1}	1.24
2.29	3.30 x 10^{-2}	2.97 x 10^{-1}	1.66 x 10^{-1}	2.29 x 10^{-1}	7.25 x 10^{-1}
5.33	1.05 x 10^{-1}	5.75 x 10^{-1}	2.69 x 10^{-1}	3.57 x 10^{-1}	1.31
5.33	8.10 x 10^{-2}	5.64 x 10^{-1}	2.78 x 10^{-1}	2.90 x 10^{-1}	1.21
6.10	1.27 x 10^{-1}	5.32 x 10^{-1}	2.67 x 10^{-1}	3.74 x 10^{-1}	1.30
7.62	8.69 x 10^{-2}	6.86 x 10^{-1}	2.89 x 10^{-1}	3.38 x 10^{-1}	1.40
9.14	6.42 x 10^{-2}	1.00	3.85 x 10^{-1}	4.61 x 10^{-1}	1.91
13.11	1.05 x 10^{-1}	3.85 x 10^{-1}	1.50 x 10^{-1}	3.98 x 10^{-1}	1.04
15.00	7.85 x 10^{-1}	6.56 x 10^{-1}	6.85 x 10^{-1}	9.71 x 10^{-1}	3.10

[a]Using data from Eldam (2016).

Table 7.2: Cheras C_w Values[a]

Depth (m)	C_w Ca (mol kg^{-1})	C_w K (mol kg^{-1})	C_w Mg (mol kg^{-1})	C_w Na (mol kg^{-1})	Sum C_w (mol kg^{-1})
0	0	3.52 x 10^{-2}	0	0	3.52 x 10^{-2}
0.50	0	3.50 x 10^{-2}	0	0	3.50 x 10^{-2}
1.00	0	5.67 x 10^{-2}	0	0	5.67 x 10^{-2}
1.50	0	9.39 x 10^{-2}	0	0	9.40 x 10^{-2}
2.00	0	0.11	0	0	0.11
3.00	0	9.81 x 10^{-2}	0	0	9.81 x 10^{-2}
4.00	0	0.30	2.20 x 10^{-2}	1.82 x 10^{-2}	0.34
5.00	0	0.33	2.08 x 10^{-2}	2.48 x 10^{-2}	0.38
5.50	0	0.22	1.23 x 10^{-2}	1.6 x 10^{-2}	0.25
6.00	0	0.33	1.56 x 10^{-2}	2.03 x 10^{-2}	0.37
7.00	0	0.27	1.12 x 10^{-2}	1.21 x 10^{-2}	0.29
7.50	0	0.23	2.17 x 10^{-2}	1.13 x 10^{-2}	0.26
8.00	0	0.95	0.01	9.12 x 10^{-2}	1.05
8.50	0	1.14	3.91 x 10^{-2}	0.81	1.99
9.00	2.97 x 10^{-2}	0.65	3.22 x 10^{-2}	0.55	1.26
9.50	2.55 x 10^{-2}	1.02	3.08 x 10^{-2}	0.67	1.74
10.00	3.87 x 10^{-2}	0.89	2.78 x 10^{-2}	0.57	1.53
11.00	6.33 x 10^{-2}	1.15	4.28 x 10^{-2}	0.90	2.16

[a]Using data from Yusoff et al. (2013).

Table 7.3: Curacavi C_w Values [a]

Depth (m)	C_w Ca (mol kg^{-1})	C_w K (mol kg^{-1})	C_w Mg (mol kg^{-1})	C_w Na (mol kg^{-1})	Sum C_w (mol kg^{-1})
0	0.94	0.56	0.59	0.66	2.75
2.30	0.78	0.4	0.55	0.53	2.26
4.80	0.95	0.61	0.60	0.74	2.89
6.80	0.96	0.69	0.68	0.87	3.21
9.10	1.06	0.68	0.78	0.84	3.36
10.70	0.95	0.70	0.77	0.79	3.21
12.90	1.12	0.60	0.66	0.79	3.17
14.30	0.89	0.51	0.626	0.61	2.65
15.50	1.21	0.40	0.71	0.74	3.06
18.80	0.99	0.58	0.66	0.73	2.96
20.50	1.10	0.57	0.70	0.79	3.16
22.30	1.01	0.43	0.70	0.71	2.85
23.80	1.04	0.46	0.63	0.78	2.91
25.10	1.00	0.42	0.72	0.67	2.81
26.80	1.03	0.40	0.66	0.68	2.77
28.30	0.85	0.51	0.60	0.55	2.50
29.80	0.91	0.6	0.66	0.71	2.88
31.70	0.97	0.66	0.62	0.78	3.02
33.30	1.02	0.79	0.72	1.07	3.60
35.00	1.19	0.60	0.82	0.98	3.58

[a]Using data from Vázquez et al. (2016).

Table 7.4: Davis Run C_w Values[a]

Depth (m)	C_w Ca (mol kg^{-1})	C_w K (mol kg^{-1})	C_w Mg (mol kg^{-1})	C_w Na (mol kg^{-1})	Sum C_w (mol kg^{-1})
0.60	2.98×10^{-3}	8.43×10^{-2}	2.59×10^{-2}	2.02×10^{-2}	0.13
1.50	3.63×10^{-3}	0.105	3.54×10^{-2}	2.82×10^{-2}	0.17
4.30	2.49×10^{-2}	0.24	8.13×10^{-2}	3.37×10^{-2}	0.377
6.70	3.62×10^{-3}	0.36	8.23×10^{-2}	1.53×10^{-2}	0.46
11.00	2.49×10^{-3}	0.47	8.13×10^{-2}	1.35×10^{-2}	0.57
15.00	7.03×10^{-2}	0.60	0.10	0.30	1.07
20.00	0.31	0.59	9.27×10^{-2}	0.83	1.83
21.00	0.36	0.63	9.13×10^{-2}	0.83	1.91
22.00	0.39	0.64	9.18×10^{-2}	0.87	1.99

[a]Using data from Pavich (1989).

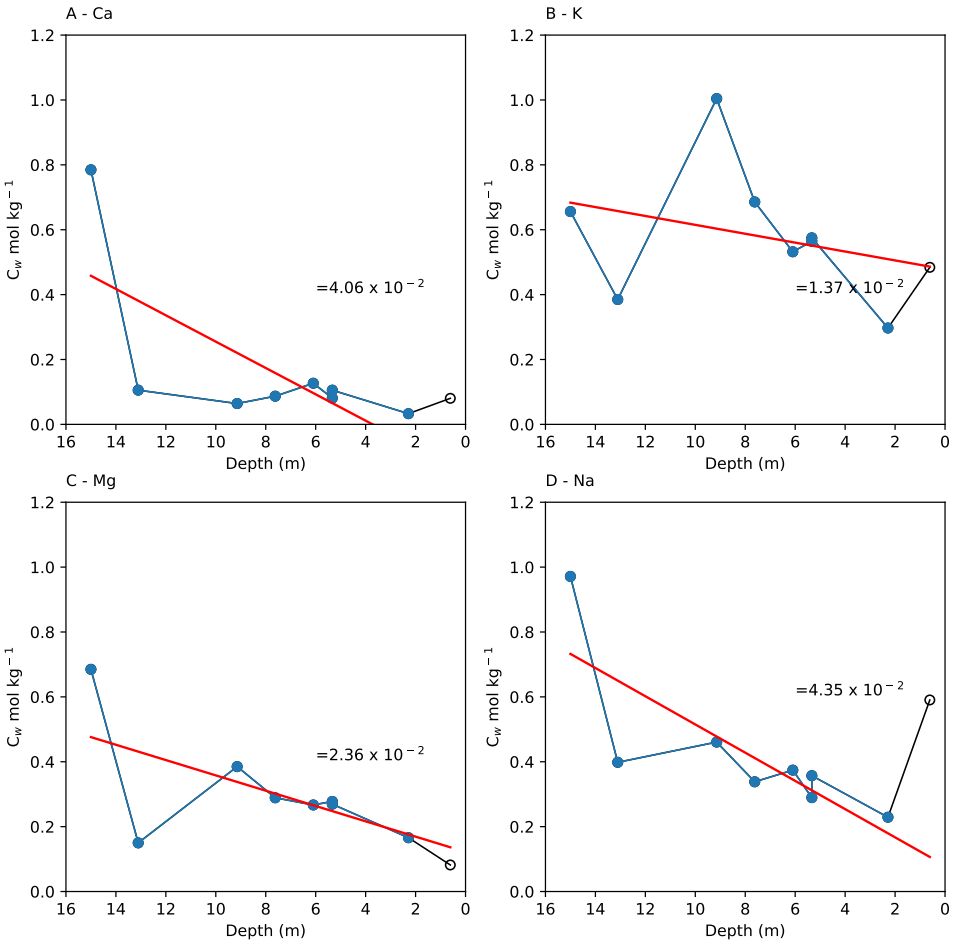

Figure 7.1: C_w values for mobile elements (a) Ca, (b) K, (c) Mg, and (d) Na within the Boulder Creek weathering profile with element specific weathering gradients (red lines and values) calculated through the zone of predominant mass loss. Blue circles indicate samples used in the calculation of the weathering gradient, while open black circles indicate values excluded from the gradient. One sample was excluded at 0.61 m due to significant increases in mobile element concentrations.

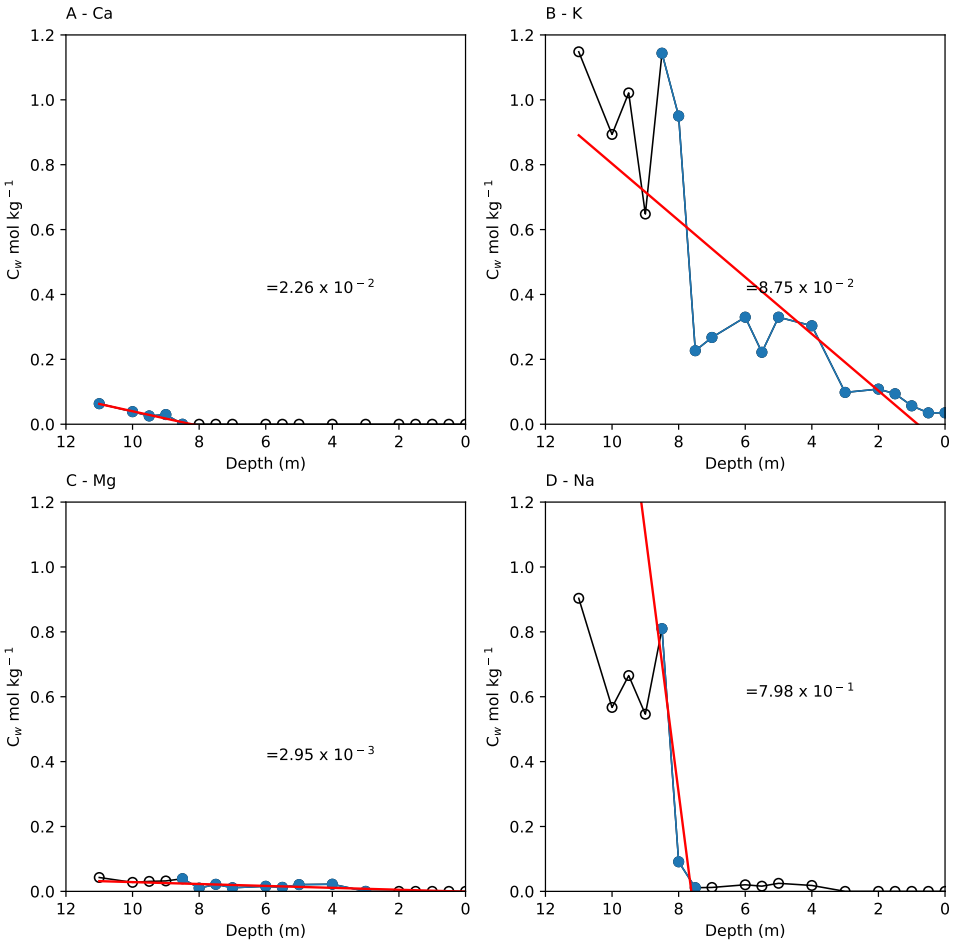

Figure 7.2: C_w values for mobile elements (a) Ca, (b) K, (c) Mg, and (d) Na within the Cheras weathering profile with element specific weathering gradients (red lines and values) calculated through the zone of predominant mass loss. Blue circles indicate samples used in the calculation of the weathering gradient, while open black circles indicate values excluded from the gradient. Several samples were excluded from the bottom and near-surface of the Ca, Mg, and Na profiles for gradient calculations due to lack of weathering and near total depletion of mobile elements, respectively.

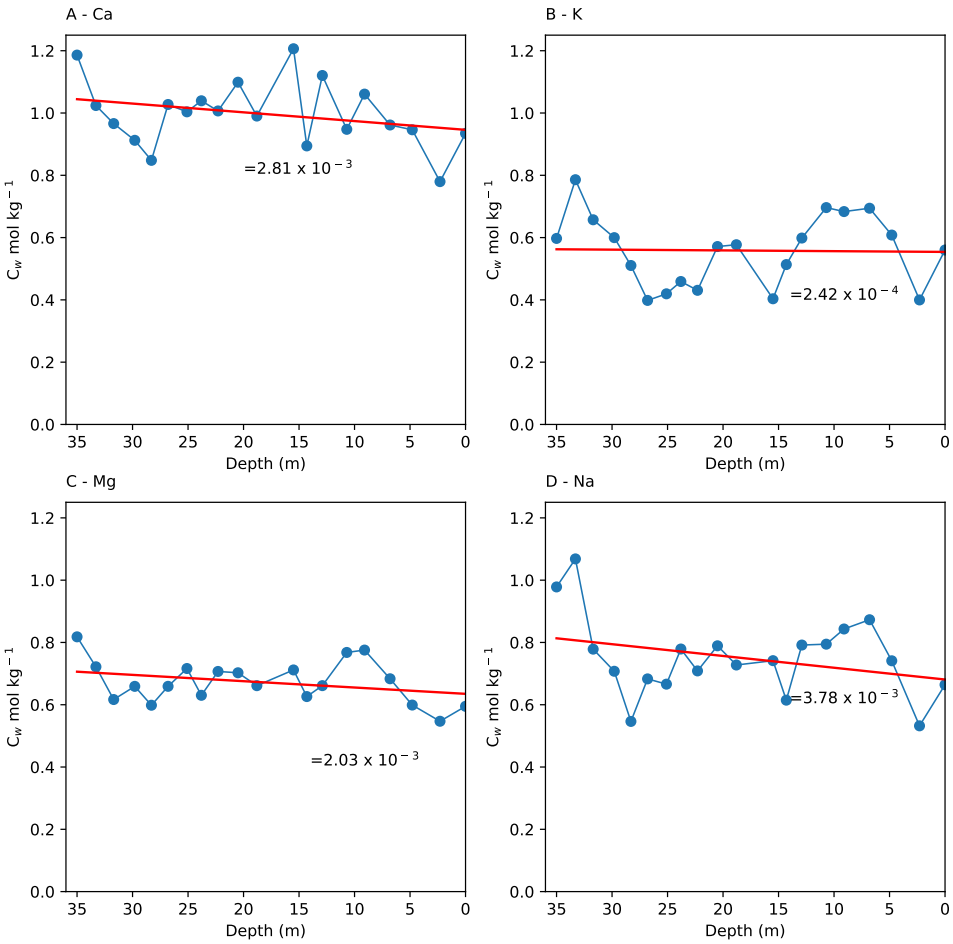

Figure 7.3: C_w values for mobile elements (a) Ca, (b) K, (c) Mg, and (d) Na within the Curacavi weathering profile with element specific weathering gradients (red lines and values) calculated through the zone of predominant mass loss. Blue circles indicate samples used in the calculation of the weathering gradient. All samples within the Curacavi profile were used in the calculation of gradient values.

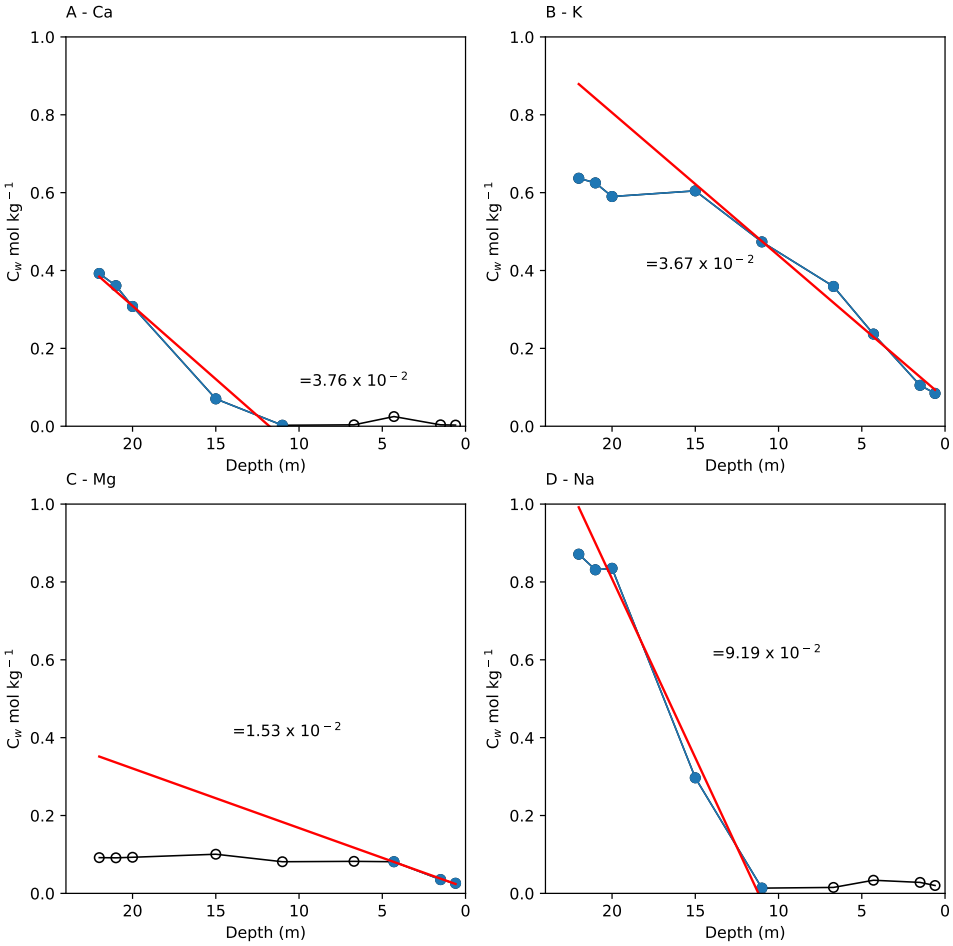

Figure 7.4: C_w values for mobile elements (a) Ca, (b) K, (c) Mg, and (d) Na within the Davis Run weathering profile with element specific weathering gradients (red lines and values) calculated through the zone of predominant mass loss. Blue circles indicate samples used in the calculation of the weathering gradient, while open black circles indicate values excluded from the gradient. Samples above 11 m in the Ca and Na gradients were excluded due to near-total depletion of these elements in samples above 11 m. Samples below 4.65 m depth in the Mg gradient were excluded due to no clear depletion trend being present within the profile below this depth.

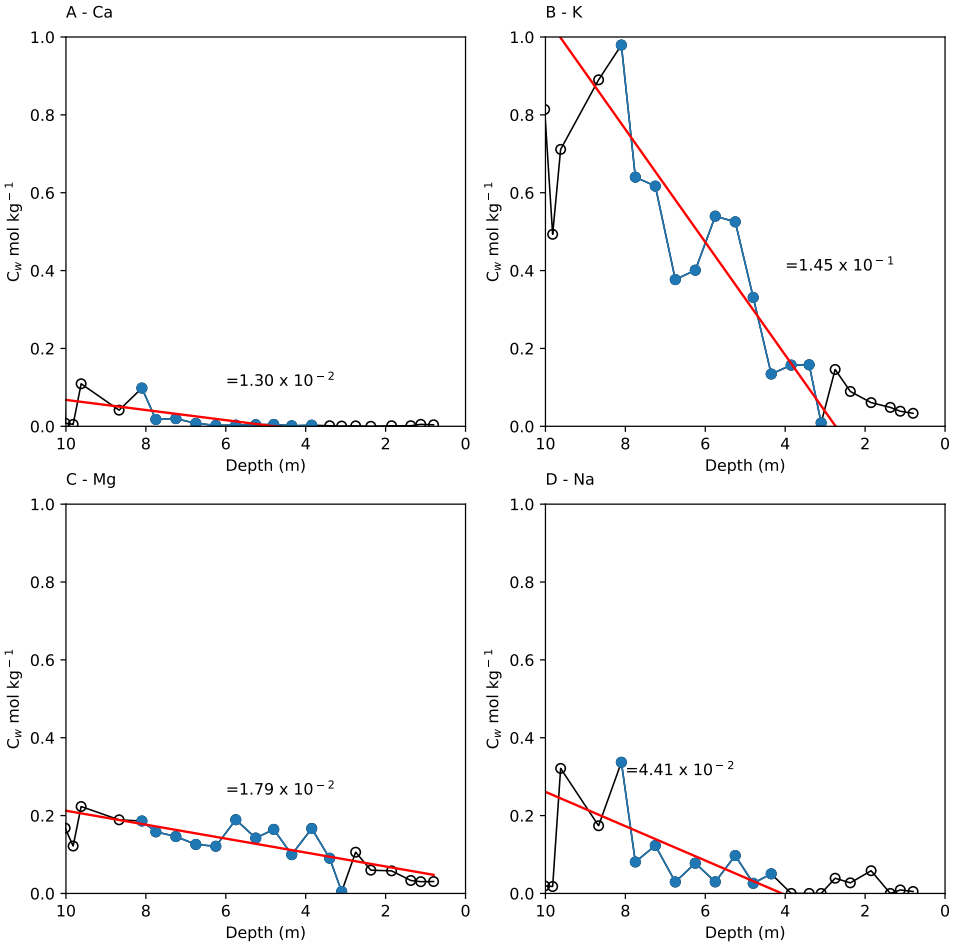

Figure 7.5: C_w values for mobile elements (a) Ca, (b) K, (c) Mg, and (d) Na within the Hakgala weathering profile with element specific weathering gradients (red lines and values) calculated through the zone of predominant mass loss. Blue circles indicate samples used in the calculation of the weathering gradient, while open black circles indicate values excluded from the gradient. Several samples from near the base and the near surface were excluded from all gradients due to lack of clear depletion trend and near-total depletion of mobile elements, respectively.

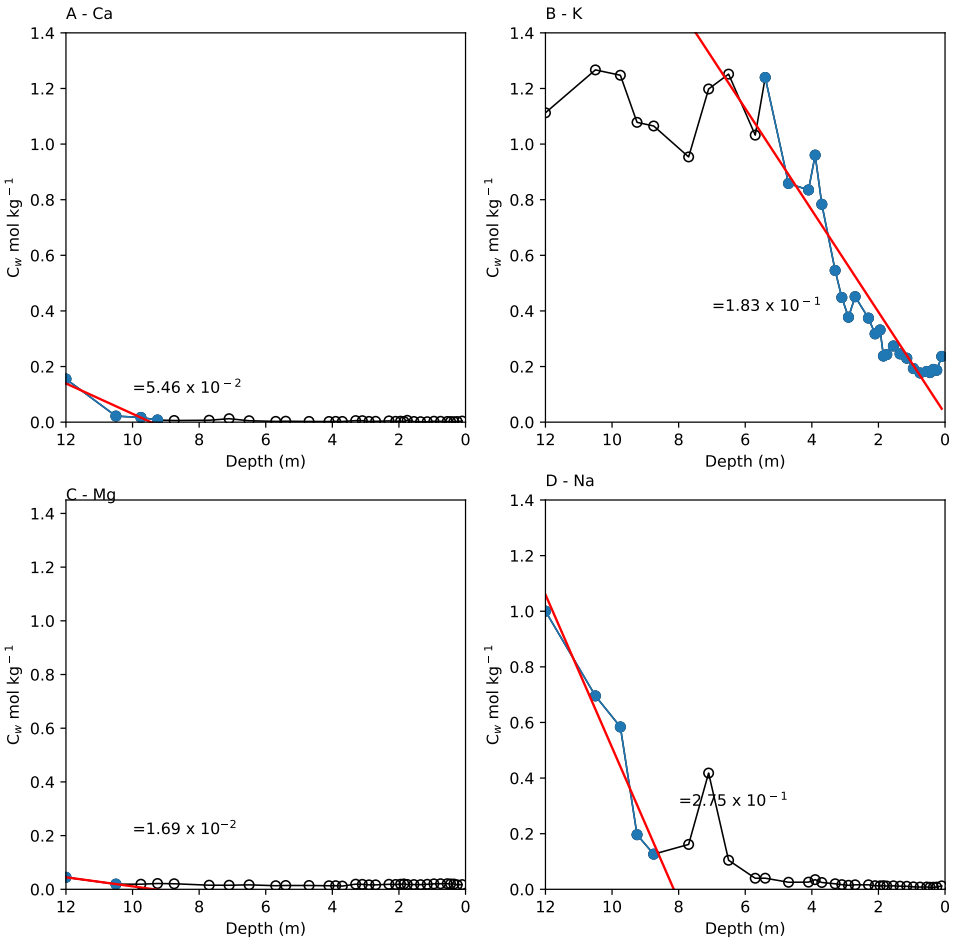

Figure 7.6: C_w values for mobile elements (a) Ca, (b) K, (c) Mg, and (d) Na within the Longnan weathering profile with element specific weathering gradients (red lines and values) calculated through the zone of predominant mass loss. Blue circles indicate samples used in the calculation of the weathering gradient, while open black circles indicate values excluded from the gradient. Most samples above 10 m were excluded from the Ca and Mg gradients due to near total depletion of these elements above 10 m. Samples below 6 m were excluded from the K gradients due to no clear depletion pattern. Samples above 8 m were excluded from the Na gradient as these samples are outside the predominant zone of mass loss within the Longnan profile.

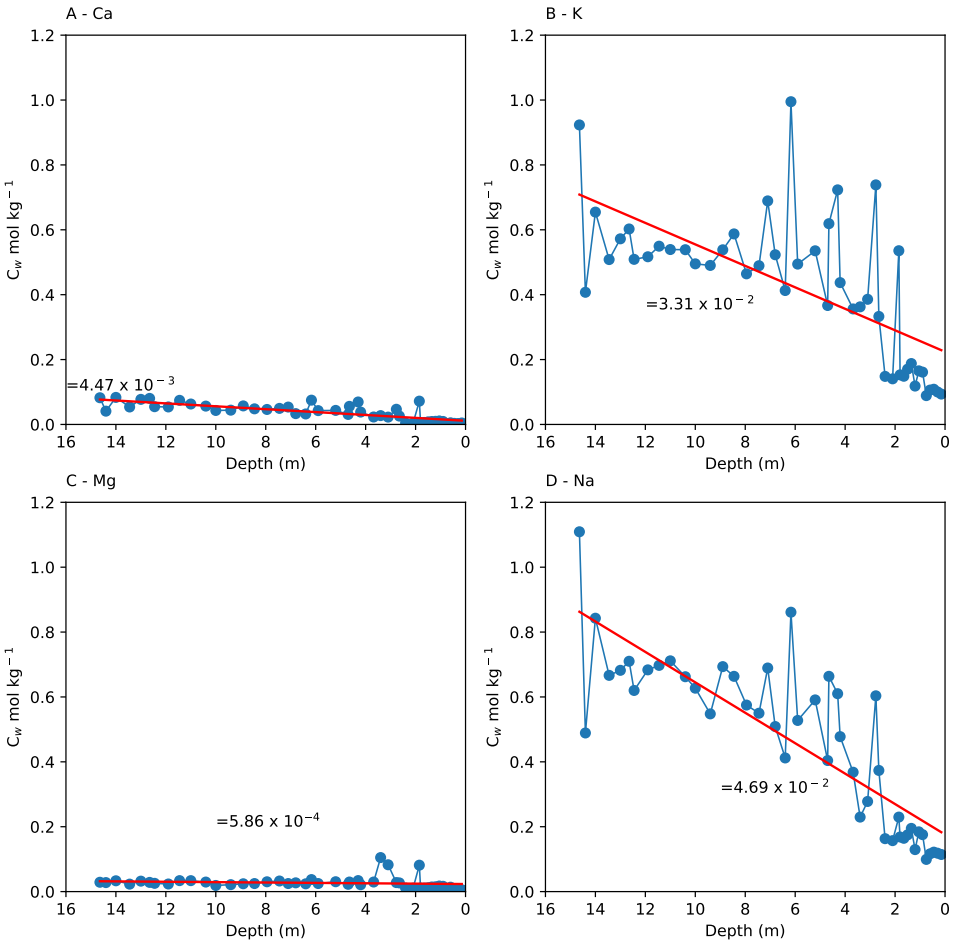

Figure 7.7: C_w values for mobile elements (a) Ca, (b) K, (c) Mg, and (d) Na within the Lysina weathering profile with element specific weathering gradients (red lines and values) calculated through the zone of predominant mass loss. Blue circles indicate samples used in the calculation of the weathering gradient. All samples were used in the calculation of weathering gradients in the Lysina profile.

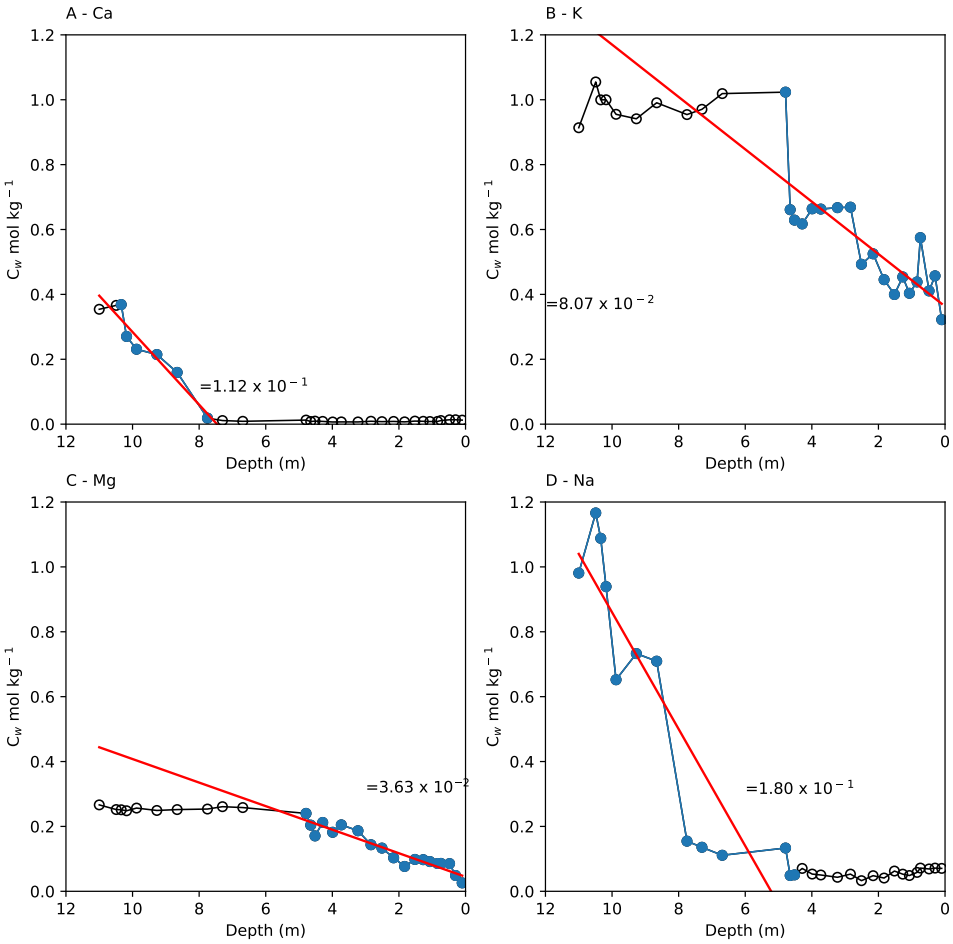

Figure 7.8: C_w values for mobile elements (a) Ca, (b) K, (c) Mg, and (d) Na within the Panola weathering profile with element specific weathering gradients (red lines and values) calculated through the zone of predominant mass loss. Blue circles indicate samples used in the calculation of the weathering gradient, while open black circles indicate values excluded from the gradient. Samples above 8 m in the Ca profile and above 4.3 m in the Na profile were excluded from gradient calculations due to near total depletion of these elements above the specified depths. Samples below 6 m were excluded from the K and Mg gradients due to no clear depletion trends below this depth.

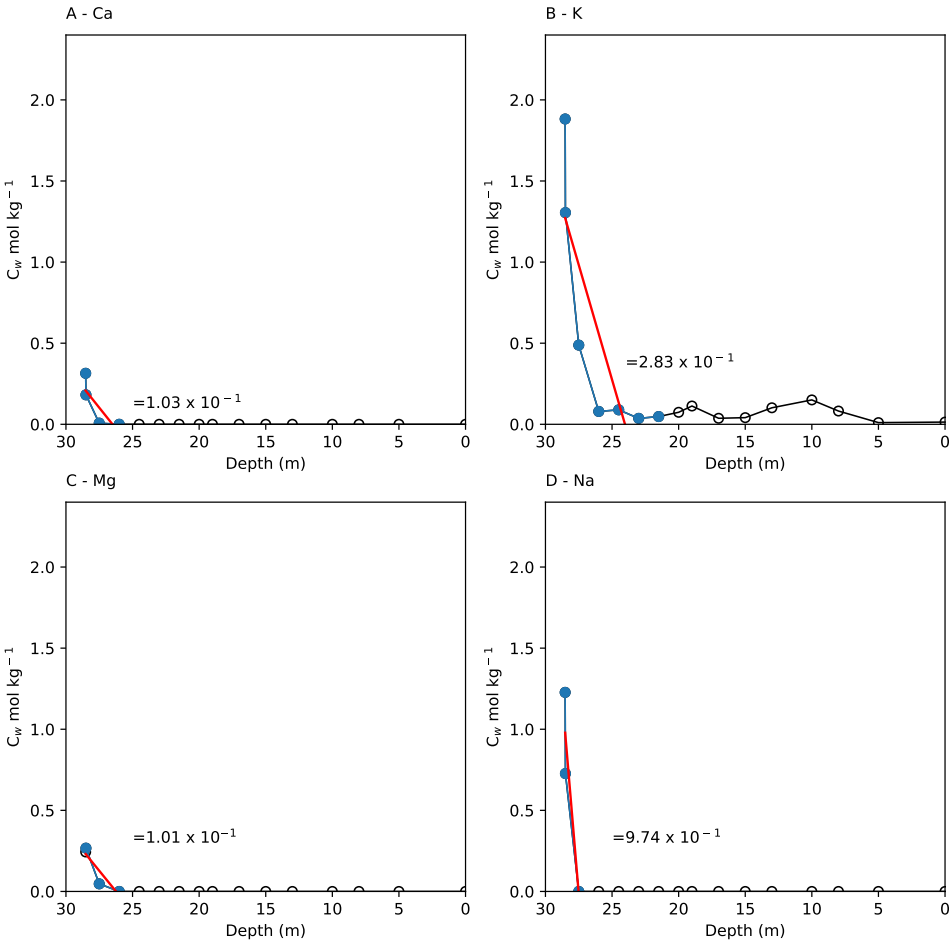

Figure 7.9: C_w values for mobile elements (a) Ca, (b) K, (c) Mg, and (d) Na within the Rawang weathering profile with element specific weathering gradients (red lines and values) calculated through the zone of predominant mass loss. Blue circles indicate samples used in the calculation of the weathering gradient, while open black circles indicate values excluded from the gradient. Most samples above 25 m depth were excluded from gradients due to near total depletion of mobile elements above this depth.

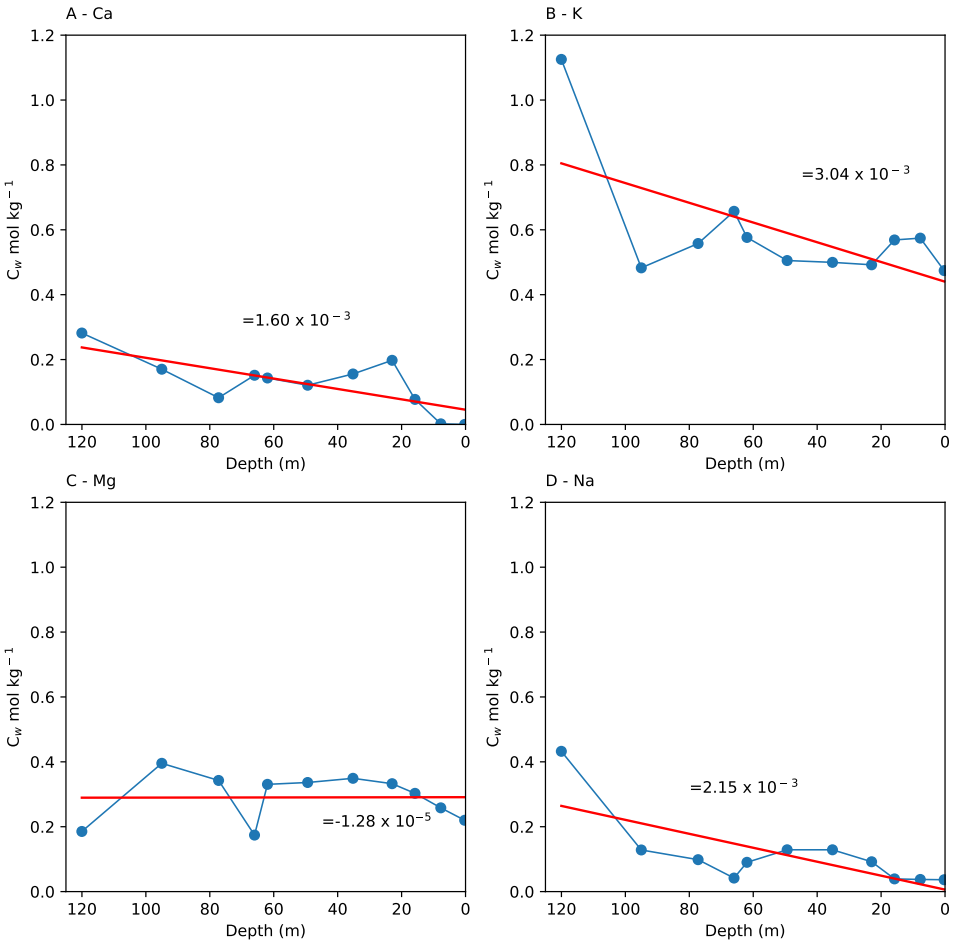

Figure 7.10: C_w values for mobile elements (a) Ca, (b) K, (c) Mg, and (d) Na within the Ringelbach weathering profile with element specific weathering gradients (red lines and values) calculated through the zone of predominant mass loss. Blue circles indicate samples used in the calculation of the weathering gradients. All samples from the Ringelbach profile were used in the calculation of weathering gradients.

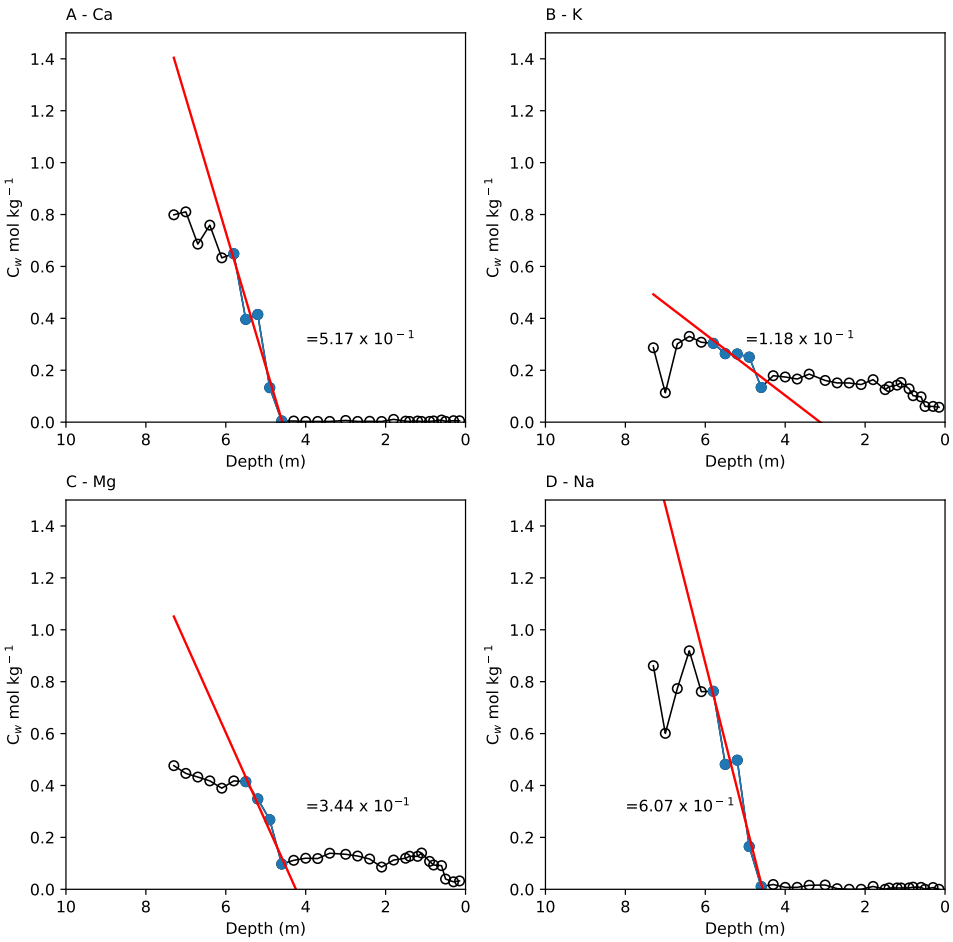

Figure 7.11: C_w values for mobile elements (a) Ca, (b) K, (c) Mg, and (d) Na within the Río Icacos weathering profile with element specific weathering gradients (red lines and values) calculated through the zone of predominant mass loss. Blue circles indicate samples used in the calculation of the weathering gradient, while open black circles indicate values excluded from the gradient. Most samples below 6 m and above 4.5 m were excluded from gradient calculations due to limited evidence of weathering and near total depletion of Ca and Na above 4.5 m, respectively. K and Mg show two zones of mass loss. Gradients for K and Mg were calculated through the zone of predominant mass loss between 6 and 4.5 m depth.

Table 7.5: Hakgala C_w Values[a]

Depth (m)	**C_w Ca (mol kg^{-1})**	**C_w K (mol kg^{-1})**	**C_w Mg (mol kg^{-1})**	**C_w Na (mol kg^{-1})**	**Sum C_w (mol kg^{-1})**
0.8	3.85 x 10^{-3}	3.34 x 10^{-2}	3.06 x 10^{-2}	4.98 x 10^{-3}	7.29 x 10^{-2}
1.12	5.00 x 10^{-3}	3.87 x 10^{-2}	3.02 x 10^{-2}	9.05 x 10^{-3}	8.30 x 10^{-2}
1.37	1.41 x 10^{-3}	4.86 x 10^{-2}	3.33 x 10^{-2}	0	8.32 x 10^{-2}
1.85	1.35 x 10^{-3}	6.08 x 10^{-2}	5.80 x 10^{-2}	5.84 x 10^{-2}	0.18
2.37	0	8.95 x 10^{-2}	5.98 x 10^{-2}	2.72 x 10^{-2}	0.18
2.75	1.03 x 10^{-3}	0.15	0.11	3.91 x 10^{-2}	0.29
3.1	5.84 x 10^{-4}	8.69 x 10^{-3}	4.88 x 10^{-3}	0	1.4 x 10^{-2}
3.4	1.38 x 10^{-3}	0.16	9.04 x 10^{-2}	0	0.25
3.85	2.78 x 10^{-3}	0.16	0.17	0	0.33
4.35	1.33 x 10^{-3}	0.13	9.97 x 10^{-2}	5.04 x 10^{-2}	0.29
4.8	4.79 x 10^{-3}	0.33	0.17	2.60 x 10^{-2}	0.53
5.25	4.04 x 10^{-3}	0.53	0.14	9.73 x 10^{-2}	0.77
5.75	2.99 x 10^{-3}	0.54	0.19	2.98 x 10^{-2}	0.76
6.25	2.32 x 10^{-3}	0.40	0.12	7.77 x 10^{-2}	0.60
6.75	7.54 x 10^{-3}	0.38	0.13	2.95 x 10^{-2}	0.54
7.25	1.98 x 10^{-2}	0.62	0.15	0.123	0.91
7.75	1.76 x 10^{-2}	0.64	0.16	8.09 x 10^{-2}	0.90
8.1	9.82 x 10^{-2}	0.98	0.19	0.34	1.6
8.67	4.14 x 10^{-2}	0.89	0.19	0.17	1.29
9.62	0.11	0.71	0.22	0.32	1.37
9.82	4.93 x 10^{-3}	0.49	0.12	1.78 x 10^{-2}	0.64
10.02	8.04 x 10^{-3}	0.81	0.17	1.94 x 10^{-2}	1.01
10.20	0.46	0.85	0.30	1.2	2.81

[a]Using data from Hewawasam et al. (2013).

Table 7.6: Longnan C_w Values[a]

Depth (m)	C_w Ca (mol kg^{-1})	C_w K (mol kg^{-1})	C_w Mg (mol kg^{-1})	C_w Na (mol kg^{-1})	Sum C_w (mol kg^{-1})
0.10	3.86 x 10^{-3}	0.24	1.74 x 10^{-2}	1.21 x 10^{-2}	0.27
0.25	2.16 x 10^{-3}	0.19	1.65 x 10^{-2}	7.83 x 10^{-3}	0.21
0.35	1.66 x 10^{-3}	0.19	1.96 x 10^{-2}	7.50 x 10^{-3}	0.22
0.45	2.04 x 10^{-3}	0.18	1.99 x 10^{-2}	7.38 x 10^{-3}	0.21
0.55	2.30 x 10^{-3}	0.18	2.08 x 10^{-2}	8.34 x 10^{-3}	0.21
0.75	2.97 x 10^{-3}	0.18	2.07 x 10^{-2}	8.08 x 10^{-3}	0.21
0.95	3.24 x 10^{-3}	0.19	2.03 x 10^{-2}	8.81 x 10^{-3}	0.22
1.15	1.49 x 10^{-3}	0.23	1.86 x 10^{-2}	1.08 x 10^{-2}	0.26
1.35	1.55 x 10^{-3}	0.24	1.73 x 10^{-2}	1.12 x 10^{-2}	0.28
1.55	2.30 x 10^{-3}	0.27	1.76 x 10^{-2}	1.25 x 10^{-2}	0.31
1.75	6.49 x 10^{-3}	0.24	1.80 x 10^{-2}	1.17 x 10^{-2}	0.28
1.85	2.38 x 10^{-3}	0.24	1.99 x 10^{-2}	1.29 x 10^{-2}	0.27
1.95	3.40 x 10^{-3}	0.33	1.89 x 10^{-2}	1.23 x 10^{-2}	0.37
2.10	2.85 x 10^{-3}	0.32	1.79 x 10^{-2}	1.29 x 10^{-2}	0.35
2.30	4.46 x 10^{-3}	0.37	1.86 x 10^{-2}	1.61 x 10^{-2}	0.41
2.70	2.97 x 10^{-3}	0.45	1.65 x 10^{-2}	1.61 x 10^{-2}	0.49
2.90	2.64 x 10^{-3}	0.38	1.65 x 10^{-2}	1.43 x 10^{-2}	0.41
3.10	5.28 x 10^{-3}	0.45	1.84 x 10^{-2}	1.67 x 10^{-2}	0.49
3.30	5.49 x 10^{-3}	0.55	1.91 x 10^{-2}	1.99 x 10^{-2}	0.59
3.70	2.46 x 10^{-3}	0.78	1.20 x 10^{-2}	2.45 x 10^{-2}	0.82
3.90	2.74 x 10^{-3}	0.96	1.34 x 10^{-2}	3.48 x 10^{-2}	1.01
4.10	2.38 x 10^{-3}	0.83	1.32 x 10^{-2}	2.58 x 10^{-2}	0.88
4.70	2.55 x 10^{-3}	0.86	1.42 x 10^{-2}	2.54 x 10^{-2}	0.90
5.40	3.40 x 10^{-3}	1.24	1.42 x 10^{-2}	0.04	1.30
5.70	2.74 x 10^{-3}	1.03	1.34 x 10^{-2}	3.97 x 10^{-2}	1.09
6.50	5.10 x 10^{-3}	1.25	1.65 x 10^{-2}	0.10	1.38
7.10	1.24 x 10^{-2}	1.20	1.51 x 10^{-2}	0.42	1.64
7.70	6.86 x 10^{-3}	0.95	1.52 x 10^{-2}	0.16	1.14
8.75	5.94 x 10^{-3}	1.07	2.07 x 10^{-2}	0.13	1.22
9.25	7.75 x 10^{-3}	1.08	2.16 x 10^{-2}	0.20	1.30
9.75	1.70 x 10^{-2}	1.25	1.89 x 10^{-2}	0.58	1.87
10.5	2.18 x 10^{-2}	1.27	1.931 x 10^{-2}	0.70	2.00
12.00	0.16	1.11	4.47 x 10^{-2}	1.00	2.31

[a]Using data from Liu et al. (2016).

Table 7.7: Lysina C_w Values[a]

Depth (m)	C_w Ca (mol kg^{-1})	C_w K (mol kg^{-1})	C_w Mg (mol kg^{-1})	C_w Na (mol kg^{-1})	Sum C_w (mol kg^{-1})
0.15	4.50 x 10^{-3}	9.36 x 10^{-2}	5.62 x 10^{-3}	1.14 x 10^{-1}	2.18 x 10^{-1}
0.30	2.77 x 10^{-3}	1.00 x 10^{-1}	4.64 x 10^{-3}	1.18 x 10^{-1}	2.26 x 10^{-1}
0.45	3.31 x 10^{-3}	1.09 x 10^{-1}	8.37 x 10^{-3}	1.22 x 10^{-1}	2.42 x 10^{-1}
0.60	5.02 x 10^{-3}	1.06 x 10^{-1}	1.35 x 10^{-2}	1.16 x 10^{-1}	2.41 x 10^{-1}
0.75	2.74 x 10^{-3}	8.89 x 10^{-2}	8.14 x 10^{-3}	9.92 x 10^{-2}	1.99 x 10^{-1}
0.90	9.23 x 10^{-3}	1.61 x 10^{-1}	1.63 x 10^{-2}	1.76 x 10^{-1}	3.62 x 10^{-1}
1.05	1.08 x 10^{-2}	1.65 x 10^{-1}	1.72 x 10^{-2}	1.84 x 10^{-1}	3.77 x 10^{-1}
1.20	9.63 x 10^{-3}	1.18 x 10^{-1}	1.48 x 10^{-2}	1.29 x 10^{-1}	2.72 x 10^{-1}
1.35	9.05 x 10^{-3}	1.88 x 10^{-1}	1.42 x 10^{-2}	1.95 x 10^{-1}	4.06 x 10^{-1}
1.50	7.94 x 10^{-3}	1.70 x 10^{-1}	1.19 x 10^{-2}	1.75 x 10^{-1}	3.65 x 10^{-1}
1.65	6.15 x 10^{-3}	1.49 x 10^{-1}	1.09 x 10^{-2}	1.64 x 10^{-1}	3.30 x 10^{-1}
1.80	4.70 x 10^{-3}	1.53 x 10^{-1}	1.09 x 10^{-2}	1.68 x 10^{-1}	3.37 x 10^{-1}
1.85	7.19 x 10^{-2}	5.36 x 10^{-1}	8.15 x 10^{-2}	2.30 x 10^{-1}	9.19 x 10^{-1}
2.10	4.16 x 10^{-3}	1.41 x 10^{-1}	1.06 x 10^{-2}	1.57 x 10^{-1}	3.12 x 10^{-1}
2.40	4.17 x 10^{-3}	1.48 x 10^{-1}	1.09 x 10^{-2}	1.63 x 10^{-1}	3.26 x 10^{-1}
2.65	2.58 x 10^{-2}	3.33 x 10^{-1}	2.68 x 10^{-2}	3.74 x 10^{-1}	7.59 x 10^{-1}
2.77	4.68 x 10^{-2}	7.38 x 10^{-1}	2.78 x 10^{-2}	6.04 x 10^{-1}	1.42
3.10	2.26 x 10^{-2}	3.86 x 10^{-1}	8.27 x 10^{-2}	2.78 x 10^{-1}	7.69 x 10^{-1}
3.40	2.72 x 10^{-2}	3.63 x 10^{-1}	1.05 x 10^{-1}	2.30 x 10^{-1}	7.24 x 10^{-1}
3.68	2.30 x 10^{-2}	3.56 x 10^{-1}	2.95 x 10^{-2}	3.68 x 10^{-1}	7.77 x 10^{-1}
4.20	3.82 x 10^{-2}	4.37 x 10^{-1}	2.11 x 10^{-2}	4.78 x 10^{-1}	9.74 x 10^{-1}
4.30	6.92 x 10^{-2}	7.23 x 10^{-1}	3.39 x 10^{-2}	6.10 x 10^{-1}	1.44
4.65	5.58 x 10^{-2}	6.19 x 10^{-1}	2.95 x 10^{-2}	6.64 x 10^{-1}	1.37
4.70	3.09 x 10^{-2}	3.67 x 10^{-1}	2.25 x 10^{-2}	4.04 x 10^{-1}	8.24 x 10^{-1}
5.20	4.33 x 10^{-2}	5.35 x 10^{-1}	3.04 x 10^{-2}	5.91 x 10^{-1}	1.20
5.90	4.26 x 10^{-2}	4.94 x 10^{-1}	2.49 x 10^{-2}	5.28 x 10^{-1}	1.09
6.17	7.49 x 10^{-2}	9.95 x 10^{-1}	3.70 x 10^{-2}	8.61 x 10^{-1}	1.97
6.40	3.23 x 10^{-2}	4.13 x 10^{-1}	2.40 x 10^{-2}	4.12 x 10^{-1}	8.81 x 10^{-1}
6.80	3.34 x 10^{-2}	5.23 x 10^{-1}	2.70 x 10^{-2}	5.09 x 10^{-1}	1.09
7.10	5.36 x 10^{-2}	6.89 x 10^{-1}	2.48 x 10^{-2}	6.89 x 10^{-1}	1.46
7.45	4.95 x 10^{-2}	4.89 x 10^{-1}	3.26 x 10^{-2}	5.50 x 10^{-1}	1.12
7.95	4.62 x 10^{-2}	4.64 x 10^{-1}	3.02 x 10^{-2}	5.75 x 10^{-1}	1.12
8.45	4.81 x 10^{-2}	5.87 x 10^{-1}	2.48 x 10^{-2}	6.64 x 10^{-1}	1.32
8.90	5.72 x 10^{-2}	5.38 x 10^{-1}	2.41 x 10^{-2}	6.93 x 10^{-1}	1.31
9.40	4.40 x 10^{-2}	4.90 x 10^{-1}	2.14 x 10^{-2}	5.48 x 10^{-1}	1.10
10.00	4.31 x 10^{-2}	4.95 x 10^{-1}	1.89 x 10^{-2}	6.27 x 10^{-1}	1.18
10.40	5.65 x 10^{-2}	5.39 x 10^{-1}	2.94 x 10^{-2}	6.62 x 10^{-1}	1.29
11.00	6.30 x 10^{-2}	5.39 x 10^{-1}	3.38 x 10^{-2}	7.11 x 10^{-1}	1.35
11.45	7.43 x 10^{-2}	5.49 x 10^{-1}	3.38 x 10^{-2}	6.97 x 10^{-1}	1.35
11.90	5.39 x 10^{-2}	5.17 x 10^{-1}	2.34 x 10^{-2}	6.84 x 10^{-1}	1.28
12.45	5.47 x 10^{-2}	5.09 x 10^{-1}	2.55 x 10^{-2}	6.20 x 10^{-1}	1.21
12.65	8.03 x 10^{-2}	6.03 x 10^{-1}	2.84 x 10^{-2}	7.10 x 10^{-1}	1.42
13.00	7.73 x 10^{-2}	5.72 x 10^{-1}	3.22 x 10^{-2}	6.82 x 10^{-1}	1.36
13.45	5.38 x 10^{-2}	5.08 x 10^{-1}	2.30 x 10^{-2}	6.67 x 10^{-1}	1.25
14.00	8.34 x 10^{-2}	6.55 x 10^{-1}	3.33 x 10^{-2}	8.43 x 10^{-1}	1.61
14.40	4.10 x 10^{-2}	4.07 x 10^{-1}	2.78 x 10^{-2}	4.89 x 10^{-1}	9.65 x 10^{-1}
14.64	8.23 x 10^{-2}	9.23 x 10^{-1}	2.88 x 10^{-2}	1.11	2.14

[a]Using data from Nwaogu (2014); Štědrá et al. (2016), and Chapter 2.

Table 7.8: Panola C_w Values[a]

Depth (m)	C_w Ca (mol kg^{-1})	C_w K (mol kg^{-1})	C_w Mg (mol kg^{-1})	C_w Na (mol kg^{-1})	Sum C_w (mol kg^{-1})
0.10	1.24 x 10^{-2}	3.22 x 10^{-1}	2.59 x 10^{-2}	7.06 x 10^{-2}	4.31 x 10^{-1}
0.30	1.36 x 10^{-2}	4.57 x 10^{-1}	4.87 x 10^{-2}	7.15 x 10^{-2}	5.91 x 10^{-1}
0.48	1.35 x 10^{-2}	4.11 x 10^{-1}	8.54 x 10^{-2}	6.89 x 10^{-2}	5.78 x 10^{-1}
0.74	1.11 x 10^{-2}	5.75 x 10^{-1}	8.59 x 10^{-2}	7.16 x 10^{-2}	7.44 x 10^{-1}
0.84	8.40 x 10^{-3}	4.38 x 10^{-1}	8.57 x 10^{-2}	5.83 x 10^{-2}	5.91 x 10^{-1}
1.07	8.07 x 10^{-3}	4.03 x 10^{-1}	9.17 x 10^{-2}	4.87 x 10^{-2}	5.52 x 10^{-1}
1.27	8.76 x 10^{-3}	4.54 x 10^{-1}	9.75 x 10^{-2}	5.29 x 10^{-2}	6.13 x 10^{-1}
1.52	9.41 x 10^{-3}	4.00 x 10^{-1}	9.82 x 10^{-2}	6.24 x 10^{-2}	5.70 x 10^{-1}
1.83	7.06 x 10^{-3}	4.45 x 10^{-1}	7.66 x 10^{-2}	4.09 x 10^{-2}	5.70 x 10^{-1}
2.16	8.40 x 10^{-3}	5.25 x 10^{-1}	1.03 x 10^{-1}	4.81 x 10^{-2}	6.85 x 10^{-1}
2.51	7.76 x 10^{-3}	4.93 x 10^{-1}	1.33 x 10^{-1}	3.28 x 10^{-2}	6.66 x 10^{-1}
2.84	8.92 x 10^{-3}	6.69 x 10^{-1}	1.44 x 10^{-1}	5.30 x 10^{-2}	8.74 x 10^{-1}
3.23	6.82 x 10^{-3}	6.67 x 10^{-1}	1.87 x 10^{-1}	4.32 x 10^{-2}	9.04 x 10^{-1}
3.73	6.94 x 10^{-3}	6.63 x 10^{-1}	2.05 x 10^{-1}	5.03 x 10^{-2}	9.25 x 10^{-1}
3.99	6.67 x 10^{-3}	6.64 x 10^{-1}	1.82 x 10^{-1}	5.31 x 10^{-2}	9.06 x 10^{-1}
4.29	8.47 x 10^{-3}	6.17 x 10^{-1}	2.12 x 10^{-1}	7.05 x 10^{-2}	9.08 x 10^{-1}
4.52	9.34 x 10^{-3}	6.29 x 10^{-1}	1.71 x 10^{-1}	5.07 x 10^{-2}	8.60 x 10^{-1}
4.65	8.07 x 10^{-3}	6.61 x 10^{-1}	2.04 x 10^{-1}	4.87 x 10^{-2}	9.22 x 10^{-1}
4.79	1.26 x 10^{-2}	1.02	2.40 x 10^{-1}	1.33 x 10^{-1}	1.41
6.69	8.76 x 10^{-3}	1.02	2.58 x 10^{-1}	1.11 x 10^{-1}	1.40
7.30	1.11 x 10^{-2}	9.70 x 10^{-1}	2.61 x 10^{-1}	1.36 x 10^{-1}	1.38
7.75	1.85 x 10^{-2}	9.54 x 10^{-1}	2.54 x 10^{-1}	1.55 x 10^{-1}	1.38
8.66	1.59 x 10^{-1}	9.91 x 10^{-1}	2.52 x 10^{-1}	7.09 x 10^{-1}	2.11
9.27	2.15 x 10^{-1}	9.41 x 10^{-1}	2.49 x 10^{-1}	7.33 x 10^{-1}	2.14
9.88	2.31 x 10^{-1}	9.55 x 10^{-1}	2.57 x 10^{-1}	6.52 x 10^{-1}	2.09
10.18	2.70 x 10^{-1}	1.00	2.48 x 10^{-1}	9.39 x 10^{-1}	2.46
10.34	3.69 x 10^{-1}	1.00	2.51 x 10^{-1}	1.09	2.71
10.49	3.66 x 10^{-1}	1.05	2.52 x 10^{-1}	1.17	2.84
11.00	3.54 x 10^{-1}	9.14 x 10^{-1}	2.66 x 10^{-1}	9.81 x 10^{-1}	2.52

[a]Using data from White et al. (2001).

Table 7.9: Rawang C_w Values[a]

Depth (m)	C_w Ca (mol kg^{-1})	C_w K (mol kg^{-1})	C_w Mg (mol kg^{-1})	C_w Na (mol kg^{-1})	Sum C_w (mol kg^{-1})
0.00	0.00	1.36 x 10^{-2}	0.00	0.00	1.36 x 10^{-2}
5.00	0.00	1.04 x 10^{-2}	0.00	0.00	1.04 x 10^{-2}
8.00	0.00	8.17 x 10^{-2}	0.00	0.00	8.17 x 10^{-2}
10.00	0.00	1.50 x 10^{-1}	0.00	0.00	1.50 x 10^{-1}
13.00	0.00	1.02 x 10^{-1}	0.00	0.00	1.02 x 10^{-1}
15.00	0.00	4.10 x 10^{-2}	0.00	0.00	4.10 x 10^{-2}
17.00	0.00	3.71 x 10^{-2}	0.00	0.00	3.71 x 10^{-2}
19.00	0.00	1.13 x 10^{-1}	0.00	0.00	1.13 x 10^{-1}
20.00	0.00	7.40 x 10^{-2}	0.00	0.00	7.40 x 10^{-2}
21.50	0.00	4.78 x 10^{-2}	0.00	0.00	4.78 x 10^{-2}
23.00	0.00	3.65 x 10^{-2}	0.00	0.00	3.65 x 10^{-2}
24.50	0.00	8.91 x 10^{-2}	0.00	0.00	8.91 x 10^{-2}
26.00	0.00	7.93 x 10^{-2}	0.00	0.00	7.93 x 10^{-2}
27.50	7.02 x 10^{-3}	4.88 x 10^{-1}	4.69 x 10^{-2}	0.00	5.42 x 10^{-1}
28.50	1.82 x 10^{-1}	1.30	2.67 x 10^{-1}	7.27 x 10^{-1}	2.48
28.52	3.14 x 10^{-1}	1.88	2.43 x 10^{-1}	1.23	3.67

[a]Using data from Yusoff et al. (2013).

Table 7.10: Ringelbach C_w Values[a]

Depth (m)[b]	C_w Ca (mol kg^{-1})	C_w K (mol kg^{-1})	C_w Mg (mol kg^{-1})	C_w Na (mol kg^{-1})	Sum C_w (mol kg^{-1})
0.27	0.00	4.74 x 10^{-1}	2.20 x 10^{-1}	3.65 x 10^{-2}	7.31 x 10^{-1}
7.74	1.86 x 10^{-3}	5.74 x 10^{-1}	2.58 x 10^{-1}	3.74 x 10^{-2}	8.72 x 10^{-1}
15.81	7.72 x 10^{-2}	5.69 x 10^{-1}	3.03 x 10^{-1}	3.92 x 10^{-2}	9.88 x 10^{-1}
22.97	1.98 x 10^{-1}	4.92 x 10^{-1}	3.33 x 10^{-1}	9.20 x 10^{-2}	1.11
35.21	1.56 x 10^{-1}	5.00 x 10^{-1}	3.49 x 10^{-1}	1.29 x 10^{-1}	1.13
49.39	1.21 x 10^{-1}	5.05 x 10^{-1}	3.36 x 10^{-1}	1.29 x 10^{-1}	1.09
61.96	1.43 x 10^{-1}	5.76 x 10^{-1}	3.31 x 10^{-1}	9.02 x 10^{-2}	1.14
66.01	1.52 x 10^{-1}	6.57 x 10^{-1}	1.74 x 10^{-1}	4.17 x 10^{-2}	1.02
77.25	8.23 x 10^{-2}	5.58 x 10^{-1}	3.43 x 10^{-1}	9.84 x 10^{-2}	1.08
95.02	1.70 x 10^{-1}	4.83 x 10^{-1}	3.95 x 10^{-1}	1.28 x 10^{-1}	1.18
120.03	2.82 x 10^{-1}	1.13	1.85 x 10^{-1}	4.32 x 10^{-1}	2.02

[a]Using data from Schaffhauser et al. (2014). [b] Ringelbach is overlain by a 27m thick sandstone layer, 0 m depth represents the base of the sandstone layer.

Table 7.11: Río Icacos C_w Values[a]

Depth (m)	C_w Ca (mol kg^{-1})	C_w K (mol kg^{-1})	C_w Mg (mol kg^{-1})	C_w Na (mol kg^{-1})	Sum C_w (mol kg^{-1})
0.15	5.35 x 10^{-3}	5.73 x 10^{-2}	3.23 x 10^{-2}	0.00	9.49 x 10^{-2}
0.30	5.66 x 10^{-3}	6.07 x 10^{-2}	2.89 x 10^{-2}	6.83 x 10^{-3}	1.02 x 10^{-1}
0.50	2.99 x 10^{-3}	6.04 x 10^{-2}	3.95 x 10^{-2}	0.00	1.03 x 10^{-1}
0.60	8.20 x 10^{-3}	9.76 x 10^{-2}	9.12 x 10^{-2}	7.41 x 10^{-3}	2.04 x 10^{-1}
0.80	4.59 x 10^{-3}	1.02 x 10^{-1}	9.36 x 10^{-2}	8.30 x 10^{-3}	2.08 x 10^{-1}
0.90	2.92 x 10^{-3}	1.29 x 10^{-1}	1.08 x 10^{-1}	5.28 x 10^{-3}	2.44 x 10^{-1}
1.10	2.79 x 10^{-3}	1.53 x 10^{-1}	1.40 x 10^{-1}	5.05 x 10^{-3}	3.01 x 10^{-1}
1.20	4.28 x 10^{-3}	1.43 x 10^{-1}	1.27 x 10^{-1}	5.16 x 10^{-3}	2.79 x 10^{-1}
1.40	2.73 x 10^{-3}	1.37 x 10^{-1}	1.27 x 10^{-1}	4.94 x 10^{-3}	2.72 x 10^{-1}
1.50	3.85 x 10^{-3}	1.25 x 10^{-1}	1.20 x 10^{-1}	0.00	2.49 x 10^{-1}
1.80	1.07 x 10^{-2}	1.64 x 10^{-1}	1.13 x 10^{-1}	1.11 x 10^{-2}	2.98 x 10^{-1}
2.10	2.68 x 10^{-3}	1.45 x 10^{-1}	8.56 x 10^{-2}	0.00	2.33 x 10^{-1}
2.40	3.29 x 10^{-3}	1.51 x 10^{-1}	1.17 x 10^{-1}	0.00	2.71 x 10^{-1}
2.70	2.79 x 10^{-3}	1.51 x 10^{-1}	1.28 x 10^{-1}	2.53 x 10^{-3}	2.85 x 10^{-1}
3.00	6.55 x 10^{-3}	1.61 x 10^{-1}	1.35 x 10^{-1}	1.66 x 10^{-2}	3.19 x 10^{-1}
3.40	2.85 x 10^{-3}	1.85 x 10^{-1}	1.39 x 10^{-1}	1.55 x 10^{-2}	3.42 x 10^{-1}
3.70	2.79 x 10^{-3}	1.66 x 10^{-1}	1.18 x 10^{-1}	7.58 x 10^{-3}	2.95 x 10^{-1}
4.00	2.73 x 10^{-3}	1.74 x 10^{-1}	1.20 x 10^{-1}	7.41 x 10^{-3}	3.04 x 10^{-1}
4.30	4.38 x 10^{-3}	1.79 x 10^{-1}	1.12 x 10^{-1}	1.85 x 10^{-2}	3.13 x 10^{-1}
4.60	4.59 x 10^{-3}	1.34 x 10^{-1}	9.73 x 10^{-2}	1.04 x 10^{-2}	2.46 x 10^{-1}
4.90	1.33 x 10^{-1}	2.51 x 10^{-1}	2.68 x 10^{-1}	1.65 x 10^{-1}	8.16 x 10^{-1}
5.20	4.15 x 10^{-1}	2.63 x 10^{-1}	3.48 x 10^{-1}	4.97 x 10^{-1}	1.52
5.50	3.96 x 10^{-1}	2.64 x 10^{-1}	4.15 x 10^{-1}	4.81 x 10^{-1}	1.56
5.80	6.49 x 10^{-1}	3.04 x 10^{-1}	4.18 x 10^{-1}	7.63 x 10^{-1}	2.13
6.10	6.33 x 10^{-1}	3.08 x 10^{-1}	3.90 x 10^{-1}	7.62 x 10^{-1}	2.09
6.40	7.59 x 10^{-1}	3.30 x 10^{-1}	4.18 x 10^{-1}	9.19 x 10^{-1}	2.43
6.70	6.86 x 10^{-1}	3.02 x 10^{-1}	4.33 x 10^{-1}	7.73 x 10^{-1}	2.19
7.00	8.10 x 10^{-1}	1.13 x 10^{-1}	4.47 x 10^{-1}	6.01 x 10^{-1}	1.97
7.30	7.99 x 10^{-1}	2.87 x 10^{-1}	4.76 x 10^{-1}	8.62 x 10^{-1}	2.42

[a]Using data from Buss et al. (2017).